Spectroscopic and Multivariate Approaches for Tumor Diagnostics and -Therapy

Dissertation
der Mathematisch-Naturwissenschaftlichen Fakultät
der Eberhard Karls Universität Tübingen
zur Erlangung des Grades eines
Doktors der Naturwissenschaften
(Dr. rer. nat.)

vorgelegt von
Miriam Corina Bassler (geb. Scholz)
aus Gießen

Tübingen
2022

Gedruckt mit Genehmigung der Mathematisch-Naturwissenschaftlichen Fakultät der Eberhard Karls Universität Tübingen.

Tag der mündlichen Qualifikation:	09.03.2023
Dekan:	Prof. Dr. Thilo Stehle
1. Berichterstatter/-in:	Prof. Dr. Marc Brecht
2. Berichterstatter/-in:	Prof. Dr. Thomas Chassé

Abstract

As a result of still increasing cancer incidences worldwide, the demand of novel diagnostics and therapies is more important than ever. The great complexity and heterogeneity of differently originating tumors make it often complicated to apply one overall diagnostic or therapeutic approach. Especially new cancer therapies require a deep knowledge and understanding of the actual operating principal, when applied to certain cancer types for the first time. The highest goals of diagnosis and therapy are to prevent an on-going progression, to improve a patient's life quality or in best cases to allow a complete cure. To achieve this, new attempts in both fields have to be discovered. One arising possibility in diagnosis are spectroscopy-supported multivariate models for tumor identification and discrimination from normal tissues. For that purpose, various spectroscopic technologies, also applied as imaging modalities, were coupled with multivariate data analysis. Their advantage is to objectively represent chemical or morphological information of tumors or tissues and to use it for their classification into different tumor or tissue types. Moreover, spectroscopy-based multivariate models enable to define reasons for the obtained differentiation and can even be used to predict undetermined tissue areas. In the first part of this thesis, new insights in spectroscopy-based multivariate models for tumor diagnostics are gained. A multi-view approach was chosen to address different aspects in spectroscopy or spectroscopic imaging and multivariate model development. This includes the comparison of Whiskbroom and Pushbroom darkfield elastic light scattering spectroscopic imaging (DF ELSS) models regarding their abilities to identify head and neck tumors in mouse tongues. It was determined, which model is more capable and advanced to diagnose the tumors, also from a practical perspective, and which is additionally more suitable to predict unknown tongue areas. The Pushbroom DF ELSS model was ascertained to be more qualified in lingual head and neck tumor identification and differentiation from gland / muscle and healthy epithelium tissue. Moreover, Pushbroom DF ELSS imaging was defined as the faster high-throughput, easier to handle and less expensive technology for this job. Furthermore, multivariate models on basis of Raman imaging and Fourier-transform infrared (FTIR) spectroscopy were developed for hardly explored salivary gland tumors of the parotid (parotid tumors) in order to differentiate between different tumor entities and to understand the effects of tissue preparation, respectively. The Raman imaging based multivariate model could successfully discriminate two types of benign parotid tumors from normal salivary gland and performed exceptionally in predicting unknown parotid tissues. Multivariate models formed by FTIR data from differently prepared parotid tumors and salivary gland could reveal that formalin fixation had almost no effect on the chemical tissue composition and formalin-fixed tissues closely resembled the native state. Additionally, paraffin and dewaxing treatments greatly impacted the tissue chemistry and in case of dewaxing even caused a loss of component information. All model outcomes were assessed by an additional histopathological characterization and the models themselves were evaluated regarding their quality by performance measures and their practical applicability in clinics. The obtained results should contribute to a transition from laboratory models to real, complementary diagnostic tools in a clinical routine.

In the second part of this thesis, new findings were obtained to understand and improve photodynamic therapy (PDT) with hypericin as a new therapeutic treatment for primary brain tumors. For this purpose, *in vitro* cell culture models were implemented, which represent glioma tumors in the brain. Important aspects of hypericin PDT for glioma treatments are the hypericin's distribution and accumulation in the tumors and the respective interactions between both under different hypericin incubation conditions. This was studied by fluorescence microscopy and fluorescence lifetime imaging microscopy (FLIM) in a tumor cell spheroid model, which better reflects the 3D cell-cell- and cell-matrix interactions. Fluorescence microscopy exhibited that hypericin gradients into the tumor spheroids occurred at short incubation periods and low hypericin concentrations, whereas long incubation times and high hypericin concentrations caused a homogeneous accumulation across the spheroid. In FLIM analysis, hypericin fluorescence lifetimes (FLT) were related to prevalent, environmental factors in the spheroids. Short incubation periods caused a FLT gradient inside, whereas long incubation times revealed more homogeneous FLTs with partially lower FLTs in the spheroid periphery than in the center. This was correlated to several environmental effects, including pH and metabolic changes, Förster resonance energy transfer (FRET)- or excimer like interactions and cellular redistribution of hypericin. To specifically understand the cell death mechanism for glioma tumors by hypericin PDT, this treatment was applied to glioma cells and analyzed by FLIM in consideration of different irradiation wavelengths. The results showed individual steps of the dying process by using two additional label components. Important steps were cell shrinkage and rounding, bleb formation, medium diffusion into the cell body and membrane bursting. Explanations for each step were deduced and the death mechanism for glioma cells was declared to be initially apoptosis followed by necrosis. With the help of these results, PDT conditions with hypericin can be adapted and its efficiency can be increased to achieve an ideal treatment for brain tumors *in vivo*.

Zusammenfassung

Aufgrund der weiterhin zunehmenden Zahl an Krebsneuerkrankungen weltweit, herrscht ein nie dagewesener Bedarf an neuen Diagnose- und Therapiemöglichkeiten. Diese sind jedoch angesichts der hohen Komplexität und Heterogenität verschiedener Tumorarten nicht allgemein anwendbar und erfordern ein tiefes Verständnis und Grundwissen des Wirkmechanismus, insbesondere bei der ersten Anwendung. Krebsdiagnose und -therapie können eine frühzeitige Erkennung der Tumore ermöglichen und im Idealfall die weitere Ausbreitung und Streuung der Krebszellen verhindern. Dadurch können eine Lebensqualitätsverbesserung oder vollständige Heilung des Patienten erzielt werden. Dies erfordert jedoch neue Diagnose- und Therapieansätze. Hierzu zählen Spektroskopie-basierte multivariate Modelle als neue Diagnostikmethoden in der Tumorerkennung und Differenzierung. Dabei werden verschiedene spektroskopische und bildgebende Methoden zur Datenerhebung eingesetzt und diese mittels multivariater Analysemethoden ausgewertet. Die dadurch gebildeten Modelle haben den Vorteil, dass sie die chemische oder morphologische Information des Tumorgewebes objektiv auf Basis spektroskopischer Daten wiedergeben und sich daher zur Klassifizierung von verschiedenen Tumor- und Gewebearten eignen. Darüber hinaus können mit Hilfe dieser Modelle gewebsspezifische Hintergründe und Ursachen für die Tumorklassifizierung bestimmt und sogar eine Prognose unbekannter Biopsate ermöglicht werden. Im ersten Teil der vorliegenden Doktorarbeit werden daher neue Spektroskopie-basierte multivariate Modelle für die Tumordiagnostik entwickelt, um somit neue Erkenntnisse in diesem Feld zu generieren. Dabei werden verschiedene Aspekte in Spektroskopie, spektraler Bildgebung und multivariater Modellbildung untersucht, die zu einer erfolgreichen Implementierung der Modelle als Diagnosemethode beitragen. Dies umfasst den Vergleich zwischen zwei bildgebenden Detektionsprinzipien (Whiskbroom und Pushbroom) zur Messung elastischer Lichtstreuung mittels Dunkelfeldbeleuchtung und deren Modelle zur Identifizierung von Kopf-Hals-Karzinomen in Mauszungen. Dabei eignete sich das Pushbroom Modell besser zur Differenzierung von Kopf-Hals-Karzinomen von gesundem Drüsengewebe, Muskelgewebe und Epithelium und kann erfolgreich für die Diagnose anhand unbekannter Kopf-Hals-Biopsate eingesetzt werden. Das Pushbroom-Verfahren hat sich zudem als schnellere und günstigere Hochdurchsatzmethode mit einfacherer Handhabung im Vergleich zur Whiskbroom-Technologie herausgestellt. Des Weiteren wurden multivariate Modelle basierend auf spektroskopisch-bildgebenden Raman Daten und Fourier-transformierten infrarotspektroskopischen (FTIR) Daten entwickelt, um die Unterscheidung verschiedener, selten untersuchter Ohrspeicheldrüsentumorentitäten zu ermöglichen und den Einfluss diverser Probenpräparationen zu studieren. Mit Hilfe des Raman Modells konnten pleomorphe Adenoma, Warthin-Tumoren und gesundes Ohrspeicheldrüsengewebe voneinander unterschieden und das Modell zur Entitätserkennung genutzt werden. Die Entwicklung und Verwendung unterschiedlicher FTIR Modelle zur Untersuchung gängiger Gewebspräparationsmethoden von Ohrspeicheldrüsentumoren ergab, dass Formalinfixierungen nahezu keinen Einfluss auf die chemische Zusammensetzung der Ohrspeicheldrüsengewebe haben und diese dem nativen Gewebe in sehr hohem Maß ähneln.

Paraffineinbettung und Entparaffinierung hingegen verändern die chemische Beschaffenheit und verursachen sogar das Herauslösen gewebsspezifischer Komponenten. Alle gebildeten multivariaten Modelle wurden zusätzlich histopathologisch validiert und im Hinblick auf Qualität anhand von Leistungsparametern und Praktikabilität bewertet. Die Ergebnisse sollen dazu beitragen einen Übergang von reinen Labormodellen hin zu ergänzenden, etablierten Diagnosemodellen im klinischen Umfeld zu schaffen.

Im zweiten Teil der vorliegenden Doktorarbeit wurden neue Erkenntnisse über die photodynamische Therapie (PDT) mit Hypericin als Behandlungsmethode für primär hirneigene Tumore generiert. Dafür wurden zunächst *in vitro* Zellmodelle implementiert, welche die Gliom-Tumoren im Gehirn repräsentieren. Für eine erfolgreiche Therapie der Hirntumore spielen die Verteilung von Hypericin, seine Aufnahme und die Wechselwirkungen mit dem Tumorgewebe im Rahmen verschiedener Hypericin Inkubationsbedingungen eine wichtige Rolle. Diese wurden mittels Fluoreszenzmikroskopie und Fluoreszenzlebensdauermikroskopie (FLIM) anhand von Tumorzellsphäroiden untersucht, welche die 3D Zell-Zell-Kontakte und Zell-Matrix-Wechselwirkungen sehr gut wiedergeben. Dabei ergab die Analyse der Fluoreszenzdaten, dass bei kurzen Inkubationszeiten und geringen Hypericinkonzentrationen ein Hypericingradient in die Tumorzellsphäroide hinein gebildet wird, wohingegen bei langen Inkubationszeiten und hohen Hypericinkonzentrationen eine homogenere Hypericinverteilung in den Tumorzellsphäroiden auftritt. Im Rahmen der FLIM-Analyse wurde für kurze Hypericin Inkubationszeiten ein Fluoreszenzlebensdauer (FLT)-gradient in die Tumorzellsphäroide beobachtet, während lange Inkubationszeiten zu gleichmäßigeren FLTs mit tendenziell kürzeren FLTs am Tumorzellsphäroid-Rand und längeren FLTs im Kern führen. FLTs sind konzentrationsunabhängig und erlauben Rückschlüsse auf die vorherrschende Umgebung in den Tumorzellsphäroiden zu ziehen. Dabei konnten Hypericin FLTs mit pH und metabolischen Veränderungen sowie mit Förster-Resonanzenergietransfer (FRET)-, Excimer-Wechselwirkungen und zellulärer Hypericinumverteilung korreliert werden. Um ein Verständnis für die Hirntumorgewebsschädigung mittels Hypericin PDT zu generieren, wurde der Zelltod von einzelnen Gliom-Zellen nach erfolgter PDT mit Hilfe von FLIM untersucht. Hierbei kamen neben Hypericin als Photosensibilisator noch zwei weitere Fluoreszenzsonden, Resorufin und Propidiumiodid (PI), für die FLIM-Messungen zum Einsatz. Die PDT wurde mit zwei verschiedenen Laserwellenlängen initiiert und es konnten einzelne Schritte des Zelltods aufgezeigt werden. Das Zusammenziehen und Abrunden des Zellkörpers, die Bildung von Zellmembranbläschen, die Diffusion von Medium in die Gliom-Zelle sowie ein explosionsartiges Aufplatzen der Zellmembran wurden dabei als zentrale Zelltod-Merkmale identifiziert. Jedes Attribut konnte erklärt und mit einem programmierten Zelltod in Bezug gesetzt werden. Dadurch wurde festgestellt, dass Hypericin PDT zunächst Apoptose und anschließend Nekrose in Gliom-Zellen auslöst. Basierend auf diesem Wissen können PDT Bedingungen angepasst und die Effizienz für eine bestmögliche Behandlung von Gehirntumoren *in vivo* gesteigert werden.

Table of Contents

Abstract I

Zusammenfassung III

1. Introduction 1

  1.1 Objectives of this Thesis 3

  1.2 Structure of this Thesis 4

2. Theoretical and Scientific Fundamentals 6

  2.1 Spectroscopic Imaging Techniques 6

    2.1.1 Principles of Fluorescence Microscopy and Imaging 9

    2.1.2 Basics of Darkfield Elastic Light Scattering Spectroscopy and Imaging 14

    2.1.3 Concept of Hyperspectral Imaging 18

    2.1.4 Fundamentals of Confocal Raman Imaging 19

    2.1.5 Fundamentals of Infrared (IR) Spectroscopy 23

  2.2 Multivariate Data Analysis 26

    2.2.1 Principal Component Analysis (PCA) 26

    2.2.2 Bayesian Discriminant Analysis (DA) 30

  2.3 Biological Model Systems 32

    2.3.1 Two-Dimensional (2D) Cell Culture 32

    2.3.2 Three-Dimensional (3D) Cell Culture 35

    2.3.3 Photodynamic Therapy (PDT) with Hypericin 38

    2.3.4 Head and Neck Mouse Models 39

    2.3.5 Salivary Gland Tumors of Parotid Glands 41

    2.3.6 Cell and Tissue Conservation Methods 42

3. Manuscript I: Comparison of Whiskbroom and Pushbroom Darkfield Elastic Light Scattering Spectroscopic Imaging for Head and Neck Cancer Identification in a Mouse Model 43

  3.1 Abstract 44

  3.2 Introduction 44

  3.3 Materials and Methods 46

    3.3.1 Mouse Model for OSCC and Carcinogenesis 46

3.3.2 Workflow of the HSI PCA-DA Model Development and Validation................................. 48

3.3.3 ELS Spectra Acquisition in Whiskbroom and Pushbroom Imaging Mode.......................... 49

3.3.4 Comparability of Whiskbroom and Pushbroom Data by Spatial Averaging 52

3.3.5 Data Preprocessing and PCA-DA Model Development... 52

3.4 Results 53

3.4.1 Histology of Murine Tongue Tissues 53

3.4.2 Whiskbroom PCA-DA Model... 54

3.4.3 Pushbroom PCA-DA Model.. 58

3.4.4 Classification of Tissue Types by PCA-DA Models... 60

3.5 Discussion 62

3.5.1 Interpretation of Whiskbroom and Pushbroom PCA-DA Models 63

3.5.2 Validation of PCA-DA Models with HE-Staining.. 64

3.5.3 Comparison of Whiskbroom and Pushbroom PCA-DA Models... 65

3.6 Conclusion.. 68

3.7 Acknowledgements 69

3.8 Declarations.. 69

4. Manuscript II: Differentiation of Salivary Gland and Tumor Entities by Raman Imaging combined with Multivariate Data Analysis.. 70

4.1 Abstract 71

4.2 Introduction 71

4.3 Materials and Methods 73

4.3.1 Patient Selection and Parotid Tissue Sample Preparation 73

4.3.2 Confocal Raman Imaging.. 74

4.3.3 Data Pretreatment and Multivariate Data Analysis 75

4.4 Results 75

4.4.1 Raman Mean Spectra Analysis.. 75

4.4.2 Raman Data Analysis by PCA-DA 78

4.5 Discussion 81

4.6 Conclusion.. 83

4.7 Declarations.. 84

5. Manuscript III: The Impact of Standard Tissue Preparation Protocols on Salivary Gland Tumors investigated by Fourier-Transform Infrared Microspectroscopy 85

5.1 Abstract 86

5.2 Introduction 86

5.3 Materials and Methods 87

5.3.1 Patient Selection 87

5.3.2 Preparation Workflow and Histologic Samples 88

5.3.3 Fourier-Transform Infrared Microspectroscopy 89

5.3.4 Data Pretreatment and Multivariate Data Analysis 90

5.4 Results 91

5.4.1 Histologic Characterization of HE-Stained Samples 91

5.4.2 FTIR Mean Spectra Analysis 91

5.4.3 FTIR Data Analysis by PCA-DA 94

5.5 Discussion 97

5.6 Conclusion 100

5.7 Declarations 100

6. Manuscript IV: Accumulation and Penetration Behavior of Hypericin in Glioma Tumor Spheroids studied by Fluorescence Microscopy and Confocal Fluorescence Lifetime Imaging Microscopy 101

6.1 Abstract 102

6.2 Introduction 102

6.3 Materials and Methods 105

6.3.1 Cell Culture 105

6.3.2 Hypericin Incubation for Different Incubation Times and Concentrations 105

6.3.3 Spheroid Fixation and Nucleus Staining 105

6.3.4 Spheroid Sectioning 106

6.3.5 Fluorescence and Brightfield Microscopy 106

6.3.6 Fluorescence Lifetime Imaging Microscopy 107

6.3.7 Fluorescence Spectra Acquisition 107

6.4 Results 107

6.5 Discussion 113

6.6 Conclusion 115
6.7 Acknowledgment 116
6.8 Declarations 116
7. Manuscript V: Investigation of Cell Death induced by Hypericin-based Photodynamic Therapy on Glioma Single Cells using Confocal Fluorescence Lifetime Imaging Microscopy 117
7.1 Abstract 118
7.2 Introduction 118
7.3 Materials and Methods 121
7.3.1 Cell Culture 121
7.3.2 Hypericin Incubation 122
7.3.3 Resorufin Conversion 122
7.3.4 PI Supplementation 122
7.3.5 Fluorescence Lifetime Imaging Microscopy (FLIM) 123
7.3.6 Widefield Fluorescence Imaging Microscopy 123
7.3.7 Fluorescence Spectra Acquisition 124
7.4 Results 124
7.5 Discussion 130
7.6 Conclusion 133
7.7 Declarations 133
8. Conclusion and Outlook 134
9. Bibliography 138
Appendix X
A1. Supplementary Information for Chapter 2.1.2: Mathematical Description of Mie Scattering X
A2. Supplementary Information for Manuscript I: Comparison of Whiskbroom and Pushbroom Darkfield Elastic Light Scattering Spectroscopic Imaging for Head and Neck Cancer Identification in a Mouse Model XIII
A3. Supplementary Information for Manuscript II: Differentiation of Salivary Gland and Tumor Entities by Raman Imaging combined with Multivariate Data Analysis XVII
A4. Supplementary Information for Manuscript III: The Impact of Standard Tissue Preparation Protocols of Salivary Gland Tumors investigated by Fourier-Transform Infrared Microspectroscopy XX

A5. Supplementary Information for Manuscript IV: Accumulation and Penetration Behavior of Hypericin in Glioma Tumor Spheroids studied by Fluorescence Microscopy and Confocal Fluorescence Lifetime Imaging Microscopy XXIII

A6. Supplementary Information for Manuscript V: Investigation of Cell Death induced by Hypericin-based Photodynamic Therapy on Glioma Single Cells using Confocal Fluorescence Lifetime Imaging Microscopy XXVIII

List of Abbreviations and Symbols XXXII

List of Figures XXXVI

List of Tables XXXIX

List of Publications XL

Published Manuscripts XL

Prepared Manuscripts XLI

Declaration of Contribution XLII

Acknowledgments XLIV

Affirmation in Lieu of an Oath XLVI

Eidesstaatliche Erklärung XLVII

1. Introduction

Spectroscopy is the study of light-matter interactions that enables a thorough physicochemical characterization of any type of macroscopic, microscopic or molecular material. It allows to uncover structural properties or mechanistical relations in order to expand our knowledge about nature. Ideally, this understanding can be translated in a practical implementation or used for new developments. The demand for investigation explains the widespread application of spectroscopy in highly diverse fields of industry and science, such as e.g. astrophysics [1,2], forensics [3], geology [4] or agriculture [5]. Additionally, spectroscopy successfully found its way in life science and medicine. Here, it contributes to answer fundamental questions in e.g. cellular signaling pathways or gene expression and can be deployed for the analysis of pharmaceutical or bioactive agents. Especially in these research areas, spectroscopy is often implemented as an imaging modality.

Spectroscopic imaging assigns the spectral information to a spatial location and an image contrast based on the spectral data is generated [6]. This creates a complex 3D data matrix that provides detailed insights of the specimen's composition, structure or function and thus contributes to an overall comprehension. Different spectroscopic principles are distinguishable and various combinations of imaging techniques are applied to investigate current topics in microbiology and biochemistry. One major issue encompasses the structural and functional examination of proteins [7]. Exemplarily, microspectroscopic imaging revealed the protein translocation and fragmentation of protein kinase C and its fragment's regulatory and catalytic roles [8]. Besides, cell organelles or sub-structural components and their multifunctional behavior were studied with electron spin imaging [9], Raman imaging [10] and super-resolution microscopic imaging (e.g. super-resolution optical fluctuation imaging (SOFI), stochastic optical reconstruction microscopy (STORM), photo-activated localization microscopy (PALM)) [11]. Compared to that, a wide-range usage of spectroscopic imaging is noticed in pharmaceutical and medicinal areas. Here, nanoparticles are commonly examined for their suitability as drug carriers [12] or new pharmaceutical formulations are characterized with the help of various imaging techniques [13,14].

As a part of medical research, spectroscopic tools also play a major role in cancer analysis. Since the number of incidences is still increasing worldwide [15], the demand for an early and accurate cancer diagnosis and a subsequent, successful treatment is of highest priority. This is especially the case for incurable cancers as a result of an insufficient surgical procedure or a failing therapeutic approach. Particularly, tumors of the head region often suffer from a poor diagnosis and a difficult surgery / therapy, also in part of their hampered accessibility. Two types of tumors belong to this group: brain and head and neck tumors. While most brain tumors solely emerge from the supporting tissue in the brain [16,17], head and neck tumors summarize a tumor class of variable origin in the head and neck region, including the oral cavity and the parotid [18]. Each of these tumor types faces individual challenges: 1) brain tumors cannot completely be removed by operative / therapeutic measures, as they aggressively invade surrounding normal tissue [19,20], 2) tumors in the oral cavity are the most abundant head and neck tumors [21] and thus their early diagnosis is of the essence, 3) the great variety of parotid salivary gland tumors demands a distinct differentiation among themselves and particularly from normal salivary gland tissue [22]. For these reasons, improvements in diagnostic skills and suitable therapeutic approaches need to be realized, which can either be achieved or assessed by spectroscopic imaging.

Several attempts as a diagnostic methodology were made in breast, lung and colon cancer by Raman, autofluorescence and Fourier-transform infrared (FTIR) imaging, respectively [23-28]. Aside from bulk tumor recognition, resection margins are most complicated to assign to either normal or tumorous tissue. Particularly, diffuse reflectance, autofluorescence and elastic light scattering were proven capable of determining these margins mainly in breast or oral cancer [29-32]. The advantage of a spectroscopy-based diagnosis is that it solely relies on chemical or morphological information, which makes it very objective. This is of great importance, as the histopathological diagnosis can sometimes be more subjective and is additionally accompanied by a sophisticated and time-consuming biopsy preparation. Still, histopathology is the golden standard in cancer diagnostics and typically implemented in any clinical routine [33]. The accuracy of histopathological evaluations is directly linked to the pathologist's experience and the quality of preparation and tissue itself. The latter are also true for spectroscopy-based diagnostics. Therefore, an increasing number of studies investigated the impact of tissue preparation and fixation by spectroscopy [34-36] and their effect on spectroscopic identification capabilities [37-39]. In case spectroscopy is additionally combined with multivariate data analysis, powerful classification models can be built. Various spectroscopy and imaging methods can be coupled with statistical algorithms and be applied for brain [40], colon [41-43], liver [44], oral [45] or breast [40,46] tumor identification [33]. Most spectroscopy-based multivariate models enable a label-free examination of the tissues and are thus fast, efficient and straightforward diagnostic approaches. However, labelling with specifically designed probe molecules can also be deployed for diagnostic purposes. This exemplarily applies to photosensitizers that function as fluorescence labels in the course of photodynamic diagnostics (PDD). At the same time, they can also be used as drugs in photodynamic therapy (PDT) [47].

PDT already accomplished great success in treating several malignant lesions and diseases, such as head and neck, prostate, bladder or lung cancer [48-52]. Especially in skin cancer [53,54], PDT is commonly established as a result of its topical application and the easy implementation of light exposure. In PDT, tumor damage is initiated due to reactive oxygen species (ROS), which are generated by light-activated photosensitizers specifically accumulated in tumors. Different photosensitizers were tested and compared in terms of their effectivity in tissue damaging [55-57] and their low dark cytotoxicity [58,59]. One of these photosensitizers is hypericin, a component of *hypericum perforatum L.*, which implies a high potential for an effective PDT due to its photophysical and chemical characteristics. Several studies focused on PDT with hypericin in pancreatic [60], thyroid [61] or head and neck tumors [62]. Since photodamage only appears in close proximity to the photosensitizer, it is important to investigate its accumulation and distribution behavior in tumors. So far, hypericin was shown to mainly enrich in cell membranes, mitochondria, Golgi apparatus, endoplasmic reticulum (ER) or lysosomes across varying tumor cell lines [63-65], but no 3D distribution was yet thoroughly studied. Hypericin PDT is a promising tool for treating primary brain tumors, since it is able to pass the disrupted blood-brain-barrier and accumulates in the tumor tissue [66-68]. One expectation of hypericin PDT is a successful elimination of resection margins or infiltrating branches, which failed so far by chemo- or other irradiation therapies [69,70]. Photodamage can follow varying pathways and lead to different cell death mechanisms (apoptosis, necrosis or paraptosis) [47,71,72] that depend on light intensity, type of photosensitizer and cell or tissue nature [73,74]. An in-depth understanding of hypericin PDT pathways for its application in primary brain tumors is crucial in order to improve PDT efficiency and define conditions for an optimal *in vivo* treatment.

1.1 Objectives of this Thesis

The first goal of this thesis is to gain new insights in spectroscopy-based multivariate models as diagnostic tools in cancer analysis by developing new models for different aspects in tumor diagnosis. With the help of these models, a demarcation of tumors from normal tissues and a tumor entity differentiation should be enabled. Moreover, an understanding of tissue preparation-related effects will be studied. All models will be evaluated by a histopathological analysis and their practicability in a clinical routine. A special focus will lie on an external model validation with unknown tumors or tissues and on an adaption and comparison of imaging modalities. Valuable data need to be generated by elastic light scattering spectroscopic imaging, Raman imaging and FTIR microspectroscopy. This data is crucial for multivariate model formation and the respective model purpose, as it represents the chemical or morphological information of the tumors and tissues. As a result, spectroscopy-based multivariate models can be used as an instrument for predicting undetermined tumor and tissue sites. Overall, this should contribute to a qualified and early diagnosis of head and neck tumors in the oral cavity and of the parotid.

The second goal of this thesis is to generate an understanding of hypericin PDT as a new approach in primary brain tumor treatment. One important part of this understanding includes how hypericin is interacting with glioma tumors. This will be studied based on a 3D *in vitro* tumor cell spheroid model, with which the hypericin accumulation and distribution will be investigated by fluorescence microscopy. The analysis of hypericin's fluorescence lifetimes (FLTs) by fluorescence lifetime imaging microscopy (FLIM) will allow the correlation of FLTs to the spheroids' microenvironment and deduce potential environmental influences. Spheroid model implementation and preparation are crucial parts of this study. Additionally, the actual damaging potential of hypericin PDT for a treatment of brain tumors will be evaluated by glioma cells as a second *in vitro* model. For this purpose, PDT will be induced in hypericin-incubated glioma cells that are simultaneously examined by FLIM. In combination with additional fluorescence markers, this should demonstrate how hypericin PDT proceeds and reveal individual degradation steps that allow a deduction of the cell death mechanism. In both studies, hypericin simultaneously functions as a probe molecule for fluorescence microscopy and FLIM and as the photosensitizer in PDT. The obtained results should support an increase of hypericin PDT efficiency and enable to specify best possible terms for the treatment of primary brain tumors *in vivo*.

1.2 Structure of this Thesis

The present thesis is organized in several subsections:

In Chapter 2, the theoretical foundation of the used spectroscopies and imaging techniques is given along with the concepts of multivariate data analysis and the applied human, animal and cellular models. This background should enable a better understanding of the performed studies in successive sections.

In Chapter 3, a comparative investigation of Whiskbroom and Pushbroom darkfield elastic light scattering models is performed to determine whether one of them is more suitable to distinguish lingual tumors from normal tongue tissues, including gland / muscle and epithelium. This is established with a head and neck tumor mouse model. Multivariate models are developed on basis of data from both imaging modalities and in accordance with the histopathological characterization of the tumors and tissues. Demarcation capabilities are assessed by performance parameters and the prediction outcome of a separate tissue data set. Their usage in clinics is evaluated in terms of acquisition time, costs and practicability. This section is published as *“Comparison of Whiskbroom and Pushbroom darkfield elastic light scattering spectroscopic imaging for head and neck cancer identification in a mouse model”* in Analytical and Bioanalytical Chemistry (2021) 413:7363-7382, https://doi.org/10.1007/s00216-021-03726-5, reproduced with permission from Springer Nature.

In Chapter 4, a Raman imaging-based multivariate model is established to discriminate between two different parotid tumors and normal salivary gland. This study relies on a representative sample set of human Warthin tumors, pleomorphic adenoma and normal salivary gland tissues. Spectral patterns are compared and assigned to relating molecular vibrations in the tissues prior to model formation. The multivariate model is generated in conformity with the histopathological evaluation and independently verified by unknown tumor and tissue samples. Model discriminating abilities are additionally defined by performance parameters. This section is based on a prepared manuscript *“Differentiation of salivary gland and tumor entities by Raman imaging combined with multivariate data analysis”*.

In Chapter 5, multivariate models of FTIR data for Warthin tumor, pleomorphic adenoma and normal salivary gland are created that show the impact of different preparative treatments on the tissues. For that purpose, four common tissue preparation and fixation protocols are applied on the parotid tumors and tissues, including cryconservation, formalin fixation, paraffin embedding and dewaxing. FTIR bands are compared and correlated to respective vibrations of tissue components prior to model generation. Performance parameters are used to quantitatively describe the multivariate model. This section is similarly published as *"The Impact of Tissue Preparation on Salivary Gland Tumors Investigated by Fourier-Transform Infrared Microspectroscopy"* in the Journal of Clinical Medicine (2023), 12, 569, https://doi.org/10.3390/ jcm12020569.

In Chapter 6, hypericin accumulation and permeation is investigated in a glioma cell spheroid model by fluorescence microscopy in consideration of different hypericin incubation times and concentrations. For that purpose, spheroid cryosections are prepared and imaged to expose the different intermediate regions from spheroid periphery to core. On this basis, hypericin uptake into the different spheroid layers can be studied effectively. These cryosections are additionally analyzed by FLIM to measure spatially resolved FLTs of hypericin that can be linked to the spheroid microenvironment. This enables to derive potential environmental factors that might influence hypericin PDT. This section is published as *"Accumulation and penetration behavior of hypericin in glioma tumor spheroids studied by fluorescence microscopy and confocal fluorescence lifetime imaging microscopy"* in Analytical and Bioanalytical Chemistry (2022) 414:4849-4860, https://doi.org/10.1007/s00216-022-04107-2, reproduced with permission from Springer Nature.

In Chapter 7, the photodamage and death mechanism of hypericin PDT is analyzed in glioma cells by FLIM in consideration of different irradiation powers and wavelengths. The initiated death progression is illustrated in a stepwise manner with the help of propidium iodide (PI) and resorufin as additional fluorescence markers. Cellular details about single damaging events with corresponding reasons can be deduced. On this basis, glioma-specific PDT stages with hypericin could be defined. This section is based on a prepared manuscript *"Investigation of cell death induced by hypericin-based photodynamic therapy on glioma single cells using confocal fluorescence lifetime imaging microscopy"*.

In Chapter 8, a comprehensive conclusion of all findings and a detailed outlook for future experiments is provided.

2. Theoretical and Scientific Fundamentals

In the following chapter, the theoretical background for this thesis is expounded to provide a basic understanding of the applied techniques, principles and concepts in spectroscopy, cell biology and statistics. This knowledge should help to appreciate the generated results throughout later chapters and how they have to be interpreted.

2.1 Spectroscopic Imaging Techniques

The diversity of spectroscopic methods enables a thorough characterization of a sample regarding its chemical and morphological constitution in either a qualitative or quantitative manner. Reasons for the different sample information content result from the various molecular processes, targeted and activated by the individual spectroscopy method. An overview of the electronic and vibrational events for all spectroscopic techniques applied in this thesis is presented by a Jablonski diagram in Fig. 2.1.

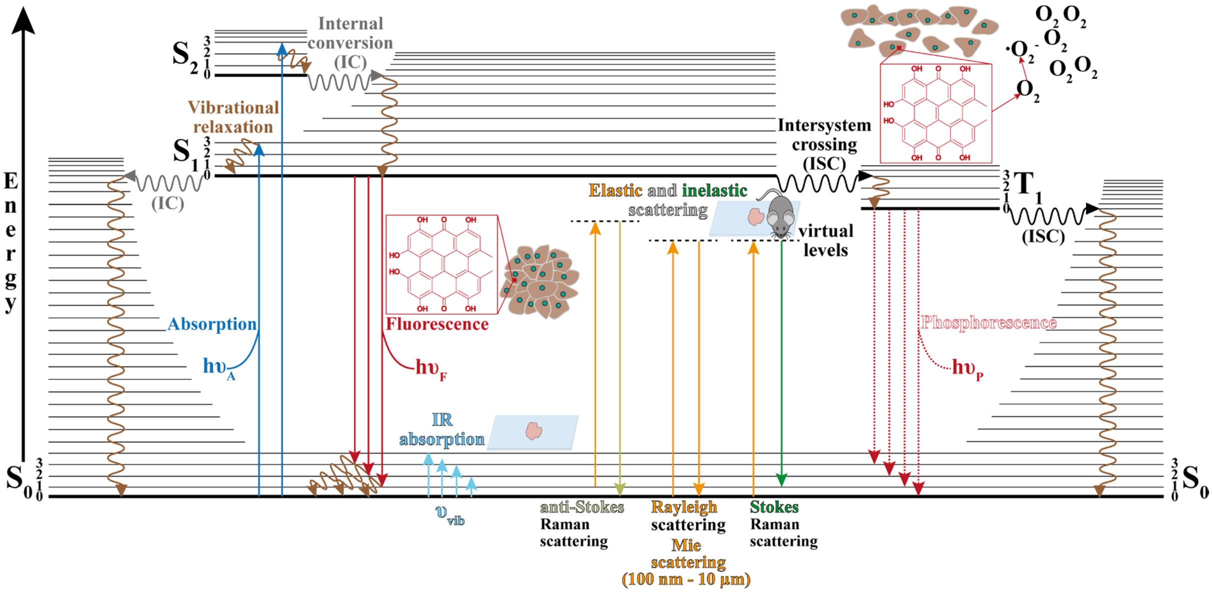

Figure 2.1. *Simplified Jablonski diagram of electronic and vibrational processes for absorption, fluorescence, Raman, Infrared (IR) absorption and phosphorescence. Upon photon absorption, a molecule can be transferred from the singlet ground state (S_0) to the first or second electronic state (S_1 or S_2). This excitation can occur towards different vibrational levels (S_1, 0, 1, 2, 3; S_2 0, 1, 2, 3) of each electronic state. Following a non-radiative transition from S_2 to a higher vibrational level of S_1 (internal conversion, IC), the molecule arrives at the lowest vibrational level of S_1 after relaxation. Here, the molecule can either return to various vibrational levels of S_0 by emitting fluorescence or undergo a spin conversion to the first triplet state (T_1) by intersystem crossing (ISC). The molecule's relaxation from T_1 is phosphorescence. In addition to electronic transitions, a molecule can be excited to a virtual state and return to S_0 without any energy transfer between molecule and photon. This causes elastic photon scattering (Rayleigh scattering). In case the elastic scattering is in the wavelength order of 100 nm – 10 µm, it is termed Mie scattering. Inelastic scattering appears due to an energy loss (Stokes) or gain (anti-Stokes) of the emitted photon from the virtual level to S_0. In comparison, IR absorption only causes an excitation of the molecule to higher vibrational levels within S_0. Adapted by [75,76].*

A spectroscopic analysis is based on the interaction of light with matter. The type of interaction is linked to the molecule's nature and the incident photon energy. Depending on both, molecules can be triggered to undergo a spectroscopic transition. Each transition represents a concrete energy difference ΔE between distinct electronic or vibrational states that need to be overcome according to the Bohr frequency condition [77]:

$$\Delta E = h\nu \tag{2.1}$$

In eq. 2.1, ΔE is related to quantized photon energies with discrete values described by the Planck's constant ($h = 6.6 \, x \, 10^{-34} Js$) and frequency ν [78,79]. Here, transitions between states only take place if the molecules absorb or emit photons with corresponding ν-values that match ΔE. These ν-varying photons can be detected with different spectroscopies. In the end, a molecule's spectrum with defined spectral bands at concrete ν-values is obtained that represents the molecular transitions [78,79].

In fluorescence spectroscopy, a molecule instantaneously absorbs a photon ($10^{-15}\,s$) upon irradiation and is excited from the singlet ground state S_0 to higher electronic states S_1 / S_2 (Fig. 2.1). Depending on the absorbed photon energy, the fluorophore can be excited to different vibrational levels of S_1 or S_2, indicated by level $0-3$. This excitation is not achievable at room temperature, as the energy difference between the singlet ground and higher electronic states is too large to cause a thermal population of S_1 / S_2. Consequently, a separate chemical, electronic or photonic source is necessary to initiate the excitation. After an excitation to S_2, the fluorophore can transition into a higher vibrational level of S_1 in the course of internal conversion ($10^{-11}\,s$). From here, a fast relaxation to the lowest vibrational level of S_1 takes place ($10^{-12}\,s$ or less), termed vibrational relaxation. Reasons for this process are non-radiative phenomena, e.g. the loss of thermal energy (heat). As a result, fluorophores populate the lowest vibrational level of S_1 and can return to varying vibrational levels of S_0. In case of a relaxation to higher vibrational levels of S_0, more than one band occurs in the corresponding fluorescence spectrum, based on the Franck-Condon principle. This band signature can be a mirror-image of the related molecule's absorption spectrum, if the vibrational levels for S_0 and S_1 are similarly spaced. Since the fluorophore's return to S_0 mainly proceeds from the ground level of S_1, the energy gap of the fluorescence photon is always smaller than the energy difference overcome in absorption. Consequently, the frequency ν of the emitted photon is also smaller and the fluorescence is red-shifted to longer wavelengths. This shift is called Stokes shift and can be observed for all fluorescent events. The fluorescence pattern is characteristic for a molecule and independent of the excitation wavelength, as a result of fast vibrational relaxation. Although a molecule can be excited to different levels, a rapid internal conversion followed by vibrational relaxation always cause its relaxation from the vibrational ground level of S_1. The short time frame of vibrational relaxation ($10^{-12}\,s$ or less) is deducible from a pronounced overlap of energetically-similar vibrational levels. Therefore, fluorescence emission is not affected by the excitation source, as summarized in Kasha's rule [80]. In rare cases, a photon emission can occur from higher vibrational or electronic states (e.g. S_2), but typically not in biological molecules [75,81].

Besides fluorescence emission, an excited molecule can also undergo an electron spin conversion and be transferred to the first triplet state T_1. This transfer emerges from two isoenergetic vibrational levels of the S_1- and T_1-states and is termed intersystem crossing (ISC), with a time scale of 10^{-8} to $10^{-6} s$ (Fig. 2.1) [82]. A molecular relaxation from the T_1 ground level to S_0 mainly occurs by weakly emitting phosphorescence, long-lasting of up to a second-scale magnitude [78]. Although a multiplicity-different transition is normally forbidden, phosphorescence is still possible due to a strong spin-orbit coupling. Each molecular electron exhibits a rotational movement around its own axis that results in a spin-related magnetic momentum. Additionally, electrons orbit the nucleus, by which an orbital magnetic momentum is generated. Both magnetic momenta interact with one another and cause a spin-orbit coupling. Depending on their relative orientations, the spin-orbit coupling can either be strong or weak. This affects the total angular momentum of the electron. Based on a parallel orientation of spin and orbital momentum, a high total angular momentum is observed. An opposed orientation results in a low total angular momentum of the electron [78]. In S_1, two paired electrons occupy the same orbital that provides no net spin angular momentum. In T_1, however, two parallel-oriented electrons cause a spin angular momentum of $\pm \hbar$, which needs to be compensated to maintain the total angular momentum of the system. This compensation is achieved by an additional alteration of the orbital angular momentum due to spin-orbit coupling [82]. The transfer from S_1 to T_1 can thus be interpreted as perturbation on the Hamiltonian [82]. Intersystem crossing is furthermore promoted by the similar geometry of the S_1 and T_1 potential energy curves and their overlap at the intersection point. The smaller the S_1 state energy and the more pronounced the potential energy curve intersection, the more likely occurs the transition from S_1 to T_1 [76,82-84].

A competing process of fluorescence is Raman scattering (Fig. 2.1). Its basic principle can be defined as a molecule's inelastic collision with a photon and their exchange of energy. If the photon induces a molecular vibration that entails a changing polarizability, energy is transferred from the photon to the molecule and the photon energy is reduced. This phenomenon is denoted as Stokes scattering. Mathematically, this can be described by a transition from a "virtual state" to a higher vibrational level of S_0. In case the molecule is already thermally oscillating with an altering polarizability, a reversed energy transfer from the molecule to the photon takes place and the photon energy is increased. This process is designated as anti-Stokes scattering. From a mathematical perspective, it can be regarded as a return from a "virtual state" to the S_0 ground level. In the event of an elastic collision, no energy is exchanged between the molecule and photon and elastic Rayleigh scattering appears [85]. The "virtual state" is not a stationary level with a quantized energy [86] and only functions as a theoretical model for Raman band calculations.

Depending on the scatterer size, different types of elastic scattering can emerge. Rayleigh scattering mostly describes the elastic photon scattering of molecules, whereas Mie scattering is associated with larger particle sizes in the range of $100\ nm - 10\ \mu m$ (Fig. 2.1) [87]. Typical biological Mie scatterers include cell organelles or tissue components. The scattering pattern is characteristic for the morphological constitution and can function as a fingerprint for the particulate arrangement.

Infrared (IR) transitions (Fig. 2.1) correspond to a photon absorption in the IR wavelength range as a result of a molecular vibration, triggering a change in dipole moment. In the course of energy absorption, a transfer from the ground level to a raised vibrational level in S_0 is accomplished and the molecule's vibrational amplitude is increased [85,88]. This transition only emerges if the photon energy coincides with the energy difference between levels. The IR light intensity attenuation after photon absorption correlates with the incident intensity and analyte concentration by the Lambert-Beer relation [85].

2.1.1 Principles of Fluorescence Microscopy and Imaging

Fluorescence spectroscopy is based on detecting emitted photons by fluorophores that are previously excited. Their excitation can match electron transitions from S_0 to S_1 / S_2. Depending on the fluorophore structure, most transitions result from a shift of either non-bonding n or π-bond electrons to antibonding orbitals π^* ($\pi^* \leftarrow \pi$, $\pi^* \leftarrow n$). Certainly, electronic transitions are only allowed under predefined circumstances [76,89]. For each transfer, the electron spin has to be unchanged, also applying to relocations between degenerated orbitals. Electron transitions are also allowed if molecules undergo certain symmetry changes, e.g. an inversion through the symmetry center [78]. The shift of electrons during excitation forces the much heavier atomic nuclei to adjust to the fast-changing electron configuration after the transition is completed. Therefore, nuclei become deflected from their equilibrium position in S_0 and attain an aligned location in S_1. To preserve energy, the transition is performed to a higher vibrational level of S_1 in accordance with the adapted nuclei equilibrium. This is also represented by the potential energy curves of S_0 and S_1, as the transition ends in a turning point of the S_1 curve, correlated to the respective vibrational level. As a consequence, a nuclei and thus molecular vibration is initiated. From a quantum mechanical perspective, the most intense transition is promoted by the largest overlap between the wavefunctions of S_0 and the vibrational level of S_1 at minimum nuclear displacement. The delayed nuclear behavior as response to an electronic transition is summarized in the Franck-Condon principle [76,78].

Upon excitation, fluorescence arises from a reversed transition of S_1 to S_0 by emission of a photon. For this transition, important characteristics are the dwelling time and decay rate in and from S_1, individual for each fluorophore. Both features are quantitatively depicted by the fluorescence lifetime and the fluorescence quantum yield. After populating S_1, molecules dwell here for a certain amount of time that enables interactions with the surrounding environment prior to relaxation. This dwell time is designated as the fluorescence lifetime τ and can be described by the radiative rate Γ and the nonradiative decay rate k_{nr} of S_1 [75]:

$$\tau = \frac{1}{\Gamma + k_{nr}} \tag{2.2}$$

As fluorescence is a randomly appearing event, τ reflects an average time for the molecule's stay in S_1. Possible influences of τ in the condensed phase are the S_1 geometry of the molecule, reactions with the local environment, differences in refractive indices or the solvent. The quantum yield Q of a fluorophore represents the proportion of emitted to absorbed photons, also represented by Γ and k_{nr} [75]:

$$Q = \frac{\Gamma}{\Gamma - k_{nr}} \tag{2.3}$$

For a high quantum yield ($Q \approx 1$), k_{nr} is much smaller than Γ. Both rates are highly influenced by molecular interactions with the environment and one rate can be in favor over the other. Therefore, each impact on one of them will directly affect τ and Q [75,76].

In case k_{nr} of the fluorophore dominates over Γ due to the prevalent surroundings, Q and τ are decreased as a result of fluorescence quenching. This process is characterized as a nonradiative deactivation of S_1 following interactions with quencher molecules, such as solvent, oxygen, halogens or ions. Different types of interrelations define various quenching natures, by which the nonradiative depopulation is initiated. One type encompasses a complex formation that prevents the radiative decay of the fluorophore. Non-excited fluorophores and quenchers can form nonfluorescent complexes (static quenching), whereas excited fluorophores can build complexes with each other at high concentrations (excimers). Compared to that, the collision of excited fluorophores with solvent molecules induces an energy transfer to the solvent and simultaneously a nonradiative relaxation of the fluorophore to S_0 (collisional quenching). All of these interplays attenuate the fluorescence intensity by increasing k_{nr}. Fluorescence quenching clarifies the dynamics and comparatively long duration of fluorescence that benefits the exchange with the environment [75,76].

Independent of the final fluorescence outcome, its measurement needs to be most accurate. Two types of fluorescence measurement principles can be differentiated, which are the steady-state and time-resolved concepts shown in Fig. 2.2.

In steady-state measurements, a fluorophore is constantly illuminated by a light source and the generated fluorescence intensity is detected as an averaged signal. Individual fluorescent events appear in a ns-timescale, but cannot be resolved due to continuous irradiation. Additionally, the continuous light exposure effects a constant number of fluorophores to remain excited and a steady-state condition is reached. The averaged fluorescence intensity is either plotted against the fluorescence wavelength in a spectrum or it is depicted as a laterally-resolved distribution in an image. Most instrumental setups can only perform steady-state measurements, since they do not provide the fast detection equipment required for quantifying single events [75,76]. The used fluorescence microscope for steady-state measurements and exemplary fluorescence images are shown in Fig. 2.2a – e.

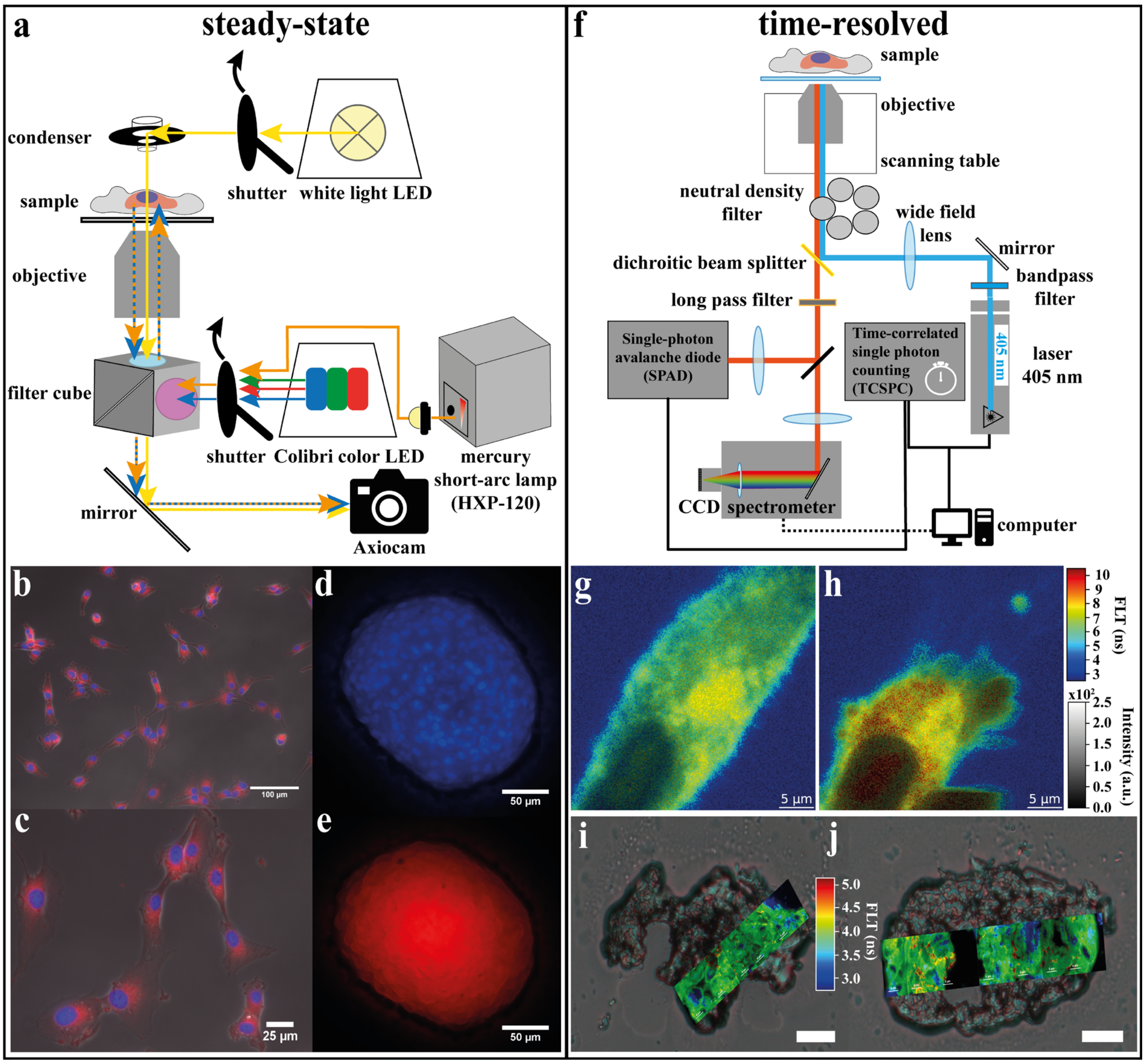

Figure 2.2. Instrumental setups for steady-state and time-resolved fluorescence imaging. A commercial fluorescence microscope is used to generate non-confocal, steady-state fluorescence images by z-stacking to obtain sharp composite images (a). The sample is either illuminated in transmission with a white light LED or inversely with a mercury short-arc lamp / colored LEDs for phase contrast or fluorescence image formation, respectively. In the transmission pathway, the sample light is collected by the objective and transferred without additional filtering to the camera (Axiocam). This enables the acquisition of brightfield or phase contrast images. In the reverse-illumination pathway, light from the mercury short-arc lamp / colored LEDs impinges on the specimen after passing through a filter setting specifically chosen for the applied fluorescence dye, with which the sample was stained. The fluorescence emission is afterwards detected with the camera and fluorescence images are generated. Image overlays of phase contrast with Hoechst 33342 and hypericin fluorescence channels for U-87 MG glioma cells are depicted in (b) and (c). Hoechst 33342 and hypericin single channel fluorescence images of a U-87 MG glioma cell spheroid are exemplarily shown in (d) and (e). A custom-built fluorescence imaging system equipped with a time-correlated single photon counting unit (TCSPC) and a single-photon avalanche diode (SPAD) is applied for time-resolved microscopic imaging (f). For the excitation pathway (light blue line), the monochromatic light of a 405 nm laser diode is adjusted and redirected via a number of optical elements to inversely illuminate the specimen. For the emission detection, the sample fluorescence passes the beam splitter and is either detected by the SPAD to create a confocal image or by the spectrometer and charge-coupled device (CCD) camera to obtain a spectrum (orange line). In time-resolved measurements, the time delay Δt between excitation and emission photons is accurately determined by the TCSPC unit and can be used to calculate the fluorescence lifetime (FLT) of the sample. The stepwise scanning and simultaneous FLT acquisition of the specimen allows to record FLIM images. Exemplary FLIM images of hypericin-incubated U-87 MG glioma cells are illustrated in (g) and (h), whereas (i) and (j) show FLIM and brightfield composite images of hypericin-treated U-87 MG spheroid sections (scale bar 25 µm) [90].

In time-resolved measurements, single fluorescence decays can be captured by a high-speed detection unit, revealing important information about the fluorophore condition or microenvironment. Two types of time-resolved principles are present, the time- and frequency-domain, that can be differentiated by their fluorophore excitation. In frequency-domain, the intensity of illumination light is modulated, whereas in time-domain, the fluorophore is excited by short laser pulses. Typically, the pulse duration is shorter than the timeframe of a single fluorescence event. Following a laser pulse excitation, the fluorescence intensity is detected over time t, which can reveal a single exponential decay behavior [75]:

$$I(t) = I_0 e^{-t/\tau} \tag{2.4}$$

The initial intensity I_0 at $t = 0$ depends on the fluorophore concentration and instrumentation-related parameters, while the time t and the decay or lifetime τ are located in the exponent. This exponential intensity decay expresses the time-distributed depopulation of S_1, which is fitted with an appropriate decay model in an iterative convolution procedure to determine decay parameters. For this purpose, the instrument response function (IRF) is required, as it is used for convolution of the applied model function. IRFs depict the shortest measurable decay, from which the travel time of the laser pulse through the instrument is ascertained. They are acquired by using the laser light reflection at a glass coverslip and their pattern further depend on the laser pulse shape, the optical elements and detector characteristics. After convolving the model function, model parameters are adapted to most accurately represent the number of photons in each time channel of the $log\ I(t)\ /\ log\ (Counts)\ vs.\ time\ t$ plot. As a result, decay-related features are obtained, of which one is τ. It reflects a statistical time average of fluorescence emission over the entire single exponential decay [75,91].

In addition to single exponential decays, more complex decays with multiple exponents can emerge, particularly in biomolecules. Whether a single or multi-exponential intensity decay is present can be identified by the overall shape of the decay curve. For a single exponential, a linear curve progression is displayed in the $log\ I(t)\ vs.\ time\ t$ plot, to which one τ is assignable. In comparison, a multi-exponential behavior reveals a curvature, of which each decay segment can be fitted to a different τ. A multi-exponential decay model is summarized in:

$$I(t) = \sum_i \alpha_i e^{-t/\tau_i} \tag{2.5}$$

whereby τ_i represents the lifetime and the α_i-values are designated as pre-exponential factors (amplitudes), often normalized to unity ($\sum_i \alpha_i$). To define an average lifetime $\langle\tau\rangle_f$ for a fluorophore with multi-exponential behavior, a fractional intensity-weighting of the lifetimes can be accomplished according to [76]:

$$\langle\tau\rangle_f = \frac{\sum_{i=1}^{n} \alpha_i \tau_i^2}{\sum_{i=1}^{n} \alpha_i \tau_i} = \sum_{i=1}^{n} f_i \tau_i \tag{2.6}$$

Besides, a fractional amplitude-related weighting can also be applied to obtain an amplitude-averaged lifetime $\langle\tau\rangle_a$. Certainly, the usefulness of one averaging method over the other has to be assessed individually.

Prior to a decay evaluation, a time-domain measurement is necessary and conducted by a time-correlated single photon counting (TCSPC) unit. In TCSPC, a time delay between an excitation laser pulse and a single fluorescence photon is quantified and depicted in a histogram. This histogram represents the photon distribution for all detected time delays and thus reflects the intensity decay of the fluorophore, in case a large number of photons is counted. To achieve a high decay accuracy, the TCSPC unit has to be adapted regarding its detection rate. It is confined to a maximum gathering of only one fluorescence photon per excitation pulse, depending on the capabilities of the applied electronics. This adjustment is required, since the TCSPC unit might otherwise not be able to capture all photons. As it can only count the first of several emission photons at higher count rates, this would lead to a shift of the histogram towards shorter delay times. Each photon counting starts with an excitation pulse of the laser that sends an onset signal to a constant function discriminator (CFD). The CFD precisely stores the starting time of the excitation pulse and redirects it to a time-to-amplitude converter (TAC), which initiates a voltage ramp by continuously increasing the voltage with ongoing time. After fluorophore excitation, a fluorescence photon arrives at the detector and triggers another signal, sent to a second CFD that accurately records the stopping time of the fluorescence pulse. As a consequence, the voltage ramp of the TAC is terminated. The time difference between starting and stopping time is proportional to the measured voltage ramp, which can be amplified by a gain amplifier (GA) and translated by an analog-to-digital converter (ADC) into a precise, digital time delay value Δt. To prevent false readouts, the voltage ramp of the TAC is limited to a defined voltage range. In case this range is not satisfied by the fluorescence pulse, the signal is deleted by a window discriminator (WD). Each time value is saved as a single event within the ns-time channels of the decay. By repeating the photon counting and time delay acquisition, the fluorescence intensity decay can be accurately reconstructed. In practice, the fluorescence pulse often functions as the starting signal in the photon counting process, whereas the excitation pulse corresponds to the stopping signal for the time delay measurement. The main reason for this “reversed mode” is the high repetition rate of pulsed light sources, which do not enable the TACs to re-configurate for the next counting event. Although both acquisition modes are viable, the “reversed mode” is the most common operation procedure for photon counting [75,76]. The custom-built instrument used in this thesis is shown in Fig. 2.2f.

A precise measurement and analysis of fluorescence decays to obtain a fluorophore lifetime can be accomplished in an imaging manner, denoted as fluorescence lifetime imaging microscopy (FLIM). In FLIM, the recording of lifetimes is performed with a confocal microscope that allows a specimen scanning and simultaneous detection of decay curves in each image pixel with a high lateral resolution. Following a decay analysis, individual lifetimes can be determined for all pixels and an image contrast is generated based on different lifetimes. Since the lifetime is independent of fluorophore (probe) concentrations, lifetime differences can reveal environmental variations in terms of pH, conformational changes, ion concentrations, molecular dissociation or metabolism [75,91,92]. Therefore, FLIM experiments can be particularly important for the investigation of cells, administered with suitable probe molecules. This plays a major role in cancer research, as FLIM can contribute to investigate effects of new cancer drugs or therapies. One of these therapeutic drugs is hypericin in brain tumor treatment that additionally qualifies as suitable FLIM probe molecule. Hypericin has been analyzed with FLIM in glioma tumor cell spheroids and tumor cells (see chapter 6 and 7), exemplarily illustrated in Fig. 2.2g – j.

2.1.2 Basics of Darkfield Elastic Light Scattering Spectroscopy and Imaging

Elastic light scattering (ELS) spectroscopy measures elastically scattered light of a single particle or a particle aggregate. This scattering results from an incident light beam partially deflected, refracted or reflected by a particle in a single or multiple fashion without the transfer of energy. Various scattering processes are delineated by different theories, only holding for specific particle sizes and boundary conditions. One theory deals with the scattering behavior of an incident plane wave on a homogeneous sphere, established by Gustav Mie [93]. It allows to predict the elastic scattering pattern by a single sphere in dependency of the particle size and refractive index.

Characteristic features of Mie scattering include a sinusoidal interference pattern, mainly visualized in ELS spectra (scattering intensity vs. wavelength) or plots of extinction / scattering cross section (Q_{Ext} / Q_{Sca}) vs. particle size (x) [94-96]. Examples of single particle darkfield (DF) microscopic images, corresponding ELS spectra and simulated scattered E-fields are shown in Fig. 2.3 for different particle sizes (915 nm, 895 nm and 684 nm) and materials (Poly(methyl methacrylate) (PMMA), polystyrene (PS)). While no differences are visible in the DF images (Fig. 2.3a, d, g), ELS spectra distinctly reveal wave-like curve progressions that are clearly influenced by the particle size and the refractive index of the material (Fig. 2.3b, e, h). Larger particles display a higher number of interference maxima compared to smaller ones, whereas the refractive index has an impact on light deflection at the particle's interface and thus contributes to the maximum positions (Fig. 2.3b, e, h). ELS spectra (black) are in high accordance with Mie scattering simulations (blue), whereby pattern variations can be ascribed to measurement offsets. The scattering patterns derive from various phenomena of light interaction inside and along the spheres and can mostly be explained by an interplay of directly transmitted with phase-shifted light as a result of particle penetration [97]. Scattering can also be interpreted as a multiple reflection of plane waves or spherical waves, in case the sphere center is considered to be perfectly reflective [97]. The degree of multiple plane wave reflection raises along with increasing particle size, which results in a more complex scattering shape. Additional factors, such as the level of particle absorption, particle geometry, polarization and wavelength range of the incident light, surrounding medium / substrate or the direction of scattering detection significantly affect and increase the complexity of the scattering pattern. In dimers or higher order aggregates, the direct interaction between the particles or constituents make the scattering behavior even more complicated and an increased number of interferences can occur in comparison to single spheres. These interferences can be small in amplitude and might be overlaid as minor ripples.

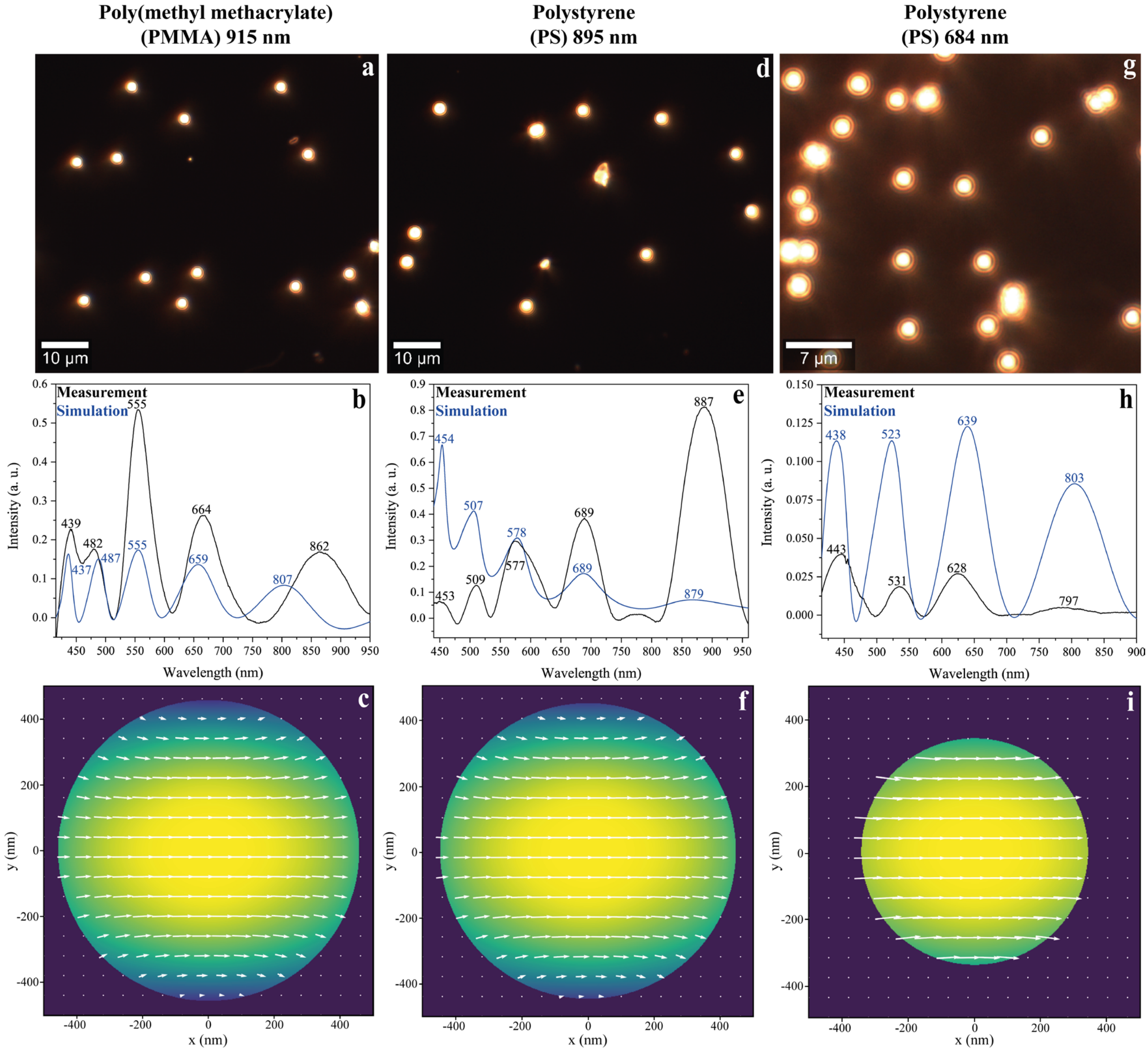

Figure 2.3. Mie scattering of single PMMA and PS particles with different sizes. DF microscopic images reveal bright PMMA particles with 915 nm diameter and PS particles with 895 nm and 684 nm diameters on dark background (a, d, g). Based on the image impression, the particles are not distinguishable from one another. For that reason, ELS line scans were performed in z-direction from the particle's top to bottom with a confocal DF microscope setup to illustrate Mie scattering patterns. Corresponding ELS spectra of central particle areas are depicted in (b, e, h; black), which exhibit sinusoidal spectral shapes with a varying number and position of maxima. All measured ELS spectra are in good agreement with the overlaid Mie scattering simulations (b, e, h; blue). However, small pattern variations might result from minor measurement offsets. Associated scattered E-fields around the particles in a near-field approximation are simulated for PMMA (915 nm) and PS (895 nm and 684 nm) single particles (c, f, i). The small, white arrows are consistently directed to the right and reveal the scattering direction of the E-fields (c, f, i). Here, the highest E-field intensity for resonant modes is visualized inside the spheres with a higher intensity closer to the surface (blue-green) than at the center (yellow) [97].

Ripple or wiggle patterns can be defined as highly frequent fluctuations of definite periodicity, which are mainly superimposed on the dominant interference scattering curve. They are often only resolved on basis of high instrumental resolution and exhibit some general properties: First, ripple's appearance is not limited to any value of refractive index and can be observed for more complex samples. Second, wiggles are not simple sine wave patterns and are more accurately described by two sine waves of slightly variable periods. In some cases, either single or double peaks in distinctive intervals can emerge [95]. In particles, they are often more pronounced if the particle's edges are primarily illuminated and can arise in scattering and absorption media [94]. Furthermore, ripples are strongly size-dependent, especially in backscattering direction, but their extrema positions and period mainly depends on the refractive index [98]. A possible explanation for this ripple behavior is derived from an interference effect between the forward diffracted wave and a second wave [95]. This second wave is defined to be a surface wave that occurs at the sphere edge and travels along its surface. As a result, the wave is attenuated and loses energy by refraction into the sphere or by becoming forward directed along the particle surface. In case, the surface wave is further weakened by multiple refraction events, it would be quenched completely at some point and no wiggles could be detected. Therefore, each refracted surface wave needs to be considered as a new surface wave that is amplified again and travels further along the sphere. This is accompanied by an increase in optical pathlength, which corresponds to a phase loss of the proceeding surface wave. If the phase shift at each refraction point is large enough, constructive or destructive interference with the main diffracted light can result and the wiggles appear superimposed [95]. Therefore, ripple formation, especially in backwards direction, can be considered as interferences between various order surface waves [97]. Differences in ripple oscillation frequencies might be deducible from varying interferences of reflected light at the sphere-medium interface with surface waves along the particle [99]. In more complex structures or particle ensembles, some of the wiggle oscillations might be canceled out, but still a highly frequent ripple pattern is often visible in the ELS spectra. All Mie scattering patterns normally result from an illumination with a monochromatic light source. However, the usage of a tungsten lamp as a polychromatic light source within this thesis makes the scattering patterns even more complicated and the application of multivariate data analysis (MVA) becomes mandatory. A mathematical description of Mie scattering for a single sphere is given in A1, Appendix.

So far, scattering of a spherical, homogeneous and isotropic particle is well characterized, but can be extended to even more complex structures. One example is tumor tissue, which can be considered as an inhomogeneous turbid matter. Turbid media consist of differently sized or shaped particles with variations in distance, density and refractive index. For tissues, this means a composition of different cell types, cell arrangements and cell organelles. A schematic representation of a tissue is shown in Fig. 2.4a. Each tissue provides a large number of scattering centers that are coupled and interfere with one another. As a consequence, multiple scattering events can occur, which overall add up to a final tissue-corresponding scattering signature [87]. For that purpose, incident light needs to penetrate into deeper tissue layers, which is mainly achieved in the visible / near-infrared (NIR) wavelength range. Most tissue components, such as cells, cell organelles or fibrous structures, resemble shapes of homogeneous spheres or ellipsoids in a size range of approx. $100\ nm - 10\ \mu m$ and are thus expected to cause Mie scattering. Important scatterers in tissues are cell organelles, of which cell nuclei, mitochondria, lysosomes and peroxisomes are mainly contributing to backward scattering. Especially, the enlargement of cell nuclei during carcinogenesis represents a crucial alteration in particle size and is thus ideally suited for the identification of tumorous tissue by ELS [100]. The backward scattering direction is also the dominant course for bulk scattering [87].

In order to measure the scattering patterns, a DF illumination and detection is most suitable, as illustrated in Fig. 2.4b [101]. Here, incident light by a polychromatic light source (yellow beams) is laterally transferred via the objective to a tissue sample, which is thus illuminated by a high-angle hollow cone of light. One part of the impinging light beam is specularly reflected by the tissue surface and not captured by the objective (grey arrows), as it propagates out of the objective's collection angle. Another part of the light beam is diffusely scattered by the tissue and passed through the objective to the detector (red arrows). This scattered light has penetrated the tissue and became singly or multiply deflected by different particulate components and aggregates, causing a sample-distinctive pattern that depends on the particle size, refractive indices, penetration depth of light, absorption by tissue constituents and the free length path [87]. Since the diffusely scattered light is often weak, a scattering amplification is required and realized by a thin gold coating on top of the objective slide. Without this DF arrangement most of the diffuse light would be overlaid by the specular light and no characteristic scattering patterns would be detectable [102]. An efficient approach for DF ELS measurements is their implementation as hyperspectral imaging technique.

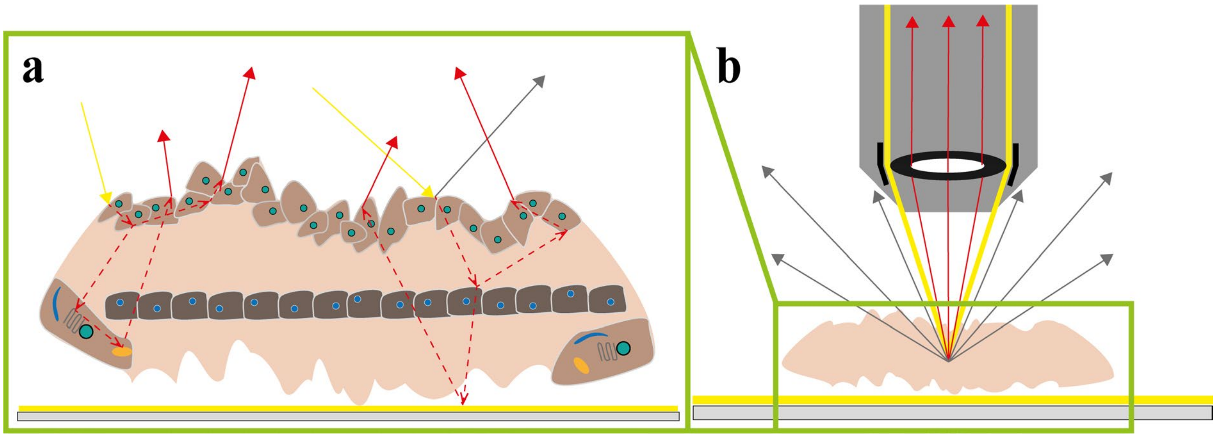

Figure 2.4. Tissue scattering effects on basis of Mie theory and DF illumination principle. Following light impingement (yellow arrows), various scattering events occur in a tissue cross-section (a). Tissues are composed of different cell types in varying arrangements and sizes (light- and dark brown cells) and thus the light is deflected differently for each cell type and even for each cell organelle (orange circles, serpentine shape). Consequently, the characteristic ELS pattern of a tissue is a composition of single, but mainly multiple scattering events (non-dashed and dashed arrows). In DF illumination (b), the incident light (yellow light beam) impinges sidewise via the DF objective on the sample, represented by a tissue specimen. This light is in part diffusely scattered (red arrows) and can thus be collected by the microscope objective. Another part, however, is specularly reflected by the tissue (grey-colored arrows) and does not enter the objective. The sample preparation on gold-coated objective slides is intended to intensify the scattered light.

2.1.3 Concept of Hyperspectral Imaging

Hyperspectral imaging (HSI) can be defined as a method for spectrum acquisition in each sensor pixel, whereby the specimen is simultaneously scanned in two spatial directions. After each finished scan, a full range spectrum is acquired for all spatial points in the 2D recorded area, representing a 3D data cube denoted as hypercube (Fig. 2.5). Mainly, three types of HSI can be differentiated according to their scanning and detection principle, which are Whiskbroom, Pushbroom and spectral scanning imaging. While the full spectral range can be measured at once in Whiskbroom imaging, the sample need to be raster-scanned point-by-point in the spatial x- and y-direction to create a complete hypercube. This allows to achieve a high spatial resolution at the cost of extensive scanning time. The usage of high-quality optics in these systems additionally lead to a high spectral resolution. In Pushbroom imaging, a whole line of pixel spectra in one spatial direction (x) can be acquired simultaneously and thus the specimen only need to be moved along the second spatial axis (y). Besides the also high spatial and spectral resolution in Pushbroom imaging, the fast scanning time is another advantage. One disadvantage, however, can be a spatial aliasing, which might occur during y-scanning as a consequence of movement disturbances. In spectral scanning imaging, both spatial axes are fixed and a spectral scan is performed by capturing the whole scene at various spectral filters. Although a high spatial resolution and a low acquisition time are realizable with this technique, a lack of spectral resolution power has to be accepted [103-105]. The choice of the most suitable HSI technology relies on the sample type, the requirements for resolution and scanning time as well as the data evaluation.

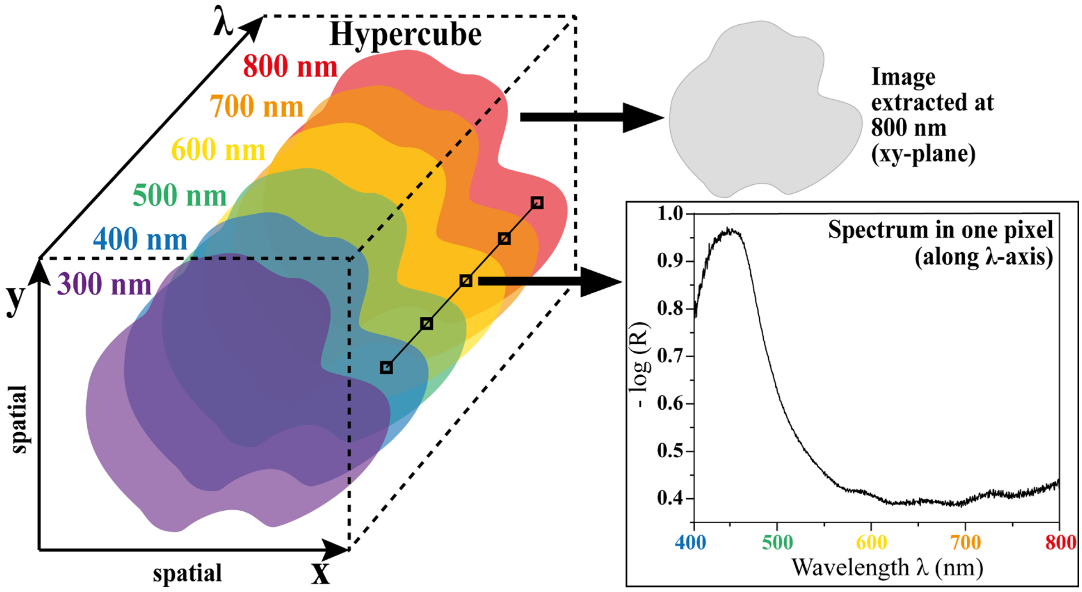

Figure 2.5. Principle of HSI. Spectral data in a predefined wavelength range (300 – 800 nm) is acquired for each sample point while the sample is simultaneously scanned in two spatial directions (x, y). This 3D matrix is termed a hypercube (left). Two evaluation approaches of the hypercube are possible: A full spectrum over the entire wavelength range (400 – 800 nm) can be extracted at each recorded sample point or a complete image of the specimen can be analyzed at one wavelength band (right). The extracted spectrum depicts the intensity of each sample point against the wavelength range. Adapted by [103,104].

Hypercube analysis can follow different data processing. By applying spectral filters at defined wavelength positions, full scanned 2D images of the scene can be extracted (e.g. 800 nm, Fig. 2.5, right). One reason for this data visualization is the demonstration of spatially-distributed sample features, highlighted at one particular wavelength band. Another hypercube processing includes the extraction of complete spectra from each pixel or sample point (Fig. 2.5, right). This is of special interest for a proceeding evaluation of the spectra with other analyzing tools, such as principal component analysis (PCA) or Bayesian discriminant analysis (DA), see chapter 2.2.1 and 2.2.2 [103-105]. The investigation of rodent tumor tissues was performed with Whiskbroom and Pushbroom DF ELS imaging, whereby whole spectra were extracted from the hypercubes to be examined by PCA-DA (see chapter 3).

2.1.4 Fundamentals of Confocal Raman Imaging

Confocal imaging techniques are increasingly popular due to their enhanced image contrast and high-resolution capabilities. In general, the principle of confocality describes the illumination spot on a sample, generated by a point-light source, and the image plane, displayed through a small aperture on the detector, to be in focus at the same time (Fig. 2.6a). The emitted light from the sample is only detectable in case it results from the defined focus point and does not originate from sample planes above or beneath the focal spot. This out-of-focus light will be blocked by a respective aperture (pinhole) in the light path and cannot reach the detector. As only a small illumination spot is created, the sample needs to be scanned as a whole in order to produce a complete spectroscopic image (Fig. 2.6a). The magnitude of the focal spot in x- and y-direction is dependent on the wavelength λ of the point-light source and the characteristics of the objective [106,107].

In addition to an improved contrast, confocal optical systems are characterized by high spatial resolution. In general, the spatial resolution of a confocal microscope can be differentiated in the lateral resolution, in x-y-direction, and in the axial resolution, depicted in z-direction. For calculating the x-y-resolution, the Rayleigh criterion is typically used. It states that two light emitters are just laterally resolved in case the central intensity maximum of the first emitter is placed in the first minimum of the second emitter [108]. Consequently, the minimum distance of two light emitters has to be:

$$d_{lim} = 0.61 \times \frac{\lambda}{NA} \tag{2.7}$$

As shown by eq. 2.7, the required distance d_{lim} to distinctly resolve two light emitting objects from one another depends on the emission wavelength λ of the two light sources and the numerical aperture (NA) of the objective. Indicated by the Rayleigh criterion, the diffraction patterns of both light sources are depicted as a sequence of constructive and destructive interferences of different intensities, first observed by George Biddell Airy. Thus, this pattern is denoted as Airy pattern, whereby the central, most intense maximum of the pattern is called the Airy disk. The varying intensity distribution of the Airy pattern is best represented by a point-spread-function (PSF) [109]. A PSF describes how a point is imaged by the microscope system and is influenced by the emitter's wavelength, its size and the objective NA [110]. By calculating or measuring the Full Width at Half Maximum (FWHM) of an Airy pattern, the lateral resolution of the confocal optical system can be identified. Considering the FWHM of a 3D PSF as the microscope's resolution, an adjusted formula for the lateral resolution can be defined as [110]:

$$FWHM_{lateral} = \frac{0.55\ \lambda_{excitation}}{NA} \tag{2.8}$$

For reasons of simplicity, eq. 2.8 only includes the excitation PSF by applying a factor of 0.55 and additionally incorporates the excitation wavelength $\lambda_{excitation}$ of the laser as well as the objective NA. In image formation, the detection PSF can differ from the excitation PSF and is particularly influenced by the nature of the emitted light and the structure of the used detector [106]. Besides the lateral resolution, an axial or depth resolution of the confocal system can additionally be determined. This is affected by the pinhole size, since a smaller pinhole removes the out-of-focus emission better than a larger one. The filtering effect is even more improved in axial direction compared to x-y, which results in a higher axial resolution, illustrated by an increased factor of 0.88 [110]:

$$FWHM_{axial} = \frac{0.88\ \lambda_{excitation}}{\left(n - \sqrt{n^2 - NA^2}\right)} \tag{2.9}$$

Again, the formula for the axial resolution (eq. 2.9) only considers the excitation PSF by $\lambda_{excitation}$ in addition to the refractive index n of the medium and the objective NA. Overall higher resolutions can be achieved in a confocal compared to a conventional setup, expressed by a FWHM difference of $\sqrt{2}$ between PSFs for both instruments [106]. In comparison, the spectral resolution is defined as the ability of optical elements to resolve two adjacent spectral peaks from one another and enable a distinct spectral separation of both signals. In a confocal setup, it mainly depends on the employed spectrometer, with which the spectral data is acquired. Main detection components, such as the used grating or pinhole, contribute to the spectral resolving power. In combined detection units, the pixel size and resolution of a charge-coupled device (CCD) camera as well as the wavelength dispersion of a spectrometer, determined by the FWHM, are important for the overall spectral resolution. A common approach to specify the resolution of the whole detection device is to acquire a spectrum of sharp atomic lines, e.g. that of mercury, and evaluate each line by means of its FWHM. This FWHM value represents the spectral resolution in good approximation [106]. This resolution advantage is used to record high-quality Raman data by employing confocal Raman imaging.

The basis of Raman spectroscopy is the measurement of inelastically scattered photons after a collision with a molecule that implicates an energy transmission. In Stokes scattering (Fig. 2.6b), energy of a photon is transferred to the molecule due to a photon-induced molecular oscillation. This is accompanied by an electron cloud deformation (Fig. 2.6b, pink cloud) and a dipole moment $\vec{\mu}$ is initiated. As a result of the energy exchange, the photon energy is reduced. In anti-Stokes scattering, energy of an already thermally-vibrating molecule with changing polarizability is transmitted to a photon and thus its energy is increased [106,88].

Inducing a dipole moment $\vec{\mu}$ is directly correlated to the initial electric field $\vec{E}$ and the polarizability $\tilde{\alpha}$ of the molecule and can be described quantitatively as:

$$\vec{\mu} = \tilde{\alpha}\vec{E} \tag{2.10}$$

In eq. 2.10, the polarizability $\tilde{\alpha}$ functions as a proportionality factor between the induced dipole moment $\vec{\mu}$ and the external electric field $\vec{E}$. It displays the extent of electron perturbation by $\vec{E}$ from an equilibrium state without any field impact. Based on the oscillation of $\vec{E}$, $\tilde{\alpha}$ can be described by a cosine function with an amplitude $\vec{E}_0$ and an oscillation frequency ω_0 according to $\vec{E} = \vec{E}_0 \cdot \cos(\omega_0 t)$. As a result of $\vec{E}$ driving the deformation of the electron density, the molecule's nuclei compensate for the electron displacement by a nuclear movement. Therefore, the polarizability $\tilde{\alpha}$ is not static, as it is influenced by electron and nuclear motions to minimize the system's energy. To determine the rate of change for $\tilde{\alpha}$ with regard to the equilibrium state q_0 and the sum of all oscillating normal modes q, $\tilde{\alpha}$ is expressed by a Taylor series expansion [106,88]:

$$\alpha = \alpha(q) = \alpha_0 + \sum_{q=1}^{N} \left[\left(\frac{\partial \alpha}{\partial q}\right)_{q_0} \cdot q + \frac{1}{2}\left(\frac{\partial^2 \alpha}{\partial q \partial q'}\right)_{q_0 q_0'} \cdot q \cdot q' + (\ldots) \right] \tag{2.11}$$

By considering the vibration of the normal modes to be harmonic and described by an oscillating motion $q = q_0 \cdot \cos(\omega_q t)$, the Taylor expansion can be reduced to the first linear term. Since alterations of α can be expressed by a deflection of normal modes q from their equilibrium q_0, the dipole moment $\vec{\mu}$ can be depicted as:

$$\mu(t) = \left[\alpha_0 + \left(\frac{\partial \alpha}{\partial q}\right)_{q_0} \cdot q_0 \cdot \cos(\omega_q t) \right] \cdot E_0 \cdot \cos(\omega_0 t) \tag{2.12}$$

Applying the trigonometric relation $\cos(A)\cos(B) = 1/2\cos(A+B) + 1/2\cos(A-B)$ results in the expression:

$$\mu(t) = \alpha_0 \cdot E_0 \cdot \cos(\omega_0 t) + \frac{1}{2}\left(\frac{\partial \alpha}{\partial q}\right)_{q_0} \cdot q_0 \cdot E_0 \cdot cos[(\omega_0 - \omega_q)t] + \frac{1}{2}\left(\frac{\partial \alpha}{\partial q}\right)_{q_0} \cdot q_0 \cdot E_0 \cdot cos[(\omega_0 + \omega_q)t] \tag{2.13}$$

Each term in eq. 2.13 relates to a vibrational component that alters with the induced dipole moment $\mu(t)$ and exhibits a different oscillation frequency ($\omega_0, \omega_0 - \omega_q, \omega_0 + \omega_q$). After the initiation of a dipole moment, an energy transfer between the molecule and the scattered photon occurs. This leads to three possible scattering frequencies of the emitted radiation, as shown by eq. 2.13. The first component reveals a photon scattering with an identical frequency as the external electric field (ω_0) and is denoted as Rayleigh scattering ($\alpha_0 \cdot E_0 \cdot \cos(\omega_0 t)$). In case of the second and third term, the inelastically scattered photons have either lost or gained energy and are thus characterized by either lower ($\omega_0 - \omega_q$) or higher frequencies ($\omega_0 + \omega_q$) compared to the excitation frequency. Both components are denominated as Stokes ($1/2\,(\partial\alpha/\partial q)_{q_0} \cdot q_0 \cdot E_0 \cdot cos[(\omega_0 - \omega_q)t]$) and anti-Stokes scattering ($1/2\,(\partial\alpha/\partial q)_{q_0} \cdot q_0 \cdot E_0 \cdot cos[(\omega_0 + \omega_q)t]$), respectively.

Stokes and anti-Stokes scattering is mainly illustrated as a Raman shift in wavenumbers ($\Delta\bar{\nu}$) within a Raman spectrum (Fig. 2.6c). The Stokes scattering is red-shifted and thus decreased in frequency, whereas the anti-Stokes scattering is shifted to the blue and has an increased frequency. Rayleigh scattering represents the elastically scattered excitation source at wavelength λ_0 and defines the “zero” wavenumber, by which the Raman shift is calculated (Fig. 2.6c). The intensity of all three events greatly varies. Rayleigh scattering is the most intense process of all (10^{-3} less intense than incident radiation), whereas Stokes and anti-Stokes scattering produce far weaker signals (together 10^{-6} less intense than incident radiation) [85]. Additionally, anti-Stokes scattering is less intense than Stokes scattering due to a decreased molecule population of higher vibrational levels in S_0 and the higher energy difference between the states [85]. At ambient temperature, molecules are mainly populated in the lowest vibrational state of S_0 that primarily cause the occurrence of Stokes scattering. Therefore, Stokes signals are most dominant in Raman spectra [85,106].

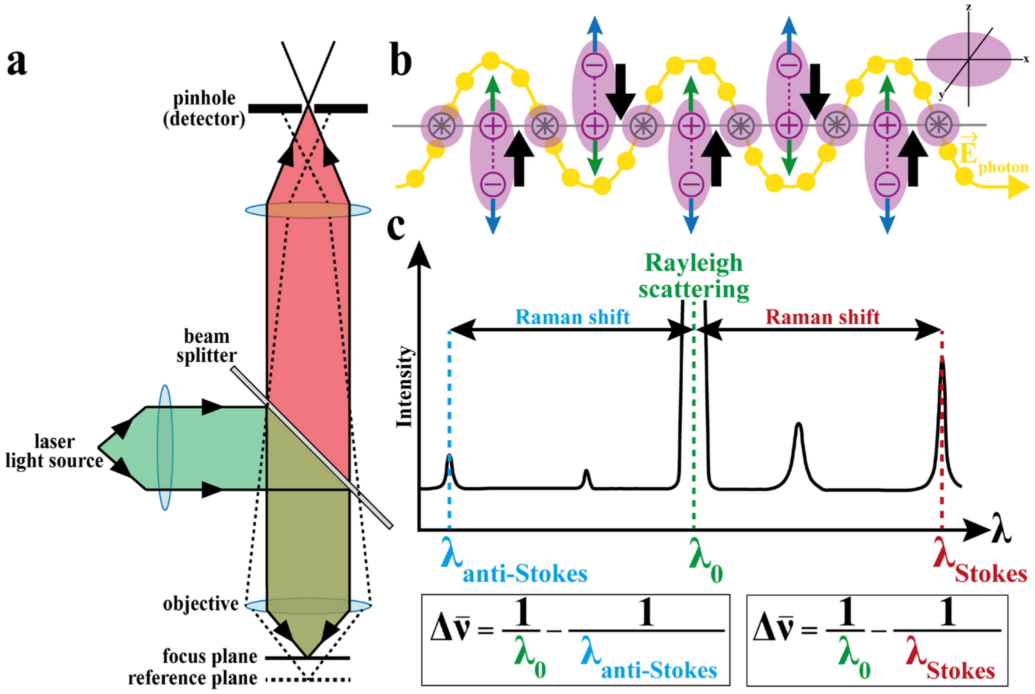

Figure 2.6. *Confocal detection principle and basics of Raman scattering. In a confocal setup, the light spot on the sample and the image spot are at the same time in focus and are thus confocal to one another. The detection of light is only allowed within the focus plane (solid line), realized by a small aperture (pinhole) (a). All light out of focus is removed by the pinhole and is consequently not detected (dotted line). The initiation of Raman scattering for an exemplary homonuclear diatomic molecule is shown in (b). The molecule is stimulated to vibrate after excitation by an external electric field ($\vec{E}_{Photon}$) of a laser. This vibration causes an electron cloud deformation (pink) and thus a change in polarizability that induces a dipole moment (+/-). The horizontal, solid line in (b) represents the molecule's proton and electron center (⊛). The oscillating dipole moment affects the emission of Rayleigh, Stokes and anti-Stokes scattering (c). Raman bands can appear at either longer (Stokes) or shorter wavelengths (anti-Stokes) with respect to the incident radiation wavelength (Rayleigh), represented by the Raman shift ($\Delta\bar{\nu}$). Adapted by [85,106,111,112].*

2.1.5 Fundamentals of Infrared (IR) Spectroscopy

In IR spectroscopy, the transition between various vibrational levels is measured due to molecular absorption. Its principle is based on the interaction of a molecule with IR radiation that can initiate a molecular oscillation. In case the vibrational motion causes an alteration of the prevalent dipole moment, IR energy is absorbed. This process is called stimulated absorption, by which the molecule is transferred from a lower to a higher vibrational level and can be expressed as [78]:

$$W_{u\leftarrow l} = B_{u,l} N_l \rho(\nu) \tag{2.14}$$

with $W_{u\leftarrow l}$ representing the rate of stimulated absorption, N_l is the molecule's population in low states and $\rho(\nu)$ describes the energy spectral density. $\rho(\nu)$ can be interpreted as the radiation energy density and $B_{u,l}$ is the Einstein coefficient of stimulated absorption. As seen in eq. 2.14, the degree of transition is subjected to the intensity of the initiating field and the population of individual levels. A high irradiation intensity facilitates an increasing absorption rate ($l \rightarrow u$) due to an enhanced probability of a photon-molecule interaction. Additionally, the chance of photon absorption is also increased by a pronounced population in low energetic states [78].

A change in dipole moment, induced by an alternating, homogeneous electric field, is shown in Fig. 2.7a. The E-field oscillation exerts forces on the partially positive and negative atomic charges and thus achieves a stretching (green arrows) and compression (blue arrows) of bonds over time. This displacement is changed in accordance with the initial photon frequency [85,88] and its extent depends on the magnitude of the dipole moment μ, characterized by the charge dimensions (e_i) and positioning (r_i) [85]:

$$\mu = \sum e_i r_i \tag{2.15}$$

To establish whether a molecular vibration is IR-active, the derivative of the dipole moment $(\partial\mu/\partial q)_{q_0}$ along the normal coordinate q in equilibrium q_0 has to be considered. This derivative has to be non-zero, as exemplarily fulfilled for the asymmetric stretching and bending vibration of a triatomic molecule (Fig. 2.7b). In an asymmetric stretching (left), the opposite directions of both bonding motions lead to a constant variation of the dipole moment along the normal coordinate. The same is true for a bending vibration (right), where the center atom is opposingly directed than the outer atoms. On the contrary, both vibrations are not Raman-active since no alteration of α is achieved and thus the derivative $(\partial\alpha/\partial q)_{q_0}$ equals zero [85,88,106]. The IR-activity of a molecule strongly depends on its geometry and degree of symmetry / asymmetry [88].

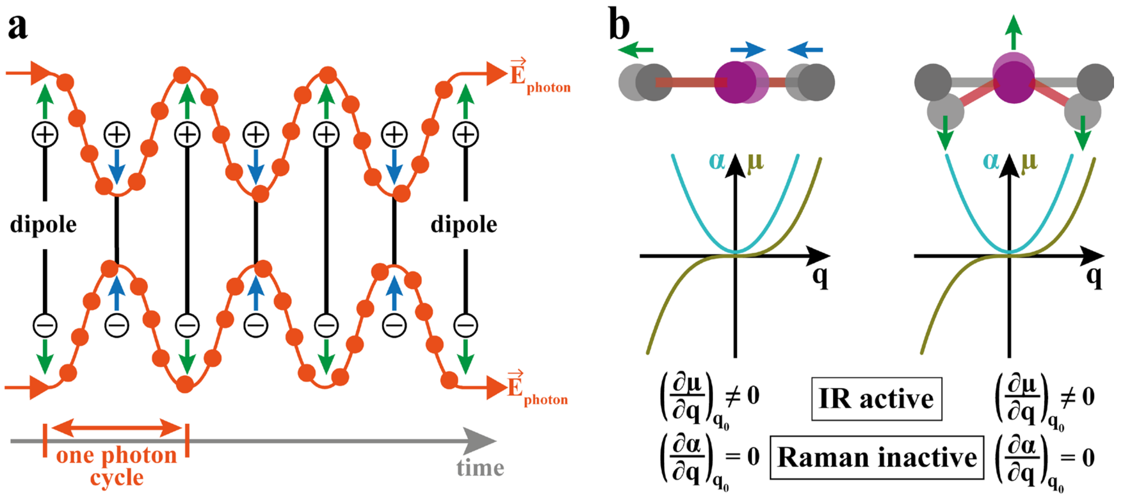

Figure 2.7. *IR absorption as a result of dipole moment variations, initiated by molecular vibrations. Upon IR irradiation, the photon electric field exerts forces on the molecule's dipole moment and the charge spacing alternately changes over time (a). This triggers a dipole moment oscillation in accordance with the photon frequency and the photon energy is absorbed. Only certain vibrational modes lead to IR absorption (b), which can be determined by the dipole moment's derivative* $(\partial\mu/\partial q)_{q_0}$*. In case the dipole moment alters along the normal equilibrium coordinate, the derivative is unequal to zero and the respective mode is IR-active. This is observed for the antisymmetric and bending vibration (b). On the contrary, both vibrations reveal symmetric polarizability changes, as expressed by the zero-polarizability derivative* $(\partial\alpha/\partial q)_{q_0}$*, and thus they are not Raman-active. Adapted by [85,106].*

An IR-initiated oscillation can simply be expressed by a harmonic vibration of a diatomic molecule. Its motion profile is described by a parabolic potential energy curve with the potential energy $V(x) = 1/2\, k_f x^2$ and the molecular displacement $x = R - R_e$. The parabolic structure implicates an infinite potential energy at maximum displacement, whereas in the molecule's equilibrium state, no potential energy is exhibited at all. k_f functions as force constant that represents the stiffness of the atomic bonds throughout the vibrational motion. Different curvature degrees of the parabolic potential energy near its minimum demonstrate this stiffness, as k_f becomes large for a stiff bond and low for a more flexible bond. A quantum mechanical description of the harmonic oscillation is given by the Schrödinger equation that considers the relative movement of each atom in the diatomic molecule [78]:

$$-\frac{\hbar^2}{2m_{eff}}\frac{d^2\Psi}{dx^2} + \frac{1}{2}k_f x^2 \Psi = E\Psi \tag{2.16}$$

Additional parameters of the Schrödinger equation entail the reduced Planck's constant ħ, the effective mass m_{eff}, the wavefunction Ψ and the eigenvalue E. For characterizing the harmonic vibration, the usage of m_{eff} is more appropriate, as it involves the different masses of the participating atoms. The solution of the Schrödinger equation finally reveals equidistantly quantized energy levels for the vibrational transition of a harmonic oscillation, depicted in wavenumbers $\tilde{\nu}$ [78]:

$$E_v = \left(v + \frac{1}{2}\right) hc\tilde{\nu} \text{ with } \tilde{\nu} = \frac{1}{2\pi c}\left(\frac{k_f}{m_{eff}}\right)^{1/2} \tag{2.17}$$

Each energy transfer occurs between equally spaced energy states, which are integer multiples of the lowest level $v = 0$. All states are defined by the vibrational quantum number v that characterizes consecutive stages with increasing ν. Noticeably, the lowest energy level does not feature zero-energy, implying that a harmonic oscillator still occupies kinetic energy and also exhibits potential energy. Resulting from eq. 2.17, IR absorption includes an increase of a lower vibrational state to a higher one, whereas IR irradiation is emitted in case of a decrease from a higher to a lower vibrational level. This leads to a concrete selection rule of $\Delta\nu = \pm 1$ for a harmonic movement. Based on the Boltzmann distribution, most molecules are in the vibrational ground state at ambient temperature, which mainly causes a transition from $\nu = 0 \rightarrow \nu = 1$, denoted as the fundamental transition [78].

Although the harmonic oscillation is a reasonable approximation for an IR-induced vibration, a more accurate description results from the consideration of an anharmonic movement. Here, a potential dissociation of the molecule at high atomic displacement is regarded and no proportionality between the gained energy $V(x)$ and the displacement x exists anymore (represented by k_f). Instead of a parabolic energy curve, the potential energy $V(x)$ is depicted by the Morse potential energy $V(x) = hc\widetilde{D}_e\{1 - e^{-ax}\}^2$ with $a = \left(m_{eff}\omega^2/2hc\widetilde{D}_e\right)^{1/2}$. This curve trend resembles the harmonic oscillation near $V(x) = 0$, but approximates the potential depth $hc\widetilde{D}_e$ with increasing displacement x. Compared to the harmonic oscillator, the Schrödinger equation for the Morse potential is structured as [78]:

$$-\frac{\hbar^2}{2m_{eff}}\frac{d^2\Psi}{dx^2} + hc\widetilde{D}_e\{1 - e^{-ax}\}^2\Psi = E\Psi \qquad (2.18)$$

and solved to reveal the vibrational energy levels, originating from the anharmonic motion that can be determined by:

$$E_\nu = \left(\nu + \tfrac{1}{2}\right)hc\tilde{\nu} - \left(\nu + \tfrac{1}{2}\right)^2 hcx_e\tilde{\nu} \text{ with } x_e = \frac{\tilde{\nu}}{4D_e} \qquad (2.19)$$

Permissible vibrational quantum numbers ν are again integer multiples $\nu = 0, 1, 2, ..., \nu_{max}$ and x_e functions as dimensionless anharmonicity constant. The structure of eq. 2.19 shows the increasing influence of the second, quadratic term, which defines the distance to the adjacent energy level. As this term is subtracted, the energy states come closer together with higher ν until they converge to the finite vibrational quantum number ν_{max}. Contrary to the harmonic vibrational transfers of $\Delta\nu = \pm 1$, transitions of $\Delta\nu > 1$ are allowed in an anharmonic oscillation and thus overtone vibrations can occur, such as $3 \leftarrow 0$ or $2 \leftarrow 0$. Anharmonicity additionally elucidates the observation of combinational vibrations. They result from the simultaneous excitation of various modes to higher vibrational levels, energetically close together due to energy state convergence [78,88].

For reasons of simplification, the concept of harmonic and anharmonic oscillation is introduced for diatomic molecules, but equally adaptable to more complex molecular compositions. In non-linear, polyatomic molecules, $N_{vib} = 3N - 6$ vibrational modes exist, which can be stimulated by external IR irradiation. Here, each mode is interpreted as an individual oscillator with a characteristic energy, specified by the vibrational quantum number ν, that can be increased by $\Delta\nu > 1$. The holistic visualization of different vibrational transfers in an IR spectrum provides information about the chemical constitution and thus can be used to identify unknown molecules [78].

2.2 Multivariate Data Analysis

The application of statistical tools is common for analyzing spectroscopic data and reducing them to the most meaningful core of information. Two of these methods are PCA and DA. They are often used in combination and allow not only to generate a profound sample understanding, but also enable the formation of powerful identification and prediction models based on the spectroscopic data sets.

2.2.1 Principal Component Analysis (PCA)

In general, PCA is deployed to restructure and divide a measured data matrix *X* into an information-bearing and residual noisy part, respectively. One major advantage of this method is the simultaneous reduction of matrix dimension and revelation of latent trends or groups, hidden in the data structure. The approach to achieve this data rearrangement is schematically illustrated in Fig. 2.8.

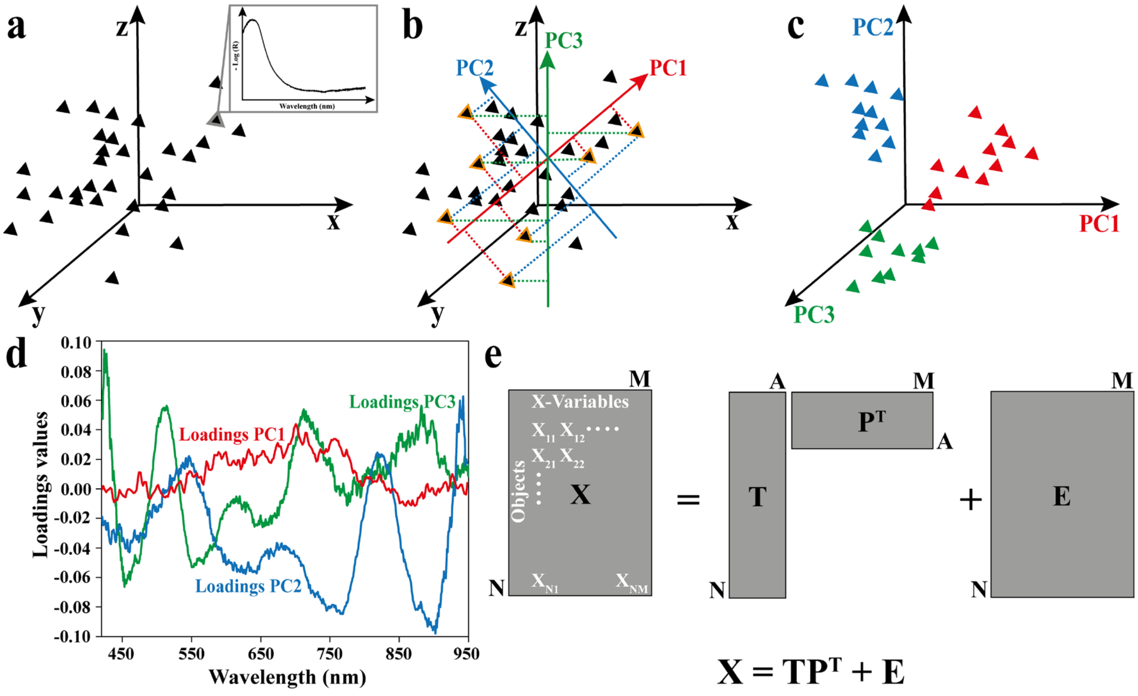

Figure 2.8. *Schematic structure and principle of PCA. A 3D data plot of a spectral data matrix is shown in (a). Each data point of the matrix represents one spectrum, equivalent to one object, of which only the first three variables are illustrated in the variable space for reasons of simplicity. The matrix arrangement reveals no distinct correlation between the data. To clearly identify possible cohesions (b), the objects need to be structured according to their maximum variance, delineated by new principal component axes (PC1, PC2, PC3). The maximum variance describes the largest data spread along the PC directions and can be found by a perpendicular projection of each object onto the PCs (dotted lines). For a complex data matrix, more than one PC is required for structuring (e.g. also PC2 and PC3). Per definition, each subsequent PC needs to be aligned orthogonally compared to the previous one. The calculated PCs define a new coordination system for the data objects, which are separated according to their largest spread and delineated by score values as new PC coordinates (c). A linkage between the original description in the x, y, z- and new PC coordination system is given by the loadings (d). Loading values represent a weighting of each original variable on the respective PC direction and thus express, which variables have the greatest impact on the data alignment. A mathematical PCA description is illustrated in (e) that defines a centered matrix X as a sum of the matrix product* TP^T *and the residual matrix E. Adapted by [113,114].*

Normally, each matrix X consists of a defined number of objects n, displaying the sample amount, and a number of variables p, representing characteristic features of each object. All objects are arranged as rows (row vectors) within the data matrix, whereas the variables are aligned as the column attributes that collaboratively describe each object. Therefore, all objects n can be differentiated by varying values for the descriptive variables p. The size of X is not limited to a number of objects or variables, but makes the usage of PCA even more essential if it is large and complex. In case the $n \times p$ matrix consists of spectra with many variables and is plotted in a p-variable coordinate system, the objects (spectra) are distributed according to their p-values in multidimensional directions. For reasons of simplicity, each object (triangle) is shown by only the first three variables in a 3D p-variable coordinate system (x, y, z) (Fig. 2.8a). In x, y, z-space, no clear correlation between the objects can be recognized. To ascertain whether an underlying correlation exists, a new object arrangement is required. For this purpose, a new axis is introduced that reflects the maximum spread of the data majority (Fig. 2.8b, red axis) and reduces the variable dimension exemplarily from three to one by orthogonal object projection (Fig. 2.8b, red dotted lines). It is denoted as the first principal component (PC1). The PC1 alignment is specifically chosen to describe the maximum data variance, as no other orientation covers a comparable data variation. Therefore, a new structuring according to the maximum variance is highlighted by PC1 that results from a hidden, underlying object characteristic. PC1 can also be regarded as an optimized axis concerning the smallest, perpendicular object spacing, which is determined in a squared distance approach. Here, its alignment needs to satisfy minimum, perpendicular distances to the objects that causes a decrease of their total squared distances. As the objects show variable spacing towards PC1, they contribute differently to the PC1 calculation. This means that most distant objects have a high impact on PC1, whereas closest elements are far less influencing (leverage). A third understanding of PC1 derives from the fact that it can be expressed as a linear combination of all p-variables [113,114].

PC1, however, is not sufficient to fully characterize X. Higher-order PCs are additionally necessary to find consecutively the highest variance in the matrix and to minimize the sum of all squared object distances. They are successively calculated and orthogonally oriented to the respective, previous PC (Fig. 2.8b, blue and green). Since the highest data variance has already been covered by PC1, subsequent PC2 arranges another data proportion of second highest variation, whereas PC3 organizes the third largest maximum variance. The resulting data alignments can again be ascribed to latent variables that demand a detailed interpretation based on data background and origin. With each increasing PC, a decreasing data variation of X is represented until only a minor residual of random noise remains. The largest possible number of PCs depends on the smallest parameter of X, which is either the quantity of objects n $(n-1)$ or the number of variables p (p) [113]. Although more PCs could be calculated for some matrix sizes, only a minimum of PCs should be striven. Regardless of the final number of PCs, they define the new and uncorrelated coordinate system, in which X is grouped regarding its maximum variation (Fig. 2.8c). The coordinate system center is located at the data average point instead of the x, y, z-origin, as a result of mean centering. In this system, the matrix can now be described by a new set of variables, called the score values, which do not inter-correlate as p-variables do in the x, y, z-space. Score values are characterized as the distance between the PC object projection and the origin of the PC coordinate system. These distances can be assigned to positive or negative values along the PC axes and are specific for each object. In a multidimensional sub-space, score values define the exact location of an object on a PC-spread surface with one coordinate value per PC. Thus, the object position is described in each PC dimension. All score coordinates for every object are summarized in the T-matrix. Here, the orthogonal column vectors reflect the individual object projection onto one specific PC. For visualization purposes, all objects are displayed in a score plot that shows a sub-space of certain score column vectors. Typically, either 2D or 3D score plots are shown, as both highlight well the correlation in-between the objects (Fig. 2.8c). In some cases, even more than one score plot is necessary to fully depict their relation, which is essential for a correct data interpretation. The score plot is a useful tool to identify outliers, trends or group formation as well as sample variability [113,114].

As a result of data translation from one coordinate system to the other, PCs can be regarded as a linear combination of the p-variable unit vectors from x, y, z-space. These linear combinations are characterized by p-coefficients, also denoted as loadings, which concretely relate p-variable unit vectors to the PCs and thus represent the interface between both data descriptions. Their magnitude reveals the impact of p-variables on the respective PC direction, which is either negatively or positively correlated. Typically, the loading values are normalized to $+1$ for positive and -1 for negative loadings. All loadings are combined in a P-matrix that comprises the orthogonal loading column vectors. These vectors reveal the correlations throughout each calculated PC. Loadings can also be illustrated in loading plots, which show the weighting of individual p-variables on each PC (Fig. 2.8d). This weighting enables an interpretation of the object structuring along the PCs, since p-variables are characteristic attributes of the objects. Conclusions can thus be drawn about the latent variables that cause the object structure. Loading plots for spectroscopic data are mainly represented as 1-dimensional plots and often resemble the spectral behavior (Fig. 2.8d) [113,114].

The mathematical description of PCA emphasizes its reduction and decomposition capabilities, as X can be expressed as a matrix sum of product TP^T and residual matrix E (Fig. 2.8e). In this expression, the T-matrix is equivalent to the score matrix and the P^T-matrix includes the loadings in transposed form. TP^T corresponds to the part of X, which is completely explained by the calculated PCA, whereas E is the proportion to be removed from X. Each PC calculation is typically performed by an adequate matrix algorithm, which computes the PC contributions as outer vector products $t_A p_A^T$ in a stepwise manner:

$$X = t_1 p_1^T + t_2 p_2^T + \cdots + t_A p_A^T + E \tag{2.20}$$

Initially, the algorithm calculates the first set of column score t_1 and loading p_1 vectors of X. This vector product $t_1 p_1^T$ represents the first PC and is afterwards subtracted from X that results in a first residual matrix E_1. It is a PC1-reduced matrix, by which the total variance of X is diminished. According to this principle, further PCs ($t_2 p_2^T$, $t_3 p_3^T$, etc.) are determined until the optimum number is found for the investigated data set. This leads to a final residual matrix E, by which X is reduced [113,114].

To achieve a satisfying PCA structuring and decomposition, various preprocessing steps prior to PCA calculation are often required. Preprocessing procedures are simple mathematical operations that prevent insignificant effects in the data to overcomplicate the PCA model. This is especially important for complex data sets. Their preprocessing can entail to remove extraneous noise or highlight smallest differences in-between the data points. Important preprocessing of spectroscopic data for this thesis includes spectroscopic transformations, smoothing, normalization, baseline correction, derivation and standard normal variate (SNV) [113,114].

Spectroscopic transformations: This tool is mainly applied to transmission or reflectance data in order to transform their p-variable values into absorbance values that follow Beer's law. Therefore, a direct, linear connection between sample absorbance and concentration can be drawn. Absorbance transformations can additionally help to decrease effects based on pathlength variations and thus hidden chemical information is more pronounced.

Smoothing: Spectral smoothing is caused by substituting the central point of a p-variable range with a p-variable mean value that results from averaging the predefined range. Different smoothing algorithms deploy various averaging strategies. The most common ones are the moving average and Savitzky-Golay algorithms. In moving average, the central value of a specified p-variable segment is replaced by the respective mean of the segment after averaging. In Savitzky-Golay, a polynomial function is fitted to a defined p-variable range for average calculation. This average value again substitutes the central value of the range. A complete smoothing is achieved by accomplishing the average formation and substitution in a stepwise manner across the whole spectrum.

Normalization: Data normalization encompasses an object-related summation of all p-variable values to generate a row sum, by which each p-variable value is divided individually. As a consequence, all row values are located in a similar domain and inter-object variations are minimized to a certain extent. This is important in case absolute values are not required, as they are e.g. for quantification purposes or concentration comparisons. Thus, normalized spectra do not differ by their magnitudes of intensity, counts or absorbance, but due to their spectral signature. Various types of normalization, such as area, range or maximum normalizations, are only distinguishable by the way of sum calculation.

Baseline correction: A baseline correction should be considered for mutual, flat, non-linear or even linear offsets across or in-between the spectra to improve the overall spectral superposition. These offsets are simply removed by their subtraction from the spectra and can exemplarily be ascribed to sampling variations. As a result of offset elimination, baselines and thus similar spectral patterns are more uniform.

Derivation: The calculation of derivatives centers the spectra around a zero line and spectral slopes are pronounced. It entails that a subsequent p-variable value is subtracted from a previous one and the resulting difference is divided by a constant centering factor. These operations are accomplished in a stepwise fashion to get a complete derivative spectrum. All derivative calculations are accompanied by a simultaneous spectral smoothing. Two types of derivation algorithms are mainly used, the gap and Savitzky-Golay algorithms. In gap derivation, a smoothing according to the moving average is initially conducted for both p-variables prior to their subtraction. One segment around each p-variable is applied for averaging and the obtained midpoints can be subtracted afterwards. In Savitzky-Golay derivation, the initial smoothing is performed by fitting the p-variables to a least square linear regression of a polynomial function in a predefined window. After that, the difference of the smoothed p-values is computed. A calculation of a first order derivative initiates all spectra maxima to become zero points, whereas a second order derivative yields the spectrum curvature. Derivations are often applied to remove additive effects in the data.

Standard normal variate (SNV): SNV enables a general centering of the data at the overall average value and causes a scaling to a unified variance. This is achieved by subtracting each p-variable from the overall p-variable mean and successively dividing this difference by the standard deviation. It is mostly applied for the removal of unwanted scattering effects, but can also help to manifest the hidden chemical / morphological information or to eliminate additive and multiplicative effects.

2.2.2 Bayesian Discriminant Analysis (DA)

All reduction and restructuring advantages of PCA can further be combined with classification approaches to create powerful prediction models for identification purposes. One of these methods is DA as part of the supervised classifications. Their principle encompasses that an unknown pattern is distinctly assigned to be an element of an existing group of resembling objects [115]. DA functions as a separation technique that determines the best possible border to optimally demarcate a training set of objects into two or more object groups (Fig. 2.9). This optimized border does not necessarily need to ensure a complete class separation. Instead, minor group overlaps are also permitted. Several border shapes can suit best for class segregation, which are most often linear, quadratic or Mahalanobis distance-based separators (Fig. 2.9). Exemplarily, quadratic borders are mainly applicable for separating groups of differently-oriented main variances. In comparison, the usage of Mahalanobis distance is appropriate for measuring the object distance to the class centers by applying ellipses as distance calculators [113].

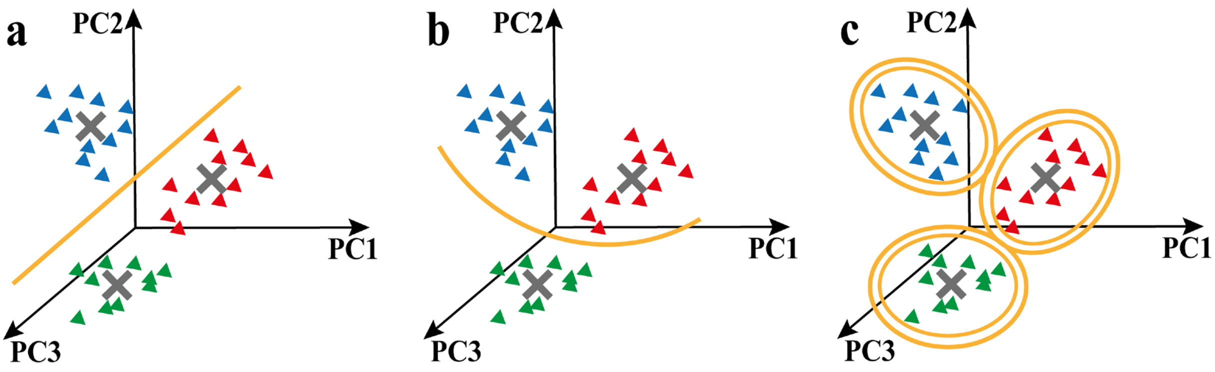

Figure 2.9. *Schematic illustration of different DA separators. The DA function mathematically describes a border of variable shape that represents the best possible discrimination of a training data set into several groups. A preliminary structuring of the training set can be accomplished by PCA to reduce its dimension. In this case, PC scores are used as variables to estimate a suitable discriminant function. Among many separators, the three most common ones are linear (a), quadratic (b) and Mahalanobis distance (c) separators (orange lines or circles).*

Each border is mathematically determined by a suitable discriminant function that considers probabilities according to the Bayes' theorem. This theorem states that an object is assigned to a class with the highest conditional / posterior probability [116,117]. To specify the posterior probability $P(l|x)$, the classes are assumed to result from an underlying data distribution according to a multivariate normal distribution, including mean μ and covariance matrix Σ. Additionally, all classes are expected to display a prior probability p_j, which is either equal or unequal for all groups. Considering all, the posterior probability $P(l|x)$ for object x belonging to class l can be expressed as [116,117]:

$$P(l|x) = \frac{f_l(x)p_l}{\sum_{j=1}^{k} f_j(x)p_j} \tag{2.21}$$

with the density function $f_j(x)$ of the data's multivariate normal distribution, group $j = 1, \dots, k$, class l and prior probabilities p_j for each group and p_l for group l. As the denominator is equal for all classes (eq. 2.21), $P(j|x)$ can directly be compared in-between the groups. At equal $P(j|x)$, two classes immediately adjoin each other and a boundary between them can be defined. Since $P(j|x)$ is composed of $f_j(x)$ and p_j, both parameters of the groups have an impact on the boundary conditions. For identical p_j, the decision border lies exactly in-between two groups where $f_j(x)$ are equal. In case of unequal p_j, the decision line is shifted towards classes with lower p_j. One reason for this shift is to prevent misclassifications by reducing classes with small p_j, as they also lower $P(j|x)$. High $P(j|x)$ are the prerequisite to deduce discriminant / classification functions that are structured differently under various conditions. In the case of equal covariance matrices of the classes $\Sigma_1 = \dots = \Sigma_k = \Sigma$, the discriminant function results in a rule with linear discriminant scores d_j for the group separation [116,117]:

$$d_j(x) = \mu_j^T \Sigma^{-1} x - \mu_j^T \Sigma^{-1} \frac{\mu_j}{2} + \log(p_j) \tag{2.22}$$

including the scalar product of the discriminant vector $b_{Bayes} = \mu_j^T \Sigma^{-1}$, the object vector x, a mean adjusting constant for each group $\mu_j^T \Sigma^{-1} \mu_j / 2$ and a $\log(p_j)$ term for adapting p_j. The largest discriminant scores d_j of a group j cause the object x to be matched to this class. Due to the linear structure of the discriminant function, the actual group separation line is also linear. To calculate d_j, the mean μ, the covariance matrix Σ and the prior probabilities p_j have to be estimated for the initial matrix X with n objects x. These parameters can vary for each data set and their determination is again subjected to certain conditions. Not all group separations are realizable by linear discriminant functions (eq. 2.22), but instead demand other discriminant rules. One example is a quadratic discriminant analysis, which does not require equal covariances as the linear function. As a result of finding the optimized discrimination function (e.g. linear, quadratic, Mahalanobis or others) for a training set, the DA is completed with regard to maximum improvement. Its usage, however, has to fulfill two criteria: 1) X includes a lower number of p-variables than objects and 2) the p-variables do not highly correlate with one another. To satisfy these conditions, PCA is mainly deployed prior to DA (PCA-DA) in order to diminish the data dimension by using PC scores instead of X. Thus, PCA-DA is often applied as a combined approach for model formation. Most algorithms additionally perform a PCA-DA validation by testing each object in the training set as if it is not actually included. This results in a prediction outcome, which is typically summarized in a confusion matrix (see Chapter 3, Appendix A2, A3, A4). The confusion matrix is the basis to calculate further parameters that define the quality and classification capability of the PCA-DA model (see Chapter 3 – 5) [116,117].

2.3 Biological Model Systems

Spectroscopic methodologies in combination with MVA can successfully be implemented to establish a fundamental, new insight of unknown compositions, structures and processes of a biological sample or molecule. This is of particular importance for the investigation of cancer, notably with regard to tumor diagnosis and auspicious new tumor drugs or therapies. To adequately study head and neck tumors as well as brain tumors by spectroscopy coupled with MVA, representative tissue specimens and cell cultures are required.

2.3.1 Two-Dimensional (2D) Cell Culture

One of the most abundant *in vitro* models are cultured cell lines. They derive from primary cultures, which are a heterogeneous mixture of cell types freshly extracted from a living organism, organ or tissue specimen and are continued to culture outside the organism. Due to regular passaging of the extracted cells, they adapt to the *in vitro* growth conditions and can be kept alive over months. For long-term preservation, cell lines are frozen in liquid nitrogen and are thus available over decades. Some cell lines exhibit a finite lifespan, as they convert into a senescent state while others are immortalized and can be cultivated for an unlimited period of time without substantial phenotypic or genotypic changes [118]. The mainly large homogeneity of cell lines with their consistent properties make them an appropriate model system to investigate essential biological and biochemical processes. Some cell lines require a substrate for cultivation and are thus denoted as adherent cells, whereas others are grown in suspension and are designated as suspension cells [118]. Most cell lines, however, are adherent and grow as a cell monolayer with a limited manifestation of cell-cell contacts (2D cell culture) (Fig. 2.10a) [119]. Typical cultivation substrates include cultivation flasks, slides or cell culture dishes. The consistent cultivation terms in a controlled substrate, nutritional and tempered environment allows for a high reproducibility and systematical study of the cellular nature [120,118].

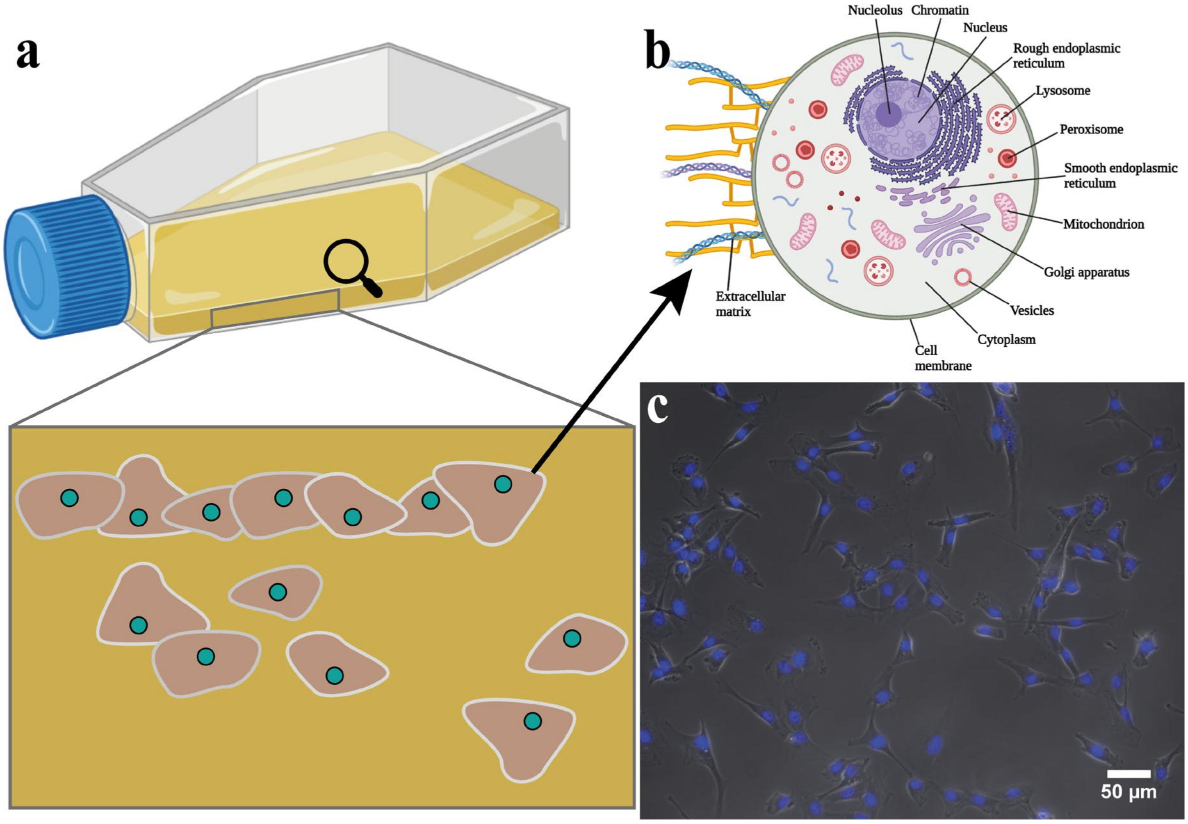

Figure 2.10. *Concept of 2D cell culture. Cells are cultivated in cell culture flasks (a), which contain the supplemented medium for nutritional purposes (yellow) and enable a gas exchange by an integrated filter in the cap (blue) to provide a constant* CO_2 *atmosphere of 5 %. Depending on the cell type, cells are either attached to the flask bottom (adherent cells) or grow in suspension without any attachment (suspension cells). In the case of adherent cell cultivation (a), the inside flask surface is normally plasma-treated to guarantee a consistent cell attachment and growth. Plasma treatment converts hydrophobic groups on the plastic surface in more hydrophilic moieties and thus facilitates cell adherence. The basic structure of a mammalian cell is depicted in (b), whereby major cell features and organelles are revealed. A phase contrast image of U-87 MG glioma cells superimposed with a fluorescence image of stained cell nuclei (blue) using Hoechst 33342 is shown in (c). This glioma cell line was used for all cell culture experiments performed in this thesis. Partly created with BioRender.com.*

A study of cell monolayers or single cells (Fig. 2.10b and c) exposes intra- and intercellular phenomena to understand their overall functionality. Particularly, the cell's structural components play a major role in all cellular processes and are connected with each another via complex signaling mechanisms. This is especially important to comprehend in tumor cells, since they are overall abnormal. The most relevant cell compartments and organelles are shortly mentioned and explained in the following with close attention to alterations in tumor cells (Fig. 2.10b) [121,122]:

Plasma membrane: It consists of a semipermeable lipid bilayer and defines the boundary between the cell interior and the surrounding environment. Due to its hydrophobic nature, only lipophilic molecules can pass the membrane while ions, water or nutrients are transferred via transmembrane pumps, channels or carriers. Transmembrane receptors are partly located on the cell exterior and function as signaling units, as they convert a binding of ligands into a cellular response (e.g. electrical potential or chemical signal). Genetic modifications of these binding sites initiate a constant growth signal in tumor cells without external stimuli and thus trigger an uncontrolled proliferation. Additionally, special adhesion proteins in the membrane allow a linkage to components of the extracellular matrix (ECM), such as fibronectin or laminins, or to adjacent cells [122]. Plasma membranes can be targeted by chemotherapeutics or other anticancer drugs as part of tumor therapy [123].

Nucleus: Nuclei contain the entire genetic information of the organism, stored in the chromosomes, which are highly condensed chromatin fibers composed of deoxyribonucleic acid (DNA) and histones [124]. Encoding of active genes in the DNA takes place via polymerases to create ribonucleic acid (RNA) copies of the genes. The most prominent type of RNA is mRNA, which codes the amino acid sequence translated for protein synthesis. Other RNAs contribute to catalytic, structural or regulatory tasks in the cell. The rate of encoding is controlled by transcription factors. Nuclei are shielded by a double membrane with pores, behaving as the interface between the cytoplasm and the nucleus inside. One subunit of the nucleus is the nucleolus that participates in ribosome formation. In tumor cells, nuclear size, shape and margin alterations are common and accompanied with increased chromatin density and micronuclei [125]. Irregularities of shape and margin are exemplarily deducible from modifications of lamins [100]. Another abnormality is an increased size of the nucleolus [126].

Mitochondrion: A fundamental energy source in all cellular processes is adenosine triphosphate (ATP), generated via oxidative phosphorylation by enzymes in the mitochondria [122]. Their structure is made up of two membranes, an inner and outer one, forming a compartment with a highly patterned folding, the mitochondrial cristae [127]. Within the inner membrane, a matrix is embedded that contains numerous catabolic and anabolic enzymes, ribosomes and the mitochondrial DNA [128]. This DNA encodes a number of mitochondrion-specific inner-membrane proteins [129]. A close interconnection between mitochondria and the ER exists, the so-called mitochondria-associated membranes (MAMs) [130]. Besides ATP production, mitochondria attend various other pathways, such as ROS generation, Ca^{2+} regulation or apoptosis initiation via mitochondrial permeability transition pores (mtPTP) [131]. Cancer-specific changes can appear as mutations in mitochondrial enzymes, as metabolic reprogramming or in mitochondrial mass due to mitophagy- and biogenesis-related regulations [132].

Endoplasmic reticulum (ER): The ER is composed of a highly-defined network of membranes, aligned in tubules, sheets or sacks, and divides into different functional areas, the rough ER, the smooth ER and the nuclear ER (nuclear envelope). While the rough ER exhibits a more granular texture due to bound ribosomes, the smooth ER is arranged in an extensively curved and convoluted manner. Based on the close proximity and interconnection to the nucleus, RNAs, mostly mRNA, and other proteins are exchanged to be further processed in the ER. By far its most dominant function is protein synthesis and folding as a result of decoding the amino acid sequence from mRNA. Additional tasks include protein translocation, integration and posttranslational modification, phospholipid and steroid synthesis and the regulation of Ca^{2+} storage and release [133,134]. In cancers, many ER-incorporated proteins are overexpressed and posttranslational modifications are dysregulated that exemplarily results in an increased release of growth factors, an altered glycosylation of secretory proteins or Ca^{2+} depletion [135,136].

Golgi apparatus: Closely linked and in active interchange with the ER is the Golgi apparatus, which consists of flattened cisternal membranes in a stacked arrangement with incorporated sacks. The Golgi apparatus receives lipids, membrane and secretory proteins for glycosylation or sugar chain modifications via vesicle transportation. During this process, protein cargos traverse the Golgi cisternae from a *cis* to *trans* side and undergo multiple steps of oligosaccharide processing before they are released into the cytoplasm [137,138]. Transformations of the Golgi apparatus morphology and trafficking in tumor cells encompass an increasing exocytotic behavior that changes the secretome composition and thus contributes to metastasis [139].

Lysosomes: Many degradation processes are accomplished in lysosomes that are impermeably membrane-surrounding organelles, storing a large variety of acid hydrolases in the lysosomal lumen. Acid hydrolases are transferred, along with other membrane proteins, to the lysosomes via the trans-Golgi network (TGN) to be used for the breakdown of macromolecules that arrive from phagocytic and endocytic routes [140,141]. Lysosome-associated differences in cancer entail a recycling of the macromolecules as metabolic precursors in building up new cell mass. Further mutations in *M6P / IGF2R* membrane proteins are responsible for an inactivation of the transforming growth factor-β (TGF-β) cytokine family, which suppress cell proliferation [142].

2.3.2 Three-Dimensional (3D) Cell Culture

Although cell monolayers qualify for a great variety of study designs (e.g. cell migration, proliferation, invasion or drug delivery) [143], they lack in adequately displaying cell-cell contacts and cell-matrix interactions [120,144]. Thus, a more reliable *in vitro* model is given by 3D cell cultures, of which tumor cell spheroids are the most frequent one. Tumor spheroids are densely-packed cell aggregates that closely reflect the complex *in vivo* tumor architecture [120]. Their compact structure results from the formation of intercellular junctions and desmosomes [144], which resembles a more tissue-like cross-linkage. Tumor spheroids are basically structured in a three-layered manner: A proliferation zone at the spheroid’s edge, a middle layer of quiescent cells adjoined to a core region at the spheroid center (Fig. 2.11a). Proliferating cells in a peripheral area result from a sufficient nutrient and oxygen supply of the surrounding medium that reaches only the outermost spheroid layers. Adjacent to that is an interlayer of quiescent cells, which are not integrated in the active cell cycle and dwell in a distinct G0-phase. They are capable of re-entering the cell cycle and start to proliferate again under changing environmental circumstances [145,146]. A necrotic core is formed in the spheroid center due to a deprivation of oxygen (hypoxia) and nutrients [144] that additionally entails a shift in energy metabolism. Under hypoxic conditions, pyruvate functions as the main substrate, which is metabolized to lactate (Warburg effect). As a result, lactate is accumulated in the core and induces an acidification, measurable by a decreasing pH value. Besides lactate, other degradation products are also hardly released and tend to enrich inside the spheroid [120]. Tumor spheroids present a number of advantages compared to 2D cell culture models, which are e.g. a tissue-resembling morphology, the adaption of ECM production and microenvironment, mechanical *in vivo* characteristics, cellular heterogeneity or *in vivo* simulating gene expression profiles [147-151].

The preparation of tumor spheroids can be conducted according to different manufacturing protocols, whereby only the forced-floating / liquid-overlay technique is introduced here (Fig. 2.11b) [151]. In this method, a predefined cell suspension of known concentration is seeded into a cultivation vessel (e.g. a U-shaped 96-well plate) with a cell-repellent coating [147,144]. Within a few hours in the incubator, tumor spheroids are generated inside the wells due to a dominant manifestation of cell-cell interactions. The cell-repellent coating prevents adherent cells to attach to the well bottom and forces them to agglomerate in medium suspension. Common well coatings comprise surface treatments with agarose, agar, poly(2-hydroxyethyl methacrylate) (poly-HEMA), poly(ethylene glycol) (PEG) or poly(methyl ethylene phosphate) [143,152,153]. The usage of 96-well platforms ensures a straightforward, reproducible and time-efficient spheroid formation in large quantities. From a practical perspective, gentile shaking and round-bottom vessel shapes further facilitates the formation of circular spheroids with high reproducibility. Additionally, the outermost wells of a 96-well plate should not be used for spheroid cultivation to inhibit an uneven medium vaporization.

Besides their suitability for spheroid production, 96-well platforms are also qualified for a defined drug incubation (Fig. 2.11c). Hypericin as the drug of interest is reproducibly administered to tumor spheroids within the 96-well plates and investigated as an appropriate photosensitizer for PDT of brain tumors.

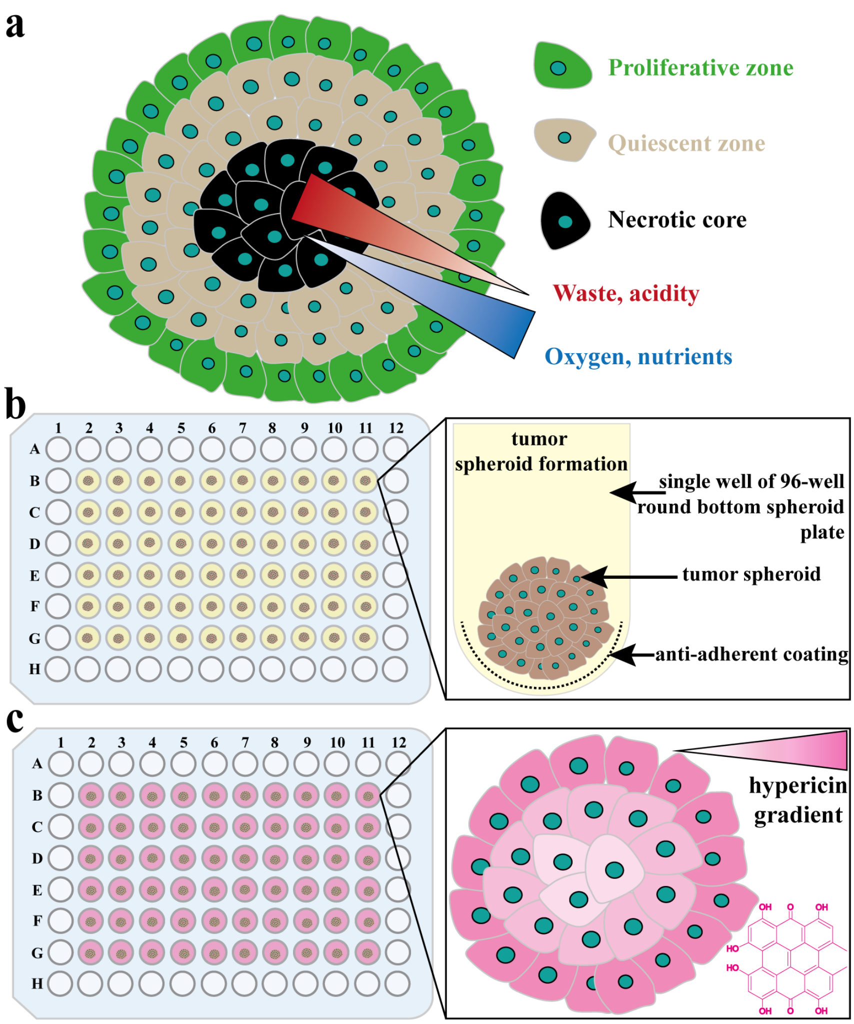

Figure 2.11. Cell spheroid structure, formation and treatment. The overall structure of a cell spheroid is schematically illustrated in (a). It consists of three different cell areas, which are a proliferative region (green), a layer of quiescent cells (light-brown) and a necrotic core (black). This structure is caused by a decreasing nutrient and oxygen gradient towards the center (blue). The lack of supply results from limited diffusion into the spheroid. Additionally, a hampered excretion of degradation products (waste) generates a reversed gradient (red) out of the spheroid. Due to hypoxic conditions at the center, an increased lactate production results and causes a high acidity. A uniform spheroid formation can be achieved with the forced-floating / liquid-overlay method shown in (b). Here, 96-well cell culture plates with a cell-repellent coating (dotted line, right) are used. This coating forces the cells to agglomerate and build spheroids. 96-well plates are simultaneously suited for a direct drug treatment of spheroids with hypericin (c). U-87 MG tumor spheroids are incubated with a predefined hypericin solution in each well. As a result, hypericin gradients appear towards the tumor spheroid center. Part (a) adapted from [154,155].

In this thesis, human glioma cells U-87 MG (ATCC® HTB-14™) are used as highly representative 2D and 3D cell culture model. They are manifested as primary brain tumors in patients and originate from glia cells, the supporting tissue that appears in the central nervous system [156]. Glia cells can be classified into oligodendrocytes and astrocytes with a different phenotype and genotype [157]. Therefore, various tumor types with different gradings according to the World Health Organization (WHO) can emerge, including oligodendrogliomas or astrocytoma. The most aggressive and invasive astrocytoma is the glioblastoma, assessed as WHO grade IV. Typical metabolic characteristics of glioblastoma encompass a high glycolytic flux resulting from mutations in *p53*, a pronounced lipid / protein metabolism due to activated *Akt* / *NF1* and an enhanced invasiveness based on *EGFR* mutations [158,159].

2.3.3 Photodynamic Therapy (PDT) with Hypericin

PDT is a promising tumor treatment based on the interaction of a photosensitizer with light in the presence of oxygen and a biological substrate [47]. A main requirement for PDT is the usage of a suitable photosensitizer, capable of initiating the cell damaging processes as a result of light illumination. Hypericin was found to be a qualified candidate for this purpose. Chemically, hypericin belongs to the sub-group of hydroxyphenanthroperylene quinones (Fig. 2.11c & 2.12, red boxes). It occurs mostly in plants and is significantly distributed in several species of the *Hypericum* genus. Its sophisticated chemical structure is ascribed to the interplay of tautomerism, dissociation, torsional isomerism and homoassociation. One aspect of hypericin's complex architecture is the high number of defined tautomers that result from the successive one-proton transfer between hydroxyl and carbonyl oxygen. This transfer directly correlates with the different dissociation degrees of the OH- and CO-groups. While the COs display a pronounced basicity, especially in the excited state* ($pK_a = -6; -7, pK_a{}^* = -3.2$), the *peri*- and *bay*-positioned phenolic OH-groups differ greatly in their deprotonation tendency (*bay*: $pK_a = 1.8$, *peri*: $pK_a \approx 9; 12$) [160]. Another structural feature is hypericin's concentration- and solvent- dependent bias for homoassociation. In polar organic solvents (e.g. dimethyl sulfoxide), hypericin is monomolecularly dissolved [161], whereas it tends to form dimers or H-aggregates in the presence of aqueous solutions. This also affects its PDT properties. From a physical point of view, absorption and emission characteristics of hypericin are distinctly linked to its dissociation and aggregation behavior, but are unaffected by tautomerism. Protonation / deprotonation of hypericin can induce a bathochromic shift in the absorption spectrum and can influence the spectral pattern and intensity around 450 nm. H-aggregates exemplarily reveal an exciton splitting and overall hypsochromical offset in their absorption spectra, compared to the monomer form. Fluorescence of hypericin is characterized by only small Stokes shifts, but is depending on its ionization or tautomeric state. To a certain degree, its fluorescence can be self-quenched as monomeric species, whereby H-aggregates are nonfluorescent at all. The mean fluorescence lifetime is defined at 5 ns [162].

In large part, the chemical and physical nature of hypericin also have an impact on the cell- and light interactions, required for PDT (Fig. 2.12). Initially in PDT, hypericin accumulates in tumor cells, mainly in the perinuclear region, with a high specificity [47]. Due to the irradiation with light (ideally in a wavelength range of the hypericin absorption maximum), hypericin is excited to higher singlet states (*). From here, it can either be relaxed via fluorescence emission or undergo a transition to the longer-living triplet state via ISC. The extent of triplet formation is increased for hypericin, which directly correlates with its high triplet quantum yield [163]. Dependent on the reactant, this triplet state hypericin (^{3}) simultaneously initiates a type I and type II reaction mechanism. A direct reaction of (^{3}) with the tumor cells is triggered in type I, which results in the emergence of substrate and hypericin radicals (●) due to an electron transfer or hydrogen removal. The formed (●) can further interact with present solvent or triplet oxygen ($^3O_2$) to generate ROS or other superoxide anion radicals. In case of a high $^3O_2$ availability, the energy of (^{3}) is mainly transferred via a type II reaction to the surrounding $^3O_2$ in order to create singlet oxygen species ($^1O_2$) and simultaneously regain ground state hypericin [164]. Whether a type I or II mechanism is triggered strongly depends on the photosensitizer and the presence of $^3O_2$ and biological substrate [71]. Both, ROS and $^1O_2$, exert a high degree of oxidative stress on the tumor cells that eventually induces cell damage and death. The mechanism of cell death is mainly apoptosis, but can also follow necrosis under intense irradiation conditions [71,144]. Only if the stress level is insufficient, the tumor cells might recover and survive. Based on the short lifespan and high reactivity of ROS, (●) and $^1O_2$, the substrate damage solely appears in close proximity to their place of origin [71]. The effectiveness of PDT is also related to the intracellular localization of the photosensitizer and its affinity to bind or pass to the plasma membrane and enrich inside the cells [71].

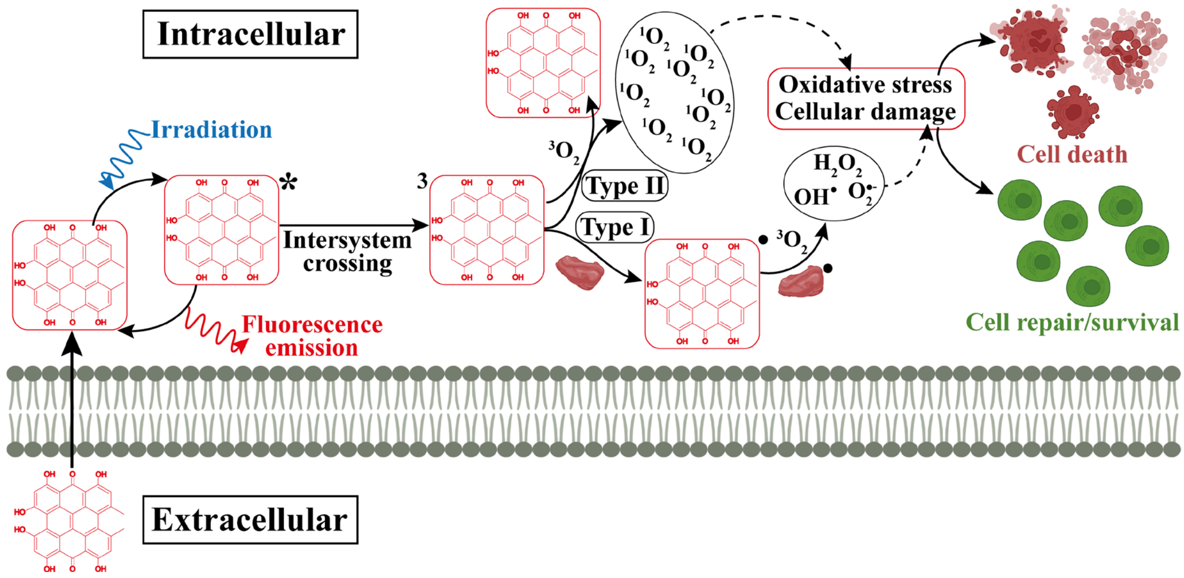

Figure 2.12. *Mechanism of PDT with hypericin. Initially, hypericin permeates from the extracellular environment via the cell membrane into the cell and is selectively accumulated. Upon irradiation (blue), hypericin is excited from the ground to higher energetic singlet states (*). On this level, hypericin can either return to the ground state via fluorescence emission (red) or undergo a spin conversion to the first triplet state. Hypericin in the triplet state (^{3}) can further react with either a biological substrate (tissue) via a type I reaction or with triplet oxygen ($^3O_2$) via a type II reaction. In type I, (^{3}) directly interacts with the biological substrate and causes the formation of radicals (●) in a first and the production of ROS in a second step. In type II, the energy of (^{3}) is transferred to $^3O_2$ and singlet oxygen ($^1O_2$) is generated, whereby deactivated hypericin is regained. ROS and $^1O_2$ trigger oxidative stress and consequently cellular damage. Depending on the stress and damage level, cells can either be repaired and survive or die. Adapted from [165] and partly created with BioRender.com.*

2.3.4 Head and Neck Mouse Models

Even more complex systems than cell monolayers and cell spheroids are animal-based tumor models. These models are typically applied to study or evaluate newly developed therapies, prevention measures or detection approaches. One common model for head and neck squamous cell carcinomas (HNSCC) is using mice with a predefined genetic background and chemically-induced tumors. Different carcinogenic chemicals can be employed for tumor growth *in vivo*, of which 4-nitroquinoline-1-oxide (4NQO) is one of the most frequent one (Fig. 2.13). Its prevalent usage can be derived from the fact that it imitates the impact of tobacco carcinogens, related to excessive smoking as one main risk factor for HNSCC formation [166]. As a result of 4NQO administration via the drinking water, DNA adducts are produced by the *in vivo* formed 4-hydroxyaminoquinoline-1-oxide (4HAQO) in mice. These DNA adducts initiate a substitution of adenosine for guanosine, which results in *HRas* gene mutations that further causes HNSCC generation (Fig. 2.13). The application of 4NQO mainly triggers a highly specific emergence of HNSCCs in the oral cavity, primarily in the mouse tongue. Besides a chemical tumor induction, mice can genetically be modified by gene knockout or transfusion to induce HNSCC development. Transgenic HNSCC mouse models allow a highly controlled gene expression and thus an even greater molecular approximation towards human HNSCC profiles [166-168]. In this thesis, a 4NQO-based mouse model is used to establish chemometric Whiskbroom and Pushbroom DF ELS models, respectively. Both models are compared regarding their capability to correctly identify HNSCCs in mouse tongues (see Chapter 3).

The popular application of 4NQO-based mouse models is ascribed to their close resemblance to human oral squamous cell carcinomas (OSCCs). OSCCS originate from mucosal epithelium and are often moderately or highly differentiated. They mostly exhibit well-defined tumor nests, round nuclei as well as nuclear and cellular pleomorphism. Another feature are keratin pearls, distributed throughout the tumor tissue [169].

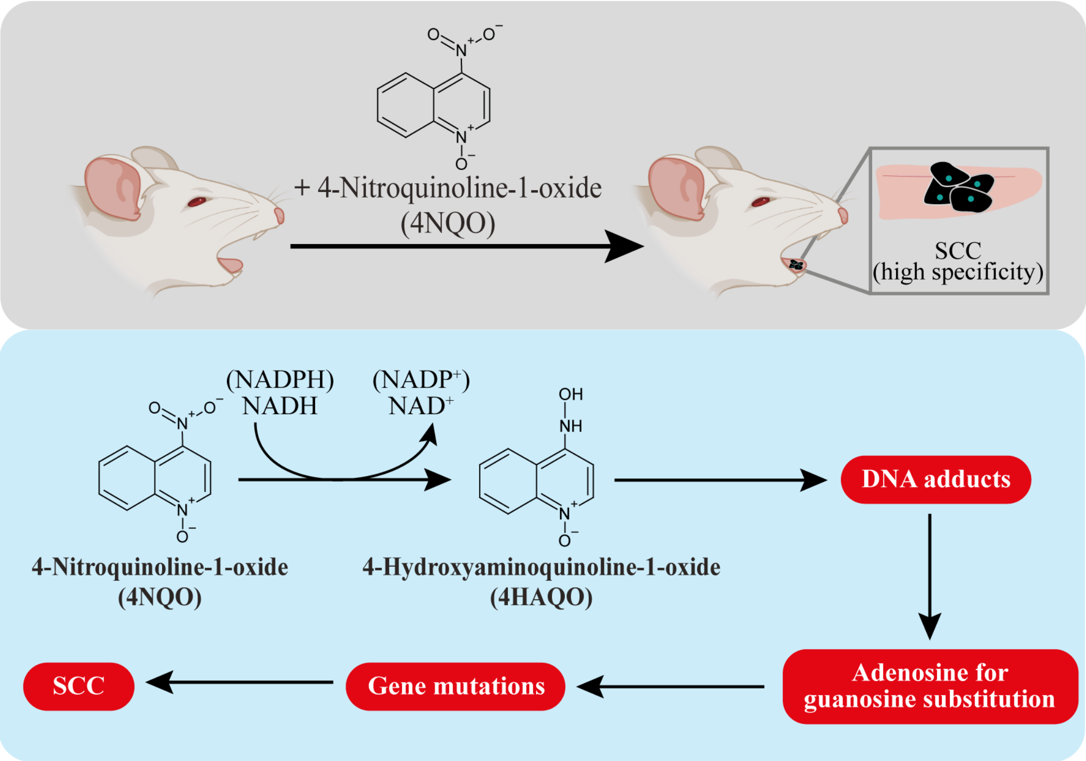

Figure 2.13. *Chemical-induced head and neck squamous cell carcinoma (HNSCC) mouse model. Mice are administered with the carcinogen 4-nitroquinoline-1-oxide (4NQO) that causes a specific development of squamous cell carcinoma (SCC) in the oral cavity, particularly in tongues. The mechanism of the 4NQO carcinogenesis reveals a preliminary conversion of 4NQO to 4-hydroxyaminoquinoline-1-oxide (4HAQO) by oxidation of nicotinamide adenine dinucleotide (NADH) / (nicotinamide adenine dinucleotide phosphate (NADPH)) to* NAD^+ */ (*$NADP^+$*). 4HAQO further initiates the formation of DNA adducts, which mainly effects the substitution of adenosine for guanosine [170]. These point mutations result in gene mutations and finally induces SCC. Adapted from [171,172] and partly created with BioRender.com.*

2.3.5 Salivary Gland Tumors of Parotid Glands

A rare sub-group of human head and neck tumors are salivary gland tumors of the parotid [173]. The great majority of these tumors are of benign nature with the pleomorphic adenoma and Warthin tumor to be two of the main representatives for this group [169]. In the clinical routine, a standardized treatment encompasses an operative resection, accompanied by a histopathological classification with the help of haematoxylin and eosin (HE)-stained tissue cross-sections. Removal of the tumorous parotid tissue might include the gland bed, neighboring contact tissue and excising the lymph nodes [174]. As an alternative to HE-evaluation, spectroscopic technologies can be applied to unstained cross-sections for parotid tumor characterization. For this purpose, resected tumor tissue needs to be prepared, according to the illustrated workflow in Fig. 2.14. In this thesis, confocal Raman spectroscopic imaging coupled with MVA is deployed to distinguish between pleomorphic adenoma, Warthin tumor and unaltered salivary gland (see Chapter 4).

From a histopathological perspective, pleomorphic adenoma can show a changeable cytomorphological characteristic and consist of varying stromal and epithelial parts. One phenomenological event are myoepithelial cells that arise from salivary ducts and transition into chondromyxoid stroma. Cell morphology entails epithelioid / spindled shapes and also keratin pearls can appear. In contrast, Warthin tumors are composed of altered epithelial cells along papillary, cystic and ductal elements. Irregular nest formation of basaloid cells with oval nuclei shapes and scant cytoplasm and a tendency to generate palisades at their border are typical attributes [169].

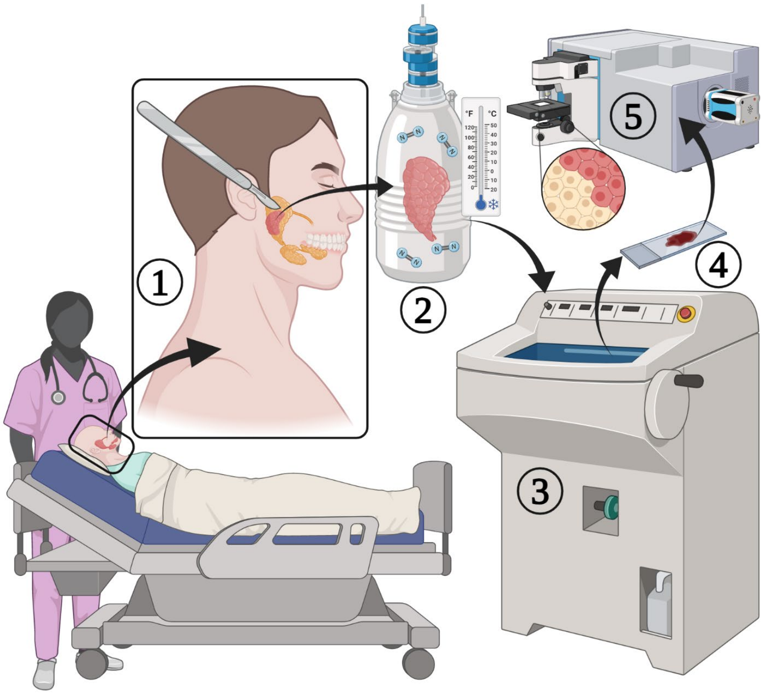

__Figure 2.14.__ Salivary gland tumor resection, preparation and spectroscopic analysis. Each patient initially undergoes a parotidectomy (1) in order to remove the parotid tumor, which is directly preserved in liquid nitrogen (2). Cross-sections of the tumors are prepared with a cryomicrotome (3), preserved by formaldehyde and placed onto objective slides (4). Their spectroscopic characterization finally reveals chemical or morphological information about the tumor (5). HE-stained cross-sections function as reference for spectroscopy. Created with BioRender.com.

2.3.6 Cell and Tissue Conservation Methods

Nearly all analytical evaluations of non-living cells or tissues demand a preceding preservation of the specimens to prevent their decomposition during data acquisition. This can be accomplished by different conservation principles. Chemical fixation is one of them and entails the usage of organic or non-organic solvents to either substitute water (dehydration) or cross-link proteins or DNA for preservation purposes [175]. It can thus be differentiated in coagulant and non-coagulant methods or fixatives. In non-coagulant conservation (Fig. 2.15a), protein, DNA or lipid side chains are interlinked by a methylene bridge after their reaction with a non-coagulant agent, such as formaldehyde or glutaraldehyde [176]. Due to their electrophilic carbonyl groups, both reagents can form highly reactive ion species in aqueous solution that target macromolecular groups with reactive hydrogen atoms. As a result, each non-coagulant molecule interconnects two side chain groups and finally a widespread network between all macromolecules is created. This maintains their structural integrity and localization [177,178]. In a coagulant preservation (Fig. 2.15b), water molecules are successively exchanged by dehydrating fixatives, such as alcohols or acetone. This water replacement destabilizes hydrophilic and hydrophobic protein regions and initiates a conformational inversion that causes at least a partial protein denaturation [175,179]. Although generally stated that fixation keeps biomolecules intact, the fixative effects of different protocols on parotid tumor and salivary gland tissues are investigated with FTIR microspectroscopy (see Chapter 5).

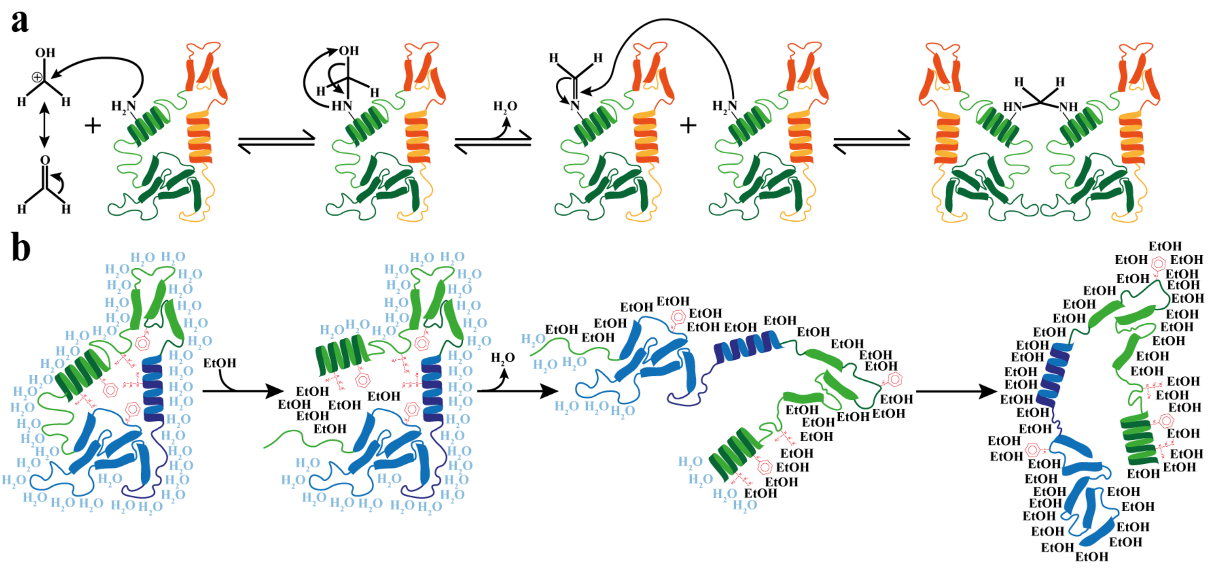

__Figure 2.15.__ Fixation mechanisms for cells and tissues. Two types of chemical fixation can be differentiated: the non-coagulant (a) and coagulant fixation (b), both exemplarily illustrated for a protein preservation. In (a), formaldehyde is used as fixative and can initially form carbonium ions (+) in aqueous solution that are easily attacked by electron-rich groups of protein side chains. Here, a protein amine group binds to the carbonium ion and a reactive hydroxymethyl-protein is created. After water elimination, a highly reactive Schiff base is formed, which reacts with another electron-rich group of a second protein. This results in a methylene bridge between the first and second protein. Due to methylene bridge cross-linkage, cells and tissues are stabilized and preserved. In (b), a protein dehydration stepwise replaces water with ethanol as coagulant fixative. This exchange can additionally initiate an inversion of the protein structure owing to a higher affinity of internal hydrophobic groups (red) towards ethanol. The inversion process implies a disruption of the protein's tertiary structure and thus its denaturation. Adapted by [180,175].

3. Manuscript I: Comparison of Whiskbroom and Pushbroom Darkfield Elastic Light Scattering Spectroscopic Imaging for Head and Neck Cancer Identification in a Mouse Model

*Miriam C. Bassler[1,2], Mona Stefanakis[1,2], Inês Sequeira[3], Edwin Ostertag[1], Alexandra Wagner[1,2], Jörg W. Bartsch[4], Marion Roeßler[5], Robert Mandic[6], Eike F. Reddmann[1], Anita Lorenz[1], Karsten Rebner[1], *Marc Brecht[1,2]*

[1]Process Analysis and Technology (PA&T) Reutlingen University, Alteburgstr. 150, 72762 Reutlingen, Germany

[2]Institute of Physical and Theoretical Chemistry University of Tübingen, Auf der Morgenstelle 18, 72076 Tübingen, Germany

[3]Institute of Dentistry, Barts and the London School of Medicine and Dentistry, Queen Mary University of London, London, UK

[4]Department of Neurosurgery, [5]Department of Pathology, [6]Department of Otorhinolaryngology, Philipps University Marburg, Baldingerstraße, 35033 Marburg, Germany

This chapter is originally published in the journal of Analytical and Bioanalytical Chemistry (https://doi.org/10.1007/s00216-021-03726-5) as

Bassler, M.C., Stefanakis, M., Sequeira, I. et al. Comparison of Whiskbroom and Pushbroom darkfield elastic light scattering spectroscopic imaging for head and neck cancer identification in a mouse model. Anal Bioanal Chem **413**, 7363–7383 (2021). https://doi.org/10.1007/s00216-021-03726-5, © 2022 Springer Nature Switzerland AG.

Reproduced with permission from Springer Nature.

3.1 Abstract

The early detection of head and neck cancer is a prolonged challenging task. It requires a precise and accurate identification of tissue alterations as well as a distinct discrimination of cancerous from healthy tissue areas. A novel approach for this purpose uses microspectroscopic techniques with special focus on hyperspectral imaging (HSI) methods. Our proof-of-principle study presents the implementation and application of darkfield elastic light scattering spectroscopy (DF ELSS) as a non-destructive, high-resolution and fast imaging modality to distinguish lingual healthy from altered tissue regions in a mouse model. The main aspect of our study deals with the comparison of two varying HSI detection principles, which are a point-by-point and line scanning imaging, and whether one might be more appropriate in differentiating several tissue types. Statistical models are formed by deploying a principal component analysis (PCA) with the Bayesian discriminant analysis (DA) on the elastic light scattering (ELS) spectra. Overall accuracy, sensitivity and precision values of 98 % are achieved for both models, whereas the overall specificity results in 99 %. An additional classification of model-unknown ELS spectra is performed. The predictions are verified with histopathological evaluations of identical HE-stained tissue areas to proof the model's capability of tissue distinction. In the context of our proof-of-principle study, we assess the Pushbroom PCA-DA model to be more suitable for tissue type differentiations and thus tissue classification. In addition to the HE-examination in head and neck cancer diagnosis, the usage of HSI-based statistical models might be conceivable in a daily clinical routine.

3.2 Introduction

Microspectroscopic imaging is a powerful tool to investigate biological materials of any kind and helps to reveal their structure, functionality and purpose within the organism. It correlates the spectroscopic data with the microscopic image and thus allows for a spatial assignment of spectral information. Important biological applications for microspectroscopic imaging, such as Raman, fluorescence or infrared (IR) imaging, are the analysis of cell systems and tissues [181,182], particularly in cancer research and diagnosis [183].

Despite intense research and therapy development, cancer still belongs to one of the most threatening diseases human kind is suffering. In 2018, approximately 18.1 million new cancer cases were estimated worldwide with higher incidence in lung cancer, female breast cancer and colorectal cancer [184], closely followed by head and neck squamous cell carcinomas (HNSCC), as the sixth most common cancer type [185]. HNSCC encompass a variety of tumors originating in the lip, oral cavity, hypopharynx, oropharynx, nasopharynx or larynx. Oral squamous cell carcinomas (OSCC), a subset of HNSCC, account for 355,000 new cases annually worldwide [186] with a 5-year survival rate of 50 % [187]. In recent studies, significant inter-tumoral heterogeneity was observed by histopathology, reflecting the tumor site of origin, proliferation, the grade of differentiation, depth of invasion and degree of inflammation [188]. Oral cancer screening is inevitable for early detection and early treatment of tumors, which could considerably improve survival rates.

Early detection of HNSCC requires sensitive identification and localization methods, able to measure small cell and tissue changes. So far, hematoxylin-eosin staining (HE-staining) represents the gold standard in histopathology to recognize head and neck (HN) lesions in several stages during the carcinogenesis. Additional early detection tools for HNSCC comprise spectroscopic technologies like narrowband imaging (NBI) [189], Raman [190] and fluorescence spectroscopy [191]. One spectroscopic technique demonstrated exceptional suitability to early detect preneoplastic variations during colorectal cancer genesis, which is elastic light scattering spectroscopy (ELSS) [192]. Already two weeks prior to the first evidence of malignant tissue alteration, marked changes were detectable by measuring nano- and microscale architectures of the colonic tissue with elastic light scattering (ELS) [192]. On the cellular level, ELSS elucidates morphological features such as size distribution of cells and nuclei or the degree of nuclei pleomorphism and hyperchromasia [193]. For the morphological tissue characterization and differentiation, great achievements with ELSS could not only be generated in colorectal cancer [194], but also in breast cancer [195], skin cancer [196], brain tumors [197] and most importantly in HNSCC [198]. Recently, our group demonstrated to distinguish formalin-fixed brain tumor tissues with a varying degree of malignancy by optical spectroscopy, including ELSS [199].

The implementation of ELSS as an imaging method allows for the combination of spatial (x,y-direction) with spectral information (λ-direction). This results in a 3D data matrix called a hypercube [200,105]. The hypercube can be evaluated in two ways: image planes can either be extracted at certain wavelength bands or the whole spectrum of one x,y-coordinate or pixel is used within the image plane [103]. Various studies of cancer diagnosis with HSI were accomplished [201-203]. HSI has yet been investigated in terms of its overall suitability in cancer detection and diagnosis using different cancer and sample types, spectral ranges, light sources, acquisition modes or evaluation algorithms [105]. Most groups so far concentrated on the successful classification of different tissue or cell types to make it useable in cancer surgery. Our study however, aims to investigate, for the first time, ELSS with two varying HSI detection principles, which are Whiskbroom and Pushbroom imaging, in order to compare their ability to detect ELS of predefined tissue samples. We want to verify whether the time-consuming point-by-point measurement of the Whiskbroom imaging is more suitable for ELS detection than the line-scanning system of a Pushbroom imager since both imaging methods exhibit different lateral and spectral resolution capabilities [105]. With respect to data acquisition, we modified our instrumental setups by installing a darkfield (DF) illumination pathway according to Ostertag et al. [204,101]. Our adaption consequently enables darkfield elastic light scattering (DF ELS) as a non-contact microspectroscopic imaging modality. For a better understanding and comparability of both scanning techniques, advantages and disadvantages are summarized in Tab. 3.1.

Table 3.1. *Advantages and disadvantages of Whiskbroom (column 2) and Pushbroom (column 3) imaging listed by several criteria (column 1). The following overview should emphasize the strength of each individual imaging method and point out customized features of the setups used in this study. Column 4 lists the references to each feature.*

Criteria	Whiskbroom imaging	Pushbroom imaging	References
spectral resolution	high	high	[105,200], customized
spatial resolution	high	high	[205]
scanning speed	time-consuming	fast	[105]
field of measurement	restricted (150 µm x 150 µm) (by piezo table)	large (340 µm x several mm) (x-direction x y-direction)	customized
spectrometer entrance	pinhole-based	slit-based	customized
spatial aliasing	no	yes	[105], customized
acquisition mode	off-line	on-line / in-line	[200]
splitting of light	uniformly high efficiency due to dispersive elements	uniformly high efficiency due to dispersive elements	[205]
costs	high ≥ 100,000 €	Low ≤ 100,000 €	[205], customized
hardware	complex	complex	[205]

As a proof-of-concept study, DF ELS Whiskbroom and Pushbroom imaging are applied on a HNSCC mouse model analyzing longitudinal-cut tissue sections of mouse tongues. The obtained spectral images are analyzed using multivariate data analysis (MVA). By combining a principal component analysis (PCA) and Bayesian discriminant analysis (DA), we generate two statistical models of the tongue tissue data based on both HSI detection techniques and compare if one of the models achieves better results in discriminating different tongue tissue types. Based on this discrimination, we derive whether noticeable differences between Whiskbroom and Pushbroom imaging appear. Finally, the performance of both statistical models is determined and verified regarding their ability to correctly classify model-unknown ELS spectra of varying tissue types. An additional comparison of the statistical-model performance with classical HE-histopathology is accomplished. If proven reliable, the statistical models could help to provide diagnostic information for physicians during surgery.

3.3 Materials and Methods

3.3.1 Mouse Model for OSCC and Carcinogenesis

For this proof-of-concept study, we used an autologous mouse model of OSCC. A total amount of four different mice was investigated. Mice were subdivided into two control mice and two mice developing tumors. Control mice (mice A and B) exhibit an intact tissue structure. Therefore, mice A and B mainly provide healthy epithelium specimens as well as glandular and muscle tissue. Mice with dysplastic alterations (mice C and D) display several stages of tissue modification like hyperplastic, dysplastic areas or invasive squamous cell carcinomas (SCC). Modified tissue, mainly composed of invasive SCC, was derived from mouse C. Altered tissue specimens of mouse D function as prediction areas for the statistical model validation. Mice were maintained on the C57Bl/6N genetic background.

Tumors are induced by chronic oral administration of the water-soluble carcinogen 4-nitroquinoline-1-oxide (4NQO) [188,206,207] that mimics the alterations caused by tobacco mutagens. 4NQO forms DNA adducts, causing substitution of adenosine for guanosine, and induces intracellular oxidative stress resulting in mutations and DNA strand breaks [170]. Additionally, 4NQO is known to induce point mutations in *HRas* with subsequent loss of heterozygosity [208], upregulation of *EGFR* [209], p53 mutations [188] and reduced expression of the cell cycle inhibitor p16 [209]. These effects are similar to the genetic alterations induced by tobacco carcinogens [188,209]. As in human OSCC, invasive tumors are preceded by epithelial hyperplasia and dysplasia [188].

Mice from both genders were maintained on the C57BL/6N genetic background and were housed under a 12-hour light / 12-hour dark cycle, at temperatures of 20 – 24°C with 45 – 65 % humidity. Starting weights of the mice ranged between 25 – 32 g. 4NQO (Sigma, diluted to 100 µg/mL in water) was administered in the drinking water and changed once a week for 16 weeks (Fig. 3.1a). After that period, C57Bl/6N mice were given drinking water without 4NQO. Mice were maintained with regular mouse chow and water (±4NQO) *ad libitum*. Once a week, 4NQO-treated mice were sedated with inhaled isoflurane and the oral cavities were screened for lesions (hyperplasias, dysplasias and SCCs) [188,207]. All animal procedures were subject to institutional ethical review and approved by the UK Home Office (in accordance with UK law, Animals Scientific Procedures Act 1986) at King’s College London prior to commencement (Project license number 70/8474). We adhere to ARRIVE guidelines as set out by the NC3Rs.

Tongue tissues were harvested and embedded in OCT (optimal cutting temperature compound, VWR). Sequential cross-sections were cut using a cryostat (CryoStar NX50, ThermoFisher) at 10 µm thickness and post-fixed in 3.7 % paraformaldehyde / PBS pH 7.4 for 15 min, washed twice in PBS and air-dried before staining. All murine tongues were cut equally in a longitudinal cutting direction. For DF ELS imaging, tissue sections were transferred to gold-coated (BioGold™ 100 nm coat thickness, Thermo Scientific™) microarray slides. Comparable tissue cross-sections were additionally placed on glass objective slides and HE-stained by conventional methods. By HE-staining, lesions were identified and classified macroscopically and microscopically. We found lesions on the dorsal and ventral tongue (Fig. 3.1b; c) and some animals presented more than one lesion. HE-images were acquired using a Hamamatsu slide scanner and analyzed using NanoZoomer software (Hamamatsu).

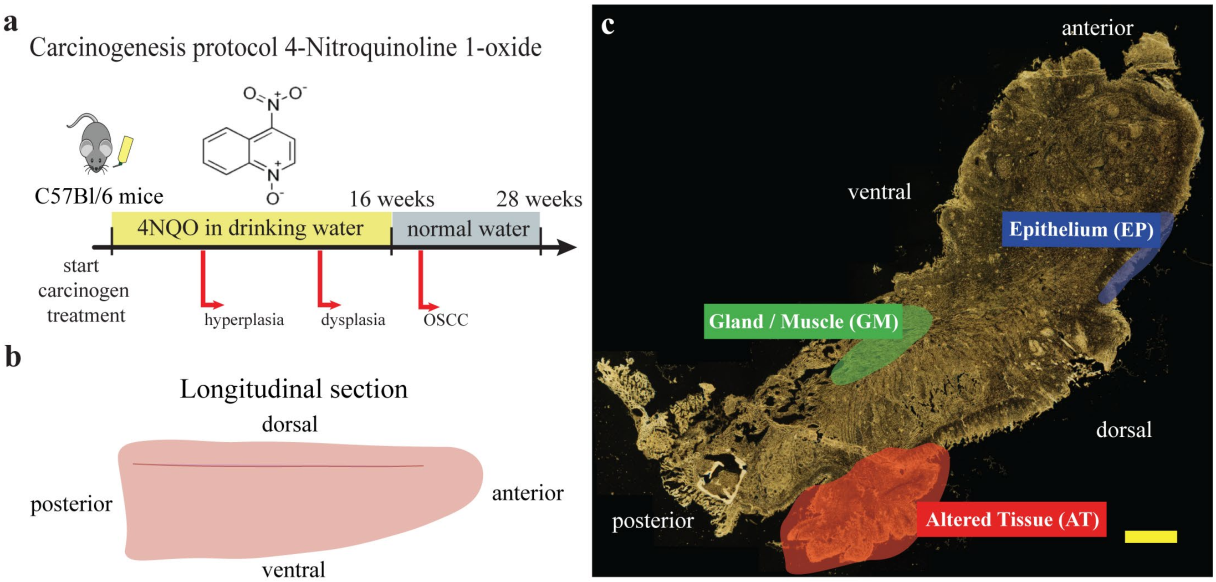

Figure 3.1. *Principle of tumor induction in C57Bl/6N genetic mice. At the beginning of carcinogen treatment, mice were administered the tumorigenic compound 4NQO via the drinking water over a total interval of 16 weeks (a). Throughout this treatment, mice developed various carcinogenic stages including hyperplasia after 6 weeks, dysplasia after 12 weeks and oral squamous cell carcinoma (OSCC) after 18 weeks. The administration of 4NQO was finished in week 16 and mice were supplied with normal drinking water at that point. Although the 4NQO administration stopped, OSCC lesions emerged. The anatomical position and direction of longitudinal tongue cross-sections is elucidated in (b). An exemplary darkfield (DF) image of a mouse tongue is shown in (c). Different tissue regions, such as gland / muscle (green), epithelium (blue) and altered tissue (red) were assigned after a histopathological evaluation of a corresponding HE-stained tissue section (Yellow Scale bar: 1000 µm).*

Tumor grading was assessed according to the presence of the following criteria: tumor cell crowding, degree of keratinization, exophytic or invasive growth, scattered mitotic figures and nuclear atypia [210]. All histological assessments were performed by a pathologist blinded to the study groups and 4NQO treatment conditions.

Owing to the great heterogeneity of tumors and modified tissues [211], we refrain from distinguishing several stages of carcinogenesis, but define all types of tumor alterations, including hyperplasia, dysplasia and invasive SCC, as altered tissue (AT) (Fig. 3.1c). The healthy counterpart consists of epithelium (EP) and a mixture of glandular and muscle tissue (GM) (Fig. 3.1c), summarized as stroma.

3.3.2 Workflow of the HSI PCA-DA Model Development and Validation

To create lingual tissue classification models, consecutive working steps need to be realized, starting from mouse breeding, drug-induced carcinogenesis protocol, tissue harvesting and tongue preparation to the final statistical evaluation of spectroscopic image data. This holistic approach is summarized in Fig. 3.2.

As displayed in Fig. 3.2, C57Bl/6N mice were bred for a total of 28 weeks and treated with 4NQO (1). After treatment, mice tongues were harvested and a sequential cross-section cutting of the tongues in longitudinal direction was performed (2). The tongue and microtome blade (2) are schematically shown in top view. Different profile sections of each mouse were prepared on individual gold-coated microscope slides (3). ELS DF Whiskbroom and Pushbroom imaging was accomplished on histopathologically predefined tissue regions of EP, GM and AT (4). For Whiskbroom imaging, measuring areas were kept at 150 µm x 150 µm, whereas measuring regions for the Pushbroom imaging can differ among images. An exemplary Pushbroom imaging region of 150 µm x 150 µm is depicted in (4). PCA-DA models were developed for both techniques in order to enable a distinct differentiation of all three tissue types (5). The Whiskbroom and Pushbroom PCA-DA models were tested by predicting model-unknown datasets of GM, EP and AT (6). The model predictions are illustrated as colored areas for each tissue type (6).

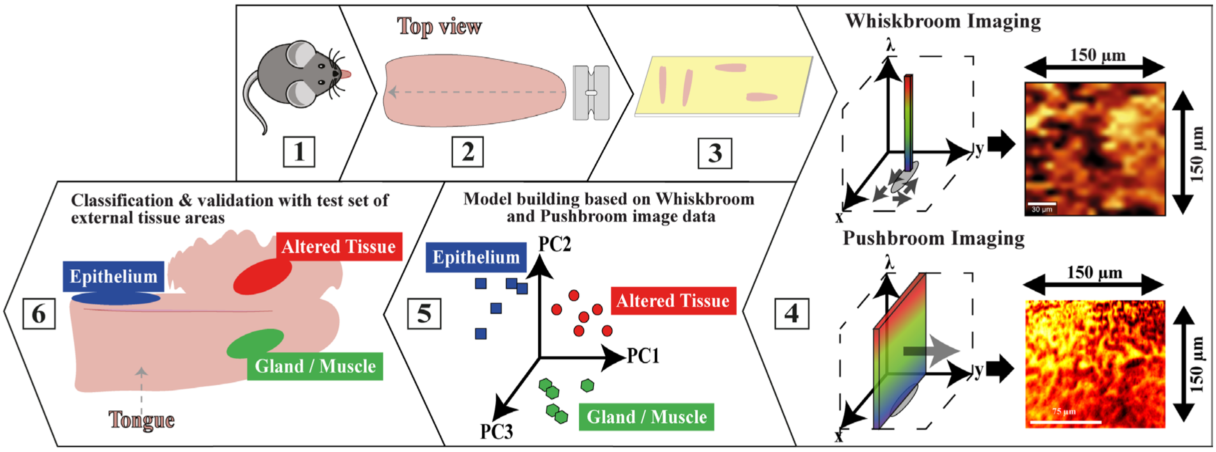

Figure 3.2. Schematic illustration of the HSI PCA-DA model development and validation workflow applied for an OSCC mouse model. In 1: C57Bl/6N mice breeding. In 2: Mice tongues harvesting and sequential cross-section cutting in longitudinal direction. In 3: Tongue cross-sections were transferred to gold-coated microscope slides. In 4: DF ELS Whiskbroom and Pushbroom imaging of predefined tissue regions for EP, GM and AT. In 5: PCA-DA model development for both techniques. In 6: Validation of the Whiskbroom and Pushbroom PCA-DA model with a testing set of different tissue spectra. The model predictions are illustrated as colored ellipses for each tissue type.

3.3.3 ELS Spectra Acquisition in Whiskbroom and Pushbroom Imaging Mode

The principle of Whiskbroom and Pushbroom imaging is illustrated in Fig. 3.3a and 3.3b. In Whiskbroom imaging (Fig. 3.3a), the sample is scanned in a point-by-point manner acquiring a whole spectrum at each x,y-coordinate. In the end, the spectral image is obtained by combining all single point measurements. In Pushbroom imaging (Fig. 3.3b), a complete line is measured at once while a spectrum at each pixel of the line is recorded. Pushbroom imaging therefore allows a much faster sample scanning compared to Whiskbroom imaging. In general, the two techniques are accompanied by varying but high spatial and spectral resolutions. Both imaging modes are applied for detecting ELS from tissue specimens within the scope of our study.

Whiskbroom images were recorded with a WITec Alpha 300 RS confocal system modified as described earlier [204] (Fig. 3.3c). The WITec instrument was equipped with a tungsten lamp (Osram, model HLX 64625), a DF module and a 20x DF objective (Zeiss, EC Epiplan Apochromat 20x/0.6 HD DIC M27). A 100 µm-core diameter multimode fiber connects the optical output to the Acton SP2300i mirror-based spectrometer fitted with an Andor DU401 DD, 35 CCD camera (EMCCD, 16 Bit, 1024 x 127 pixel, 26 µm x 26 µm, operating temperature: -60 °C). The spectrometer was centered at 700 nm using a 150 g/mm (BLZ = 800 nm) grating. A spectral range of 412 – 975 nm was thus measurable. The complete optical setup achieves a spectral resolution of 1.6 nm. Maximum scan areas encompass 150 x 150 µm limited by the range of the piezo table. Each spectrum was obtained with an integration time of 0.04 s. A total number 400 ELS spectra (20 x 20 spectra) was acquired in a scan area of 150 x 150 µm. The applied scan steps equal to 7.5 µm and the scan speed corresponds to 0.874 s/line. Spectralon® was used as reference material measured with the same acquisition parameters. The instrumental dark current was additionally determined as dark current spectrum. Following data acquisition, ELS images were normalized with Spectralon® and dark current spectra were subtracted.

Additionally, an ELS hypercube was generated with a Zeiss MPM 800 microscope photometer implemented with a Pushbroom imaging system. The Pushbroom imager consisted of a spectrograph (Inno-Spec) and a CCD camera (QImaging, EXi Blue fluorescence microscopy camera, model: EXI-BLU-R-F-M-14-C) (Fig. 3.3d). Polychromatic light is generated by a tungsten lamp (Osram, model HLX 64625) and transferred via an optical fiber (core diameter 6.35 mm) onto the tissue sample. Elastically back-scattered light was collected by the above-described 20x DF objective (Zeiss, EC Epiplan Apochromat 20x/0.6 HD DIC M27) and was finally recorded with the pushbroom imager. The entrance slit dimension of the spectrometer corresponds to a width of 30 µm and a length of 14 mm. The spectral range encompasses 398 – 715 nm using a 600 g/mm grating. The area of light-sensitive pixels on the Pushbroom CCD chip contains 1392 x 1040 pixels whereby the first pixel number depicts the spectral axis (398 – 715 nm) and the second one represents the lateral axis. Each measured line-image exhibits a spatial width of 340 µm consisting of 1040 pixels. The lateral resolution is therefore 3 pixels/µm. Scan table increments were optimized to 0.3 µm. The number of line image scans depends on the actual tissue region and can vary between scans. The scan speed is 10 s/line. A spectral resolution of 1.2 nm can be defined for our customized setup. Comparable to the Whiskbroom data treatment, Spectralon® reference spectra as well as dark current spectra were acquired.

Corresponding excitation and detection light paths for the WITec Alpha 300 RS and the Zeiss MPM 800 microscope photometer are visualized in Fig. 3.3c&d. By implementing a DF illumination, the incident light laterally impinges on the specimen. Thus, only the diffuse ELS is detected, whereas specular light is undetectable (Fig. 3.3c&d). Otherwise, the specular reflected light from the tissue superimposes the diffuse ELS carrying the information content and therefore hampers its detection. Due to the DF setup, no additional glare removal is necessary [212] and the diffuse ELS measurement of the sample is facilitated. Furthermore, we prepared our tissue samples on gold-coated objective slides in order to amplify the ELS of the specimen (Fig. 3.3a&b). Based on these adjustments, we intend to improve the overall ELS detection in order to achieve high-quality ELS data.

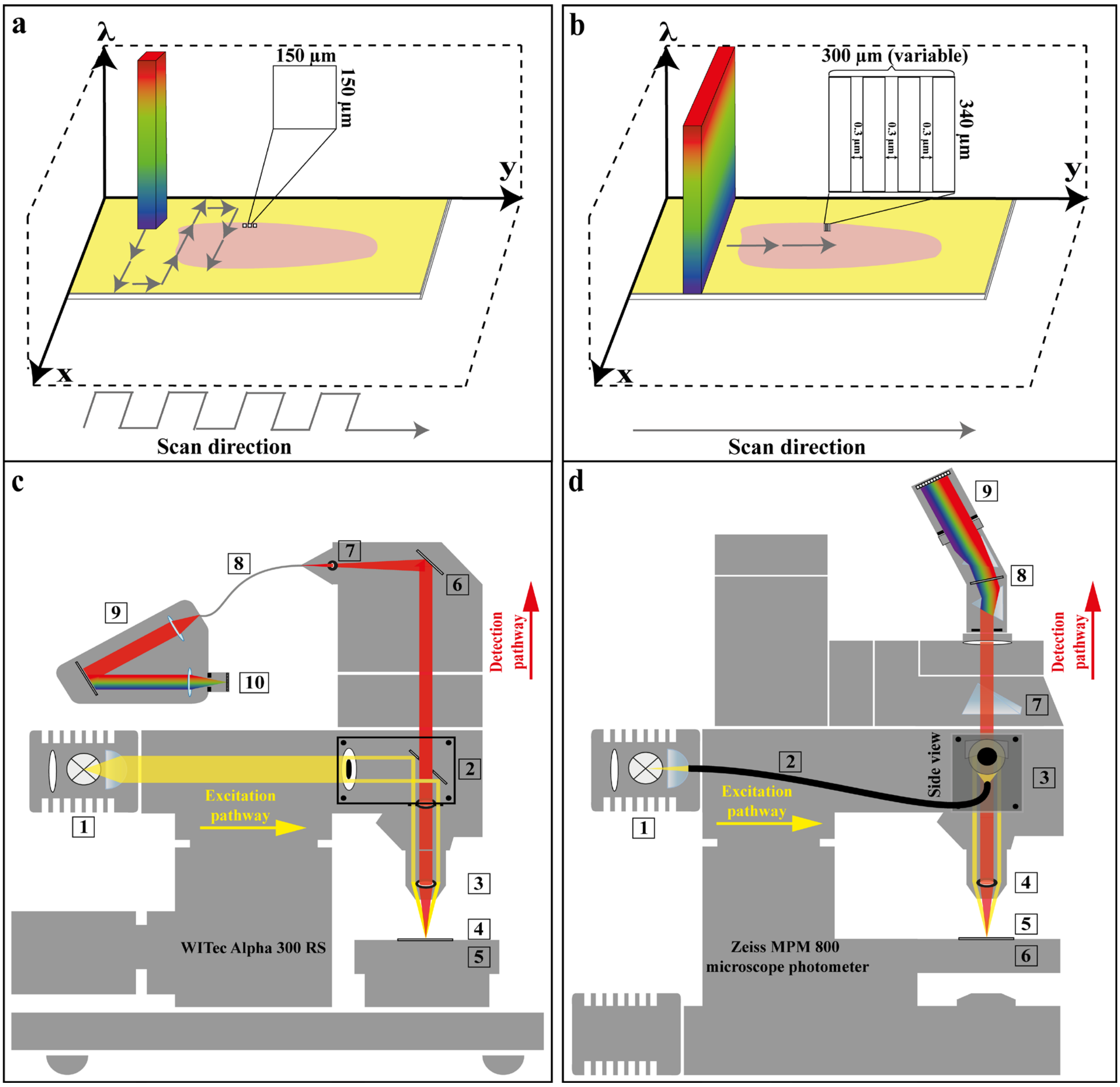

Figure 3.3. *Comparison of Whiskbroom and Pushbroom principles (a,b) accomplished by the two instrumental setups (c,d). In Whiskbroom imaging (a), the sample is scanned point-by-point and a whole spectrum is recorded at each x,y-coordinate. The final spectral image derives from all single point measurements combined. Each scanned point along the tongue was performed in a step-wise manner and is equivalent to a 150 µm x 150 µm scan size, as depicted by the zoom-in of one scan area. The small scan sizes illustrated on the mouse tongue should reveal the size proportion between scan area and tongue. In Pushbroom imaging (b), a complete line of pixels is measured simultaneously and full spectra are acquired in each pixel. The length of each scan in x-direction is fixed to 340 µm, whereas the movement in y-direction is variable. Applied scan ranges in y-direction encompassed 180 – 300 µm. Ideal step sizes were predetermined to be 0.3 µm. One image consists of the scanned x- and y-direction. Whiskbroom imaging was performed by the WITec instrument (c) and Pushbroom imaging was executed by the MPM microscope photometer equipped with a Pushbroom detection system (d). WITec components are described by (c1-c10), c1: tungsten lamp, c2: darkfield module, c3: darkfield objective, c4: sample holder, c5: piezo scan table, c6: deflection mirror, c7: pinhole, c8: multimode optical fiber, c9: spectrometer, c10: CCD camera. MPM components are displayed by (d1-d9), d1: tungsten lamp, d2: optical fiber for white light transmission, d3: darkfield module (side view), d4: darkfield objective, d5: sample holder, d6: scan table, d7: prism, d8: spectrometer with optical elements, d9: Imaging CCD camera.*

3.3.4 Comparability of Whiskbroom and Pushbroom Data by Spatial Averaging

In order to compare Whiskbroom and Pushbroom data in a set scan area, a spatial averaging of spectra must be performed. This is due to the different lateral resolutions of both methods. In our study, a scan area size of 75 x 75 µm yields 100 ELS spectra for Whiskbroom imaging, whereas Pushbroom imaging generates 50,625 ELS spectra in the same area. By averaging 100 spectra for Whiskbroom into one spectrum and 50,625 spectra for Pushbroom imaging into a second spectrum, comparability can be ensured. These averaged spectra for both methods thus represent the identical area size of 75 x 75 µm. Although DF imaging can achieve high lateral resolutions of 0.5 – 1 µm, the obtained information content is too detailed for our purpose. Therefore, we chose the above-mentioned area size of 75 x 75 µm.

For the Whiskbroom PCA-DA model, a total number of 48 EP, 28 GM and 60 AT mean spectra were generated, as described above (100 spectra averaged to one spectrum for a defined area size of 75 x 75 µm). The Pushbroom model was created by 33 EP, 24 GM and 44 AT mean spectra (50,625 spectra averaged to one spectrum for a defined area size of 75 x 75 µm). For prediction purposes, a test set of spectral data was additionally measured and averaged in the previously described manner. The Pushbroom prediction data consisted of 6 EP, 7 GM and 22 AT average spectra. On the contrary, Whiskbroom data yielded 4 EP, 4 GM and 16 AT average spectra.

3.3.5 Data Preprocessing and PCA-DA Model Development

For PCA-DA model formation and testing, the software The Unscrambler® X (Camo Software, Version: 10.5) was used. Spectra of both acquisition methods were preprocessed equally with the software. At first, ELS image spectra were displayed as absorption spectra (-log(R)). A spectral smoothing according to Moving Average with 47 segment points was applied. Next, a baseline offset correction was performed and followed by a gap derivation (1st derivative, gap size: 15 pts.). All spectra were conclusively range-normalized.

A PCA for Whiskbroom and Pushbroom spectra was calculated with mean-centering using the NIPALS-algorithm and the Leverage correction method for validation purposes. A total number of four principal components (PC) was required to represent the spectral data. Model outliers were displayed by the influence plot illustrating the F-residuals vs. the Hotelling's T^2 statistic with a critical limit of 5 %. Spectral outliers were manually verified and removed from the model if proven to be true. Outlier spectra mostly appeared to be noisy background spectra measured in tissue holes. In combination with the PCA, a DA was accomplished with a quadratic distance calculation using four PCs.

Several validation parameters like sensitivity, specificity and precision were calculated for both PCA-DA models in accordance with the confusion matrix terminology. They enabled a characterization of the models and demonstrated their functionality. All three parameters were computed as following

$$Sensitivity = \frac{True\ Positives}{True\ Positives + False\ Negatives} \tag{3.1}$$

$$Specificity = \frac{True\ Negatives}{True\ Negatives + False\ Positives} \tag{3.2}$$

$$Precision = \frac{True\ Positives}{True\ Positives + False\ Positives} \tag{3.3}$$

Each validation parameter was weighted considering the number of ELS tissue spectra, which contribute to the model.

The graphical representation of spectral and statistical data is executed with OriginPro 2018G (OriginLab Corporation).

3.4 Results

3.4.1 Histology of Murine Tongue Tissues

The identification of different tissue types within a tongue tissue section requires a histological assessment, commonly performed using HE-staining. For our study, various tissue regions of longitudinal-cut murine tongue cross-sections were HE-stained and histologically classified by our pathologist Marion Roeßler. Based on the pathologist's evaluation, two distinct healthy tissue areas could be distinguished in all mice, from which epithelium and stroma could be assigned. Epithelial tissue defines the outer most layer of the tongue lining the entire organ from the ventral to the dorsal side (Fig. 3.4a). The epithelial tissue consists of several cell layers, which are a highly proliferative basal region, followed by a dense and metabolically highly active suprabasal layer and finally a keratinized layer on top that forms the filiform papillae of the dorsal tongue (Fig. 3.4a1, dashed area). Due to the layered structure of the epithelium, this tissue is highly heterogeneous from a cross-sectional point of view. The epithelium sits on a stromal region that consists of fibroblasts, immune cells and small capillaries in conjunction with extracellular matrix. Adjacent to the epithelial stroma, a mixed-tissue of gland and muscle, the stroma, affiliates (Fig. 3.4a1). Muscle fibers run along the cross-sectional middle part of the tongue in a highly defined and structured manner (Fig. 3.4b1). In-between those muscle fibers, glandular tissue is embedded, but mainly located beneath the epithelial layer (Fig. 3.4b and 3.4b1). Carcinogen-treated mice additionally display morphological or cell-structural alterations of epithelial tissue with several tumor stages defined as hyperplasia, dysplasia or SCC. An invasive SCC has been characterized in our mouse tongues originating from healthy epithelium after carcinogen treatment (Fig. 3.4b2, b3). Early epithelial changes include thickened epithelium and hyperkeratosis, followed by cellular and nuclear pleomorphism with abnormal cellular size and shape changes, nuclear hyperchromatism, increased and abnormal mitotic figures. Moderate dysplasia present loss of cell polarity, disordered maturation from basal to squamous cells and increased cellular density. Invasive SCCs grow into underlying tissue areas by disrupting the basal membrane and loss of epithelial stratification (Fig. 3.4b2). In some specimens, SCCs also show invasion into gland and muscle layers (Fig. 3.4b). One SCC tissue segment could even be specified as a carcinoma variation with an adenocarcinoma part (Fig. 3.4b3) [169]. Representative areas of healthy and altered tissue regions were chosen for DF ELS imaging according to the pathologist's evaluation.

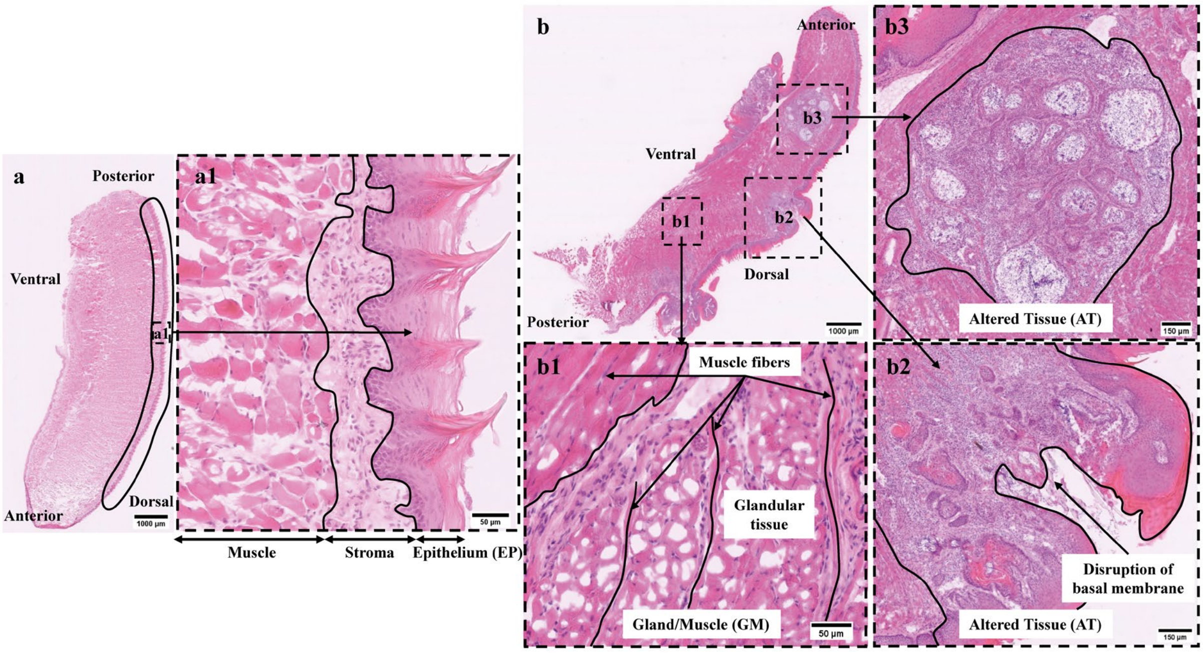

Figure 3.4. *Histological description of representative tissue regions for epithelium (EP), gland / muscle (GM) and altered tissue (AT). A longitudinal tongue section of mouse A with its anatomical orientation is shown in A. Epithelium in dorsal direction is marked by the black frame (a). An enlarged view of the dorsal epithelium (a1, dotted line) points out its multilayered structure. The keratinized top layer merges into a metabolically active epithelium layer allying to the stroma. The metabolic active epithelium is separated from the stroma by the basement membrane. Within the uppermost layer, filiform papillae are imbedded in a tip shape. Typical gland / muscle (b1, dotted line) and OSCC tissue areas (b2, b3, dotted line) are located in an overview tissue section of mouse C (b). Glandular tissue is mainly implemented into muscle tissue indicated by the vertically oriented muscle fibers (b1). OSCCs are visible in b2 and b3. OSCC undergoes epithelial-mesenchymal transition, invading subjacent tissues and interrupts the highly organized epithelium layer (b2). One OSCC branch additionally exhibits adenocarcinoma parts (b3).*

3.4.2 Whiskbroom PCA-DA Model

All tissue type spectra were area-averaged, as described above, to a final number of 48 EP, 28 GM and 60 AT mean spectra used for the PCA-DA model formation (s. Materials & Methods). The used spectra originated from three different mice (mouse A-C). In Fig. 3.5a, three exemplary Whiskbroom ELS spectra of EP, GM and AT without any data preprocessing steps are shown. The ELS spectra are dominated by a wave-like appearance superimposed by even finer scattering patterns [213]. These typical features are not always directly visible in ELS spectra since the diffuse scattering intensity is often weak and the spectral shape is dominated by the gold substrate (Fig. 3.5a). The y-axial intensity displacement amongst EP, GM and AT spectra can mainly be ascribed to influences of different slice thicknesses (Fig. 3.5a). Thus, data preprocessing is mandatory to extract the hidden scattering information from the ELS spectra and to remove unwanted effects. The Whiskbroom PCA-DA calculation was only accomplished with preprocessed ELS spectra (s. Materials & Methods). Exemplary preprocessed spectra are illustrated in Supplementary Material, Fig. S3.1a (A2, Appendix).

The resulting PCA for ELS Whiskbroom spectra is illustrated in Fig. 3.5b&c. The 3D scores plot shows PC1, PC2 and PC4 representing 85 % for PC1, 5 % for PC2 and 1 % for PC4 of the total variance. All three PCs are required to achieve a separation of the investigated tissue types. Although partly overlapping, each tissue type forms one conglomeration. PC1 assigns mostly below-average score values to the spectral GM and EP clusters, whereas the AT group is mainly characterized by above-average score values (Fig. 3.5b). In contrast to PC1, the impact of PC2 is less pronounced since it only affects a complete separation of the GM agglomeration from the AT group. It does not improve the segregation of the EP cluster. The EP group lies diagonally in-between GM and AT within the PC2 vs. PC1 plain of the scores plot (Fig. 3.5b). Overall, PC2 promotes a slanted differentiation of the three tissue type clusters. Corresponding loading plots of PC1 and PC2 reveal greatest effects on the cluster formation in a wavelength region of 400 – 600 nm with two loading maxima at 430 nm and 503 nm for PC1 and one major negative maximum at 540 nm for PC2 (Fig. 3.5c, dashed and dotted line). Above 600 nm, a poorly distinct ripple structure is visible for both loading plots. The loadings curves demonstrate the effect of the spectral ELS signature on the tissue cluster separation. PC4 finally enables a significantly improved separation of all three tissue agglomerations (Fig. 3.5b). The main influence of PC4 is the differentiation of GM and EP spectra from one another and it more precisely defines and shapes the tissue clusters. Examination of the PC4 loadings plot shows a repeatedly occurring pattern partly overlaid by even smaller ripple elements, which refer to Mie scattering (Fig. 3.5c, solid line). The segregation of the tissue clusters is dominated by these effects.

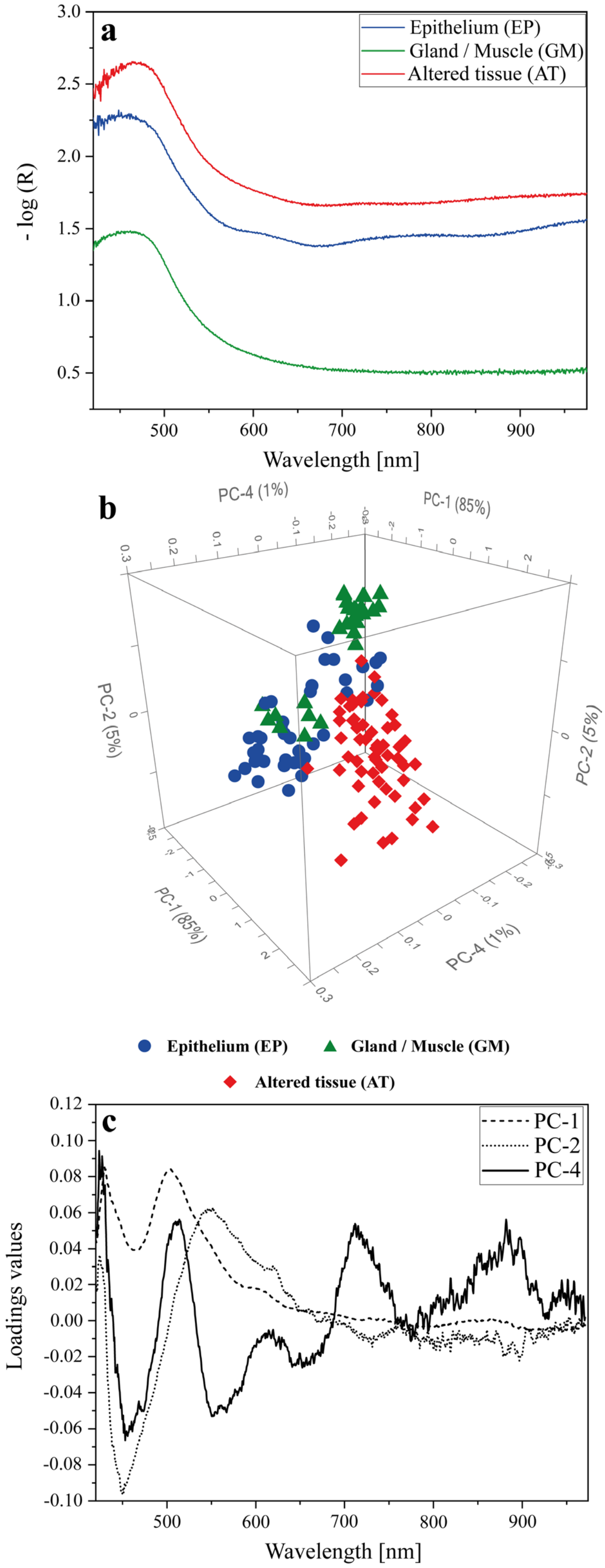

Figure 3.5. *PCA model based on Whiskbroom data for the differentiation of EP (blue), GM (green) and AT (red). In (a): Exemplary ELS spectra of EP (blue), GM (green) and AT (red) tissue are depicted without any data preprocessing steps. They are displayed as absorption spectra (-log(R)). In (b): The 3D scores plot of the PCA reveals the separation of GM, EP and AT groups by PC1, PC2 and PC4 explaining 85 %, 5 % and 1 % of the overall variance. It shows the importance of a third PC to achieve a distinctly improved segregation. Only preprocessed ELS spectra are considered for the PCA calculation. Preprocessing steps encompass: moving average smoothing with 47 segment points, baseline offset correction, gap derivation (1st derivative, gap size: 15 pts.) and range-normalization. In (c): Corresponding loading plots for each PC of the calculated PCA. In Supplementary Material: The 2D scores plot of PC4 against PC3 as well as PC3 against PC2 with the related loadings plots are shown (Fig. S3.2, A2, Appendix).*

Based on the PCA calculation, a DA was subsequently computed and combined to a final PCA-DA model that allows the classification of ELS spectra from unknown lingual tissue areas. The actual model was created by a training set of ELS spectra for EP, GM and AT and optimized with respect to best classification results. By applying the DA, a validation of the used quadratic distance algorithm with 4 PCs was performed and illustrated as a confusion matrix (s. Supplementary Material, Tab. S3.1, A2, Appendix). As part of the confusion matrix results, the training spectra themselves were predicted by the algorithm and afterwards grouped dependent on the prediction outcome. An overview of the training spectra prediction is summarized in Tab. 3.2. Except for the AT group, the DA algorithm correctly predicted all EP and GM training sets (Tab. 3.2). The overall model accuracy corresponds to 98 % for the Whiskbroom data in total.

For a precise characterization of the PCA-DA, further model parameters such as sensitivity, specificity and precision were determined to represent the model's performance. The parameters were calculated from the confusion matrix (s. Supplementary Material, Tab. S3.1, A2, Appendix) and describe the model quality. Dependent on the amount of ELS training data for each tissue type, the training spectra contribute differently to the calculation of the respective model parameters. This contribution was considered in terms of different weightings for the tissue groups. A summary of the weighted sensitivity, specificity and precision is presented in Tab. 3.2. The Whiskbroom model shows holistic sensitivity and precision values of 98 % and even exhibits a specificity of 99 %. These parameters demonstrate that the model was optimized as effectively as possible with the training set. Thus, reasonable classifications of unknown ELS spectra are expected.

Table 3.2. *Model-related quality parameters of the Whiskbroom PCA-DA. In addition to the total number of training spectra (column 2), their prediction results by the DA are listed as absolute numbers and in percentage terms (column 3 and 4). The last columns (column 5-8) represent the overall accuracy, sensitivity, specificity and precision of the PCA-DA model.*

Tissue type	Total spectra in model	Correctly predicted model spectra	Proportion of correctly predicted model spectra [%]	Accuracy [%]	Sensitivity [%]	Specificity [%]	Precision [%]
Gland/Muscle (GM)	28	28	100	98	98	99	98
Epithelium (EP)	41	41	100				
Altered tissue (AT)	58	56	97				

3.4.3 Pushbroom PCA-DA Model

For the Pushbroom PCA-DA model, 33 EP, 24 GM and 44 AT spectra were area-averaged in the above-described manner (s. Materials & Methods). All spectra were obtained from three different mice (mouse A-C). Exemplary Pushbroom spectra of each tissue type without any data preprocessing steps are illustrated in Fig. 3.6a. As mentioned above, ELS spectra show a typical sinusoidal shape overlaid by smaller scattering patterns [213], which is hardly visible in the Pushbroom spectra (Fig. 3.6a). Therefore, a data preprocessing is again necessary to gain the actual scattering information and remove measuring- or sample-ascribable effects, such as the y-axial intensity displacement due to varying slice thicknesses or the impact of the gold substrate on the overall spectral trend (Fig. 3.6a). The Pushbroom PCA-DA calculation was only accomplished with preprocessed ELS spectra (s. Materials & Methods). Exemplary preprocessed spectra are illustrated in the Supplementary Material, Fig. S3.1b (A2, Appendix).

The PCA for the ELS Pushbroom spectra is displayed in Fig. 3.6b&c. Three PCs are required to achieve an almost complete segregation of the EP (blue), GM (green) and AT clusters (red). The 3D scores plot shows PC1, PC2 and PC4 representing 61 % for PC1, 19 % for PC2 and 1 % for PC4 of the total variance. Due to PC1 and PC2, the tissue clusters are arranged around the scores plot center with only minor overlapping of all three groups. PC1 mainly separates the GM and EP tissue clusters from the AT conglomeration. Since GM and EP are mostly defined by below-average score values and AT by above-average ones, all groups are organized in the described manner. PC2, however, primarily enables a segregation of the EP group from the GM and AT clusters with a partial overlay of the conglomerations. The related loadings plots for PC1 (Fig. 3.6c, dashed line) and PC2 (Fig. 3.6c, dotted line) explain the arrangements of the three tissue groups in the scores plot based on dominating spectral effects. Within the loadings plot for PC1 (Fig. 3.6c, dashed line), two spectral maxima at 411 nm and 495 nm are observable. The loadings plot for PC2, however, shows one main negative peak at 420 nm. For both, a periodic spectral course is implied in a higher wavelength range of 550 – 700 nm. PC4 is essential to achieve an almost complete differentiation of the EP, GM and AT aggregation (Fig. 3.6b). The scores plot (Fig. 3.6b) demonstrates that PC4 not only accomplishes a total segregation of the AT cluster from EP and GM, but also further separates the EP group from the GM one. Nevertheless, a slight overlapping between the EP and GM clusters remains. The examination of the PC4 loadings plot (Fig. 3.6c, solid line) reveals negative maxima at 411 nm and 450 nm as well as a distinct spectral ripple pattern dominating above 530 nm, which refer to Mie scattering (Fig. 3.6c, solid line).

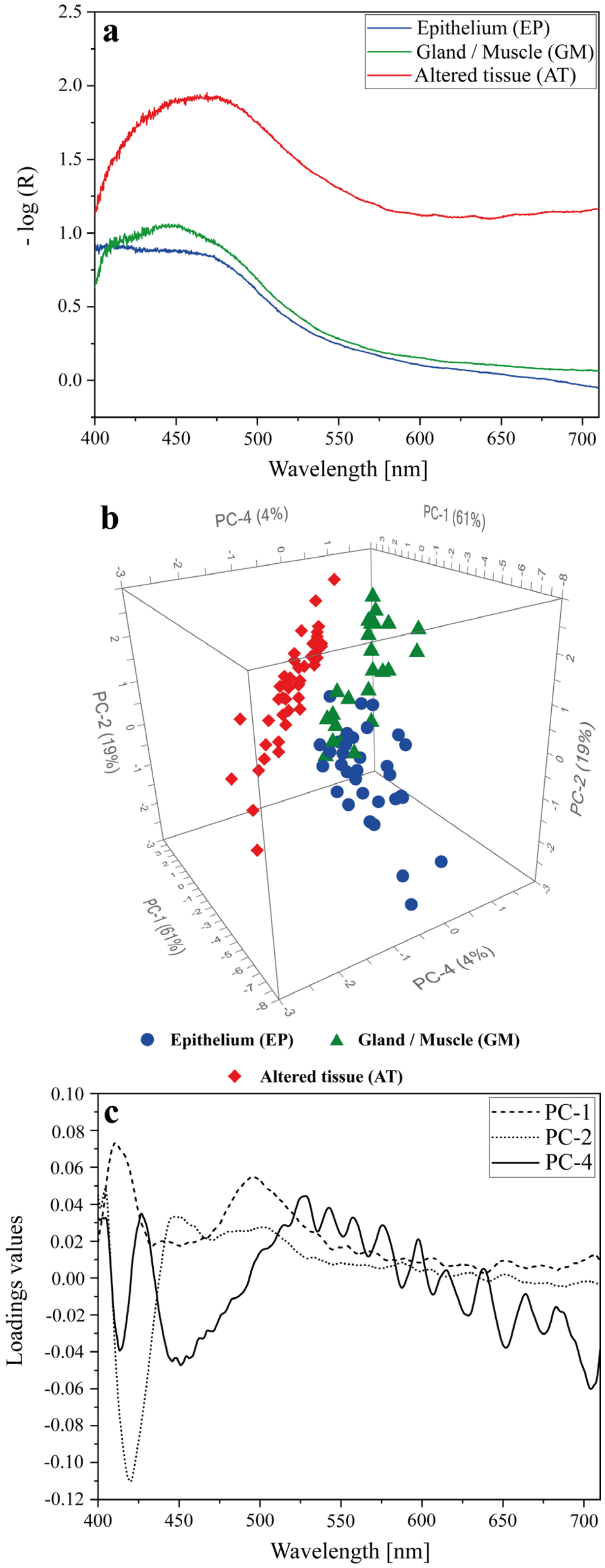

Figure 3.6. *PCA model based on Pushbroom data for the differentiation of EP (blue), GM (green) and AT (red). In (a): Exemplary ELS spectra of EP (blue), GM (green) and AT (red) are depicted without any data preprocessing steps. They are displayed as absorption spectra (-log(R)). In (b): The 3D scores plot of the PCA reveals the separation of GM, EP and AT groups by PC1, PC2 and PC4 explaining 61 %, 19 % and 4 % of the overall variance. It shows the importance of a third PC to achieve a distinctly improved segregation. Only preprocessed ELS spectra are considered for the PCA calculation. Preprocessing steps encompass: moving average smoothing with 47 segment points, baseline offset correction, gap derivation (1st derivative, gap size: 15 pts.) and range-normalization. In (c): Corresponding loading plots for each PC of the calculated PCA. In Supplementary Material: The 2D scores plot of PC4 against PC3 as well as PC3 against PC2 with the related loadings plots are shown (Fig. S3.3, A2, Appendix).*

Subsequently, a DA was calculated, as already described for the Whiskbroom model. By assigning the ELS training spectra with the used DA algorithm, the model performance was verified. The performance results were summarized in a confusion matrix (s. Supplementary Material, Tab. S3.2, A2, Appendix). As the majority of training spectra were correctly matched by the model, an overall accuracy of 98 % was achieved (Tab. 3.3). All investigated AT spectra were entirely dedicated to AT, whereas 32 EP and 23 GM spectra out of 33 EPs and 24 GMs were also attributed to EP and GM, respectively.

Identical model parameters were also calculated to characterize the model more accurately (Tab. 3.3). They indicate the model's applicability for classification purposes. All parameters were again calculated as weighted values that consider the different quantities of EP, GM and AT spectra in the training set (Tab. 3.3). Results for the weighted accuracy, sensitivity, specificity and precision were comparable to the Whiskbroom model.

Table 3.3. *Model-related quality parameter of the Pushbroom PCA-DA. In addition to the total number of ELS training spectra (column 2), the classification results of the training set were listed as absolute numbers and in percentage terms (column 3 and 4). The last columns (column 5-8) represent the overall accuracy, sensitivity, specificity and precision of the PCA-DA.*

Tissue type	**Total spectra in model**	**Correctly predicted model spectra**	**Proportion of correctly predicted model spectra [%]**	**Accuracy [%]**	**Sensitivity [%]**	**Specificity [%]**	**Precision [%]**
Gland/Muscle (GM)	24	23	96	98	98	99	98
Epithelium (EP)	33	32	97				
Altered tissue (AT)	44	44	100				

3.4.4 Classification of Tissue Types by PCA-DA Models

Our classification approach is visualized in Fig. 3.7. At first, a histopathological identification of all three tissue types by HE-stained tissue sections had to be performed in order to localize the tissues on the ELS-ready tissue sections (Fig. 3.7a&b). Based on this tissue assignment, ELS test spectra of the tissue types were acquired and finally classified by the PCA-DA model (Fig. 3.7b, white crosshairs). To validate whether the classification of the model is true, the classification results were compared with the HE-diagnosis of the exact same tissue regions. As indicated by the white crosses or check marks (Fig. 3.7c), the prediction by the model was either conform to the HE-identification (check mark) or differed from it (cross). The corresponding prediction results are summarized in Tab. 3.4.

For both PCA-DA models, the test set of EP, GM and AT spectra were obtained as described earlier (s. Materials & Methods). Since the classification models were created by ELS training spectra of three different mouse samples (mouse A-C), the tissue of a fourth mouse (mouse D) was considered for testing the AT classification. The additional mouse sample should emphasize that the model can correctly assign unknown AT spectra of a completely new tissue sample. Furthermore, unknown EP and GM tissue regions of mouse samples A, B and C were also examined with the PCA-DA models.

A classification of 12 different AT regions of mouse D, four EP regions and two GM areas of mouse C was performed by the Whiskbroom model. A test set of 6 different EP spectra of mouse A, 7 GM spectra of mouse B and 22 AT spectra of mouse D, however, was used to verify the classification abilities of the Pushbroom model. A summary of the model classification results and the alignment with the HE-diagnosis is shown in Tab. 3.4. Since the PCA-DA models were mainly developed for the AT recognition in tongues, mostly AT tissues were included in the testing set. Overall, our classification procedure reveals the true prediction capability of our models.

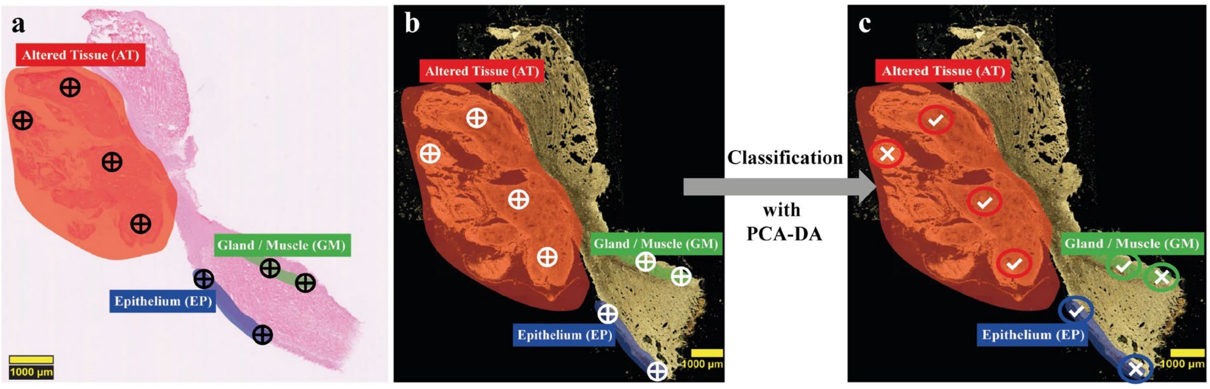

Figure 3.7. *Classification principle of the PCA-DA models. In (a): A HE-based identification of different tissue types from a to-predict tissue section. The crosshairs in (a) indicate the tissue spots, which need to be located in (b) for ELS spectra measurements. In (b): Localization of the same tissue regions and spots on corresponding tissue sections used for ELS data acquisition. According to this localization, ELS test spectra for the different tissue types were measured at each spot (white crosshairs) and were afterwards classified by the PCA-DA model. In (c): As implied by the white crosses or check marks, the prediction of the ELS test spectra by the model either coincides with the HE identification (check mark) or differs from it (cross).*

Table 3.4. *Summary of the PCA-DA model classification results and HE-diagnosed conclusions. ELS test spectra of different tissue regions for AT, EP and GM were classified by the both models and HE-evaluated by a blinded pathologist. Epithelium regions (1-4) of the Whiskbroom model adjoin to one of the AT areas and are thus declared as EP margin. If the model classification and the HE-diagnosis coincide, they are marked in green. Otherwise, they are highlighted in red and bold.*

Whiskbroom classification				**Pushbroom classification**			
Defined tissue type	Prediction region	Model classified as	HE diagnosed as	Defined tissue type	Prediction region	Model classified as	HE diagnosed as
Altered tissue (AT)	1	**EP**	**AT**	Altered tissue (AT)	1	**EP**	**AT**
	2	AT	AT		2	**GM**	**AT**
	3	**EP**	**AT**		3	AT	AT
	4	**EP**	**AT**		4	AT	AT
	5	AT	AT		5	AT	AT
	6	AT	AT		6	AT	AT
	7	AT	AT		7	AT	AT
	8	AT	AT		8	AT	AT
	9	AT	AT		9	AT	AT
	10	AT	AT		10	AT	AT
	11	AT	AT		11	AT	AT
	12	**EP**	**AT**		12	AT	AT

Whiskbroom classification				**Pushbroom classification**			
Defined tissue type	Prediction region	Model classified as	HE diagnosed as	Defined tissue type	Prediction region	Model classified as	HE diagnosed as
Epithelium (margin) (EP)	1	**EP**	**AT**		13	AT	AT
	2	AT	AT		14	AT	AT
	3	AT	AT		15	AT	AT
	4	AT	AT		16	AT	AT
Gland/Muscle (GM)	1	GM	GM		17	AT	AT
	2	GM	GM		18	AT	AT
					19	AT	AT
					20	AT	AT
					21	AT	AT
					22	AT	AT
				Epithelium (EP)	1	EP	EP
					2	**GM**	**EP**
					3	EP	EP
					4	EP	EP
					5	**GM**	**EP**
					6	EP	EP
				Gland/Muscle (GM)	1	GM	GM
					2	GM	GM
					3	GM	GM
					4	GM	GM
					5	GM	GM
					6	GM	GM
					7	GM	GM

3.5 Discussion

In this proof-of-concept study, we compare Whiskbroom and Pushbroom DF ELSS imaging and apply both to a HNSCC mouse trial. ELS image data of murine lingual cross-sections were acquired and subsequently pre-processed to eliminate recording-related influences. Afterwards, the ELS data were subjected to a PCA to allow a data reduction and extraction of the important tissues scattering information. By combining the PCA-structured ELS data with a DA, a Whiskbroom and Pushbroom PCA-DA model was formed. These models were used to classify unknown mouse tissue spectra and to distinguish between different tongue tissue types. A verification of the PCA-DA models was performed with an external set of ELS test spectra. Identical tissue regions were histologically evaluated and compared to the models' classification results for validation purposes. This comparison finally allows determining if one of the PCA-DA models is more suitable to correctly identify the investigated tissue state. To our knowledge, the comparison of two different DF ELSS HSI detection principles in terms of tissue identification was conducted for the first time. So far, HSI only coupled with other spectral techniques was applied for the differentiation of healthy and cancerous tissue, such as Raman [214], fluorescence [215] or FTIR imaging [203].

The application of a PCA is mandatory for the enormous amount of data recorded by Whiskbroom and Pushbroom imaging. The PCA is an objective and unbiased analyzing tool [216], which helps to structure the ELS data matrix. Suitable data preprocessing removes sample- and acquisition-associated effects, such as substrate background or section thickness. Due to the effects of PCA and data preprocessing, main spectral influences for the tissue differentiation can be determined [217]. This is very important because the interpretation of ELS spectra is a demanding task as the spectral bands are not directly linked to a chemical group / vibration. The ELS patterns originate from various tissue constituents with changing refractive index, size and shape and are complicated to assign to one specific tissue component.

3.5.1 Interpretation of Whiskbroom and Pushbroom PCA-DA Models

A combined interpretation of cluster locations within the scores plot and the corresponding loadings plots allows a deduction of spectral influences that cause the tissue group separation. The tissue clusters in the Pushbroom PCA seem to be slightly better separated from one another with an overall less pronounced overlay compared to the Whiskbroom PCA (Fig. 3.5b, Fig. 3.6b). Analyzing the related loadings plots of PC1 and PC2 for both PCAs (Fig. 3.5c; Fig. 3.6c) reveals great effects within a wavelength range of 400 – 600 nm. Since PC1 of both PCAs separates the two healthy tissue groups from the tumor cluster, the impact of this wavelength region could be ascribed to changes in the cell nuclei of the tissues [218]. Nuclei in tumorous tissues are often enlarged and vary in size and shape compared to healthy nuclei [219]. Within the same wavelength range, the PC2 loadings plot shows a negative maximum at 450 nm for the Whiskbroom and at 430 nm for the Pushbroom PCA (Fig. 3.5c, Fig. 3.6c). In this case, this effect is mostly responsible for the cluster order along the PC2 axis. Based on the Whiskbroom cluster order, the below-average PC2 loadings maximum could give a hint to the structural organization of the three tissues. Since AT arises from intact EP, some tissue areas within the cancer region can still be healthy and thus might have the typical epithelium structure. This would explain the higher overlapping degree of the AT and EP group regarding PC2. The GM, however, is built up in a completely different manner in comparison to the EP or AT and consequently forms the most separated cluster. A small overlay of EP and GM groups according to PC2 can be explained by the close proximity of both tissues. For the Pushbroom PC2, however, the tissue group order is different. Although histologically identical tissue regions were chosen, the tissue structure and heterogeneity of the selected areas can differ compared to the Whiskbroom model and thus result in a varying cluster order. Above 600 nm, a sinusoidal curve progression is additionally indicated in both PC1 and PC2 loadings plots (Fig. 3.5c; Fig. 3.6c). These curve shapes are presumed to result from the superposition of many scattering events. Such patterns are amplified by the underlying gold substrate because of the gold's pronounced reflectivity above 600 nm [220]. The application of PC4 causes an even more improved tissue cluster segregation for the Whiskbroom and Pushbroom PCA (Fig. 3.5b, Fig. 3.6b). This improvement can directly be attributed to the periodic structure that dominates throughout the entire spectral range in the PC4 loadings plots (Fig. 3.5c, Fig. 3.6c). Again, the periodic shape is expected to correlate with the scattering events related to cellular changes in the tissues [101,213]. Alterations in cellular or subcellular units affect the sophisticated tissue structure and thus its morphology and texture [221,222]. Differences in pattern frequency are observable in both PC4 loadings plots. The Whiskbroom PC4 loading reveals a long-wave sinusoidal shape superimposed by small ripple patterns, whereas the Pushbroom loadings plot of PC4 is characterized by a ripple pattern of much higher frequency (Fig. 3.5c, Fig. 3.6c). A possible explanation can be deduced from the detection variations of both imaging setups. Since the Whiskbroom setup is a confocal scanning system, the scattering detection just takes place in the confocal volume and is thus very sensitive. Therefore, scattering of small tissue particles in addition to larger ones are accurately detectable influencing the observed pattern for the Whiskbroom PC4 loading. The high-frequency curve shape of the Pushbroom PC4 loading, however, might be correlated to the much larger detection spot of the Pushbroom setup. Therefore, no distinction of different tissue microstructures is possible and thus results in an overall scattering impression of higher frequency. 98 % of all Whiskbroom and Pushbroom model-included spectra were accurately attributed to their corresponding tissue group (Tab. 3.2&3.3). Additional model parameters confirmed the good performance of both models (Tab. 3.2&3.3). Other studies could show comparable sensitivity values of 91 % for detecting gastric tumors [223] and an accuracy of 88 % in a colorectal *ex vivo* study [224]. By using a PCA-DA approach, a good tissue group formation could be achieved. The high degree of similarities between our models demonstrates the great robustness of DF ELSS imaging. Overall variances of both PCA-DA models are illustrated as accumulated PC-variances in Fig. S3.4 (A2, Appendix).

3.5.2 Validation of PCA-DA Models with HE-Staining

A test set of ELS spectra was predicted by both PCA-DA models and identified either as EP, GM or AT. The prediction outcome is compared with the HE-diagnosis of identical tissue regions and verified whether the results match or not. For the Whiskbroom model, twelve tissue areas are expected to be AT. Eight of these regions were assigned to the AT cluster, whereas the remaining four were diagnosed as EP tissue (Tab. 3.4). One explanation for this discrepancy in prediction is the tumor heterogeneity. Tumorous tissue cannot only consist of different tumor subpopulations, but also of histologically healthy areas [225,211,226]. Another plausible explanation could be that HNSCC tumors can exhibit variable levels of cellular differentiation. The same tumor can have regions of lower differentiation, possibly recognized as AT, whereas other, not healthy, regions are better differentiated and therefore classified as EP. A partial identification of the prediction regions as EP is thus possible. The corresponding HE-diagnosis illustrates an overall AT impression and thus mostly coincide with the Whiskbroom results. Comparable outcomes were achieved by the Pushbroom model, which was able to assign 20 prediction regions out of 22 as AT tissue (Tab. 3.4). Only two areas were classified as EP and GM. The HE-investigation confirmed that the tissue is modified. The two wrongly identified Pushbroom regions are once more explainable by healthy regions within an otherwise tumorous tissue [227,211]. Additionally, two sets of EP spectra were tested against the Whiskbroom and Pushbroom models. The Whiskbroom PCA-DA was verified with four potential EP areas adjacent to an HE-identified carcinoma region (Tab. 3.4). These EP areas were chosen to investigate whether the tissue has already morphologically changed or is still intact. As a result, the model classified three of four EP regions as AT and only one was identified as epithelial tissue (Tab. 3.4). By close examination of the associated HE-areas, all regions were categorized as AT. This comparison reveals how sensitive the ELS-based Whiskbroom model is in terms of detecting small morphological changes. Various EP regions were also assigned by the Pushbroom model. Four of six EP areas were attributed to the EP group and two of them were identified as GM (Tab. 3.4). The HE-examination, however, revealed a distinct classification of all six test regions as EP. Both failing model-predictions can be explained by the close vicinity of the GM tissue to the EP. For the GM prediction, two different testing regions were defined for the Whiskbroom and seven GM areas were chosen for the Pushbroom model (Tab. 3.4). Since the GM classification only plays a minor role, fewer ELS spectra were tested. Both GM regions were correctly allocated by the Whiskbroom PCA-DA, which also matches with the HE-evaluation (Tab. 3.4). Comparable results were achieved with the Pushbroom model and were additionally approved by the HE-analysis. Here, seven out of seven test regions were identified as GM (Tab. 3.4). A high conformity with HE-diagnosis was reached and thus the Whiskbroom and Pushbroom model predictions were proven reliable. The comparison of a statistical-based prediction model with the histopathology as gold standard is a common approach and was also accomplished by others [228].

3.5.3 Comparison of Whiskbroom and Pushbroom PCA-DA Models

Both imaging models demonstrated good predictive skills, which are in high accordance with the HE-diagnosis. The model structures of the Whiskbroom and Pushbroom PCA-DA models are almost identical in terms of number and types of PCs. Besides, a great similarity was also depicted for all three loadings plots of both models (Fig. 3.5c, Fig. 3.6c). Although the acquisition principles and resolutions differ between Whiskbroom and Pushbroom imaging, comparable statistical models could be formed with almost identical values for accuracy, sensitivity, specificity and precision (Tab. 3.2, Tab. 3.3). Based on the prediction results, the Pushbroom model seemingly achieved an overall better classification than the Whiskbroom model for all investigated tissue types (Tab. 3.4). In this context, some aspects need to be considered. First, the overall number of ELS test spectra was higher for the Pushbroom prediction in comparison to the Whiskbroom one. Therefore, one or two mis-classifications by the Whiskbroom model have a significant higher impact on the relative prediction outcome than for the Pushbroom model with a greater testing population. This creates the impression of a better Pushbroom prediction prognosis compared to the Whiskbroom one and favors this model in terms of its prediction capability. Considering identical testing populations, the correct classification ability might change between both models. For this reason, a comparison of the model’s prediction is difficult. Fortunately, a great amount of correctly predicted spectra and a small number of false classifications for both models occurred. Nevertheless, the differences of false prediction results between the models is minor and thus a clear capability preference for one or the other model is challenging to define. Second, the test regions of the EP margin turned out to be mostly AT as was confirmed by the Whiskbroom model and a detailed HE-diagnosis (Tab. 3.4). In further experiments, explicit EP regions need to be identified and examined by Whiskbroom imaging in order to validate whether the EP identification is fully possible. Still, the Whiskbroom results are reliable. The Pushbroom model testing, however, is thus more representative. Nevertheless, an enlarged testing of unknown tissue areas would be necessary to verify and confirm that the Pushbroom PCA-DA is the better model for the HNSCC application. An extension of the ELS training set for both models should also be realized to further advance their statistical validity. Additional improvements will encompass an expansion of the mouse model with a much higher amount of different HN tissue samples. Therefore, tissue heterogeneity will become less prominent from a statistical point of view.

For assessing whether the Whiskbroom or Pushbroom method is more suitable for the tissue classification, the different spatial and optical resolutions are considered. The applied spatial resolution for Whiskbroom imaging is equivalent to 7.5 µm. Using this resolution in combination with a confocal setup, no spatial information is mixed and an overview image of the investigated tissue extract is generated. Although higher spatial resolutions would have been possible with the instrumental setup, the detected spatial information content was sufficient to create an accurate Whiskbroom PCA-DA model. Based on this model, a high number of correct tissue assignments was achievable (Tab. 3.4). However, a high spatial resolution would be necessary to detect the small tissue-related differences in a single-point measurement fashion. This is particularly important for the recognition of tissue margins. Future experiments need to reveal whether the chosen spatial resolution is suitable for a potential tissue-border identification or if an adaption in resolution is required. For this study, most tissue classifications were performed with pathologically distinct tissue regions. Within this context, we thus demonstrated that the used Whiskbroom model is applicable to clearly classify these tissue regions and our scanned images generated the spectral information necessary for this purpose. In order to resolve the spectral scattering patterns of each image, the high spectral resolution of 1.6 nm for the Whiskbroom setup is essential. The combination of this spectral resolution and the applied data preprocessing enabled the visualization and extraction of the Mie-patterns with superimposed small ripples, as visualized by the loading plots (Fig. 3.5c). Within the context of data preprocessing, a relatively high degree of spectral smoothing and a spatial averaging were applied. Both measures eliminated noise signals, but simultaneously maintained the superimposed small ripple patterns (Fig. 3.5c). Differences in tissue-section thicknesses were removed by a data normalization and are thus not represented by the scattering patterns (Fig. 3.5c). In addition to the spatial and spectral resolution of the Whiskbroom imaging, the chosen spectral range of 412 – 975 nm might also play an important role for tissue classification. In this spectral region, the 3rd overtone of the NIR region is present and influences not only the model's tissue cluster formation (Fig. 3.5b), but also the classification outcome of the tissue predictions. We ascertain the NIR region to be substantial for the PCA tissue cluster separation and also for the good classification results by the Whiskbroom model. Certainly, this also results from the high photon penetration in this spectral range. Compared to Whiskbroom imaging, the Pushbroom imager reveals a similar spectral resolution of 1.2 nm, but higher spatial resolutions in x- and y-direction. In x-direction, the resolution is diffraction-limited, whereas in y-direction it is equivalent to 1.5 µm. The resolution in x-direction depends on the number of pixels along the axis, the microscope magnification power (20x) and the resolution limit of the optics. In y-direction, the spatial resolution is additionally influenced by the experimentally defined step size of 0.3 µm. The combination of spatial resolution and step size in y-direction results in a scanning overlap of 1.2 µm and thus five scanning steps cover identical spectral information. From a spatial perspective, Pushbroom images thus contain a much higher information content in comparison to Whiskbroom images. Each tissue section within the Pushbroom scan range is measured and small tissue differences can be gathered. Using this data, a robust Pushbroom PCA-DA model was formed and a high level of correct tissue predictions was accomplished (Tab. 3.4). We assume the high spatial resolutions to be much more appropriate for tissue-margin identification than the current Whiskbroom spatial resolution. In prospective experiments, the effect of the Pushbroom's spatial resolutions in terms of border recognition also needs to be studied. So far, the applied classifications only included border-free tissue regions, which were successfully predicted by the Pushbroom model. Therefore, the overrepresentation of identical spectral information due to the scanning overlap does not seem to negatively affect the classification outcome, as most prediction areas were correctly assigned by the model. Nevertheless, the spatial resolution in y-direction as well as the step size need to be adjusted in a way that all the spatial information is covered and no scan time is wasted on identical spots. Additionally, the impact on the scan direction of the tissue (east to west, north to south and vice versa) needs to be investigated. In combination with the overrepresentation of identical spectra, the earlier described data preprocessing (spectral smoothing and spatial averaging) might have caused in this case a loss of spectral information. Due to the additional spatial averaging, smaller Mie-patterns might have been eliminated and the overall shape is much smoother in comparison to the Whiskbroom patterns, illustrated by the loadings (Fig. 3.6c). Still, the obtained spectral Mie-patterns are representative enough to allow a distinct PCA clustering and a high level of correctly-assigned tissue classifications (Fig. 3.6b, Fig. 3.6c, Tab. 3.4). One positive effect of the spectral overrepresentation might be an increasing robustness of the Pushbroom PCA-DA model, which might also be reflected by the classification results. Compared to the Whiskbroom imaging, the spectral range of the Pushbroom imaging encompassed 398 – 715 nm and thus the 3rd overtone of the NIR region is not considered. This is a drawback of our specific Pushbroom imager since the NIR region has an important impact on the tissue cluster formation and classification results, as stated earlier for the Whiskbroom model. We assume that the large statistics of the Pushbroom model compensates for the missing spectral impact of the NIR region and thus generates an even better model performance and classification ability compared to the Whiskbroom model.

Considering all the previously mentioned arguments, we assess the Pushbroom imaging to be more suitable for the detection and classification of our mouse tissue samples in comparison to Whiskbroom imaging. The authors point out that Pushbroom imaging can only be better suitable for a specific application than Whiskbroom imaging if the scanning overlap and spectral overrepresentation is optimized with an appropriate setup. Consequently, Pushbroom imaging as a fast, easy-applicable and low-cost instrument might be applicable as a prospective diagnostic tool in a clinical daily routine.

3.6 Conclusion

In conclusion, we successfully adapted two spectroscopic setups with a DF modulation to improve the detection of ELS and enabled the application of DF ELSS as imaging modality. One of the imaging systems was based on a Whiskbroom point-by-point scanning, whereas the other was equipped with a Pushbroom imager to record ELS spectra in two different manners. Both imaging methods were employed on a HNSCC mouse model in a proof-of-concept study and generated a valuable ELS spectra set of different lingual tissue types. The ELS data were treated with several preprocessing steps to eliminate confounding factors of the sample or during the measurements. By assessing the treated ELS data with a PCA and a subsequent DA, we investigated whether DF ELSS imaging is capable of discriminating different tissue types and if either Whiskbroom or Pushbroom detection might be more suitable for this purpose. Our results show that DF ELSS is a very sensitive imaging technique able to distinguish between EP, GM and AT based on their characteristic ELS pattern. PCAs for Whiskbroom and Pushbroom imaging revealed a distinct separation and thus differentiation of the three tissue type groups, although the Pushbroom PCA achieved a better cluster segregation. ELS is directly linked to the tissue's morphology and thus the PCA separation is based on morphological changes between the tissues. Using both detection principles, accurate PCA-DA models were generated, with which model-unknown ELS spectra were predicted and matched with the corresponding HE-staining. These results demonstrated that Whiskbroom and Pushbroom predictions are largely consistent with the histopathological evaluation. Nevertheless, we define the Pushbroom method to be more suitable for these samples with their specific absorption and scattering properties investigated in this study. Although the main goal of our study was the comparison of two DF ELSS imaging techniques and their suitability in HNSCC differentiation, the possible application of a Pushbroom setup as a non-destructive, cheap and high-throughput technique in a clinical daily routine should be emphasized.

3.7 Acknowledgements

We thank Fiona Watt and her lab (King's College London) as well as the King's College London Biological Services Unit for support with the mouse experiments. Additionally, our thanks go to Garrit Koller (King's College London Dental Institute) for helpful discussions and his support for our collaboration. Furthermore, we thank Barbara Boldrini (Reutlingen University) for her supporting contributions as an expert in hyperspectral imaging as well as Ashutosh Mukherjee (Reutlingen University) for his large expertise in the WITec Alpha 300 RS confocal system and all his helpful discussions concerning the instrumental setups. Last but not least, we thank Tim Rammler (University of Tübingen) for adjusting the Pushbroom microscope system and are also grateful for all the helpful discussions and his expertise in this field.

3.8 Declarations

Conflicts of interest/Competing interests: The authors declare nor conflict of interest.

Funding: Inês Sequeira acknowledges the support of a Barts Charity Lectureship (grant MGU045). Additionally, this study was funded by the doctoral program of the University of Tübingen and Reutlingen University ''Intelligente Prozess- und Materialentwicklung in der Biomateriomics (IPMB)'', which is supported by the MWK Baden-Württemberg (PhD student fellowship to MCB and MS).

Availability of data and material: The data sets generated and/or analyzed during the current study are not publicly available since they are part of ongoing PhD theses. However, the data sets can be accessible on reasonable request from the corresponding author.

Ethics approval: All animal procedures were subject to institutional ethical review and approved by the UK Home Office (in accordance with UK law, Animals Scientific Procedures Act 1986) at King's College London prior to commencement (Project license number 70/8474). We adhere to ARRIVE guidelines as set out by the NC3Rs.

4. Manuscript II: Differentiation of Salivary Gland and Tumor Entities by Raman Imaging combined with Multivariate Data Analysis

Miriam C. Bassler[1,2], Mona Stefanakis[1,2], Elena Gerhard-Hartmann[3], Ashutosh Mukherjee[1,2], Almoatazbellah Youssef[3], Rudolf Hagen [4], Agmal Scherzad[4], Manuel Stöth[4], Edwin Ostertag[1], Maria Steinke[5], Marc Brecht[1,2], Stephan Hackenberg[6], Till Jasper Meyer[4]*

[1]Process Analysis and Technology (PA&T) Reutlingen University, Alteburgstr. 150, 72762 Reutlingen, Germany

[2]Institute of Physical and Theoretical Chemistry University of Tübingen, Auf der Morgenstelle 18, 72076 Tübingen, Germany

[3]University of Würzburg, Institute of Pathology, Josef-Schneider-Str. 2, 97080 Würzburg, Germany

[4]University Hospital Würzburg, Department of Oto-Rhino-Laryngology, Plastic, Aesthetic & Reconstructive Head and Neck Surgery, Josef-Schneider-Str. 11, 97080 Würzburg, Germany

[5]University Hospital Würzburg, Chair of Tissue Engineering and Regenerative Medicine, Röntgenring 11, 97070 Würzburg, Germany

[6]RWTH Aachen University Hospital, Department of Otorhinolaryngology – Head and Neck Surgery, Pauwelsstr. 30, 52074 Aachen, Germany

This chapter is prepared as a finished article for submission.

4.1 Abstract

Parotid tumors are a relevant sub-group of head and neck tumors, which are often hardly distinguishable from one another. One attempt for this differentiation is confocal Raman imaging coupled with multivariate data analysis. By measuring a sample set of Warthin tumor, pleomorphic adenoma and salivary gland tissue, Raman data was obtained and a thorough Raman band analysis was performed. This evaluation revealed highly overlapping Raman patterns with only minor spectral differences. Consequently, a principal component analysis (PCA) was calculated and further combined with a discriminant analysis (DA) to enable the best possible parotid distinction. The PCA-DA model was characterized by accuracy, sensitivity, selectivity and precision values above 90 % and validated by predicting model-unknown Raman spectra, of which 93 % were classified correctly. Thus, we state our PCA-DA to be suitable for parotid tumor and salivary gland discrimination and prediction. This approach could be used as a supporting diagnostic tool for pre- and intraoperative evaluation.

4.2 Introduction

Within the clinical routine, the determination of tumor dignity and entity belongs to the daily business in cancer diagnosis. Besides standardized histopathology, spectroscopic methods in combination with multivariate data analysis (MVA) find an increasing acceptance to support tumor diagnostic methodologies [229-234]. By applying different spectroscopy principles, either chemical or morphological signatures are gained, which reveal tissue-related features and are thus highly tissue-specific. Due to improvements in spatial resolution and scanning speed, spectroscopic imaging became increasingly popular for data acquisition [235,236,105]. As a consequence, large imaging data sets with a high spatial and spectral resolution are obtained [237,200]. The linkage with MVA techniques, such as principal component analysis (PCA), allows to extract the most relevant spectral characteristics from the imaging data and to distinguish the samples based on the previously extracted attributes [238,217]. A combination of PCA with discriminant analysis (DA) additionally describes the distinction in a quantitative manner and enables a prediction of non-included spectra or samples. Typical imaging methods applied for tumor diagnosis are Fourier-transform infrared spectroscopy [239], fluorescence [240], and Raman imaging [241], which are mainly associated with statistical tools, such as PCA, DA, support vector machine, k-nearest neighbor algorithm or artificial neural network analysis [242-244,239]. The spectroscopy-based models are used for the identification or distinction of brain [245], colon [246], breast [24] or head and neck tumors [247].

Parotid tumors are a sub-group of head and neck tumors and account for almost 3 % to 6 % of all head and neck neoplasms [248]. Most of the parotid tumors are of benign nature, representing approx. 80 % of all incidences [249,250]. More than thirty different malignant and benign salivary gland tumors are known according to the 2017 World Health Organization (WHO) classification, of which the two main benign tumors are the cystadenolymphoma (Warthin tumor) and the pleomorphic adenoma [169]. Since the overall incidence of head and neck cancer increases [251,252], a rising demand of distinct diagnostic tools is the consequence. Furthermore, an accurate and reliable pre- and intraoperative dignity determination is necessary to avoid revision surgery [253]. Unfortunately, histopathological and cytological methods used for parotid dignity and entity determination cannot adequately fulfill this purpose, as they are often associated with uncertainties [254]. One of these methods is the fine-needle aspiration cytology, commonly applied in preoperative diagnostics [255,256]. Other techniques in parotid tumor diagnosis encompass core needle biopsy and open biopsy [257]. Due to the restrictions of cyto- or histopathology based pre- and intraoperative parotid diagnostics, spectroscopic approaches are anticipated to overcome this lack.

First spectroscopic attempts of parotid tumor identification were performed using Raman spectroscopy coupled with support vector machine [258]. Further studies focused on identifying differences in lipid composition and changes in secondary protein structure between cancerous and non-cancerous salivary gland tissue using Raman imaging [259]. Our group just recently published a study with Raman spectroscopy and PCA analysis to enable a differentiation between benign pleomorphic adenomas and low-malignant adenoid cystic carcinomas [260]. Although primary efforts in differentiating salivary gland and several parotid tumors were achieved, no study concentrated yet on deploying spectral differences to implement a Raman-MVA model as diagnostic alternative and review its functionality.

Therefore, our study deals with the implementation of a PCA-DA model using Raman imaging data of normal salivary gland, Warthin tumor and pleomorphic adenoma to differentiate between the tissue types and predict unknown parotid samples. Especially, the distinction and correct prediction of Warthin tumor and pleomorphic adenoma is of major importance, as they are the most common benign tumors and need to be accurately identified. Relevant tissue regions of unstained parotid cross-sections are chosen based on a hematoxylin and eosin (HE) assessment and measured by Raman imaging. The obtained imaging data is initially analyzed by a detailed Raman band evaluation. Afterwards, a PCA is computed to achieve the best possible tissue type separation due to tissue-specific information and combined with a DA to enable the classification of model-unknown Raman spectra. By applying the final PCA-DA, new tissue areas of interest are tested and classified in a proof-of-principle concept. The assignments are validated by a corresponding HE-diagnosis to confirm whether the PCA-DA predictions are correct. Final model classification abilities are expressed by the overall accuracy, sensitivity, specificity and precision. As a result of a successful PCA-DA implementation, its utilization in the clinical routine is expected to support and improve the parotid tumor determination.

4.3 Materials and Methods

4.3.1 Patient Selection and Parotid Tissue Sample Preparation

This study was approved by the institutional ethics committee on human research of the Julius-Maximilians-University Würzburg (vote 224/18). All experiments were performed according to the Declaration of Helsinki. All patients agreed to participate in this study by informed consent.

Patients with a salivary gland tumor (parotid tumor) were preoperatively screened and respective tissue specimens were selected. Suitable tissue samples consist of either Warthin tumor (n = 5) or pleomorphic adenoma (n = 4) and normal salivary gland tissue (n = 9) in order to be included into the final sample set. A trained pathologist confirmed the histopathological diagnosis.

Tissue specimens were initially cut into smaller tissue pieces, which were arranged to display tumorous and normal salivary gland tissue. Afterwards, the tissue pieces were frozen in this arrangement and a series of 10 µm-thick consecutive cryosections was prepared. Parotid cryosections were placed onto quartz objective slides (Suprasil® 1, Aachener Quarzglas-Technologie Heinrich GmbH & Co. KG) and subsequently fixed with a 4 % paraformaldehyde solution (ROTI®Histofix 4 %, Carl Roth) for 30 min. Following cross-section fixation, three washing steps with phosphate buffered saline were performed and the samples were dried overnight at ambient temperature. These unstained sections were used for Raman imaging.

A detailed histopathological evaluation was applied based on corresponding 3 µm-thick HE-stained cross-sections. The HE-staining was accomplished according to a standardized protocol. HE-cross-sections were analyzed and photographed using the BZ-9000 BIOREVO System (Keyence, Neu-Isenburg, Germany).

4.3.2 Confocal Raman Imaging

Raman data acquisition was performed with a confocal microscopic setup (Alpha 300 RS, WITec, Ulm, Germany) according to the summarized measurement and data extraction workflow illustrated in Fig. 4.1.

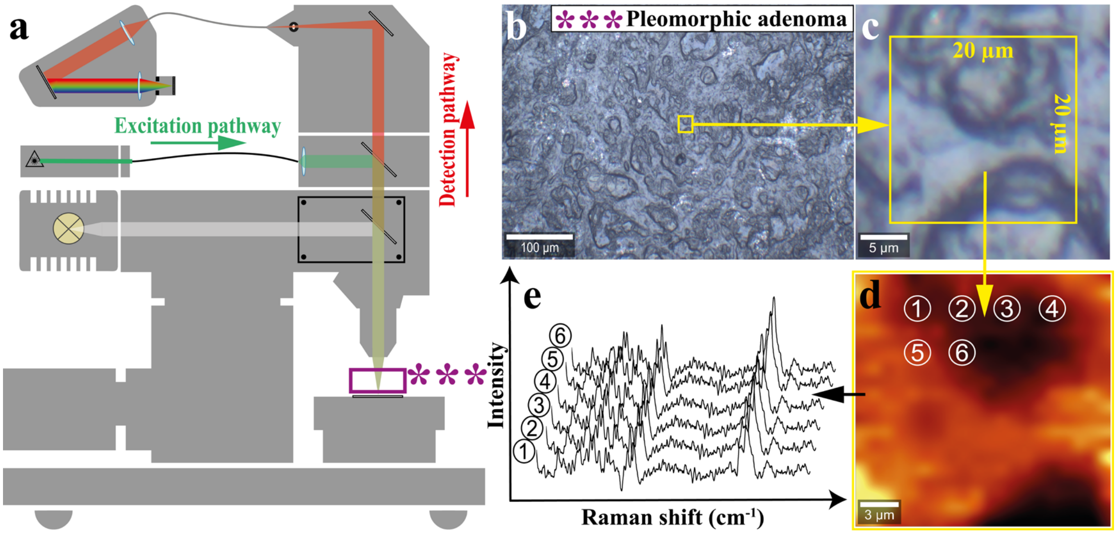

Figure 4.1. *Schematic acquisition workflow for Raman imaging of parotid tissue cross-sections and data extraction. Raman images were recorded with the WITec Alpha 300 RS using a 532 nm frequency-doubled Nd:YAG laser for excitation purposes (a). Initially, a suitable tissue region was chosen in an overview brightfield image, which was in accordance with the corresponding HE-evaluation (b). In this overview image, a 20 µm x 20 µm tissue area of interest ((b), (c), yellow box) was determined and Raman imaged in a stepwise manner. The obtained Raman image (d) is composed of single Raman spectra (1 - 6) located at concrete x,y-positions. Raman spectra were extracted individually for PCA-DA model formation (e).*

The confocal microscope system, equipped with a lens-based spectrometer (UHTS 300, WITec, Ulm, Germany) and a charge-coupled device (CCD) camera (DU970, Andor Technology, Belfast, United Kingdom), was used for Raman imaging [261]. Excitation was performed with a 532 nm frequency-doubled Nd:YAG laser transmitted via a single-mode fiber onto the tissue cross-sections. The inelastically scattered light was collected with a 20x objective (EC Epiplan, 20x / 0.4, Carl Zeiss AG, Oberkochen, Germany) and transferred to the spectrometer and CCD camera (EMCCD, 16 Bit, 1600 x 200 pixel, 16 µm x 16 µm, thermoelectrically cooled: -60° C) via a 100 µm-core diameter multimode fiber. Each Raman image encompassed a size of 20 µm x 20 µm and was acquired with a scan step size of 1 µm and a scan speed of 30 s/line. Thus, 20 x 20 spectra within the image were recorded with an integration time of 1.5 s per spectrum, resulting in a total number of 400 Raman spectra per tissue area. The Raman shift was recorded from 50 cm^{-1} to 3670 cm^{-1} by usage of a 600 g/mm (BLZ = 500 nm) grating and centering the spectrometer at 2000 cm^{-1}. The spectral resolution of the optical system was 2 cm^{-1} [204]. Overall, three tumorous areas (Warthin tumor or pleomorphic adenoma) and three salivary gland areas per tissue sample and patient were selected for Raman imaging. Following image acquisition, Raman spectra were subtracted from the quartz background and treated with a baseline fluorescence correction (shape: 100) and a cosmic ray correction (filter size: 2, dynamic factor: 8).

4.3.3 Data Pretreatment and Multivariate Data Analysis

MVA was performed with The Unscrambler X 10.5 (Camo Analytics AS, Oslo, Norway). All model-included Raman mean spectra were preprocessed equally by applying a Standard normal variate transformation followed by a Savitzky-Golay smoothed 1st order derivative (2nd polynomial order, symmetrical 41 points). The spectral area of 900 – 1750 cm^{-1} was used for MVA calculations, while additional spectrum ranges (50 cm^{-1} to 900 cm^{-1}, 1750 cm^{-1} to 3670 cm^{-1}) without relevant information were excluded due to variable reduction. The PCA was calculated with mean centering, a full cross validation and the singular value decomposition algorithm to distinguish between the different parotid tissue types. Model outliers were identified in the influence plot Hotelling's T^2 versus F-residuals (outlier limits 5 % each) and excluded from the model if proven to be true.

PCA was combined with DA by using the Mahalanobis distance algorithm and PCA score values. The number of deployed principal components (PCs) for the DA was similar to the shown PCA model. In total, 5 PCs were applied for calculating the DA. The overall accuracy, sensitivity, specificity and precision of the PCA-DA model were additionally calculated based on the confusion matrix terminology [199,262].

4.4 Results

4.4.1 Raman Mean Spectra Analysis

To reveal significant spectral differences, Raman mean spectra for normal salivary gland, Warthin tumor and pleomorphic adenoma were compared and calculated by averaging all respective Raman spectra to one overall mean spectrum, illustrated in Fig. 4.2. Potential differences between the spectra can be a varying number of Raman bands, a changing relation between bands, different intensities or variations in shape. From 500 cm^{-1} to 3500 cm^{-1} (Fig. 4.2a), no clear spectral variations are distinguishable. Two major bands at 746 cm^{-1} and 2927 cm^{-1} correspond to a ring breathing of DNA / RNA bases and to CH / CH_3 vibrations of lipids and proteins, respectively, and are identical in each spectrum. A detailed band analysis in the range of 900 – 1700 cm^{-1} was accomplished and only main spectral differences were highlighted (Fig. 4.2b, (1) – (14)). A superimposed illustration of this range is shown in Fig. S4.1, Supplementary Information (A3, Appendix) and a summary of all Raman signal assignments is presented in Tab. 4.1.

At 915 cm^{-1}, one distinct weak Raman band (1) occurs for normal salivary gland, which is less pronounced or even absent for both parotid tumors (Fig. 4.2b), and can be assigned to vibrations of ribose RNA (Tab. 4.1). Instead, pleomorphic adenoma reveals a band at 920 cm^{-1} that can be ascribed to a C-C stretch of collagen proline, which is also visible in the Warthin tumor, but far less distinctive. A further spectral band at 1043 cm^{-1} (2) is clearly illustrated for the salivary gland, but missing for both tumors that can also be assigned to collagen proline (Fig. 4.2b, Tab. 4.1). Varying intensity relations can be observed for two bands at 1158 cm^{-1} and 1168 cm^{-1} (3). In case of salivary gland, the band at 1158 cm^{-1} is more highlighted than the second band at 1168 cm^{-1}, which is opposed for Warthin tumor and pleomorphic adenoma. Both Raman bands can mainly be deduced from C-N and C-C stretching vibrations of proteins and C-C / C=C lipid oscillations (Tab. 4.1). While salivary gland and pleomorphic adenoma exhibit a Raman band at 1197 cm^{-1} (4), the Warthin tumor exposes a slightly shifted band maximum at 1204 cm^{-1} (4, Fig. 4.2b). The bands can either be allocated to antisymmetric phosphate (1197 cm^{-1}) or amide III and CH_2 wagging vibrations (1204 cm^{-1}) of glycine backbone or proline side chains (Tab. 4.1). Changes of band intensity, shape and position between the tissue types are indicated for band 1222 cm^{-1} (5). It is most intense for salivary gland, but varies in intensity and shape for Warthin tumor and is even slightly shifted for pleomorphic adenoma (1228 cm^{-1}) (Fig. 4.2b). The two signals (1222 cm^{-1} and 1228 cm^{-1}) are mainly assignable to amide III vibrations of proteins and thymine / adenine stretch of DNA / RNA (Tab. 4.1). Between 1300 – 1400 cm^{-1}, a series of distinct Raman bands (6 – 9) occurs in all three Raman mean spectra with pronounced shoulders or double maxima mainly for Warthin tumor (6 – 8), but also for salivary gland (9) and pleomorphic adenoma (8), respectively. Reasons for the occurring Raman bands are oscillations of lipids, collagens, proteins, tryptophan and β-carotene within the respective tissues (Tab. 4.1). Additional differences in intensity relations emerge between two Raman band maxima at 1443 cm^{-1} and 1454 cm^{-1} (10), which reveals a slightly more emphasized first maximum at 1443 cm^{-1} in the salivary gland and Warthin tumor spectrum compared to the second band at 1454 cm^{-1}. In contrast, pleomorphic adenoma shows equally dominant Raman bands for both (Fig. 4.2b). The two bands are mainly caused by CH_2 / CH_3 stretching of proteins, lipids, triglycerides and collagen (Tab. 4.1). A Raman band at 1517 cm^{-1} (11) is observed for salivary gland with highest intensity, followed by Warthin tumor and pleomorphic adenoma with a decreasing peak appearance. This band is ascribable to a C-C stretching mode of β-carotene (Tab. 4.1). The Raman band at 1585 cm^{-1} (12) solely exhibits an additional shoulder in the Warthin tumor spectrum, which is missing in the salivary gland and pleomorphic adenoma spectra and corresponds to a C=C olefinic stretch of proteins (Tab. 4.1). Signature differences between the parotid tissues can further be attributed to Raman bands at 1628 cm^{-1} / 1640 cm^{-1} (13) and 1654 cm^{-1} (14), which mainly result from a $C_\alpha=C_\alpha$, C-C and C=O stretching mode of proteins, collagen and lipids (Tab. 4.1). Aside from these few spectral differences (1) – (14), the Raman patterns are highly similar and overlapping with small signatures that can hardly be assigned to distinct vibrational modes. Therefore, a PCA evaluation is inevitable to extract minor pattern variations as a result of a high spectral similarity.

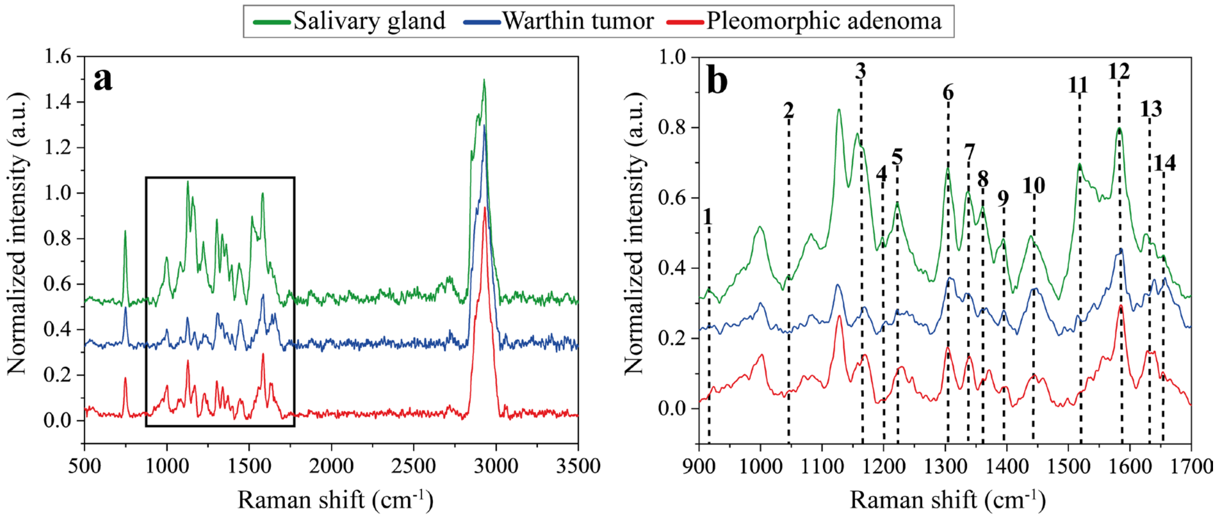

Figure 4.2. *Overall Raman mean spectra of normal salivary gland (green), Warthin tumor (blue) and pleomorphic adenoma (red), illustrated in a Raman shift region of 500 – 3500 cm^{-1} (a). Main spectral differences were noticed between 900 – 1700 cm^{-1}, which was analyzed in more detail (b). In this region, distinct Raman band assignments were performed (1 – 14). Corresponding molecular vibrations and causes are comprehensively listed in Tab. 4.1.*

Table 4.1. *Raman band assignments for salivary gland, Warthin tumor, pleomorphic adenoma. Column 1 indicates the number assigned to the corresponding Raman band in the overall mean spectra (Fig. 4.2b). Column 2 reveals the distinct relative shift (cm^{-1}) of each Raman band identified in the mean spectra. The molecular vibration (column 3) resulting from specific molecules (column 4) within the tissues are listed. In column 5, all references of the Raman band assignments are summarized.*

Number	**Raman shift (cm^{-1})**	**Assignment**	**Cause**	**References [263]**
1	915; 920	-; C-C stretch	ribose RNA; collagen	[264], [265]
2	1043	ring stretching	collagen proline	[265]
3	1158; 1168	C-N stretching; *v*(C=C); *v*(C-C)	proteins / lipids	[266], [267]
4	1197; 1204	antisymmetric phosphate vibrations; amide III, CH$_2$ wagging vibrations	glycine backbone or proline side chains	[267], [268]
5	1222; 1228	C-N stretching and N-H bending, thymine, adenine stretch	amide III, proteins, DNA / RNA	[266], [269]
6	1304	CH$_2$ / CH$_3$ deformation, twisting or bending	lipids, collagen	[265], [270]
7	1337	CH$_2$ / CH$_3$ wagging, twisting and/or bending mode	collagens, lipids, amide III (proteins)	[264], [267], [271]
8	1360	-	tryptophan	[263]
9	1396	-	β-carotene	[263]
10	1443; 1454	CH$_2$ deformation; CH$_2$ stretching / CH$_3$ asymmetric deformation	lipids, proteins, triglycerides (fatty acids); elastin, collagen, phospholipids	[270], [272], [273], [274]
11	1517	C-C stretch mode	β-Carotene accumulation	[272]
12	1585	C=C olefinic stretch	proteins	[273], [275]
13	1628; 1640	C$_\alpha$=C$_\alpha$ stretch; -	proteins; amide I (proteins)	[263], [276]
14	1654	C-C stretch, C=O stretching mode	amide I (proteins), collagen, lipids	[265], [267], [270]

4.4.2 Raman Data Analysis by PCA-DA

Due to only minor Raman band differences in the overall mean spectra, an improved discrimination of all three tissue types is demanded. This was accomplished by a PCA calculation. As the PCA allows to extract the most relevant and differing chemical information of the Raman spectra, a precise distinction of the tissue types is enabled. For this purpose, three tumorous areas (Warthin tumor or pleomorphic adenoma) and three salivary gland areas were selected for Raman image acquisition, which resulted in 6 x 400 Raman spectra (2,400 spectra) for each patient. Consequently, 9 x 6 x 400 Raman spectra (21,600 spectra) were measured overall. Mean spectra were formed by averaging 100 adjacent, processed spectra, which yielded four spectra per tissue area. Therefore, a total number of 216 Raman mean spectra (48 pleomorphic adenoma, 60 Warthin tumor and 108 salivary gland) were used to generate the PCA model. The final PCA is illustrated in Fig. 4.3. Since the most dominant changes were previously identified within 900 – 1750 cm^{-1}, PCA was performed only on basis of this region.

The PCA model encompasses a total number of five PCs to distinguish between the different parotid tissues and reaches a total explained variance of 77 %, considering PC1 – PC5. Within the 3D score plot (Fig. 4.3a), PC1, PC2 and PC5 are presented, explaining 40 %, 18 % and 4 % of the explained variance, respectively. A separation of the Warthin tumor cluster (blue triangles) is already realized by PC1 and PC2. Here, the Warthin cluster is arranged almost completely below-average for PC1 and above-average for PC2. Additionally, PC1 and PC2 cause a group splitting of the salivary gland (green circles) and pleomorphic adenoma (red squares) cluster into mixed tissue type groups, respectively. Here, salivary gland and pleomorphic adenoma are randomly organized above- and below-average of PC1 and PC2 with no apparent cluster formation. This is more clearly shown in the 2D score plot illustration in Fig. S4.2, Supplementary Information (A3, Appendix). Therefore, PC5 is required to clearly demarcate between salivary gland and pleomorphic adenoma. Within the PC2 / PC5-plane, the salivary gland cluster is completely structured below-average, whereas the pleomorphic adenoma group is organized above-average in terms of PC5 (Fig. 4.3a). The Warthin group, however, is arranged above-average for PC2 and almost completely below-average for PC5 within this setting. As a result, a clear group separation between Warthin tumor, pleomorphic adenoma and salivary gland is achieved with only minor cluster overlaps at the center (Fig. 4.3a). Although PC3 and PC4 explain 15 % of the model variance, this represented information does not contribute to the tissue type differentiation. An overview of the complete PCA model including all PCs (PC1 – PC5) as well as related 2D score and loading plots is represented in Fig. S4.2, Supplementary Information (A3, Appendix). Additionally, different orientations of the 3D score plot are shown in Fig. S4.3, Supplementary Information (A3, Appendix), to prove the good cluster segregation.

In Fig. 4.3b, the corresponding loading plots of PC1, PC2 and PC5 are illustrated. The loading plots display the highest spectral influence on the tissue type separation in the 3D score plot. Some of the main influencing loadings maxima can even be referred to Raman bands assigned in Fig. 4.2. Small variations between loadings maxima and Raman bands result from derivation formation in PCA that affect a minor maximum shift. Negative maxima at 1164 cm^{-1} and 1530 cm^{-1} in the PC1 loadings cause a major impact on the tissue separation (Fig. 4.3b). Further influencing maxima can be defined at 1596 cm^{-1} and 1643 cm^{-1} according to the PC1 loadings. The PC2 loading plot shows the most dominating impact between 1440 – 1680 cm^{-1} with main positive maxima at 1440 cm^{-1} and 1643 cm^{-1} and negative maxima at 1467 cm^{-1} and 1680 cm^{-1} (Fig. 4.3b). Within the PC5 loadings, a few pronounced positive maxima can be determined at 1450 cm^{-1} and 1546 cm^{-1} as well as negative ones at 1285 cm^{-1} and 1384 cm^{-1}.

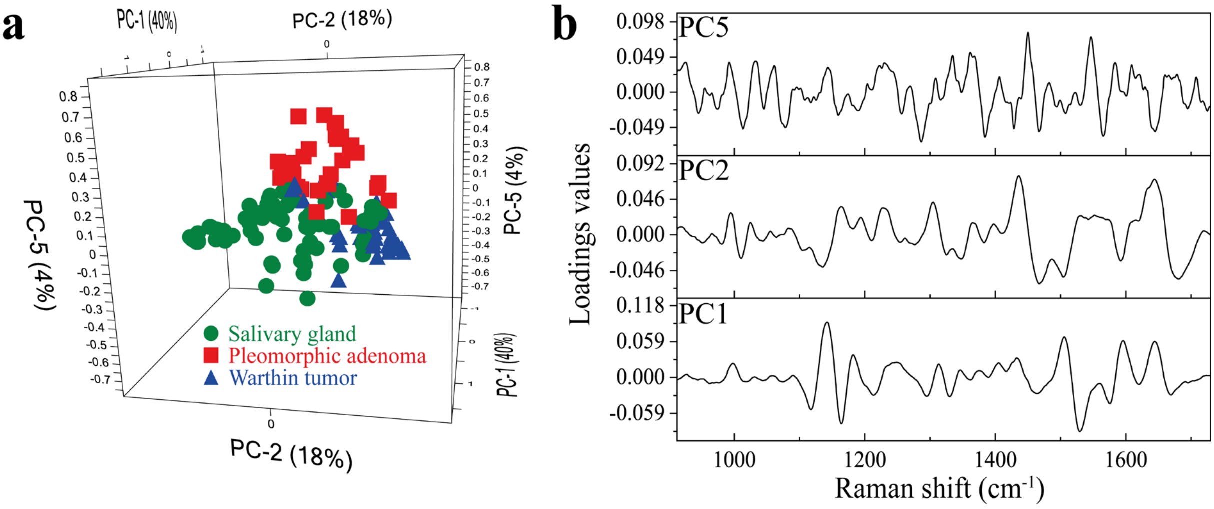

Figure 4.3. PCA model for the differentiation of salivary gland, Warthin tumor and pleomorphic adenoma. The 3D score plot is illustrated in (a), displaying PC1 (40 %), PC2 (18 %) and PC5 (4 %). A successful separation of salivary gland (green circles), Warthin tumor (blue triangles) and pleomorphic adenoma (red squares) clusters is achieved with only minor group overlaps in the center. The corresponding loading plots are shown in (b), revealing the main influencing Raman shift of PC1, PC2 and PC5 for the group segregation. Additional 2D score and respective loading plots of all model-included PCs are summarized in Fig. S4.2, Supplementary Information (A3, Appendix).

Based on the formed PCA model, a DA was subsequently calculated by using the PCA score values of PC1 to PC5 and the Mahalanobis distance algorithm. The PCA-DA performance is evaluated by an internal validation process. For this purpose, each model-included spectrum was allocated to one tissue cluster as if it was not contained in the model. As a result, a confusion matrix is obtained (Tab. S4.1, Supplementary Information, A3, Appendix), which describes the accordance of the model's assignments and the pathologist's diagnosis and is used to compute the model's accuracy, sensitivity, specificity and precision (Tab. 4.2). Salivary gland model spectra were most accurately assigned with 97 %, whereas Warthin tumor spectra resulted in 91 % of correctly matching spectra. Pleomorphic adenoma is still allocated correctly by 89 %. Due to the excellent group assignment of the model spectra, high performance parameters of 94 % accuracy, 94 % sensitivity, 95 % specificity and 94 % precision were accomplished (Tab. 4.2).

Table 4.2. Model performance parameters for the tissue entity distinction. All model-included Raman mean spectra (column 2) were ascribed to one tissue group in order to validate the PCA-DA. The total and relative (%) number of correctly assigned model spectra are listed in column 3 and 4. Overall accuracy, sensitivity, specificity and precision of the model are summarized in columns 5 – 8.

Entity	Total spectra	Correctly assigned	Correctly assigned / %	Accuracy / %	Sensitivity / %	Specificity / %	Precision / %
Salivary gland tissue	94	91	97	94	94	95	94
Pleomorphic adenoma	35	31	89				
Warthin tumor	47	43	91				

The PCA-DA was finally used to predict model-unknown Raman mean spectra of all investigated parotid tissues in order to verify the model classification abilities. For this purpose, histopathologically distinct regions of normal salivary gland (Fig. 4.4, 1-5, light blue squares) and tumor entities (Fig. 4.4, 1-5, black squares) were previously defined as suitable prediction regions on HE-sections (Fig. 4.4, a). These HE-regions were afterwards identified on the consecutive, unstained cross-section used for Raman imaging (Fig. 4.4, b; 1-5, light blue and black squares). After Raman image acquisition, mean spectra of the tissues were again calculated by processing and averaging 100 adjacent Raman spectra (Fig. 4.4, c and d). This second group of 15 Raman mean spectra (5 per entity; 1,500 spectra) was predicted by the final PCA-DA model and evaluated whether they were classified falsely (red cross) or correctly (green check mark) (Fig. 4.4, e). This corresponded to an external model validation. The model prediction outcome was finally corroborated by the initial HE-diagnosis that allowed a final assessment of the PCA-DA.

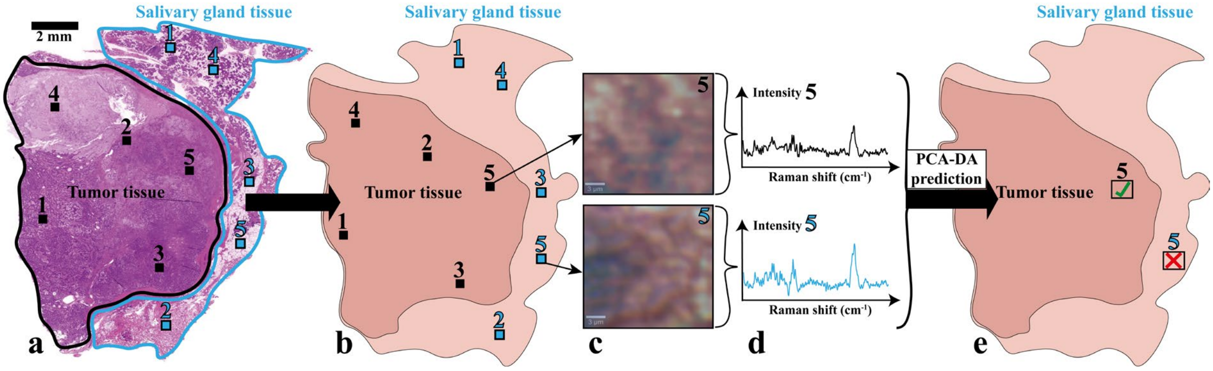

Figure 4.4. Schematic description of the external PCA-DA validation. At first, histopathologically appropriate tissue regions were defined on the HE-stained cross-sections (1 – 5 tumor tissue, 1 – 5 salivary gland tissue in (a)). Afterwards, these regions were identified on the corresponding unstained cross-sections used for Raman imaging (1 – 5 tumor tissue, 1 – 5 salivary gland tissue in (b)). Raman images (c) and resulting Raman mean spectra (d) were acquired and calculated to be predicted by the PCA-DA model. The tested Raman mean spectra are either correctly (✓) or falsely (✗) classified by the model (e), which is evaluated by the initial HE-diagnosis in step (a).

The classification results of unknown Raman mean spectra by the PCA-DA model are summarized in Tab. 4.3. Almost all Raman mean spectra were assigned to the correct tissue type, except for one pleomorphic adenoma spectrum, which was classified as salivary gland.

Table 4.3. Prediction outcome of model-unknown Raman mean spectra. Five Raman mean spectra for salivary gland, Warthin tumor and pleomorphic adenoma (column 1 and 2) were classified respectively by the PCA-DA model (column 3) and compared with the initial HE-diagnosis (column 4). Correctly predicted Raman mean spectra are indicated in green and bold, whereas wrong classifications are depicted in red and regular font.

Entity	Prediction spectra	Model classified as	HE diagnosed as
Salivary gland tissue	1	**Salivary gland tissue**	**Salivary gland tissue**
	2	**Salivary gland tissue**	**Salivary gland tissue**
	3	**Salivary gland tissue**	**Salivary gland tissue**
	4	**Salivary gland tissue**	**Salivary gland tissue**
	5	**Salivary gland tissue**	**Salivary gland tissue**
Pleomorphic adenomas	1	**Pleomorphic adenomas**	**Pleomorphic adenomas**
	2	**Pleomorphic adenomas**	**Pleomorphic adenomas**
	3	Pleomorphic adenomas	Salivary gland tissue
	4	**Pleomorphic adenomas**	**Pleomorphic adenomas**
	5	**Pleomorphic adenomas**	**Pleomorphic adenomas**
Warthin tumor	1	**Warthin tumor**	**Warthin tumor**
	2	**Warthin tumor**	**Warthin tumor**
	3	**Warthin tumor**	**Warthin tumor**
	4	**Warthin tumor**	**Warthin tumor**
	5	**Warthin tumor**	**Warthin tumor**

4.5 Discussion

As the distinct identification of parotid tumor entities is important, new approaches are required to facilitate a correct diagnosis. Thus, we focused on Raman spectroscopic imaging combined with MVA to create a valid and robust PCA-DA model for the differentiation of salivary gland, Warthin tumor and pleomorphic adenoma.

A comparison of Raman mean spectra in the range of 900 – 1700 cm^{-1} enabled to reveal individual spectral patterns and thus spectral changes between the different tissue types (Fig. 4.2b, Tab. 4.1). Throughout the investigated Raman shift, most of the identified Raman bands match between the tissue types with only a few distinct band differences (1) – (14), (Fig. 4.2b). Most of these differences allow a discrimination of normal salivary gland from parotid tumors. This is expressed by several bands or band relations, which are different for normal salivary gland than for both tumors. A distinctly appearing band (1) for the salivary gland, which is less pronounced or shifted within the tumor spectra, indicates variations in RNA. Comparably, band (5) also implies changes in DNA / RNA between the tissue types. DNA / RNA differences can be correlated to the abundance of DNA / RNA in tumors due to an intensified proliferation and metabolic activity of cancer cells [277,278]. Aside from DNA / RNA related differences, mainly protein and lipid associated vibrations (3) – (5) allow a demarcation of normal salivary gland from Warthin tumor and pleomorphic adenoma (Fig. 4.2b). This can be attributed to a dysregulated synthesis of certain lipids and proteins, often enhanced in tumors [279,280]. Additionally, characteristic tumor signal relations are observed at (3), (10), (13) for Warthin tumor and pleomorphic adenoma that are also related to triglyceride, lipid and protein variations and help to discriminate between tumor and non-tumor tissue. These band relations additionally enable to distinguish among the tumor entities themselves, as shown e.g. for (13). This is expected to result from individual protein or lipid expression levels of both tumors [281]. Furthermore, the triglyceride indication can be ascribed to a high endogenous synthesis of fatty acids, which is estimated to be linked to the high degree of tumor cell proliferation [282]. Further bands (1; 920 cm^{-1}), (2), (10), (14) enable to differentiate salivary gland from parotid tumors (Fig. 4.2b), which are expected to correlate with collagen vibrations of the tumor's extracellular matrix. Collagen was proven to be increasingly accumulated and expressed in tumorous tissue and thus contribute to tumor progression, invasion and metastasis [283,284]. As a result, the collagen abundance, type and composition might be different in the three tissue types, which allow also a distinction of the parotid tumors.

Although spectral differences are already indicated by the band allocations, smallest changes that contribute to a clear parotid differentiation might not be assignable or even be missed. To identify these, a PCA analysis between 900 – 1750 cm^{-1} was performed (Fig. 4.3). The final tissue type separation was achieved by PC1, PC2 and PC5 (Fig. 4.3a) and can be deduced from corresponding loading plots (Fig. 4.3b). Main loadings maxima allow to identify spectral regions or bands with the highest impact on the tissue demarcation. As the Warthin tumor is almost fully separated by PC1 and PC2, main influences in both loadings are assumed to affect this segregation. Within the PC1 loadings, maxima at 1164 cm^{-1}, 1530 cm^{-1}, 1596 cm^{-1} and 1643 cm^{-1} are identified to have a major impact on the Warthin cluster position. The impact at 1164 cm^{-1} is associated with a tyrosine variation in the tissues that mainly cause a separation of Warthin tumor from pleomorphic adenoma. Tyrosine was found to be accumulated as crystals in pleomorphic adenoma, assumed to result from a disordered protein synthesis [285]. This seems not to be the case for other parotid tumors, such as the Warthin tumor, which explains the discrimination of both tumor entities at 1164 cm^{-1} and also the differentiation from salivary gland. Another PC1 loading maximum corresponds to 1530 cm^{-1}, which can be correlated to a carotenoid vibration. Carotenoids were mainly shown to suppress tumor metastasis or progression, but were also suggested to promote tumor invasion by actively interfering into various signal pathways [286]. Variations of carotenoids in Warthin tumor might thus result in a differently up- or downregulated gene expression, which affects changes on molecular mechanisms and tissue composition. As a consequence, the Warthin tumor group is better distinguishable from salivary gland and pleomorphic adenoma on PC1. Furthermore, the influence of PC1 loadings at 1596 cm^{-1} and 1643 cm^{-1} are mostly ascribable to amide III oscillations of proteins and lipids that were previously discussed to be highly abundant in tumors as a result of protein and lipid dysregulation [279,280]. Consequently, this contributes to a segregation of the tumors from normal salivary gland.

PC2 is additionally needed to achieve a complete separation of the Warthin tumor group. Here, the loading at 1440 cm^{-1} refers to a cholesterol vibration that might cause a separation of Warthin tumor and pleomorphic adenoma from salivary gland. This can be explained by the fact that the cholesterol concentration is increased in tumors, especially in proliferating cancer cells [287], which was shown for numerous cancers [287,288]. Additional PC2 loadings at 1467 cm^{-1}, 1643 cm^{-1} and 1680 cm^{-1} indicate again a high impact of proteins and lipids on the separation of the Warthin tumor cluster that implies a varying protein and lipid composition for Warthin tumors.

PC5, however, was required to enable a complete distinction between pleomorphic adenoma and normal salivary gland. Mostly influencing PC5 loading maxima are shown at 1285 cm^{-1}, 1384 cm^{-1}, 1450 cm^{-1} and 1546 cm^{-1}. The PC5 loading at 1285 cm^{-1} points to the impact of collagen on the distinction between pleomorphic adenoma and salivary gland. This again confirms that tumors differ from normal tissues by their collagen composition, type and abundance as was already discussed. Another influence is also assigned to cytosine, which is associated with tumorigenesis due to cytosine methylation [289]. Compared to that, pronounced PC5 loadings at 1384 cm^{-1} and 1450 cm^{-1} result from CH_2 / CH_3 bending modes that are at least partly malignant-specific. A further assignment of these loadings to CH_2 / CH_3 modes of biomolecules, including proteins and lipids, is possible. Both loading allocations can be interpreted as an increase in biomass, typically observed for tumors [290], and are thus highly-specific for pleomorphic adenoma. At a PC5 loading value of 1546 cm^{-1}, bound / free nicotinamide adenine dinucleotide (NADH) and tryptophan are expected to additionally trigger the separation of pleomorphic adenoma from salivary gland. This is reasonable since tumors reveal an increased metabolism that correlates with a higher NADH and tryptophan demand [278,291]. Furthermore, the extent of bound-to-free NADH differs between normal and tumorous tissue and thus contributes to a better distinction between salivary gland and pleomorphic adenoma [292].

The final PCA-DA model was used to predict model-unknown Raman mean spectra of the three tissue types and test its classification suitability. Model performance parameters are all beyond 90 % and thus demonstrate the model's applicability for prediction purposes. Except for one misclassification of pleomorphic adenoma, all Raman mean spectra were predicted correctly according to the corresponding HE-diagnosis (Tab. 4.3). A possible reason for the failing prediction might be the high tissue heterogeneity of pleomorphic adenoma, which could hamper its classification by the model. However, all other pleomorphic adenoma spectra were distinctly identified by the model and thus suggest that the PCA-DA covers the variations in tissue heterogeneity. This indicates the high potential of the PCA-DA model to be a supporting diagnostic tool. Although a good classification accuracy is achieved, the time-consuming Raman imaging prevents the measurement of a large number of patient samples. Consequently, an automatization is required to enable a high imaging throughput in the future.

4.6 Conclusion

This study focused on the identification and differentiation of normal salivary gland, Warthin tumor and pleomorphic adenoma by Raman imaging combined with MVA. Representative regions of all three tissue types were Raman imaged in a point-scanning manner with an adequate spatial and high spectral resolution. This allowed us to conduct a thorough Raman band analysis in order to identify differences in the spectra and understand the biological background. Spectral variations were mainly observed for RNA / DNA-, lipid-, protein- and collagen-related bands or band relations that primarily contribute to a discrimination of tumorous and non-tumorous tissues. Due to the high spectrum similarity between the tissues, a subsequent PCA calculation with the Raman data was necessary to uncover the tissue-specific impact, responsible for a distinct differentiation. This revealed major influences of tyrosine, carotenoids, cholesterol, cytosine, NADH and tryptophan aside from proteins and lipids that caused a clear parotid tissue separation by PCA. These results emphasized the necessity of PCA to extract the hidden information, not determinable to this extent by a Raman band analysis. By combining the PCA with a subsequent DA, a reliable PCA-DA model was formed, which achieved an accuracy of 94 %, sensitivity of 94 %, specificity of 95 % and precision of 94 %. To verify the model prediction capability, an external proof-of-principle validation of model-unknown Raman mean spectra was accomplished. The results revealed an almost completely correct prediction outcome except for one false pleomorphic adenoma classification. Possible reasons for that were ascribed to its pronounced heterogeneity. All prediction results were additionally confirmed by corresponding HE-diagnoses. Consequently, we consider our PCA-DA model to be an excellent supportive means in routine diagnostics of parotid tumors and normal salivary gland.

4.7 Declarations

Funding: This study was funded by the doctoral program of the University of Tübingen and Reutlingen University “Intelligente Prozess- und Materialentwicklung in der Biomateriomics (IPMB)”, which is supported by the MWK Baden-Württemberg (PhD student fellowship to MCB and MS). Additionally, this work was supported by a MINT-funded project from Vector Stiftung Stuttgart and the framework Ingenieur Nachwuchs 2016 (project: CompeTERS) by the German Federal Ministry of Education and Research (BMBF; Grant no.: 13FH596IX6).

5. Manuscript III: The Impact of Standard Tissue Preparation Protocols on Salivary Gland Tumors investigated by Fourier-Transform Infrared Microspectroscopy

Mona Stefanakis[1,2*] *and Miriam C. Bassler*[1,2*], *Tobias R. Walczuch*[1], *Elena Gerhard-Hartmann*[3], *Almoatazbellah Youssef*[3], *Agmal Scherzad*[4], *Manuel Stöth*[4], *Edwin Ostertag*[1], *Rudolf Hagen*[4], *Maria Steinke*[5], *Stephan Hackenberg*[6], *Marc Brecht*[1,2**] *Till Jasper Meyer*[4**]

[1]Process Analysis and Technology (PA&T) Reutlingen University, Alteburgstr. 150, 72762 Reutlingen, Germany

[2]Institute of Physical and Theoretical Chemistry University of Tübingen, Auf der Morgenstelle 18, 72076 Tübingen, Germany

[3]University of Würzburg, Institute of Pathology, Josef-Schneider-Str. 2, 97080 Würzburg, Germany

[4]University Hospital Würzburg, Department of Oto-Rhino-Laryngology, Plastic, Aesthetic & Reconstructive Head and Neck Surgery, Josef-Schneider-Str. 11, 97080 Würzburg, Germany

[5]University Hospital Würzburg, Chair of Tissue Engineering and Regenerative Medicine, Röntgenring 11, 97070 Würzburg, Germany

[6]RWTH Aachen University Hospital, Department of Otorhinolaryngology – Head and Neck Surgery, Pauwelsstr. 30, 52074 Aachen, Germany

*These authors contributed equally to this work.

This chapter is similarly published in the Journal of Clinical Medicine (https://doi.org/10.3390/jcm12020569) as

Stefanakis, M.; Bassler, M.C.; Walczuch, T.R.; Gerhard-Hartmann, E.; Youssef, A.; Scherzad, A.; Stöth, M.B.; Ostertag, E.; Hagen, R.; Steinke, M.R.; et al. The Impact of Tissue Preparation on Salivary Gland Tumors Investigated by Fourier-Transform Infrared Microspectroscopy. J. Clin. Med. **2023**, 12, 569. https://doi.org/10.3390/ jcm12020569, © 2023 Licensee MDPI, Basel, Switzerland.

5.1 Abstract

Due to the high variety of benign and malignant salivary gland tumors, an entity and a dignity determination based on histomorphological criteria is difficult and sometimes impossible. Spectroscopic procedures can acquire molecular biological information, without destroying the tissue within the measurement processes. Since several standardized tissue preparation procedures exist, our study investigated the impact of these preparations on the chemical composition of healthy and tumorous salivary gland tissue by Fourier-transform infrared (FTIR) microspectroscopy. Consecutive tissue cross-sections were prepared from native, formalin-fixed and formalin-fixed-paraffin-embedded (FFPE) tissue and analyzed. The FFPE cross-sections were dewaxed and remeasured. By using principal component analysis (PCA) combined with a discriminant analysis (DA), robust models for the distinction of sample preparations were built individually for each parotid tissue type. As a result, the PCA-DA model evaluation showed a high similarity between native and formalin-fixed tissues based on their chemical composition. Thus, formalin-fixed tissues are highly representative for the native samples and facilitate a transfer from scientific laboratory analysis into the clinical routine due to their robust nature. Furthermore, the dewaxing of the cross-sections entails the loss of molecular information. Our study successfully demonstrated how FTIR microspectroscopy can be used as a powerful tool within existing clinical workflows.

5.2 Introduction

As a consequence of digitalization in health care, digital pathology becomes more important within the daily clinical workflows [293-296]. As part of this process, modern diagnostics also develops and changes to allow an even faster and more reliable statement of a patient’s condition and thus identify threatening diseases as soon as possible. This is of great importance, especially in cancer diagnosis. Here, spectroscopic methodologies increasingly find their way to be used as effective diagnostic tools in tumor identification and demarcation. One powerful method is Fourier-transform infrared (FTIR) microspectroscopy [297,203,298,244], which is already introduced in various medicinal applications as a fast and robust technology [299,300]. This technique allows a spatially-resolved sample analysis by detecting the different bonding vibrations of the tissue molecules. Commonly, FTIR spectroscopy is also combined with multivariate data analysis (MVA) to systematically reduce large data sets and extract the most relevant tissue-related information [301-304]. Many studies were performed using FTIR spectroscopy or imaging coupled with MVA in tumor diagnostics [305-308].

Although FTIR spectroscopic approaches are increasingly popular in tumor analysis, no study was yet performed for salivary gland tumors (SGTs) of the parotid. Unfortunately, the investigation of parotid SGTs is rare due to a lack of sample availability and quality. Salivary gland tumors (SGT) are responsible for approximately 3 – 6 % of all head and neck neoplasms [309]. The large variety of benign and malignant SGTs becomes obvious by the World Health Organization (WHO) classification of Head and Neck tumors in 2017, which differentiates between more than thirty different benign and malignant SGTs [310]. Some studies focused on the differentiation of SGT entities or their protein and lipid composition determination by other spectroscopic methods [260,258,259], but so far only few groups used FTIR spectroscopy for head and neck tumors in general [311].

Overall, the outcome of a spectroscopic analysis is directly related to the quality of the sample set, on which basis all measurements and evaluations are performed. The quality, however, directly correlates with the gained tissue itself and the sample preparation. As the preparations chemically affect the tissues, a good understanding of these changes is required. Typical tissue processing steps encompass cryoconservation, formalin fixation, paraffin or O.C.T.™ embedding and dewaxing [312-316]. Predominantly, the influence of these tissue fixations is rather unexplored. Only a few studies addressed the effects of specimen preparation and fixation by spectroscopy methodologies [317,273,318,319]. Zohdi et al. analyzed the impact of formalin fixation on rodent heart and liver tissue sections by FTIR microspectroscopic analysis [320], whereas Hackett et al. investigated cryofixed and formalin-fixed murine brain tissue sections by FTIR imaging and PIXE elemental mapping [321]. Recently, we investigated the effect of formalin fixation on human brain tumors [322]. Besides the impact of tissue fixation on tissue constitution or morphology, the suitability of a fixation for a digital, spectroscopic-based diagnosis of tumors as well as its practical implementation into the clinical workflow are also of great importance.

In this study, we examined the influence of standardized preparation procedures on parotid salivary gland tissue, Warthin's tumor and pleomorphic adenoma by FTIR microspectroscopy. For this purpose, four different preparation protocols were applied, including cryoconservation, formalin-fixation, formalin-fixation-paraffin-embedding (FFPE) and dewaxing. FTIR mean spectra of the differently-prepared cross-sections and the used embedding or fixation chemicals are initially generated and compared to identify spectral differences between the preparation procedures. This comparison is accomplished for each of the three tissue types individually. Additionally, a chemometric approach is performed by calculating a principal component analysis (PCA) combined with a Bayesian discriminant analysis (DA) in order to achieve an IR spectra-based separation of all preparations. This allows us to reveal the spectral impact responsible for the preparation discrimination and possible reasons can be deduced. Based on our evaluations, we can ascertain the most suitable preparation method for parotid tissues, which can also be implemented within the clinical daily routine.

5.3 Materials and Methods

5.3.1 Patient Selection

Patients with a parotid gland tumor planned for parotidectomy were preoperatively screened and included in this study. Overall, 9 parotid gland tumors from 9 patients were collected, of which 5 tumors were identified by trained pathologists as Warthin tumors (age: 62.5 ± 10.7 years; male:female 2:3) and 4 tumors were diagnosed as pleomorphic adenomas (age: 55.9 ± 15.1 years; male:female 1:3). In the course of parotidectomy, surrounding areas of intact salivary gland tissue were unavoidably removed as well.

This study was approved by the institutional ethics committee on human research of the Julius-Maximilians-University Würzburg (vote 224/18). All experiments were performed according to the Declaration of Helsinki. All patients agreed to participate in this study by informed consent.

5.3.2 Preparation Workflow and Histologic Samples

Imminently after the parotidectomy, parotid tissue samples were sectioned in equal tissue pieces to ensure that the slicing surfaces contain healthy salivary gland tissue and tumor tissue. One tissue piece was chosen and prepared according to four different preservation protocols (described as “native”, “formalin”, “in paraffin”, “dewaxed”).

The native tissue piece was frozen, consecutive cross-sections were cut with a cryomicrotome (Leica CM 1900, Wetzlar, Germany) and stored at –80 °C. Based on this preparation, we defined these specimens as “native”. A second set of consecutive cross-sections was prepared identically, but was additionally fixed with 4 % neutral buffered formalin (ROTI®Histofix, Carl Roth, Karlsruhe, Germany) incubated for 1 min. These samples were determined as “formalin”. After preparing the “native” and “formalin” cross-sections, the residual tissue piece was fixated overnight in 4 % neutral buffered formalin (ROTI®Histofix, Carl Roth, Karlsruhe, Germany) and subsequently paraffin-embedded (Thermo Fisher Scientific Inc., Waltham, Massachusetts, USA). Here, the paraffin section preparation took place at ambient temperature. The paraffin embedded tissues were stated as “in paraffin”. After the FTIR microspectroscopic analysis of the “in paraffin” sections, a dewaxing (ROTICLEAR®, Carl Roth, Karlsruhe, Germany) with subsequent rehydration steps was performed for each specimen. This sample set was declared as “dewaxed”. For each preparation method, 10 µm-thick sequential sections were cut and placed on gold-coated objective slides (BioGold SuperChip, Thermo Fisher Scientific Inc., Waltham, Massachusetts, USA).

For histologic assessment, consecutive 3 µm-thick cross-sections were cut immediately after sectioning the samples for each preparation method and stained with haematoxylin and eosin (HE) according to a standard protocol. Due to this approach, the tissue diagnosis based on the HE cross-sections can directly be translated to the spectroscopic cross-sections. HE-stained sections were placed on glass objective slides and digitized with a slide scanner (Hamamatsu Photonics, Hamamatsu, Japan) for diagnostic evaluation with the CaseViewer software (Version 2.4, 3DHISTECH, Budapest, Hungary). A simplified overview of the complete workflow is summarized in Fig. 5.1.

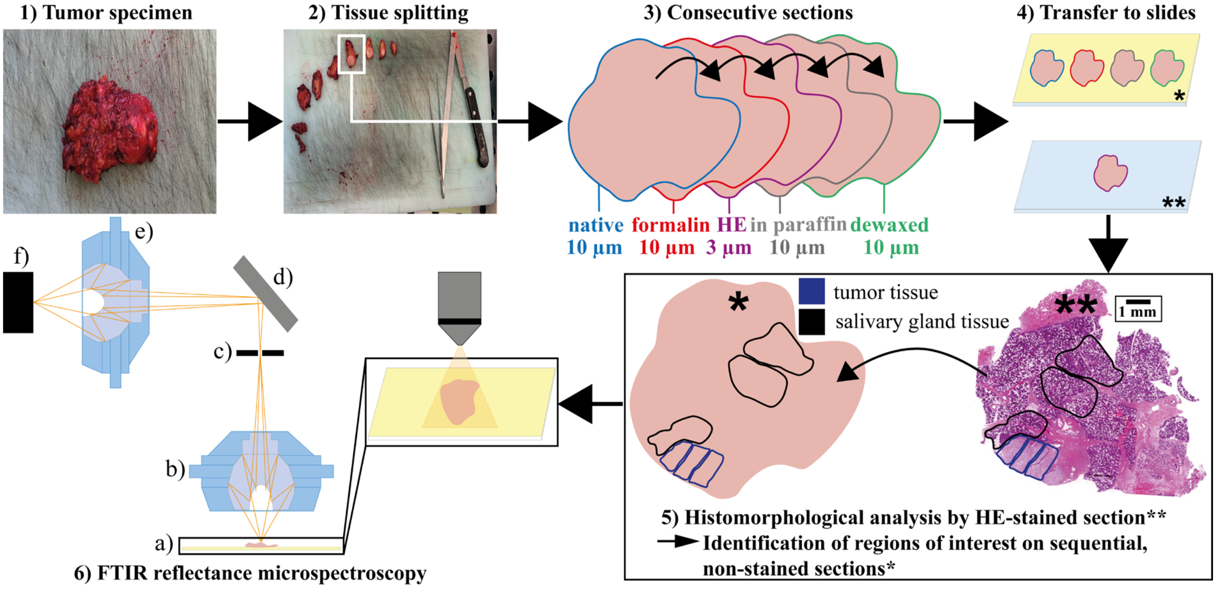

Figure 5.1. Workflow of tissue preparation for FTIR microspectroscopic measurements. Salivary gland and tumorous tissues were resected (1) and cut into pieces (2). One tissue piece was chosen and prepared according to four different preparation protocols ("native", "formalin", "in paraffin" and "dewaxed") and complemented with a separate HE-staining (3). Cross-sections were prepared and mounted onto gold-coated objective slides for the four different preparation protocols (4) and onto glass objective slides for the HE-staining (4**). The HE-stained sections were used to identify regions of interest on sequential non-stained sections (5). Finally, the "native", "formalin", "in paraffin" and "dewaxed" cross-sections were measured in reflectance mode with a FTIR microspectrometer (6): in a) tissue sample on a gold-coated objective slide, b) Cassegrain objective, c) remote aperture position, d) mirror for excitation and detection light path, e) Cassegrain MCT, f) MCT detector.*

5.3.3 Fourier-Transform Infrared Microspectroscopy

For each of the nine patients, four cross-sections according to the preservation protocols ("native", "formalin", "in paraffin", "dewaxed") were investigated. Three tumorous and three salivary gland tissue regions were selected for each cross-section (Fig. 5.2). Ten randomly chosen spectra were collected per tissue region, resulting in 60 measurements of each tumor cross-section. In total, 2160 single FTIR spectra were recorded in reflectance mode with an infrared microscope (Autoimage, Perkin Elmer, Waltham, Massachusetts, USA) coupled to a FTIR spectrometer (FTIR System 2000, Perkin Elmer, Waltham, Massachusetts, USA) shown in Fig. 5.1 (6).

Following sample illumination, the reflected light was collected with a thermoelectric cooled mercury cadmium telluride (MCT) detector. The system was referenced against air and 256 accumulations for each measurement with a gain of 4 were acquired. The spectral resolution was 4 cm^{-1} and the optical path difference velocity was 2 cm/s. The wavenumbers range from 4000 cm^{-1} to 700 cm^{-1}. An aperture size of 50 µm x 50 µm was used, which represents the measured area integrated for each single FTIR spectrum.

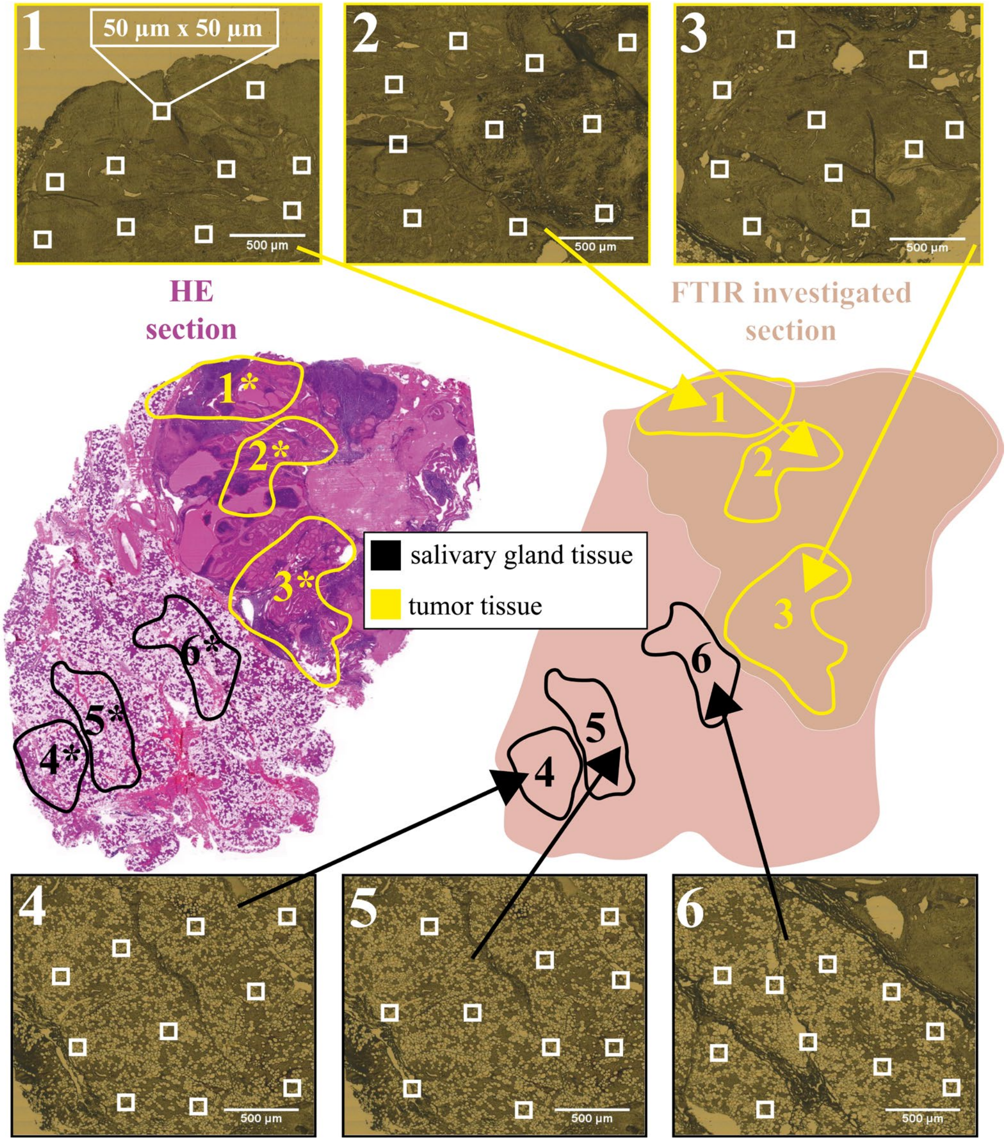

Figure 5.2. *Identification of different tissue measurement regions for FTIR microspectroscopy. For each preservation method, standardized HE-stained sections were used to assign various tissue regions of interest, defined as regions* 1^**-*6^* *(HE-section left). Identical salivary gland and tumor regions were defined in consecutive, non-stained tissue sections, schematically illustrated in region 1-6 (schematic section right). These predefined regions were additionally captured by the FTIR video image camera (images 1-6 on top and bottom). Within the video images, 10 single FTIR spectra were randomly acquired in a measuring area of 50 µm x 50 µm (white squares), respectively.*

5.3.4 Data Pretreatment and Multivariate Data Analysis

Multivariate data analysis (MVA) was performed with The Unscrambler X 10.5 (Camo Analytics AS, Oslo, Norway). All spectra from 4000 cm^{-1} to 700 cm^{-1} were preprocessed in the same way: An area normalization was conducted and followed by calculating the 2nd Gap (smoothed) derivative (5 points). The wavenumbers from 4000 cm^{-1} to 3700 cm^{-1} and 2600 cm^{-1} to 1850 cm^{-1} were excluded due to variable reduction. The tissue types (salivary gland, pleomorphic adenoma and Warthin tumor) were evaluated separately to investigate the effect of the preservation protocols “native”, “formalin”, “in paraffin” and “dewaxed”.

The PCA was calculated with mean centering, leverage correction and the singular value decomposition algorithm to distinguish between the tissue preparation protocols. Model outliers were identified in the influence plot Hotelling's T^2 versus F-residuals (outlier limits 5 % each). For the comparison of tissue types, each PCA was combined with a Bayesian discriminant analysis (DA) with Mahalanobis distance (Warthin tumor and pleomorphic adenomas) or Euclidean distance (salivary gland tissue). The number of used principal components (PCs) for the DA was similar to the shown PCA models. The overall accuracy, sensitivity, specificity and precision were calculated based on the confusion matrix terminology [199,262].

5.4 Results

5.4.1 Histologic Characterization of HE-Stained Samples

Typical benign SGTs are pleomorphic adenomas and Warthin tumors, which are macro- and microscopically well circumscribed. Histologically, pleomorphic adenomas show a mixture of ductal epithelial structures, myoepithelial cells as well as mesenchymal stromal elements in different proportions. In contrast, Warthin tumors are characterized by cysts and papillary structures lined by a two-layered oncocytic epithelium and associated lymphoid stroma with occasional lymphoid follicles with germinal centers (Fig. 5.3).

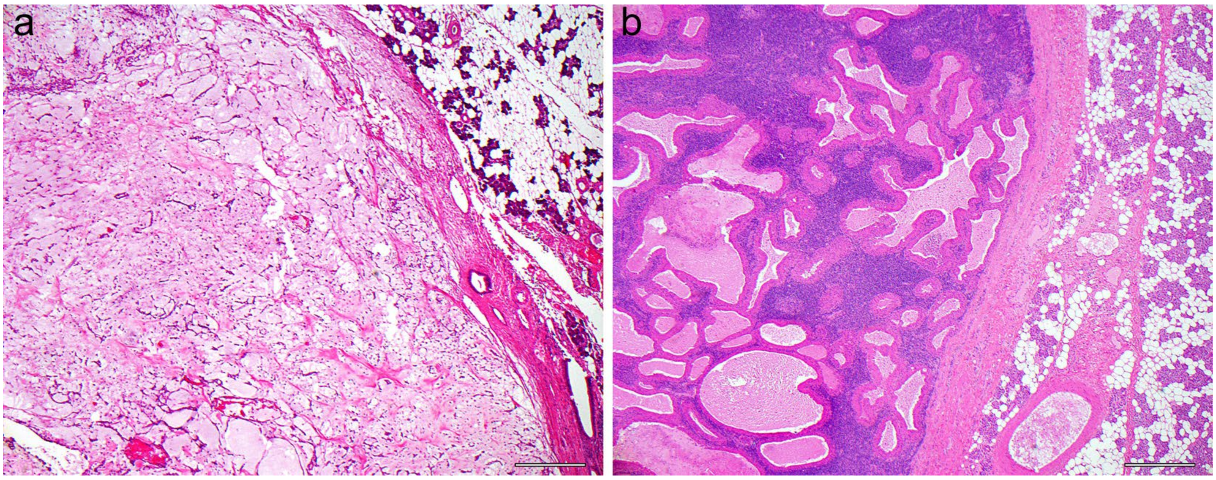

Figure 5.3. *HE-stained examples of pleomorphic adenoma (a) and Warthin tumor (b) examined in this study (original magnification 40x; length of the scale bar: 50 µm). In both images, tumor-free salivary gland parenchyma is included on the right side of the image and a sharp demarcation of the benign tumor from the surrounding parenchyma can be seen.*

5.4.2 FTIR Mean Spectra Analysis

In a first step, FTIR spectra were acquired to identify spectral changes resulting from each preservation procedure ("native", "formalin", "in paraffin", "dewaxed"). FTIR mean spectra were calculated for the salivary gland tissue and both tumor entities using all measured single spectra (Fig. 5.4). Additionally, FTIR spectra of the applied preservation and embedding chemicals ("formalin pure", "paraffin pure") were also acquired (Fig. 5.4). Tissue-related and preparation-related influences can be deduced by comparing the spectral bands. A superimposed illustration of the different FTIR mean spectra for each preparation protocol and tissue type is depicted in Fig. S5.1, Supplementary Information (A4, Appendix).

Fig. 5.4 shows the FTIR mean spectra from 3700 – 700 cm^{-1} (2600 – 1850 cm^{-1} excluded) of the four preparation protocols ("native" (blue), "formalin" (red), "in paraffin" (grey), "dewaxed" (green)) as well as the used preparation chemicals ("formalin pure" (purple), "paraffin pure" (dark yellow)). Initially, a broad band maximum is noticeable at 3290 cm^{-1} for all preparations and tissue types (1), which can either be assigned to an O-H vibration from proteins or water (Tab. 5.1). This band, however, does not appear in the "pure paraffin" spectrum and is only slightly pronounced within the "formalin pure" spectrum (1, purple, yellow). Within a wavenumber region of 3000 – 2800 cm^{-1}, a sum of three to four spectral bands is visible for the different preparations of all tissue types and the "paraffin pure" (2). These bands can be ascribed to combinations of CH_3 / CH_2 vibrations, either resulting from lipids within the tissues or the paraffin itself (Tab. 5.1). Here, similar spectral trends occur between the "native" and "formalin" tissue as well as between the "in paraffin" tissue and the "paraffin pure". On the contrary, the "dewaxed" tissue reveals a different spectral pattern in this region (2).

The mean spectra of "native" and "formalin" tissues reveal a small spectral band at 1750 cm^{-1} for all tissue types, which is missing in all other preparation mean spectra (3). The 1750 cm^{-1} band is assignable to a C=O vibration of triglycerides or esters (Tab. 5.1). A sequence of four following FTIR maxima at 1660 cm^{-1} (4), 1544 cm^{-1} (5), 1466 cm^{-1} (6) and 1390 cm^{-1} (7) can be identified for all preparation protocols and tissue types as well as for the "paraffin pure" spectrum (6). These signals, however, do not occur in the "formalin pure" spectrum. All FTIR maxima in this wavenumber range can be deduced from C=O, amide I, N-H, amide II stretching vibrations and CH_3 / CH_2 bending vibrations of either lipids or proteins (Tab. 5.1).

Additional FTIR bands appear within the fingerprint region of the four preparation procedures and tissue types. Two signals are particularly prominent at 1239 cm^{-1} and 722 cm^{-1}. A distinct assignment of this spectral region is difficult, but maxima at 1239 cm^{-1} and 722 cm^{-1} (8, 9) can be matched with a PO^{2-}, out-of-plane bending vibration of DNA / RNA and a stretching C-H vibration of lipids, respectively (Tab. 5.1). The latter band (9) is also highly dominant in the "in paraffin" tissues. FTIR spectra of the preparation chemicals "formalin pure" and "paraffin pure", however, do not show a pronounced band pattern within the fingerprint region.

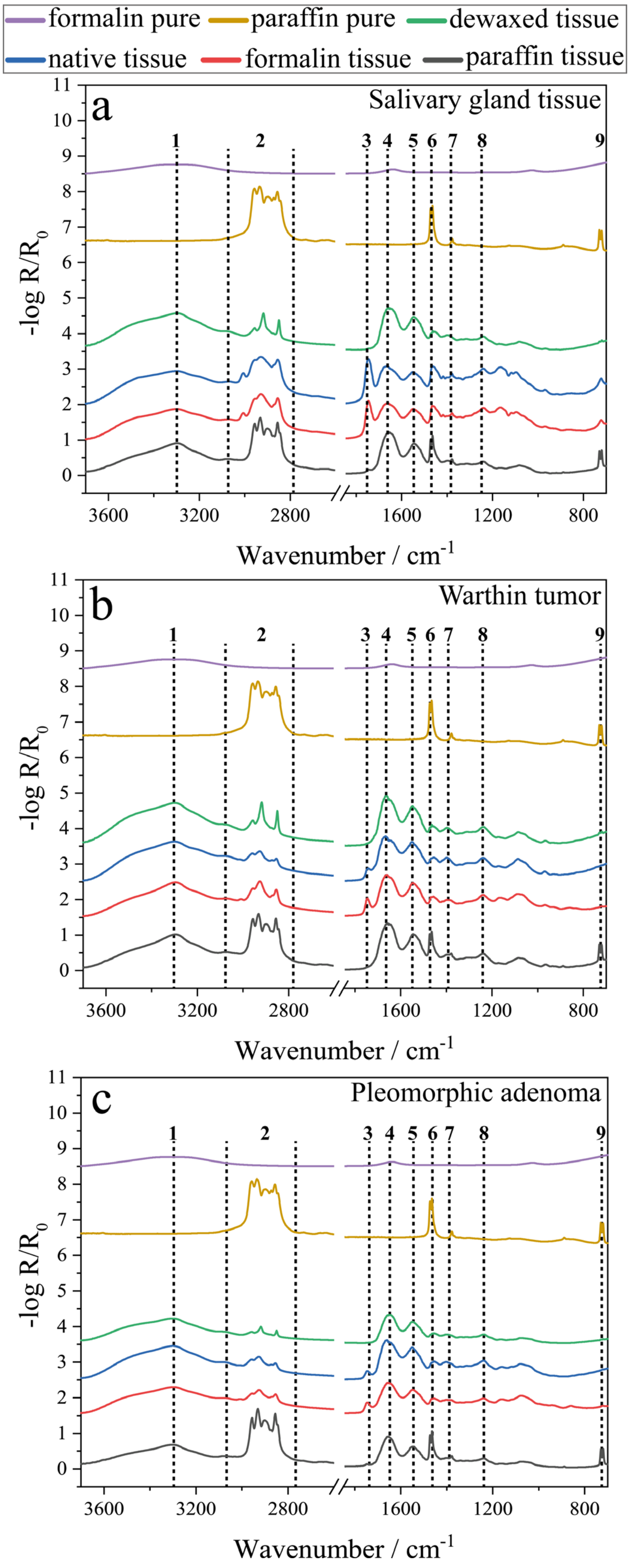

Figure 5.4. *FTIR average spectra of each preservation method ("native" (blue), "formalin" (red), "in paraffin" (grey), "dewaxed" (green)) for the three investigated tissue types, salivary gland tissue (a), Warthin tumor (b) and pleomorphic adenoma (c). "Formalin pure" (purple) and "paraffin pure" (yellow) average spectra were additionally presented to reveal the IR oscillations resulting from the preparation chemicals. All average spectra are placed by an offset for an improved comparability of signals, also indicated by the dotted lines and numbers (1-9).*

A summary of all identified IR bands is listed in Tab. 5.1. Although no distinct assignment of bands within the fingerprint region is possible, this wavenumber range is very characteristic.

Table 5.1. *Spectral band assignment for the salivary gland tissue, Warthin tumor, pleomorphic adenoma, formalin pure and paraffin pure FTIR average spectra. All assignments are based on [323-326].*

Number	Wavenumber / cm^{-1}	Assignment	Cause
1	3290	ν N-H amide, ν O-H	proteins, water
2	3000 – 2800	$\nu + \nu_{as}$ CH_3, CH_2	paraffin, lipids
3	1750; 1700 – 1500	ν C=O triglyceride and ester, protein region	lipids
4	1660	ν C=O, amide I	proteins
5	1544	δ N-H, amide II	proteins
6	1466	$\delta + \delta_{as}$ CH_3, CH_2	lipids
7	1390; 1350 – 1000	$\delta + \delta_{as}$ CH_3, CH_2, stretching vibration CH_2	lipids
8	1240 / 1239; 1000 – 700	$\nu + \nu_{as}$ PO_2^-, out of plane bending vibration	DNA / RNA
9	722	ν C-H	lipids

5.4.3 FTIR Data Analysis by PCA-DA

Statistical analysis by PCA-DA enables to reveal the smallest spectral influences and thus provide the basis to discriminate the differently-prepared parotid tissues. Fig. 5.5 shows the PCA models for all three tissue entities (salivary gland tissue (Fig. 5.5a), Warthin's tumor (Fig. 5.5b) and pleomorphic adenoma (Fig. 5.5c)), distinguishing the four preparation protocols ("native" (light blue), "formalin" (green), "in paraffin" (red), "dewaxed" (blue)). Spectral ranges of 3700 cm^{-1} to 2600 cm^{-1} and 1850 cm^{-1} to 700 cm^{-1} were considered for calculating the models. The 3D scores plot of the salivary gland tissue reveals a separation into three groups (a1). Three PCs are required to explain 80 % of the data (PC1 54 %, PC2 17 % and PC3 9 %). PC1 demarcates the below-average "in paraffin" group from the other clusters, which are aligned above-average. PC2 arranges the "dewaxed" group below-average, the "in paraffin" group in-average and the "formalin" and "native" group above-average. PC3, however, exhibits only minor differences between the "native" and "formalin" group. Reasons for this clustering are displayed in the corresponding loading plots of PC1, PC2 and PC3 (a2). All three loading plots show a major impact in the wavenumber region of 3000 – 2800 cm^{-1}, 1700 – 1500 cm^{-1} and the fingerprint region below 1500 cm^{-1}. The loading plot of PC1 distinguishes three main bands in a wavenumber range of 3040 – 2800 cm^{-1}, 1500 – 1440 cm^{-1} and 740 – 700 cm^{-1} (a2). In the PC2 loadings, an overall higher spectral influence is noticeable within wavenumber ranges of 3040 – 2810 cm^{-1}, 1780 – 1610 cm^{-1}, 1500 – 1360 cm^{-1}, 1160 – 1050 cm^{-1} and 750 – 700 cm^{-1}. Similar spectral effects are shown in the PC3 loadings (3010 – 2820 cm^{-1}, 1790 – 1700 cm^{-1}, 1500 – 1360 cm^{-1}, 1220 – 1090 cm^{-1}, 750 – 700 cm^{-1}).

The 3D scores plot of the Warthin's tumor also demonstrates a segregation into three groups according to the different preparation procedures. A total explained variance of 84 % was reached by the first three PCs (PC1 65 %, PC2 15 % and PC3 4 %). For PC1, the "in paraffin" group is separated from the below-average groups "formalin", "dewaxed" and "native" due to its above-average positioning. PC2 reveals an above-average arrangement of the “native” and “formalin” group, whereas the “dewaxed” one is positioned below-average. The “in paraffin” group lies in-between both and is thus organized in-average. PC3 additionally displays an in-average arrangement of the “in paraffin” and “dewaxed” group. “Formalin” and “native” prepared groups, however, are either positioned above- or below-average by tendency. This overall separation results from the spectral information represented by the corresponding loading plots of all three PCs (b2). The PC1 loadings reveal three distinct wavenumber regions (3000 – 2810 cm^{-1}, 1500 – 1350 cm^{-1}, 750 – 700 cm^{-1}), which mostly affect the group separation. Compared to the PC1 loadings, the PC2 loadings plot exhibits a more wide-spread spectral impact, including wavenumber ranges of 3700 – 3550 cm^{-1}, 3020 – 2800 cm^{-1}, 1775 – 1580 cm^{-1}, 1500 – 1400 cm^{-1}, 750 – 700 cm^{-1}. A comparable spectral influence is also discernible in the PC3 loading plot with two additional maxima at 1750 cm^{-1} and 1470 cm^{-1}.

The 3D scores plot of the pleomorphic adenoma shows a similar group separation for all investigated preparation approaches (PC1 84 %, PC2 4 % and PC3 2 %, explained variance 90 %). As described earlier for the Warthin’s tumor, the above-average “in paraffin” group is completely separated from the below-average groups “native”, “formalin” and “dewaxed” by means of PC1. The demarcation due to PC2, however, reveals a below-average positioning for the “dewaxed” group, an above-average arrangement of the “formalin” and “native” group and the “in paraffin” group is in-average. For PC3, the “dewaxed” and “in paraffin” groups are represented in-average position, whereas the “formalin” group is tendentially organized above-average and the “native” one tendentially ranges below-average with regard to PC3. The arrangement of the clusters in the 3D scores plot is identical to the Warthin’s tumor evaluation. The reasons for this segregation can be deduced from the corresponding loading plots (c2). The PC1 loadings reveal three wavenumber regions (3000 – 2810 cm^{-1}, 1500 – 1430 cm^{-1}, 750 – 700 cm^{-1}). Comparable wavenumber ranges are also identified in the PC2 loadings with additional impacting wavenumber regions of 3700 – 3550 cm^{-1} and 1770 – 1370 cm^{-1} as well as a dominating maximum at 1470 cm^{-1}. The spectral influence in the PC3 loadings is also very similar to the range described by PC2 loadings, except for two additional maxima at 1750 cm^{-1} and 1470 cm^{-1} as well as the wavenumber range between 1230 – 950 cm^{-1}.

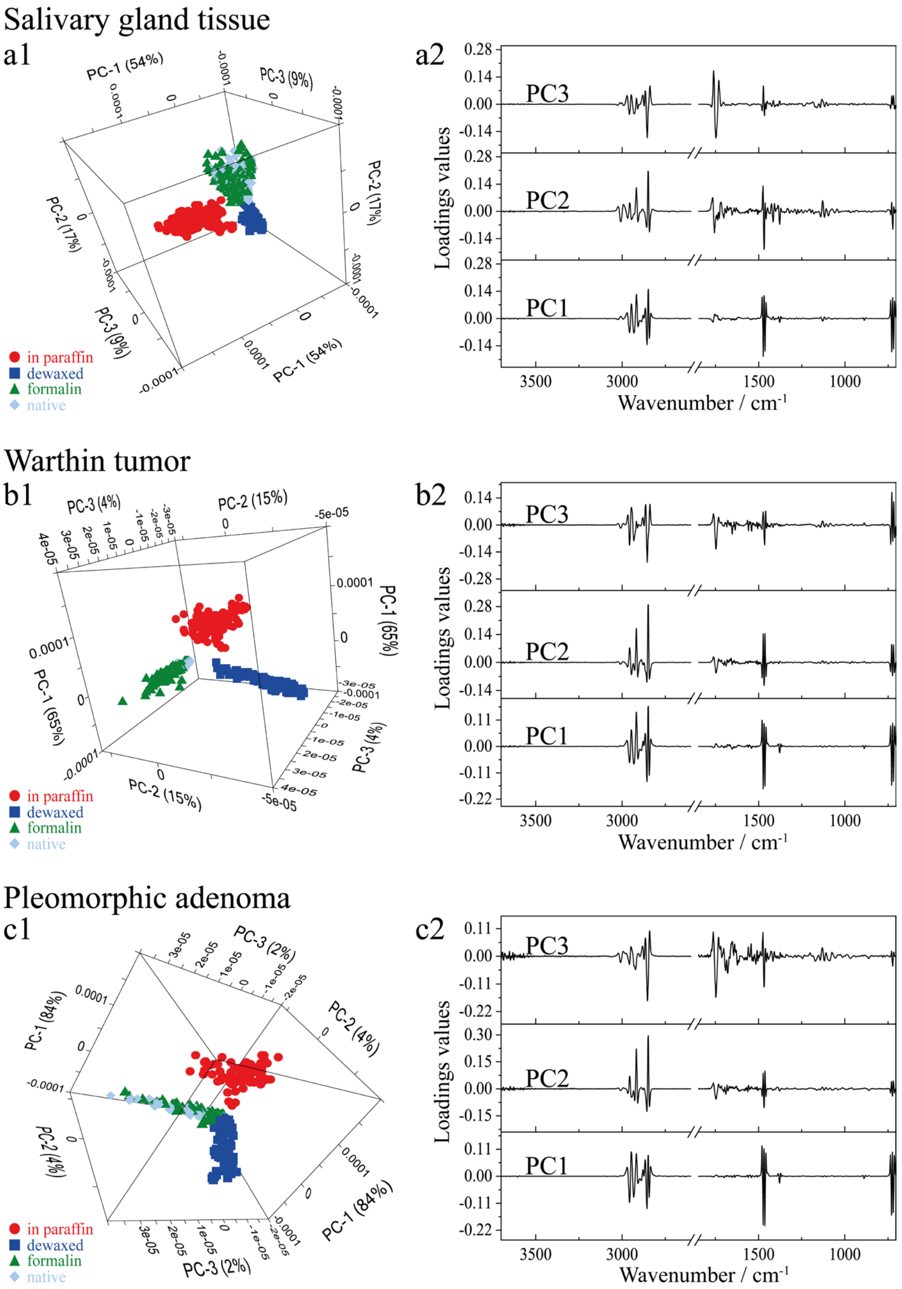

Figure 5.5. *PCA models for salivary gland tissue (a), Warthin's tumor (b) and pleomorphic adenoma (c) in terms of different preservation procedures ("native" (light blue), "formalin" (green), "in paraffin" (red), "dewaxed" (blue)). a1, b1 and c1 represent the 3D scores plots, whereas a2, b2 and c2 show the corresponding loadings.*

In all three models, PC1 distinguishes "in paraffin", whereas PC2 differentiates "dewaxed" and PC3 cannot clearly demarcate between the "native" and "formalin" preparation procedure. Therefore, the PCA scores were used in a DA to quantitatively calculate the clustering. This is based on the confusion matrix values. Confusion matrices of each model are listed in Tab. S5.1 – S5.3, Supplementary Information (A4, Appendix). An overview of the PCA-DA model parameters is summarized in Tab. 5.2.

Table 5.2. Model quality parameters for the salivary gland tissue, Warthin tumor and pleomorphic adenoma PCA-DA models. The robustness of the models can be deduced from the total and percentage amount of correctly assigned FTIR spectra for each preservation method. Based on this assignment, the average model parameters accuracy, sensitivity, specificity and precision can be calculated.

Entity	Fixation method	Total spectra	Correctly predicted	Correctly predicted / %	Accuracy / %	Sensitivity / %	Specificity / %	Precision / %
Salivary gland tissue	in paraffin	270	270	100	83	84	94	83
	formalin	270	192	71				
	native	270	174	64				
	dewaxed	269	260	97				
Warthin tumor	in paraffin	150	150	100	89	89	96	90
	formalin	150	131	87				
	native	150	103	69				
	dewaxed	150	150	100				
Pleomorphic adenoma	in paraffin	120	120	100	76	77	92	76
	formalin	120	84	70				
	native	120	48	40				
	dewaxed	120	114	95				

Due to an overlap of the “native” and “formalin” group within the PCA, the misclassification of “formalin” and “native” is distinct (e.g. 40 % native pleomorphic adenoma), whereas in the “in paraffin” and “dewaxed” group almost all spectra are predicted correctly (e.g. 100 % in paraffin salivary gland tissue). This is attributed to a high similarity between “native” and “formalin”. All three tissue types exhibit model parameters higher 75 % and thus built robust models. If “native” and “formalin” groups are combined as one class in a PCA-DA calculation, the model quality parameters reached over 97 %. Confusion matrices of the three-class models are listed in Tab. S5.4 – S5.6, Supplementary Information (A4, Appendix). An overview of the PCA-DA model parameters for a combined “native” and “formalin” approach is summarized in Tab. S5.7, Supplementary Information (A4, Appendix).

5.5 Discussion

Tissue preparation and fixation for preservation and subsequent analysis are an important issue in a clinical daily routine, in particular for a qualified diagnosis. For this reason, the impact of the most common tissue fixation methods needs to be understood in order to deduce their applicability for spectroscopic analysis as diagnostic tool. Thus, preparation-specific differences in salivary gland tissue, Warthin tumor and pleomorphic adenoma were investigated by FTIR microspectroscopy.

By comparing FTIR mean spectra of differently-prepared parotid tissues among each other and with the fixation and embedding chemicals, spectral band variations and similarities can be identified (Fig. 5.4). In a wavenumber range of 3000 – 2800 cm^{-1} (2) (Fig. 5.4, Tab. 5.1), the “dewaxed” spectrum reveals a different IR signature compared to the other preparations and the “paraffin pure” spectrum. We expect these differences to result from tissue alterations due to dewaxing, which directly affects the tissue's nature. Additionally, spectral bands of "native" and "formalin" are highly similar at 3000 – 2800 cm^{-1}, which leads to the conclusion that the formalin-fixation does not have an impact on these bands. Besides, signal intensities within 3000 – 2800 cm^{-1} are highest for the "in paraffin" and lowest for the "dewaxed" mean spectra compared to the other preparations (Fig. S5.1, SI). This indicates that the incorporated paraffin contributes to the CH_2 / CH_3 vibrations within the "in paraffin" spectrum. The low signal intensity in "dewaxed", however, suggests that not only paraffin, but also proteins or lipids were removed from the tissues by dewaxing. Furthermore, the IR band at 1466 cm^{-1} (6) can be detected in all preparations, except for the "formalin pure" spectrum (Fig. 5.4, Tab. 5.1). Its highest signal intensity is observed in the "paraffin pure" and the "in paraffin" spectra compared to the other preparations. This shows again that the "in paraffin" signal intensity is amplified by the embedded paraffin, as was already observed for 3000 – 2800 cm^{-1}. In the fingerprint region, the band pattern differs between "native" / "formalin" and "in paraffin" / "dewaxed", indicating that already paraffin and also dewaxing affected the molecular composition.

A PCA was calculated to identify the effects of each preparation method, since only minor changes in terms of band signature, shape and intensity are observed in the spectra. A summary of the PCA analysis for the analyzed preparation methods is illustrated in Fig. 5.5. The 3D score plots of all tissue types reveal a similar group arrangement for the "in paraffin", "dewaxed", "formalin" and "native" preparations (Fig. 5.5 a1, b1, c1). PC1 distinctly separates the "in paraffin" from the other treatment groups. Thus, the greatest influence is assumed to derive from the paraffin. Three specific spectral areas can be addressed, which affect the "in paraffin" positioning (3000 – 2800 cm^{-1}, 1466 cm^{-1}, 722 cm^{-1}) (Fig. 5.5 a2, b2, c2). These can be correlated to CH_2 / CH_3 and C-H signals from paraffin, but also to vibrations of tissue components. Therefore, these band regions can be interpreted as a paraffin overlap on top of the CH_2 / CH_3 and C-H signals of the tissues. PC2, however, clearly distinguishes between the "dewaxed" and "native" / "formalin" group in all 3D scores plots. By comparing the PC2 loadings of all tissue types (Fig. 5.5 a2, b2, c2), an increased impact of the C=O and N-H bonding vibrations (1750 – 1500 cm^{-1}) is observed, whereas a decrease of CH_2 / CH_3 and C-H maxima (3000 – 2800 cm^{-1}) is noticed. Additionally, the fingerprint region is also more pronounced. The influence of 1750 – 1500 cm^{-1} and the fingerprint region (1050 – 500 cm^{-1}) can be ascribed to a C=O band at 1750 cm^{-1} and a weak IR signal at 722 cm^{-1}, which are only present in the "native" / "formalin" spectra, but missing in the "dewaxed" spectrum. Thus, both signals mainly contribute to the separation of "dewaxed" from "native" / "formalin" on PC2. A possible explanation is again that dewaxing not only extracts paraffin, but also other lipophilic substances from the tissues and consequently this spectral information is removed from the "dewaxed" spectrum. Furthermore, a pronounced influence of the 1750 – 1500 cm^{-1} area is illustrated for the salivary gland tissue in the PC2 loadings. This can be explained by the significantly higher amount of lipid vacuoles and adipocytes in salivary gland tissue compared to both tumor entities. Therefore, this 1750 – 1500 cm^{-1} region represents mainly the influence of lipids for the salivary gland. PC3 additionally indicates a partial distinction of the “native” and “formalin” group for all tissue types. The associated PC3 loading plots (Fig. 5.5a2, b2, c2) show the highest discrimination influence again at lipid and protein-corresponding wavenumbers (2855 cm^{-1} CH_2 / CH_3, 1750 cm^{-1} C=O, 1134 cm^{-1} CH_2 / CH_3). One explanation is that lipids in comparison to proteins might not be preserved by formalin fixation, which causes a partial differentiation. This is supported by various studies, which state that formalin is only partially or even not able to preserve lipids [175]. However, others claim formalin to be appropriate for this purpose [327]. Another reason for the high overlap between the “native” and “formalin” group is that the formalin fixation on the one hand stabilizes the molecules by their cross-linking and on the other hand the native tissue degradation only slowly proceeds, so that tissue compositions are assumed to be almost identical for both. Additionally, an increasing influence of 1750 – 1500 cm^{-1} and 1500 – 1050 cm^{-1} is shown for the tumor entities in the PC3 loadings. These might point to a tissue heterogeneity, of which pleomorphic adenoma is the most heterogeneous one, followed by the salivary gland tissue and the Warthin tumor.

All findings are further confirmed by the additionally performed DA (Tab. 5.2). The PCA-DA shows the best classification results for the “in paraffin” and “dewaxed” groups with correct prediction outcomes between 95 – 100 % of all tissue types. Compared to that, the “formalin” group is with 70 - 87 % less accurately predicted. The “native” group, however, is classified even worse with 64 % for salivary gland tissue, 69 % for Warthin tumor and 40 % for pleomorphic adenoma. These classifications show that despite the pronounced group overlap between “native” and “formalin”, still 70 - 87 % of the “formalin” group were correctly identified. This demonstrates the high stabilization effects of the tissues by the formalin method and thus its robustness. The poor classification for the “native” group is influenced by the tissue homogeneity, as the very heterogeneous pleomorphic adenoma is subjected to worst prediction results, whereas the most homogeneous Warthin tumor achieved the best outcome in this group. Nevertheless, overall accuracy, sensitivity, specificity and precision are above 75 % for all tissue types, demonstrating the models to be very robust. If “native” and “formalin” are grouped as one class due to their high similarity, all model quality parameters are above 97 %.

An accurate patient diagnosis is directly linked to the quality and information content gained from the tissue samples, which are also influenced by the respective tissue preparation protocol. Therefore, the effects of these preparations on tissues are important to know. As demonstrated by our FTIR investigations, the different preparation methods have an impact on the chemical composition of the parotid tissues. The paraffin embedding and dewaxing were shown to either superimpose the signals or cause a loss of information due to additional tissue component removal. For native and formalin-fixed tissues, the chemical structure is very similar and thus a differentiation based on their chemical information is almost not possible. Based on our results, formalin fixation is declared to be the most appropriate preparation method, not only from a highly stabilizing and less interfering conservation aspect, but also from its suitability for spectroscopic tissue analysis. As spectroscopic diagnostics are more and more implemented in clinics, a suitable tissue preparation is mandatory. Additionally, formalin fixation allows an easy handling and thus good integration in a daily clinical workflow for the preservation of salivary gland tissue and tumors.

5.6 Conclusion

Since the effects of tissue preparation methods are hardly explored, a better understanding is required, especially in the context of digital diagnostics with optical spectroscopy. This is of high importance also in a further development of parotid tumor diagnosis. For this purpose, the impact of four classical sample preparations on salivary gland and parotid tumor tissues was investigated by FTIR microspectroscopy. Spectral variations among FTIR mean spectra of the differently-prepared tissues and the used preservation chemicals were initially identified. Due to only minor IR differences, a subsequent PCA-DA was performed to determine the spectral effects caused by sample preparation and to deduce its impact on the chemical composition of parotid tissues. A complete PCA separation according to the preparations was achieved for the “in paraffin” and “dewaxed” groups. Our results revealed that the embedded paraffin often overlaid or amplified the CH_2 / CH_3 vibrational signals of the tissues. Furthermore, a tissue dewaxing caused an additional removal of tissue proteins / lipids and thus a loss of information. The “formalin” and “native” group mainly superimposed in PCA score plots due to the high chemical similarity, also reflected by the comparable IR patterns. We assumed the stabilizing effects by formalin and the just slowly proceeding decomposition of native tissue to be responsible for their high overlap. All results were also reflected by the calculated quality parameters for the four classes PCA-DA model above 75 %. In case, native and formalin-fixed tissues are combined to one class, the resulting three classes PCA-DA model reached quality parameters above 97 %. This confirms the high chemical similarity between native and formalin-fixed tissue. Due to the overall stabilizing and low interfering impact of the formalin fixation, its usage is highly suitable for parotid tissue treatment, especially in the context of a spectroscopic-based diagnosis. Additionally, formalin fixation is easy implementable in a tissue preparation workflow within the clinical daily routine, facilitating the transfer from science to application. For a reliable tumor characterization, FTIR spectroscopy can provide additional histochemical information.

5.7 Declarations

Funding: This study was funded by the doctoral program of the University of Tübingen and Reutlingen University “Intelligente Prozess- und Materialentwicklung in der Biomateriomics (IPMB)”, which is supported by the MWK Baden-Württemberg (PhD student fellowship to MCB and MS). This research was funded by the Interdisciplinary Centre for Clinical Science (IZKF) at the University of Würzburg, Grant Number Z-2/78 to TJM.

6. Manuscript IV: Accumulation and Penetration Behavior of Hypericin in Glioma Tumor Spheroids studied by Fluorescence Microscopy and Confocal Fluorescence Lifetime Imaging Microscopy

Miriam C. Bassler[1,2], Tim Rammler[2], Frank Wackenhut[1], Sven zur Oven-Krockhaus[2], Ivona Secic[1], Rainer Ritz[3], Alfred J. Meixner[2], Marc Brecht[1,2*]*

[1]Process Analysis and Technology (PA&T) Reutlingen University, Alteburgstr. 150, 72762 Reutlingen, Germany

[2]Institute of Physical and Theoretical Chemistry University of Tübingen, Auf der Morgenstelle 18, 72076 Tübingen, Germany

[3]Department of Neurosurgery, Schwarzwald-Baar Clinic, Klinikstr. 11, 78052 Villingen-Schwenningen, Germany

This chapter is originally published in the journal of Analytical and Bioanalytical Chemistry (https://doi.org/10.1007/s00216-022-04107-2) as

Bassler, M.C., Rammler, T., Wackenhut, F. et al. Accumulation and penetration behavior of hypericin in glioma tumor spheroids studied by fluorescence microscopy and confocal fluorescence lifetime imaging microscopy. Anal Bioanal Chem 414, 4849–4860 (2022). https://doi.org/10.1007/s00216-022-04107-2, © 2022 Springer Nature Switzerland AG.

Reproduced with permission from Springer Nature.

6.1 Abstract

Glioblastoma WHO IV belongs to a group of brain tumors that are still incurable. A promising treatment approach applies photodynamic therapy (PDT) with hypericin as a photosensitizer. To generate a comprehensive understanding of the photosensitizer-tumor interactions, the first part of our study is focused on investigating the distribution and penetration behavior of hypericin in glioma cell spheroids by fluorescence microscopy. In the second part, fluorescence lifetime imaging microscopy (FLIM) was used to correlate fluorescence lifetime (FLT) changes of hypericin to environmental effects inside the spheroids. In this context, 3D tumor spheroids are an excellent model system since they consider 3D cell-cell interactions and the extracellular matrix similar to tumors *in vivo*. Our analytical approach considers hypericin as probe molecule for FLIM and as photosensitizer for PDT at the same time, making it possible to directly draw conclusions of the state and location of the drug in a biological system. The knowledge of both, state and location of hypericin, just makes a fundamental understanding of the impact of hypericin PDT in brain tumors possible. Following different incubation conditions, the hypericin distribution in peripheral and central cryosections of the spheroids were analyzed. Both, fluorescence microscopy and FLIM, revealed a hypericin gradient towards the spheroid core for short incubation periods or small concentrations. On the other hand, a homogeneous hypericin distribution is observed for long incubation times and high concentrations. Especially, the observed FLT change is crucial for the PDT efficiency, since the triplet yield, and hence the O_2 activation, is directly proportional to the FLT. Based on the FLT increase inside spheroids, an incubation time > 30 min is required to achieve most suitable conditions for an effective PDT.

6.2 Introduction

Cancer is still one of the most threatening diseases of humankind. In 2020, 19.3 million new cancer cases were diagnosed worldwide [328]. Promising therapeutic and treatment approaches are constantly being developed to prolong the patient’s life and hopefully allow a complete cure. One of these auspicious treatments is photodynamic therapy (PDT) using various photosensitizers, including hypericin [329] that was already characterized chemically [162] and optically [330-333]. In PDT, photosensitizers that enter the excited triplet state upon irradiation either damage the biological substrate directly or generate reactive oxygen species inducing photodamage [165]. So far, PDT with hypericin has been applied to several cancer types, including dermal, colon and bladder cancer [334,335]. However, its applicability in glioma tumor treatment necessitates further research.

Most hypericin PDT applications are often tested in 2D cell cultures *in vitro* [336] after hypericin treatment of the cells. Various studies in cell monolayers showed that hypericin is mainly enriched in the endoplasmic reticulum or Golgi apparatus [64,337], others also observed hypericin accumulation in mitochondria or lysosomes [338]. This localization was proven to be dependent on incubation time of hypericin [338]. Cellular uptake mechanisms of hypericin in monolayer experiments were discussed to be either an energy-dependent uptake, e.g. by receptor-mediated endocytosis / pinocytosis [339], or passively driven by diffusion through the cell membrane [340]. Compared to 2D cell cultures, tumor spheroids are a more representative *in vitro* model, since they better reflect 3D cell-cell interactions and the extracellular matrix (ECM) of tumors *in vivo* (Fig. 6.1) [341]. Due to a decreasing nutrient and oxygen supply towards the spheroid center, tumor spheroids can be differentiated into three zones: a proliferative zone at the spheroid's margin, a transitional zone of quiescent cells and a necrotic core [342]. Differences between these zones can be ascribed to the cell cycle, as proliferative cells participate in the cell cycle and quiescent cells have left it. Hence, the response of a drug can directly be linked to the cell cycle state of the tumor cells within each zone [343]. Often, a higher response of anticancer drugs was detected in proliferative compared to quiescent cells that are less targeted by the drugs [344]. The drug response can further depend on microenvironmental conditions, like hypoxia, acidosis, complex tumor cell-cell interactions or the ECM constituents [345], which can be perfectly studied with tumor spheroid models.

The analysis of drug-spheroid interactions is useful for a successful therapeutic implementation, as shown in several studies [346], but only a small number of studies were performed on spheroids and hypericin [347-350]. In this context, the distribution and localization of the drug as well as the cellular uptake and transfer by the tumor spheroids are important [351]. Huygens et al. investigated hypericin penetration in bladder spheroids relating to the expression of E-cadherin, a cell molecule contributing to cell-cell adhesion [349]. An additional study involving bladder spheroids concluded that the ECM might also contribute to the hypericin penetration and in this case limit the hypericin intake [348]. Hypericin's lipophilicity and binding ability to surrounding lipoproteins additionally influence its accumulation and permeation behavior [352]. A deep understanding of these intake and penetration mechanisms in spheroids is essential to realize its full potential for PDT.

An additional impact on PDT performance is expected to result from different local cellular environments throughout tumors and tumor spheroids, caused by the changing availability of nutrients, oxygen and glucose [346,353]. Based on the prevalent conditions, like hypoxia or starvation, within spheroids, cells can react differently in terms of metabolism, gene and protein expression [354,355], which might directly influence not only the hypericin accumulation, but also the effectiveness of PDT. A powerful tool to detect these cellular, environmental variations is fluorescence lifetime imaging microscopy (FLIM). In FLIM, the excited state decay rate of a probe molecule, represented by the fluorescence lifetime (FLT), is measured with the spatial resolution of a confocal microscope and can be related to the local cellular environment [92]. Several studies used FLIM to measure FLT changes of NAD(P)H in 2D and 3D cell culture systems [356,357] or to reveal the cell cycle S-phase of spheroids [358]. Recent single molecule studies of hypericin show that the local environment has a strong influence on its FLT [330,332]. However, applications of FLIM with hypericin in general and especially in a cellular context are rare. Nevertheless, FLIM was used to analyze the hypericin release from nanocarriers or pharmaceutical preparations into the intracellular environment [359] and the interaction and localization of hypericin in cells [360,361]. For this reason, FLIM with hypericin can be used to investigate microenvironmental effects within tumor spheroids, particularly regarding the application of PDT. The obtained knowledge about the cellular environment is essential for the adaptation and optimization of the PDT treatment.

In our study, we use fluorescence microscopy and FLIM to investigate hypericin within glioblastoma tumor spheroids. Fluorescence microscopy allows us to study the accumulation and distribution of hypericin to better understand the extent and dynamics of its penetration into glioma spheroids. Additional analyses of spheroids by FLIM enable the detection of cellular environmental effects due to hypericin FLT changes, from which valuable information about prevalent cellular conditions can be deduced. Since hypericin functions not only as probe molecule for FLIM, but is considered as photosensitizer for PDT at the same time, the detailed analysis of hypericin's localization and its environmental characterization in the glioma spheroids allow us to understand the impact of both parameters on the hypericin PDT for brain tumors. For our investigations, spheroids are treated for variable incubation times and with different incubation concentrations to examine hypericin uptake, permeation and FLT. For each incubation condition, spheroid cryosections are prepared and outer and inner sections are compared to study local differences. Our results generate a fundamental understanding of photosensitizer interactions with tumor spheroids as complex biological systems. This knowledge delivers vital information to improve PDT efficiency in tumors and is applicable to other photosensitizers used for PDT treatment.

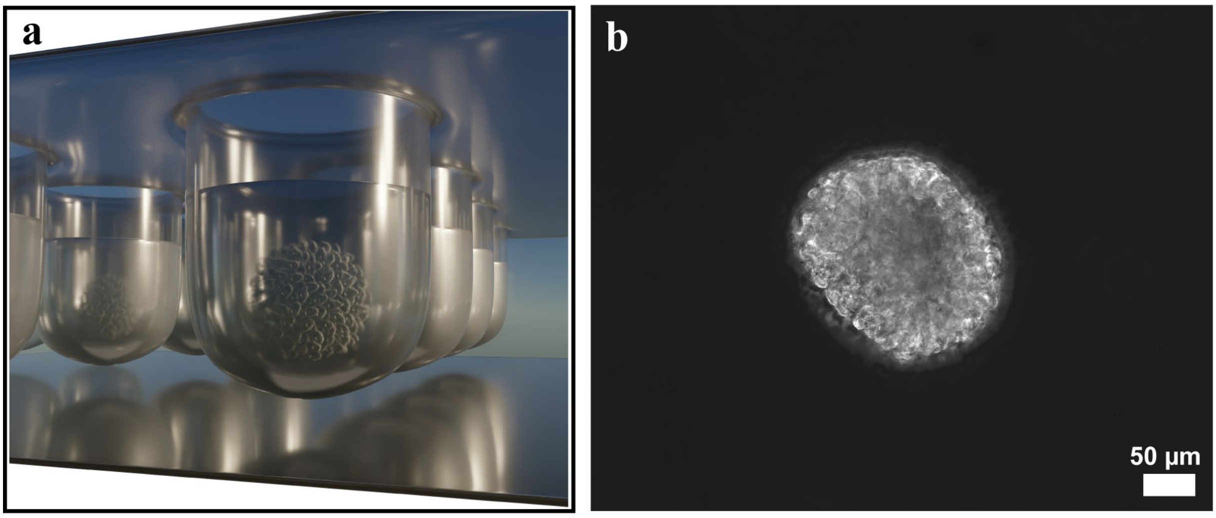

Figure 6.1. *(a) Schematic illustration of tumor spheroid formation in a 96-well plate by the forced-floating method. Due to a cell-repellent coating inside the well, the included cell suspension is forced to agglomerate to a spheroid. Additionally, the round bottom of the cavities promotes and accelerates the formation of spherical tumor clusters in reproducible size and shape. (b) Phase contrast image of a U-87 MG tumor spheroid with a seeding density of 1500 cells/cm^2 and a cultivation time of 35 h + 15 min.*

6.3 Materials and Methods

6.3.1 Cell Culture

Tumor spheroids derive from the glioblastoma cell line U-87 MG (ATCC® HTB 14™). U-87 MG spheroids were generated and cultivated in round-bottom, cell-repellent 96-well plates for 24 h (Greiner bio One) at a density of 1500 cells/cm^2 using the forced-floating method (Fig. 6.1a). Eagle's Minimum Essential Medium (MEM, no glutamine and phenol red, Gibco™) serves as cultivation medium and is supplemented with 10 % fetal bovine serum (FBS), 1 % L-glutamine, 1 % sodium pyruvate and 1 % penicillin-streptomycin (all purchased from Gibco™). Cultivation conditions for the U-87 MG spheroids encompassed 37 °C and a 5 % CO_2 atmosphere.

6.3.2 Hypericin Incubation for Different Incubation Times and Concentrations

All preparation steps were performed in the dark. Stock solutions of hypericin (PhytoLab GmbH & Co.KG) in DMSO (Molecular Probes™ D12345) with concentrations of 0.1 mM, 0.25 mM, 0.125 mM, 0.05 mM and 0.005 mM were prepared and frozen at -20 °C. Aliquots of this stock were freshly thawed for each experiment. After thawing, a 1:100 dilution of hypericin (1 µM, 2.5 µM, 1.25 µM, 0.5 µM, 0.05 µM) in complete cultivation medium and additional 10 % FBS was prepared. This procedure was adopted from [339]. Excess medium was removed from each single well and the hypericin/MEM mixture was added at a final concentration of 1 µM for incubation time experiments. Spheroids were incubated for 5 min, 30 min, 125 min, 10h + 30 min and 35h + 15 min in the hypericin cultivation medium, respectively. Varying hypericin concentrations (2.5 µM, 1.25 µM, 0.5 µM, 0.05 µM) were incubated for a predefined time period of 30 min. Non-hypericin-incubated control spheroids were treated with a 1:100 dilution of DMSO in complete cultivation medium and additional 10 % FBS for 30 min. Afterwards, the hypericin and control incubation were disrupted by removing the incubation medium and applying three washing steps with phosphate buffered saline (PBS). Following the washing steps, U-87 MG spheroids were directly preserved by fixation. All experiments were executed in triplicate.

6.3.3 Spheroid Fixation and Nucleus Staining

All preparation steps were performed in the dark. PBS of the spheroid washing steps was discarded, followed by a formaldehyde fixation (ROTI®Histofix 4 %) with an incubation time of 30 min. Afterwards, the fixation solution was removed, and spheroids were washed three times with PBS. For cell nucleus staining, Hoechst 33342 was used as fluorescence dye (NucBlue™ Live ReadyProbes™ Reagent (Hoechst 33342), Invitrogen™). The Hoechst 33342 solution was diluted in PBS according to the NucBlue Reagent protocol. This dilution was added to each U-87 MG spheroid and incubated for 20 min at room temperature. Nucleus staining with Hoechst 33342 was not performed for FLIM. After fixation and Hoechst 33342 incubation, a series of three PBS washing steps was applied. Fixed tumor spheroids were stored in PBS in the dark until microtome sectioning.

6.3.4 Spheroid Sectioning

For preparation of microtome sections, tumor spheroids were embedded in the cryoembedding medium OCT (Optimal cutting temperature compound, Sakura Finetek™ Tissue-Tek™ O.C.T. Compound). Each spheroid was transferred into one embedding mold filled up with OCT and quickly cooled down with dry ice to prevent water crystal formation. The frozen OCT blocks were cut with a cryomicrotome (Leica CM3050 S cryostat) and cryosections of 5 µm thickness were produced. Temperatures of the cooling chamber and the sample holder were kept at -30 °C. Subsequent cutting series of the whole spheroids were manufactured to obtain outer and inner sections of the tumor spheroids. All cutting sections were placed onto a coverslip and stored in the dark for further microscopic imaging experiments.

6.3.5 Fluorescence and Brightfield Microscopy

Acquisition of fluorescence images was performed with a Zeiss Axio Observer.Z1 fluorescence microscope equipped with a mercury short arc lamp (HXP 120) and colored LEDs (Colibri light source, Zeiss). For the fluorescence excitation of Hoechst 33342, a Colibri LED with 385 nm was used. The corresponding filter cube (Zeiss filter set 49) had an excitation wavelength range of 335 – 383 nm, whereas emission was detected between 420 – 470 nm. LED intensity was set to 70 % and the exposure time for one Hoechst image was 250 ms. Hypericin fluorescence was excited with the HXP 120 lamp in a filter wavelength region of 580 – 604 nm and fluorescence emission was detected between 615 nm and 725 nm (Zeiss filter set 71). The HXP 120 lamp intensity was defined at the highest intensity level and fluorescence images were acquired with 150 ms per image. All fluorescence images were recorded with a 20x objective (Zeiss Plan-Apochromat 20x/0.80, Ph 2, M27) and fluorescence detection was conducted with an Axiocam 506 microscope camera. Tumor spheroid sections were imaged by z-stacking. Subsequent image processing entailed the application of the Extended depth-of-field fusion algorithm using wavelet transform in order to obtain a sharp composite image (Zeiss ZEN 2.3 software, blue edition). Brightfield microscopy was accomplished with a second Zeiss Axio Observer microscope (Z1/7) using a white light LED. All brightfield images were recorded with a 20x objective (Zeiss LD A-Plan 20x/0.35, Ph 1) and an Axiocam 305 microscope camera. White light LED intensity was set to 11.5 % and exposure times per image were equal to 18 ms.

6.3.6 Fluorescence Lifetime Imaging Microscopy

The time resolved confocal fluorescence microscope was custom built. The used light source was a pulsed laser diode (LDH P-C-405, PicoQuant GmbH, Germany) with an excitation wavelength of 405 nm and at a repetition frequency of 40 MHz. The pulse duration was 50 ps. The beam was focused on the sample by an oil immersion objective lens (Zeiss Plan-Apochromat, 100x, 1.4 Oil DIC, Carl Zeiss AG, Germany). An additional long-pass filter (EdgeBasic™ Long Wave Pass 405) separated the excitation light from the sample emission. Confocal imaging was achieved using a single photon avalanche diode (SPAD; PDM series, Micro Photon Devices, Italy). By coupling the SPAD with a time-correlated single photon counting (TCSPC) unit (HydraHarp 400, PicoQuant GmbH, Germany) and the pulsed laser diode, time resolved measurements were performed. The scanning stage, SPAD, laser diode and TCSPC unit were controlled by SymphoTime® software (PicoQuant GmbH, Germany). Time resolved measurements were also analyzed and evaluated with the SymphoTime® software.

6.3.7 Fluorescence Spectra Acquisition

Fluorescence spectra were recorded using a spectrometer (Acton SP300i, Princeton Instruments, USA) with a thermoelectrically cooled CCD camera (PIXIS 100, Princeton Instruments, USA). The wavelength range of the spectrometer was set to 480 – 760 nm. A long pass filter (EdgeBasic™ Long Wave Pass 405) was applied to remove the laser signal from the spectra. The acquisition time for each hypericin spectrum was 250 ms. Fluorescence spectra were acquired using Winspec® software (Princeton Instruments, USA).

6.4 Results

A first characterization of whole tumor spheroids was performed by fluorescence microscopy. Fig. 6.2a shows a fluorescence intensity image of a 5 min-incubated tumor spheroid before sectioning. Hypericin fluorescence is shown in red, whereas the nucleus staining with Hoechst 33342 is shown in blue. Based on these colors, cell nuclei and hypericin can be identified in the spheroids (Fig. 6.2a). Afterwards, cryosections were prepared to analyze and compare the spatial distribution of hypericin in outer and inner spheroid regions in more detail. Fig. 6.2b and 6.2c show fluorescence intensity images of outer and inner sections. As a consequence of spheroid cutting, section elongation, compression and regions without cells can occur. Thus, sections might appear differently shaped or patchy compared to whole spheroids. The technically limited size of the FLIM images (24 x 24 µm) required us to stitch together successive images to cover the entire width of the spheroid sections with FLIM and superimpose them on the respective brightfield images. Fig. 6.2d and 6.2e show the respective composite images.

In Fig. 6.2b, hypericin appears to be homogeneously distributed across the outer spheroid section after 5 min incubation, as visualized by the homogenous fluorescence intensity (Fig. 6.2b; red). For the inner section, hypericin was mainly accumulated in a peripheral zone of the section and only a small portion penetrated deeper towards the spheroid center (Fig. 6.2c; red). All observations are corroborated by the single channel fluorescence images in Fig. S6.1 (A5, Appendix). Control experiments on spheroids without hypericin incubation only reveal the fluorescence intensity of the cell nuclei across the sections (Fig. S6.2a, SI, blue, A5, Appendix).

FLIM composite images show a mostly uniform spatial distribution of hypericin FLTs (3.5 ns) throughout the outer section (Fig. 6.2d). Contrarily, the inner section revealed an FLT gradient across the section. The spheroid edge exhibits an FLT of 3.5 ns, which decreases to 2.5 ns towards the center of the spheroid. As both the hypericin FLT and its intensity are detected simultaneously, these experiments additionally confirm the results obtained by fluorescence microscopy. Although similar trends of hypericin fluorescence intensity and FLT are observable, reasons for both are different since FLTs are concentration-independent, but strongly influenced by the cellular environment [92,362,363]. For this reason, hypericin FLTs are used to deduce microenvironmental effects inside the spheroids. FLTs of non-hypericin-treated control spheroids are below 2.5 ns throughout the sections, resulting from the autofluorescence of the spheroids. This represent the untreated spheroid constitution (Fig. S6.2b, SI, A5, Appendix).

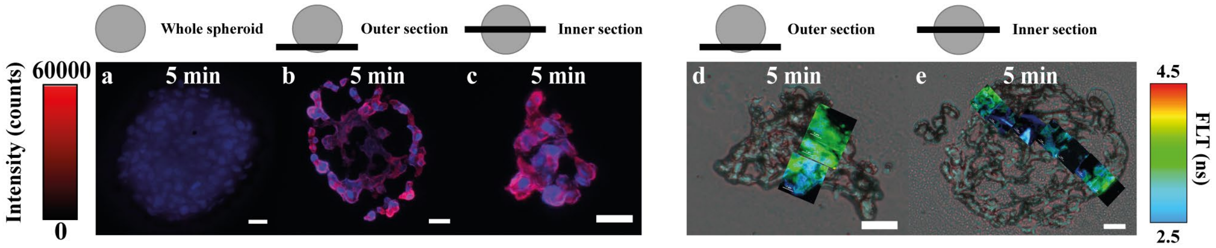

Figure 6.2. Investigation of hypericin penetration into spheroids by comparing outer and inner spheroid sections. The penetration was examined with fluorescence microscopy and FLIM for an incubation time of 5 min. Fluorescence images of the whole spheroid (a) and spheroid sections (b, c) are displayed. The fluorescence intensity of Hoechst in the nuclei (blue) and hypericin fluorescence (red) are superimposed in (a c). The outer section reveals a homogeneous hypericin intensity (red) throughout the section compared to the inner one (b, c). In the inner section, an intensity gradient is observed (c). All fluorescence images have scale bars of 25 µm. To represent FLTs across the sections, FLIM images (24 x 24 µm) are superimposed on corresponding brightfield images to generate a composite image (d, e). Scale bars of the brightfield images represent 25 µm. Hypericin FLTs vary between 3.5 – 2.5 ns depending on the position inside the spheroid (peripheral to central area). An FLT gradient can be observed from the spheroid outside (3.5 ns) to the inside (2.5 ns) (e).

This behavior of hypericin in varying spheroid layers points to a difference in uptake and transfer inside the spheroid, which most likely depend on the hypericin incubation concentration. This was successfully shown in fluorescence images of four different hypericin concentrations with a constant incubation time of 30 min, summarized in Fig. 6.3.

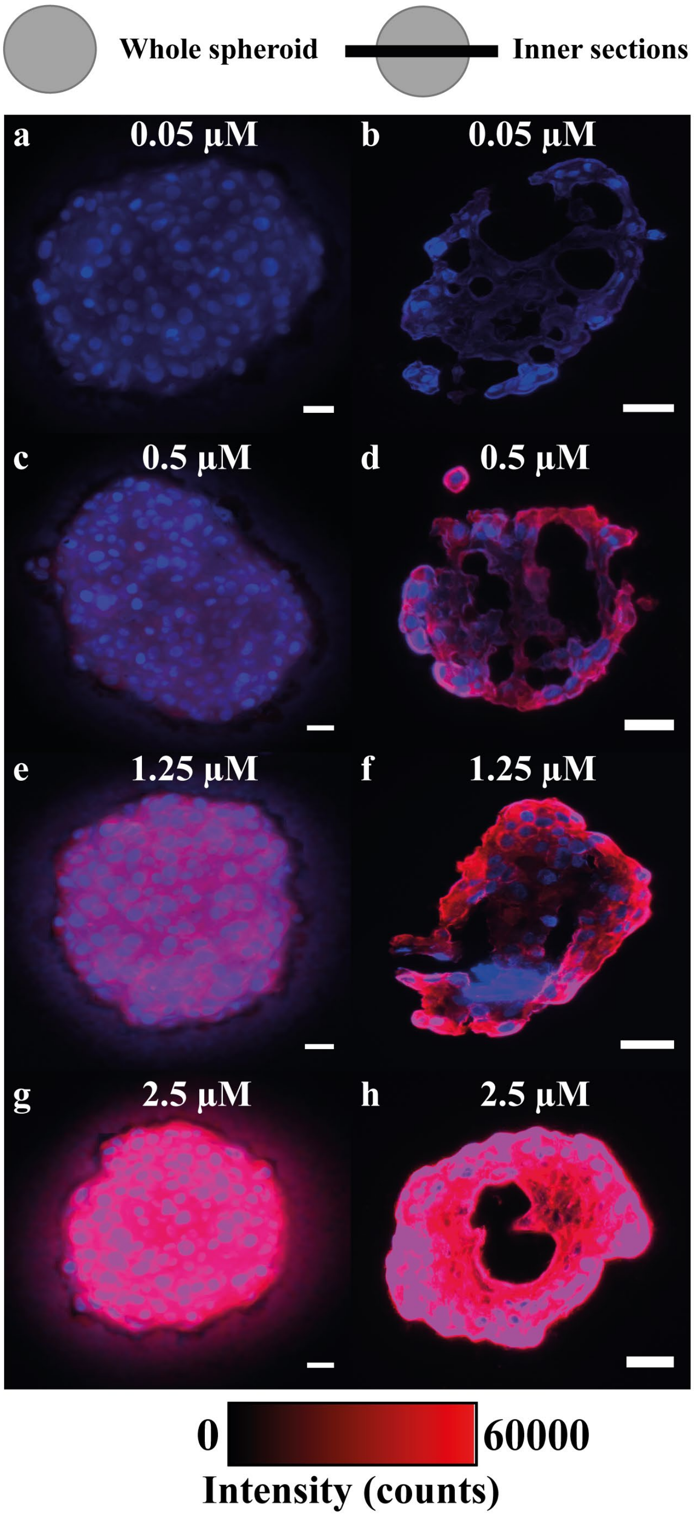

Figure 6.3. *Influence of different incubation concentrations on hypericin uptake and penetration, investigated by fluorescence microscopy. Fluorescence images of whole spheroids, incubated with different hypericin concentrations (0.05 µM, 0.5 µM, 1.25 µM, 2.5 µM) for 30 min, are illustrated in (a), (c), (e) and (g). Corresponding fluorescence images of their inner sections are displayed in (b), (d), (f) and (h). The Hoechst fluorescence intensity in the nuclei (blue) proves cell occurrence throughout the whole spheroids. Hypericin fluorescence intensity (red) of whole spheroids increases with larger incubation concentrations (a, c, e, g). As shown by the inner sections, an increase in incubation concentration also results in a higher internal intensity, at least partly, in an annular area at the sections edges (b, d, f, h; red). Intensity gradients occur for all investigated concentrations (b, d, f, h), although hardly visible for the 2.5 µM incubation concentration (h). The scale bars of all fluorescence images are 25 µm.*

This incubation time was chosen to guarantee a sufficient hypericin amount for fluorescence microscopy, especially at low incubation concentrations. Again, whole spheroids were analyzed prior to cryosectioning (Fig. 6.3; a, c, e, g). As illustrated by the Hoechst staining, cell nuclei are evenly distributed throughout the tumor spheroids (Fig. 6.3a, c, e, g; blue). Additionally, the fluorescence intensity of hypericin continuously increases with increasing incubation concentration (Fig. 6.3a, c, e, g; red). Inner sections were prepared to investigate the accumulation and permeation of hypericin inside the spheroids as a function of incubation concentration and are shown in Fig. 6.3b, d, f, h. Incubation concentrations of 0.05 µM, 0.5 µM and 1.25 µM show an annular accumulation of hypericin in the outer regions of the spheroid sections (Fig. 6.3b, d, f; red). Additionally, intensity gradients of hypericin occur towards the spheroid center (Fig. 6.3b, d, f; red). Although weak, the fluorescence of hypericin at the core is still detectable for these incubation concentrations. The presence of hypericin in central areas was proven by corresponding single channel images in Fig. S6.3, SI (A5, Appendix) and in spectral line scans in Fig. S6.4, SI (A5, Appendix). Incubation with a 2.5 µM hypericin solution caused a high hypericin uptake, indicated by the high fluorescence intensity (Fig. 6.3h; red). Although hypericin seems to be almost uniformly spread across the whole inner section (Fig. 6.3h; red), an intensity gradient is also observable, as was confirmed by the single channel images in Fig. S6.3, SI (A5, Appendix). Most pronounced fluorescence intensities of hypericin are observed throughout the section for this incubation concentration. Two large holes, caused by the cutting procedure, preclude the innermost hypericin concentration of this section from analysis.

Besides the impact of concentration, the duration of hypericin incubation should also influence its uptake, distribution and FLT inside the spheroids. For this purpose, tumor spheroids were incubated for five different incubation periods (5 min, 30 min, 125 min, 10 h + 30 min and 35 h + 15 min), using a 1 µM hypericin solution. This concentration was chosen to guarantee a sufficient hypericin amount, especially at short incubation times, for fluorescence microscopy. Fluorescence intensity and FLIM composite images for inner spheroid sections after different hypericin incubation periods are depicted in Fig. 6.4.

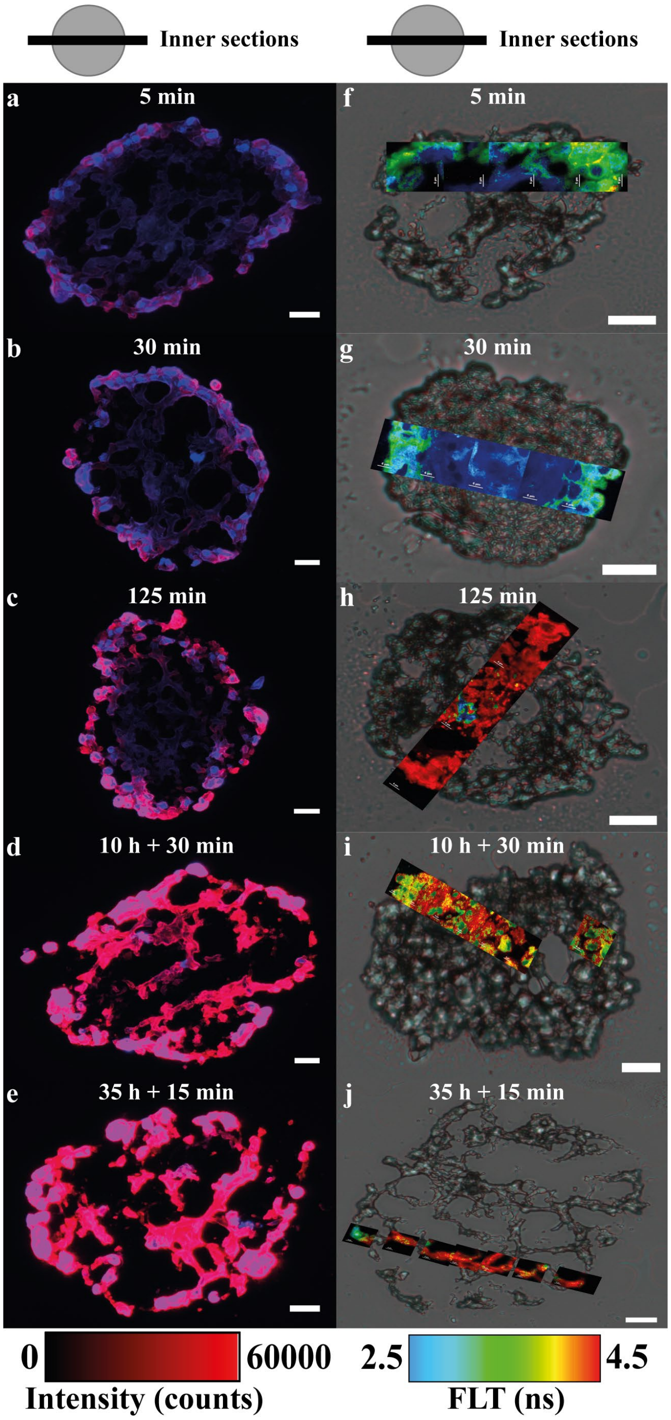

Figure 6.4. *Impact of different incubation times on hypericin at the spheroid center, examined by fluorescence microscopy and FLIM. Inner sections of the spheroids were investigated by both techniques after incubation times of 5 min, 30 min, 125 min, 10h + 30 min and 35h + 15 min, respectively. Cell nuclei were identified by their blue Hoechst fluorescence (a-e). Fluorescence images of the sections reveal hypericin intensity gradients (red) for a 5 min, 30 min and 125 min incubation, with decreasing intensity towards the core (a-c). An evenly distributed hypericin fluorescence intensity is observed for long incubation times of 10h + 30 min and 35h + 15 min (d, e). Additionally, a larger amount of hypericin penetrates deeper into the spheroid at longer incubation times. Overall, an increasing hypericin fluorescence intensity (red) is observed for increasing incubation times (a-e). The scale bars of all fluorescence images are 25 µm. Composite images were again generated by combining FLIM images (24 x 24 µm) and corresponding brightfield images (f-j). Corresponding scale bars of the brightfield images also equal 25 µm (f-j). Composite FLIM images show a FLT range of 2.5 – 4.5 ns for hypericin throughout the inner sections of the tumor spheroids (f-j). Gradients of hypericin FLT appear for short incubation times (f, g), whereas a mostly homogeneous FLT distribution occurs at longer incubation times (h-j).*

A comparison of inner and outer sections is shown in Fig. S6.5, SI (A5, Appendix). FLIM images are again combined with the related brightfield image to create a composite image. Shorter incubation times

(5 min, 30 min, 125 min) caused a mainly peripheral hypericin accumulation within the inner section, as can be observed by the higher hypericin fluorescence intensity in this area (Fig. 6.4a c). At the center of the tumor spheroid, only a weak hypericin fluorescence intensity is observed, indicating a small hypericin enrichment (Fig. 6.4a c). Thus, a similar penetration gradient is noticeable, as previously determined for different incubation concentrations (Fig. 6.3b, d, f). At even longer incubation times (10 h + 30 min and 35 h + 15 min), the uniform fluorescence intensity shows that hypericin is homogeneously accumulated throughout the whole tumor section (Fig. 6.4d, e).

FLIM composite images of the 5 min and 30 min incubations revealed a FLT gradient towards the center of the spheroid's inner sections (Fig. 6.4f, g). Here, the FLT drops from 3 – 3.5 ns in the outer region to 2.5 ns towards the central area of the sections. However, this gradient is not caused by the hypericin concentration gradient observed in the fluorescence intensity image, but by alterations of the cellular microenvironment. For longer incubation times (125 min, 10h + 30 min, 35h + 15 min), the FLTs of hypericin increase to 3 – 4.5 ns with small areas exhibiting shorter FLTs (2.5 – 3 ns). Compared to the 5 min and 30 min incubations, no FLT gradient can be observed. Instead, a more homogenous FLT is detected across the spheroid sections (Fig. 6.4h, i, j). Although similar trends of hypericin fluorescence intensity and FLT are observable, reasons for both are different since FLTs are concentration-independent, but strongly influenced by the cellular environment [92,362,363]. For this reason, hypericin FLTs are used to deduce microenvironmental effects inside the spheroids.

In general, the observed FLT change could occur due to chemical modifications, e.g. deprotonation or isomerization, of hypericin [364,365,331]. In order to exclude such effects, fluorescence spectra of hypericin are shown in Fig. 6.5a as line scans across inner spheroid sections and no alteration of the emission spectra can be observed throughout the sections.

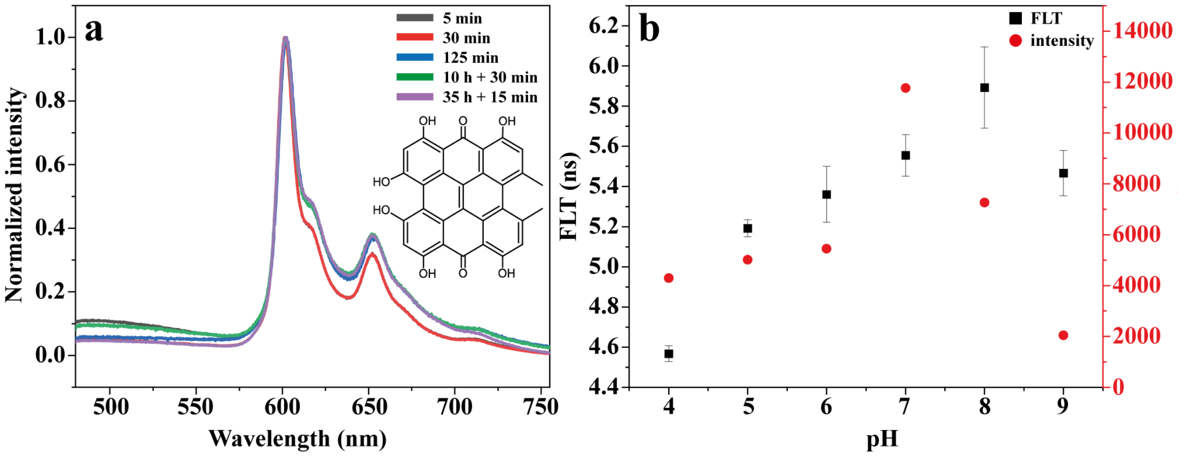

Figure 6.5. *Hypericin fluorescence spectra of inner spheroid sections treated for different incubation times (a) and FLTs as well as hypericin maxima intensities depending on pH (b). In (a): Fluorescence spectra are averaged line scans across the sections and normalized to maximum intensity. In (b): FLTs of hypericin and maximum intensities of the 1st hypericin fluorescence maximum (600 nm) are shown for different pH levels (pH 4 – 9). The largest hypericin FLT of 5.9 ns appears at pH 8, whereas the lowest FLT of 4.5 ns is observed at pH 4. In comparison to FLTs, the highest intensity was measured at pH 7 and the lowest at pH 9.*

The measurement of line scans additionally confirmed the presence of hypericin all over the sections (Fig. 6.5a). This was also particularly demonstrated in 2D surface plots for the 5 min incubation in Fig. S6.4, SI (A5, Appendix). Hence, a chemical reaction leading to hypericin degradation is unlikely. One factor that potentially impacts hypericin FLTs, is the pH, which also shows a gradient towards the spheroid core [366]. Therefore, we investigated FLTs of hypericin in incubation media with different pH levels (pH 4 – 9). The result is shown by the black squares in Fig. 6.5b. The physiological pH of the hypericin incubation medium is 8, here the largest hypericin FLT of 5.9 ns can be observed (Fig. 6.5b, black squares). Decreasing the pH value down to a value of 4 leads to a decrease of the hypericin FLT to 4.5 ns. However, an increase of the pH value to 9 also reduces the hypericin FLT to 5.5 ns (Fig. 6.5b, black squares). Besides the influence on the FLT, the pH also influences the fluorescence intensity, which is presented as red circles for the emission maximum at 600 nm (Fig. 6.5b). Corresponding fluorescence spectra at different pH levels are illustrated in Fig. S6.6, SI (A5, Appendix). The highest fluorescence intensity at 600 nm is observed at pH 7, whereas the smallest one can be identified for pH 9. Between pH 4 – 6, the fluorescence intensity does hardly change, as reported in literature [367]. Comparable trends of the FLT and the maximum intensity can be observed and highest values for both appear in a physiological pH range of 7 – 8, decreasing for either lower or higher pH values (pH 4 – 6, pH 9).

6.5 Discussion

The uptake and the accumulation of hypericin inside U-87 MG glioblastoma cell spheroids using fluorescence microscopy was studied. All results presented by fluorescence microscopy reveal two major phenomena. First, a hypericin gradient is formed from outer to inner spheroid regions for low incubation concentrations or short incubation times, causing an increased hypericin accumulation at the spheroid edge (Fig. 6.2, Fig. 6.3, Fig. 6.4, Fig. S6.1, S6.4, SI, A5). Second, hypericin distributes homogeneously throughout the spheroids for long incubation periods or high concentrations (Fig. 6.2, Fig. 6.3, Fig. 6.4, Fig. S6.1, S6.4, SI, A5). Several effects might be responsible for this accumulation and penetration behavior [347,350]. Hypericin uptake could be affected by the different spheroid zones, as the drug response can be associated with the cell cycle state that differs in each zone [343]. In the proliferative region, cells pass through the whole cell cycle and are thus more susceptible for drugs, whereas in quiescent areas, cells have left the cell cycle and are consequently less targeted [344]. Thus, the hypericin gradient could be directly related to the cell cycle state. Additionally, metabolic activity also differs between the zones and thus either an active or passive uptake mechanism might be dominant. At the outer spheroid region, an actively-driven intake of hypericin due to high cell viability is conceivable, which proceeds to a passive permeation as the metabolic activity decreases in deeper cell layers. These effects can also explain the hypericin fluorescence gradient, as the hypericin concentration continuously decreases between adjacent cell layers due to an inward passive diffusion. With increasing incubation times and concentrations, passive diffusion could cause a larger amount of hypericin to penetrate deeper into the spheroids, as was observed by its homogenous distribution for these incubation conditions. Besides, spheroid-related features, such as cell-cell contacts, ECM [348], and protein activity, e.g. for E-cadherin / P-glycoproteins, might additionally influence hypericin penetration [349]. In any case, we expect passive diffusion of hypericin to be the transfer principle in the necrotic core. Comparable to our results, a similar uptake behavior was also observed for bladder spheroids [347].

In addition to fluorescence microscopy, FLIM was applied to study hypericin FLT differences, which allow to draw conclusions about the cellular environment within spheroids [368]. Compared to the FLT of hypericin on glass (6.34 ± 2.98 ns) or in PVA (4.23 ± 0.89 ns) [330], FLTs are overall shorter in tumor spheroids (2.5 – 5 ns). This only partially correlates with the refractive indices predominant in cells (nucleus: 1.355–1.365, cytosol: 1.360–1.390, mitochondria: 1.400–1.420) [369]. Since cellular refractive indices are similar to the one of PVA (1.48), comparable hypericin FLTs of approx. 4 ns would be expected [370,371]. However, most hypericin FLTs in spheroid sections are below 4 ns, so additional factors must be considered. As FLTs are independent of local probe concentration [362], the observed FLT gradients do not result from different hypericin concentrations across the spheroid. Instead, FLTs are strongly dependent on the microenvironment, including the pH level. Based on the spheroid's structure, a diminished supply with nutrients / oxygen [372] and a hampered removal of metabolic waste [346] cause hypoxia in the core and the lactate production increases [366,373]. This leads to a lactate-induced acidosis and the pH decreases towards the spheroid center (pH 6 – 7) [366]. Therefore, the pH inside the spheroid can affect the FLT of hypericin. Fig. 6.5 clearly demonstrates that a decreasing pH is accompanied by a decline in hypericin FLT, which can, at least partly, explain the FLT gradients for short incubation times. However, the FLT decrease is larger and the average FLT is smaller in the spheroids than the ones observed in Fig. 6.5b, hence additional parameters need to be considered. Associated with hypoxia and acidosis, cellular metabolism changes in deeper spheroid layers, where lactate serves as an alternative substrate for ATP synthesis [374]. The altered metabolism inside the spheroids might also cause a change in microenvironment and thus influence the FLT gradient for short incubation periods. Therefore, hypericin FLTs could be utilized to reveal metabolic activity inside spheroids. However, these assumptions only seem to be true for hypericin-treated spheroids for short incubation times (5 min, 30 min). For long incubation times, a homogeneous FLT distribution with no gradient towards the center can be observed. However, the FLT is decreased in the outer layers compared to inner ones (Fig. 6.4i, Fig. S6.5s, t, SI, A5). In part, this is also observed for the 35 h + 15 min incubation in Fig. 6.4j. In general, FLTs are independent of the probe concentration [362], but this is not true for excessively high concentrations, where most molecules are agglomerated [361]. Non-fluorescent hypericin aggregates are formed, that cause fluorescence self-quenching and decrease the FLT at the spheroids edge. The impact of fluorescence quenching, however, might not be sufficient to describe the FLT behavior completely. The occurrence of intermolecular FRET from hypericin monomers to aggregates [361] or hypericin-hypericin excimer-like interactions [375] could additionally contribute to the FLT decrease at the spheroid's margin. Additionally, the incubation time was shown to alter the hypericin accumulation in cell organelles, causing a shift of the primary accumulation site from mitochondria to lysosomes for U-87 MG monolayers after 6 h (500 nM) [338]. Hypericin-enriched lysosomes (2 h incubation, 2.5 µM) in U-87 MG were also observed in our experiments (data not shown). In spheroids, the outer regions are incubated comparatively longer than inner ones as hypericin permeates towards the core. Thus, hypericin might predominantly accumulate in lysosomes of the outer spheroid layers, whereas it is mostly located in mitochondria in the inner spheroid. Furthermore, the metabolic activity is increased in the outer regions, which might also favor the redistribution of hypericin towards lysosome uptake. This lysosome enrichment can decrease the hypericin FLT due to an increased refractive index of 1.600 compared to 1.410 in mitochondria [369]. These effects, influencing the excited states lifetimes, have a direct impact on the PDT efficiency, since the triplet formation yield is directly proportional to the FLT [376]. Hence, long FLTs promote the transition to the triplet state, resulting in an increased O_2 activation and higher PDT efficiency. To achieve long FLTs inside glioblastoma spheroids, incubation times of at least 30 min are required to ensure appropriate conditions for PDT treatment.

6.6 Conclusion

In this study, we examined the accumulation and penetration behavior of hypericin in U-87 MG tumor spheroids and correlated FLT changes of hypericin to cellular, environmental conditions. Here, hypericin was simultaneously regarded as probe molecule for FLIM and as photosensitizer for PDT. Hypericin uptake and FLTs were studied in spheroid cryosections, as a function of hypericin concentration and incubation time. Low incubation concentrations and short incubation times caused an increased enrichment at the peripheral region of the spheroids with hypericin gradients towards the center. These FLT gradients were explained by pH or metabolism-associated influences, as the FLT is independent of the actual concentration for small hypericin concentrations. In this context, active or passive internalization mechanisms as well as other spheroid-related attributes are discussed to be the driving force in hypericin uptake and permeation. In contrast, high incubation concentrations and long incubation periods lead to a more homogeneous hypericin distribution throughout the spheroid. However, short FLTs in the peripheral spheroid regions were explained by agglomeration-based fluorescence quenching and possible FRET and excimer-like interactions as a consequence of excessive hypericin accumulation. A further explanation was deduced from the incubation-time-dependent enrichment of hypericin in different cell organelles. The knowledge about hypericin FLTs can be used to significantly influence PDT, since the triplet formation yield, and thus the O_2 activation, is directly proportional to the FLT. Hence, small FLTs after short incubations are indicative of an insufficient PDT inside tumor spheroids. Therefore, incubation times of at least 30 min are required to achieve an increased hypericin FLT within spheroids and thus improve the efficiency of PDT. Our findings reveal important insights concerning the localization and state of hypericin in an improved *in vitro* tumor model, which is essential in order to understand the effects of hypericin PDT for glioma tumors.

6.7 Acknowledgment

We would like to express our sincere thanks to Prof. Dr. Ralf Kemkemer and Prof. Dr. Petra Kluger (Reutlingen university) for support in the cell culture experiments. Furthermore, we thank Karen Ende (Reutlingen university) for cell biological input and her revision of the manuscript.

6.8 Declarations

Conflicts of interest/Competing interests: The authors declare nor conflict of interest.

Funding: This study was funded by the doctoral program of the University of Tübingen and Reutlingen University ‘‘Intelligente Prozess- und Materialentwicklung in der Biomateriomics (IPMB)’’, which is supported by the MWK Baden-Württemberg (PhD student fellowship to MCB).

Availability of data and material: The data sets generated and/or analyzed during the current study are not publicly available since they are part of an ongoing PhD thesis. However, the data sets are available from the corresponding authors on reasonable request.

7. Manuscript V: Investigation of Cell Death induced by Hypericin-based Photodynamic Therapy on Glioma Single Cells using Confocal Fluorescence Lifetime Imaging Microscopy

Miriam C. Bassler[1,2*], *Jonas Hiller*[2*], *Frank Wackenhut*[1**], *Sven zur Oven-Krockhaus*[2], *Rainer Ritz*[3], *Kai Braun*[2], *Alfred J. Meixner*[2], *Marc Brecht*[1,2**]

[1]Process Analysis and Technology (PA&T) Reutlingen University, Alteburgstr. 150, 72762 Reutlingen, Germany

[2]Institute of Physical and Theoretical Chemistry University of Tübingen, Auf der Morgenstelle 18, 72076 Tübingen, Germany

[3]Department of Neurosurgery, Schwarzwald-Baar Clinic, Klinikstr. 11, 78052 Villingen-Schwenningen, Germany

*These authors contributed equally to this work.

This chapter is prepared as a finished article for submission.

7.1 Abstract

Malignant primary brain tumors are a group of highly aggressive and often infiltrating tumors that lack of adequate therapeutic treatments to achieve complete tumor removal. Therefore, new therapeutic approaches are required to reach this goal. One promising possibility to eliminate remaining resection margins and infiltration branches is photodynamic therapy (PDT) with hypericin as photosensitizer, since hypericin can successfully pass the disrupted blood-brain-barrier (BBB) and is selectively accumulated in tumor tissue. Furthermore, hypericin offers outstanding photophysical characteristics that make it an excellent candidate for PDT. To investigate hypericin PDT as a treatment for primary brain tumors, a new approach using fluorescence lifetime imaging microscopy (FLIM) with three different fluorescence probes is accomplished. In this work, we show the PDT-induced photodamaging and dying steps of single, living glioma cells, as representative *in vitro* tumor model, especially for glioblastoma. Finally, this approach allows to draw conclusion on the cell death mechanism. Aside from hypericin as one of the used fluorescence probes, also resorufin and propidium iodide (PI) are deployed to uncover cellular changes and generate the required FLIM image contrast based on different fluorescence lifetimes (FLTs). Hypericin PDT and FLIM image acquisition are simultaneously induced by a single laser beam and sequences of FLIM images are recorded to analyze the PDT progression. FLIM observations are additionally corroborated by fluorescence spectra, which also greatly differ between the three fluorescence dyes. Additionally, we investigate the PDT progress for two irradiation laser wavelengths of 405 nm and 561 nm. The two wavelengths initiate a different hypericin excitation, but do not cause FLT changes for both. This study finally unveils new insights of hypericin PDT on the basis of single glioma cells and contribute to its successful implementation as therapy for primary brain tumors.

7.2 Introduction

Malignant primary brain tumors are one of the deadliest and most treatment-challenging cancers worldwide. They encompass different tumor types depending on the cellular origin [377] and are known to grow aggressively and infiltrating into surrounding healthy brain tissue [378,379]. Many of the emerging primary brain tumors are astrocytomas, of which glioblastoma is the most common representative [380,381]. According to the World Health Organization (WHO), it is classified as WHO grade IV astrocytoma due to its aggressive and fast growth and the high degree of tissue infiltration [382]. Until today, glioblastomas are not curable and require an elaborate treatment to improve the patient’s quality of life in their remaining survival time [383].

The established treatment of primary brain tumors includes an initial tumor resection in the course of a surgical procedure by using a fluorescence-supported tumor tissue visualization [384]. For this purpose, the patients are administered a fluorescence dye, which is able to pass the disrupted blood-brain-barrier (BBB) and become selectively accumulated in the brain tumor. A repetitive alteration of white light and dye-excitation light during surgery allows an improved recognition of the tumor tissue to be removed by the surgeon [385]. The application of 5-aminolevulinic acid (5-ALA), as a precursor fluorescence dye, has developed to be the gold standard for primary brain tumor surgery [386,387]. Its major advantage is its good water-solubility, which facilitates its implementation as pharmaceutical formulation, and thus its administration to the patient. After accumulating in the brain tumor, 5-ALA is enzymatically transformed into protoporphyrin IX (PPIX) [388], which is the actual fluorescence dye for tumor visualization. Brain tumor surgery is followed by a chemo- or radiotherapy to reduce tissue resection margins and thus enable an overall improved tumor removal [69,389]. However, these therapies are not capable to selectively treat tumor tissue and damage of healthy, surrounding brain tissue has to be tolerated. As a result, a high demand for therapeutic alternatives is essential, which do not lack in specificity.

One new therapeutic attempt was derived from 5-ALA / PPIX as already implemented fluorescence precursor / dye to be additionally deployed as photosensitizer in photodynamic therapy (PDT) [390]. In PDT, photosensitizers are excited upon light irradiation followed by a transition to the triplet state, which further reacts with biological substrates or surrounding oxygen to form highly reactive oxygen species (ROS) [391]. These species induce a high oxidative stress and finally a pronounced level of photodamage inside the cells that ends up in cell death. As 5-ALA and thus PPIX are specifically enriched in brain tumors, their application in PDT was expected to be a promising approach. Several studies were performed to investigate the potential of 5-ALA-PDT [392-394]. Eskiler et al. revealed the effectiveness of 5-ALA-PDT as breast cancer treatment [395], whereas its damaging capabilities were additionally demonstrated in rhabdomyosarcoma by Atif et al. [396]. Although photodamaging effects were achieved, they might not be effective enough to eliminate all remaining brain tumor parts [57]. For this reason, other photosensitizers are demanded that overcome this drawback.

One auspicious alternative as photosensitizer for PDT is hypericin, since it is also able to pass the disturbed BBB, but additionally has a high triplet quantum yield that allows an effective ROS formation [397,67]. Hypericin was shown to accumulate in the perinuclear region (Fig. 7.1a) in various tumor cell lines with main enrichment sites in the endoplasmic reticulum (ER), the Golgi apparatus, mitochondria and lysosomes [64,398,338]. This accumulation behavior has a major influence on PDT progression and might affect the actual dying mechanism. Additionally, hypericin uptake and distribution was also studied in some tumor spheroid models [90] followed by hypericin PDT in some cases [347]. To actually understand hypericin PDT, the mechanistical steps of the damaging and dying process need to be revealed. Cellular damage can follow a certain pathway until the cells are finally dead, which is very characteristic and can be assigned to concrete cell death principles. The two most common programmed cell deaths are apoptosis and necrosis [399,400], but are by far not the only ones present. Apoptosis can be triggered intrinsically via a mitochondrial pathway or extrinsically via external stimuli [400]. Depending on the pathway type, it undergoes a cascade of various protein or enzyme activations, including Bax, apoptotic protease, caspases or procaspase 8, that initiate the systematic progression of cellular degradation [400]. Typical morphological features of apoptosis are cell and nucleus shrinkage, nuclear chromatin condensation, nucleus break up and membrane blebbing [401,402]. Necrosis, however, is induced via caspases-independent pathways and shows a partly different morphological outcome, entailing bleb formation, cellular swelling, chromatin condensation and cellular lysis [403,404]. Further cell death mechanisms comprise ferroptosis or paraptosis as well as several hybrid forms, which are all either morphological or genetically distinguishable from one another [405,406]. So far, hypericin PDT was tested on umbilical vein endothelial, HepG2 and A431 human epidermoid carcinoma cells that displayed apoptosis to be the dominant cell death principle [407-409]. Others demonstrated necrosis to be the ongoing type of cell death mechanism in human colon adenocarcinoma HT-29 cells [410], whereas further studies identified paraptosis in OVCAR-5 cells as the underlying concept of cell death [72]. Glioma cell lines as *in vitro* brain tumor models were additionally investigated and treated with hypericin PDT, which initiates either apoptosis or necrosis as the primary cell death mechanism [411,339,412,47]. These studies were mainly performed with flow cytometry, confocal, conventional and total internal reflection fluorescence microscopy or biological assays. However, no fluorescence lifetime imaging microscopy (FLIM) investigation of hypericin PDT on glioma cells was yet performed to reveal their damage and death mechanism in a visualized and stepwise manner.

Our study deals with the investigation of hypericin PDT on single, living glioma cells in order to reveal the photodamaging progression and finally identify the type of cell death mechanism. For this purpose, we apply a completely new analyzing approach by using FLIM in combination with three different fluorescent probes: hypericin, resorufin and propidium iodide (PI). By applying FLIM, image contrast is achieved based on different fluorescence lifetimes (FLT) of the probes, which allow a clear distinction not possible by classical steady-state fluorescence spectroscopy. All three fluorescent probes have different FLTs, which allows to easily distinguish between them and monitor their different localization behavior (Fig. 7.1c). FLIM image acquisition and hypericin PDT are simultaneously initiated by a single laser beam and image sequences are recorded for single glioma cells. Hypericin PDT-induced photodamage and cell death are presented by a series of FLIM composite images, comprised of FLIM images superimposed on steady-state fluorescence images. This enables to deduce a semi-quantitative impression of the localization of the fluorescence probes inside the cell, represented by the intensity of false-color FLTs. The investigation of two varying laser wavelengths (405 nm and 561 nm) further unveils whether changes in hypericin PDT progression appear and if different morphological features of cell damage and death occur. Although two laser wavelengths are used and thus hypericin is excited differently, the obtained FLTs are unchanged for both wavelengths.

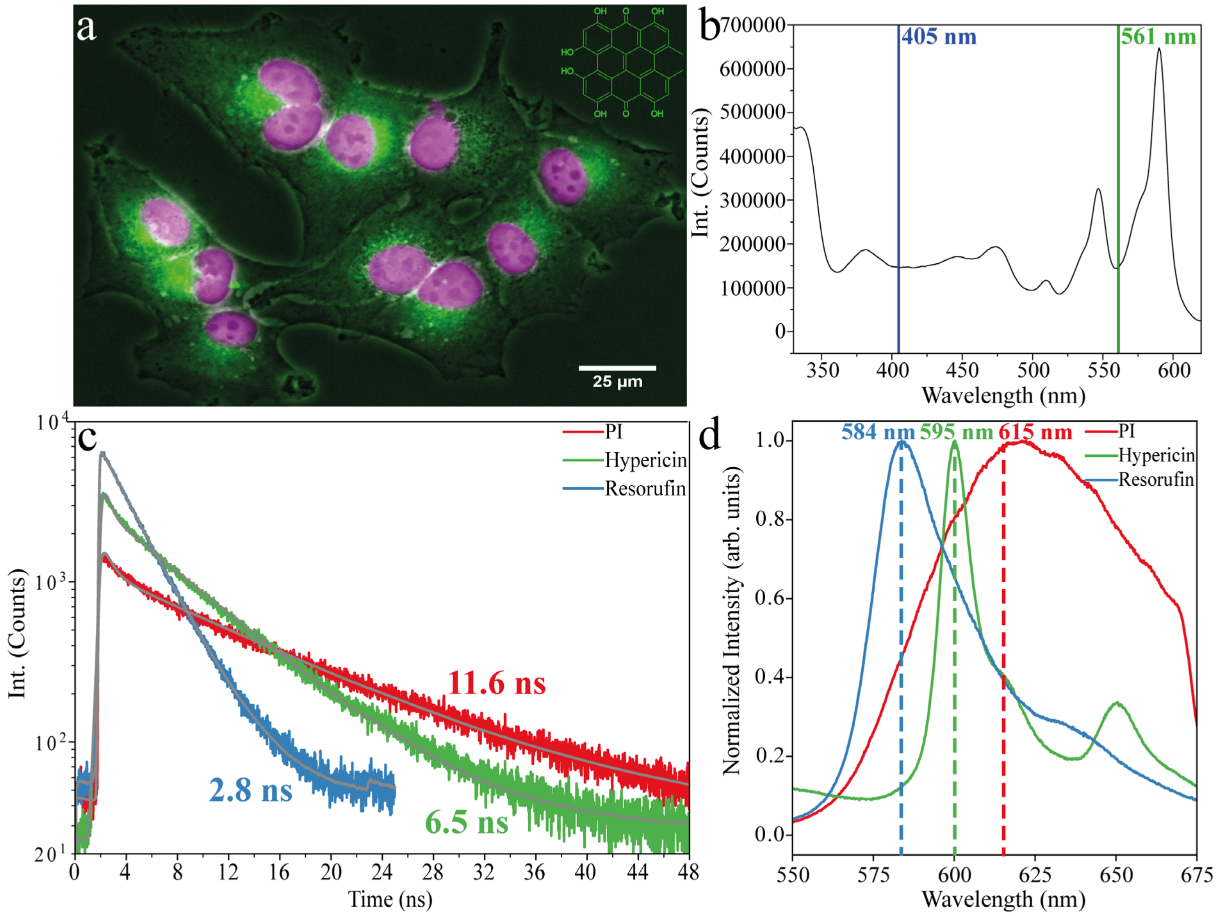

Figure 7.1. *Investigation principle of hypericin PDT on single glioma cells. In (a), glioma cells are initially incubated with hypericin, which is mainly accumulated in the perinuclear region of the cells (green). The cell nucleus is shown in pink after a Hoechst 33342 staining. In (b), the absorption spectrum of hypericin is illustrated, which additionally highlights the two laser wavelengths of 405 nm (blue) and 561 nm (green) used to initiate the PDT. In (c), FLT decay curves for hypericin (green), resorufin (blue) and PI (red) are shown, which are acquired by excitation with a 405 nm laser. Hypericin functions as the photoactive substance, whereas resorufin is a cell metabolite and mainly released into the surrounding medium. PI indicates the cell death after intercalating into DNA or binding to RNA. Decay curves were measured in medium solution, showing significantly different FLTs for hypericin (6.5 ns), resorufin (2.8 ns) and PI (11.6 ns) after curve fitting (grey). In (d), fluorescence spectra of the dyes exhibit characteristic spectral shapes with intensity maxima at 584 nm for resorufin, 595 nm for hypericin and 615 nm for PI. All fluorescence spectra were detected by 405 nm laser irradiation.*

7.3 Materials and Methods

7.3.1 Cell Culture

Cell experiments were performed with the glioma cell line U-87 MG (ATCC HTB-14). Cells were grown in Eagle's Minimum Essential Medium (MEM, no glutamine and phenol red, Gibco™) supplemented with 10 % fetal calve serum (FCS), 1 % penicillin / streptomycin, 1 % L-glutamine and 1 % sodium pyruvate (all purchased from Gibco™). They were seeded with densities between 5000 cells/cm^2 and 20,000 cells/cm^2 and cultivated in glass-bottom cell culture dishes (Willco Wells, HBST-5040) for 24 h prior to further treatment. Cell culture dishes were equipped with glass coverslip bottoms of 170 µm thickness on average and coated with FCS to improve cell adherence. After 24 h, cells were mostly attached to the cell culture dish bottoms and used for hypericin incubation. Cultivation was accomplished at 37 °C and 5 % CO$_2$ atmosphere.

7.3.2 Hypericin Incubation

Aliquots of hypericin (PhytoLab GmbH & Co.KG) stock solutions in DMSO (Molecular Probes™ D12345) with a concentration of 0.1 mM were freshly thawed for each cell incubation. Dilutions of this stock in complete cultivation medium and additional 10 % FCS were prepared to achieve a final hypericin concentration of 1 µM. This procedure was adapted from [339]. Dilutions of DMSO in complete cultivation medium and additional 10 % FCS were used for controls, resulting in 1 % DMSO within the final cultivation mixture. The hypericin and DMSO cultivation mixtures were added to the cells and incubated for 30 min at 37 °C and 5 % CO_2 conditions, respectively. Both incubations were disrupted by removing the cultivation mixtures and washing three times with phosphate buffered saline (PBS). Afterwards, fresh cultivation medium was added to the hypericin-incubated and control cells. All preparation steps and incubation experiments were performed in the dark. Cells were kept at 37 °C and 5 % CO_2 atmosphere until resorufin and PI treatments or FLIM measurements.

7.3.3 Resorufin Conversion

U-87 MG cells were additionally incubated with a resazurin incubation mixture to convert resazurin to resorufin by metabolism in the cells. For this purpose, a resazurin stock solution with a concentration of 0.011 mg/ml in PBS was diluted 1:10 in complete cultivation medium and the final resazurin incubation mixture was added to the cells overnight at 37 °C and 5 % CO_2 atmosphere. During this time period, resazurin was quantitively metabolized to resorufin, which was mainly released into the cultivation medium by the cells. Resorufin conversion was completed after the incubation mixture turned from blue (resazurin) to pink (resorufin). No further exchange of cultivation medium was performed, since the released resorufin was needed for FLIM experiments. Hypericin-incubated samples and controls were treated similarly according to this procedure. All preparation steps and incubation experiments were performed in the dark. Cells were kept at 37 °C and 5 % CO_2 atmosphere until PI supplementation or FLIM measurements.

7.3.4 PI Supplementation

Aliquots of PI stock with a concentration of 500 µg/ml in PBS were freshly thawed for each cell treatment. To obtain a final PI concentration of 33 µg/ml in the cell culture dish, 100 µl PI stock was added to the cultivation medium after 100 µl cultivation medium was removed. This approach was accomplished equally for hypericin-incubated cells and control cells. All preparation steps and incubation experiments were performed in the dark. Cells were kept at 37 °C and 5 % CO_2 atmosphere until FLIM measurements.

7.3.5 Fluorescence Lifetime Imaging Microscopy (FLIM)

FLIM experiments were performed with two custom-built, time-resolved confocal microscopes. Sample excitation was either conducted with a 20 MHz-pulsed 405 nm laser diode (LDH P–C-405, PicoQuant GmbH, Germany) or a 20 MHz-pulsed white light laser (SuperK Extreme EXB-4, NKT Photonics), equipped with a multi-channel tunable filter accessory (AOTF SuperK SELECT UV/VIS-nIR, NKT Photonics) and set to 561 nm. Both lasers were inversely directed onto the sample and focused on the cells with an oil immersion 100x objective lens (Zeiss Plan-Apochromat, 100x, 1.4 Oil DIC and alpha Plan-Fluar 100x/1,49 Oil M27, Carl Zeiss AG, Germany). Two additional long-pass filters (458 nm: RazorEdge LP Edge Filter 458 RU, Semrock; 532 nm: LP EdgeBasic™ Filter 532, Semrock) were used for emission detection in both setups to separate the excitation from the emission light. A single photon avalanche diode (SPAD; PDM series, Micro Photon Devices, Italy) coupled with a time-correlated single photon counting unit (TCSPC-unit; HydraHarp 400, PicoQuant GmbH, Germany) was used to acquire time-resolved confocal images with an excitation wavelength of either 405 nm or 561 nm. The whole microscope setups, including scanning stage, SPAD, laser diode and TCSPC unit, were controlled by the SymphoTime® software (PicoQuant GmbH, Germany), which was also used for data analysis and evaluation.

Positioning and focusing of the cells was performed with small laser powers of 200 – 300 nW to guarantee no cell damage prior to PDT induction. A laser power between 0.7 µW and 1 µW was set for PDT initiation of hypericin-incubated cells, whereas control cells were measured at a minimum of 1 µW or even higher laser powers up to 2 – 3 µW. The laser power was adjusted and regularly checked with a power meter (Optical power meter 1830-C Picowatt Digital, Newport) throughout the measurement session to ensure power stability. In total, 60 single cells were measured by FLIM for all incubation conditions to confirm all observations and achieve a high reproducibility (n = 60).

7.3.6 Widefield Fluorescence Imaging Microscopy

The recording of widefield fluorescence images was performed with the second custom-built, confocal microscope, using a white light laser (SuperK Extreme EXB-4, NKT Photonics) provided with a multi-channel tunable filter accessory (AOTF SuperK SELECT UV/VIS-nIR, NKT Photonics) and controlled by the NKT Photonics CONTROL 1.2 software. The laser wavelength was set to 405 nm and a laser power of 600 µW was adjusted. A separation of the emission from the laser light was again enabled with two long-pass filters (458 nm: RazorEdge LP Edge Filter 458 RU, Semrock; 532 nm: LP EdgeBasic™ Filter 532, Semrock). Widefield illumination was achieved by a lens (Ø1" UVFS Plano-Convex Lens, f = 150.0 mm, ARC: 350 – 700 nm, Thorlabs LA4874-A-ML), which focused on the back focal plane of the objective (alpha Plan-Fluar 100x/1,49 Oil M27, Carl Zeiss AG, Germany). After light collection, a second lens (Biconvex lens; N-BK 7; D=25.4; F=100; mounted, Qioptiq G063854000) was used to focus the sample's fluorescence on the detection camera (ORCA-Flash4.0 V2 camera, Hamamatsu

Photonics). Image acquisition was controlled by the camera software (HoKaWo 3.0), which was set to an exposure time of 1 s and an interval time of 10 s. Each recording was manually stopped after cell death.

7.3.7 Fluorescence Spectra Acquisition

Fluorescence spectra were acquired with an Acton SP300i spectrometer (Princeton Instruments, USA), equipped with a thermoelectrically cooled CCD camera (PIXIS 100, Princeton Instruments, USA). To remove the laser signal from the fluorescence spectra, two long pass filters (458 nm: RazorEdge LP Edge Filter 458 RU, Semrock; 532 nm: LP EdgeBasic™ Filter 532, Semrock) were installed in the detection pathway. The wavelength range of the spectrometer was 410 – 690 nm and the acquisition time was set to 1 s for each spectrum. Spectra acquisition was controlled by Winspec® software (Princeton Instruments, USA).

7.4 Results

Three different fluorescence markers are used for FLIM composite image acquisition. The first fluorescence probe is hypericin, which acts as the photosensitizer for PDT with a FLT of 6.5 ns in complete cell culture medium (Fig. 7.1c, green). The second fluorescence probe is resorufin (Fig. 7.1c, blue), which is cellularly metabolized from resazurin. Since resorufin is mainly released into the medium and only a small amount remains in the cell's cytoplasm, it is suitable to act as a marker for the surrounding medium with a FLT of 2.8 ns, thus allowing to draw conclusion about the integrity of the cell membrane. The third fluorescence probe is PI (Fig. 7.1c, red) that is not diffusible across intact cell membranes, but can enter in case of decreasing membrane integrity or even rupture and intercalates into cellular RNA or DNA. PI is only fluorescent when intercalated into DNA / RNA and thus mainly functions as an indicator for cell death after its DNA intercalation in the cell nucleus. It shows a distinctive FLT of 11.6 ns in complete cell culture medium.

FLIM composite images were acquired to reveal cell damaging steps and determine the final cell death mechanism of glioma cells during hypericin PDT. Composite images consist of FLIM images merged with steady-state fluorescence intensity images and the image contrast is based on FLT variations. Underlying steady-state fluorescence intensities indicate a semi-quantitative probe distribution in the cells, which is displayed by the intensity of false-color FLTs. The FLT recording was accomplished by fast FLIM measurements registering the arrival time of each photon and the FLTs represent an average value of all emitting species in the excitation focus. Hence, all FLT values are the average of different proportions of the used fluorescence probes and the cellular autofluorescence, which can differ between the cells. Fast FLIM was chosen as measuring mode since the acquisition of individual fluorescence decay curves is very time-consuming and PDT would progress too fast to resolve individual PDT steps.

To prevent PDT initiation while locating the cell, low laser powers between 100 – 300 nW are applied for detecting the first FLIM composite image. FLT acquisition and hypericin PDT was initially induced by the same laser beam in single glioma cells after hypericin incubation and resorufin conversion. Individual damaging stages of these cells are shown in Fig. 7.2. At the beginning, the cell is still intact, as illustrated by its morphology with an elongated shape with narrow branches and the bulky body center with the cell nucleus (black), (Fig. 7.2a). No shape deformation or unusual behavior can be noticed. Hypericin is mainly accumulated in the ER around the nucleus (black), but can also be found within the cytoplasm, indicated by FLTs between 4.5 – 6 ns (green, red). Here, the hypericin FLT is slightly decreased in comparison to its FLT in complete cell culture medium (Fig. 7.1c), which is caused by differences of the local environment inside the cells. Resorufin is mostly found in the medium surrounding the cell with a FLT of 3 ns (blue). Corresponding fluorescence spectra at different positions inside and outside the glioma cell are summarized in Fig. 7.2h. The spectrum of resorufin is measured outside the cell (position 1) and strongly differs in its shape from the spectrum of hypericin in the ER (position 3), (Fig. 7.2h). The main fluorescence maximum of resorufin can be observed at 585 nm followed by a broad shoulder towards larger wavelength, whereas hypericin has two distinct fluorescence intensity maxima at 595 nm and 650 nm. Both spectra corroborate that hypericin is mainly enriched in the ER and resorufin can mostly be found in surrounding medium. Additionally, the two compounds can be detected in the cell nucleus (Fig. 7.2h, position 4) and the cytoplasm (Fig. 7.2h, position 2), but to a much smaller extent. The detection of very small concentrations is possible, since the microscope setups are built for single molecule detection and are thus very sensitive. With ongoing PDT progression (Fig. 7.2b – d), cell shrinkage and rounding can be observed, which is accompanied by formation of large cell membrane blebs (Fig. 7.2d, white arrow). Blebs mainly occur at membrane sites around the ER and extent to create actual bubbles. Compared to earlier stages, a rounded cell nucleus is observed, also implying the overall shape deformation. Hypericin FLTs are slightly decreased inside the ER (5 – 5.5 ns) and also its fluorescence intensity is further reduced, as shown in the fluorescence spectrum (Fig. 7.2i, position 3). As a result of the hypericin fluorescence decrease in the ER, this spectrum closer resembles the spectrum of the cytoplasm. Both spectra of the surrounding medium and the cell nucleus are unchanged (Fig. 7.2i, position 1; position 4). However, at these stages the cell membrane is severely distorted by the blebs, but its integrity is still maintained, since the amount of resorufin in the cell is hardly altered. At the final stages of PDT (Fig. 7.2e – g), decreasing FLTs of 3 – 5 ns (Fig. 7.2e – f) and 3 – 3.5 ns (Fig. 7.2g) indicate that the cell is progressively filled with the surrounding medium, since resorufin is the dominant fluorescence marker within the entire glioma cell. This suggests that cell membrane stability is eased, although no obvious membrane damage can be resolved in the images. This leads to cell expansion until its final shape is completely round. Cell organelles are hardly visible anymore (Fig. 7.2g at position 3, 4). This is also verified by the associated fluorescence spectra (Fig. 7.2j). Here, the spectra at each point inside and outside the cell mainly resemble the spectrum of resorufin. Nevertheless, hypericin can still be observed in the spectra of the cell membrane (position 5), the ER (position 3) and the nucleus (position 4), which also coincides with a slightly increased FLT for these organelles (Fig. 7.2f – g, greenish touch). A second series of FLIM composite images for a hypericin incubated and resorufin surrounded cell is displayed in Fig. S7.1 (A6, Appendix). Additionally, control experiments of cells without hypericin incubation are illustrated in Fig. S7.2 and Fig. S7.3 (A6, Appendix).

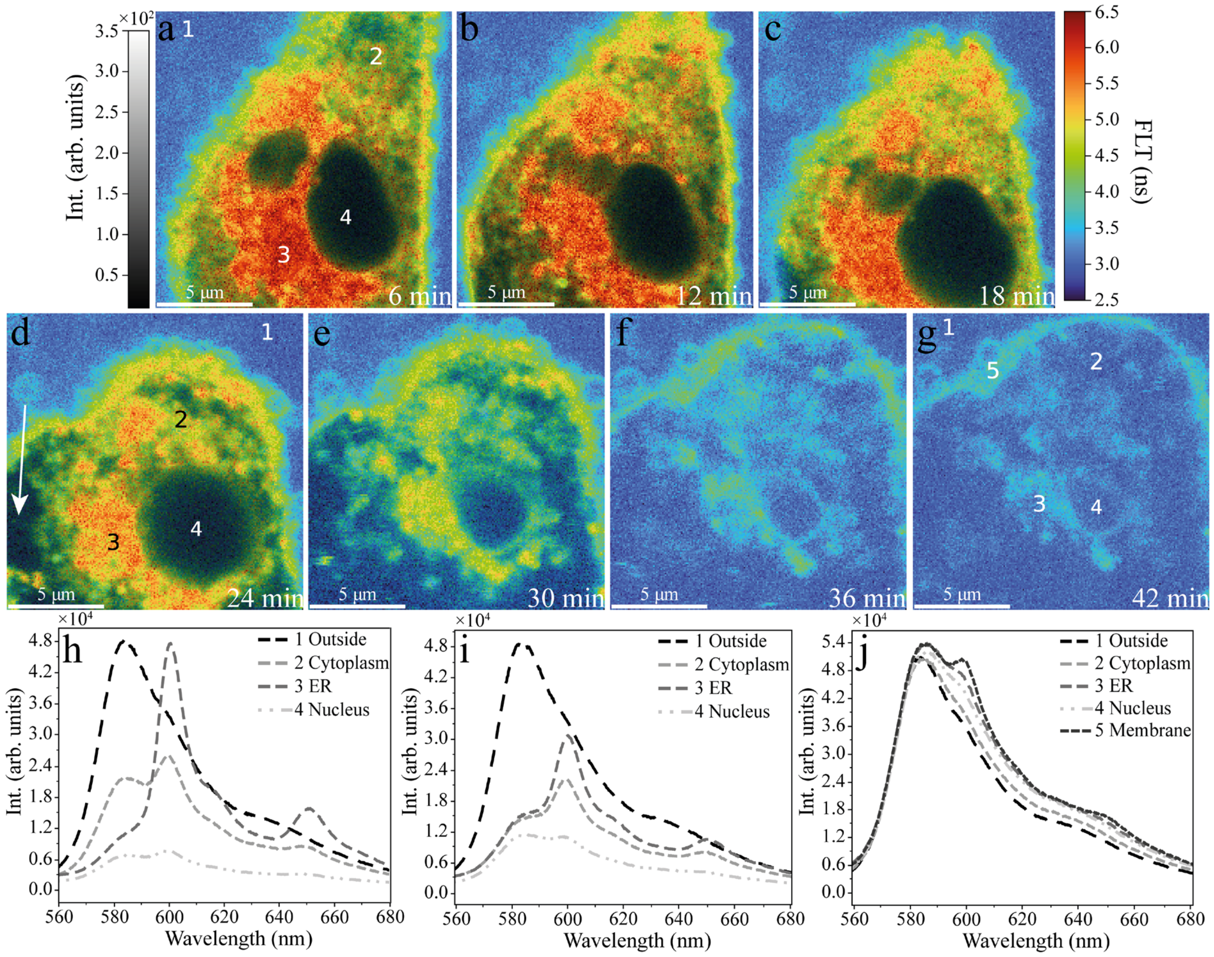

__Figure 7.2.__ FLIM and fluorescence spectra analysis of hypericin PDT on a single glioma cell following hypericin- and resorufin-treatment. Different phases of PDT-induced cell death are illustrated by FLIM composite images in (a-g) and corresponding fluorescence spectra are presented in (h-j). In (a), the cell is still intact, indicated by its overall morphology. The cell nucleus is shown in black. Hypericin is accumulated in the cell membrane (4.5 – 5.5 ns), the cytoplasm (4.5 – 6 ns), but primarily in the perinuclear region including the ER (5.5 – 6.0 ns). In (b – d), the cell is damaged as the result of hypericin PDT, causing cell shrinkage and membrane blebbing (d, white arrow). In (e – g), the progressive reduction of FLT (3 – 3.5 ns) is caused by resorufin and indicates the permeation of surrounding medium into the cell. In (h), resorufin is mainly located outside the cell (position 1), but to a small extent also in the cytoplasm (position 2) and nucleus (position 4). Hypericin primarily accumulates in the ER (position 3), but is also found in the cytoplasm and nucleus. In (i), hypericin is still mainly located in the ER (position 3) and cytoplasm (position 2), however its intensity is decreased. The spectra shown in (j) are dominated by resorufin, due to medium entering the cell. Nevertheless, a small amount of hypericin can be found in the cytoplasm (position 2), nucleus (position 4), ER (position 3) and the membrane (position 5).

One major damaging phenomenon are the blebs and to determine the actual time of death, PI was added as a third fluorescence marker. PI can hardly enter the cell in case of an intact cell membrane and it is only fluorescent if it intercalates into DNA or RNA. After PI passes to the cell nucleus, its intercalation into DNA causes a very intense PI fluorescence, indicating the cell death. The investigation of hypericin PDT with resorufin and PI as additional fluorescence marker is displayed in a series of FLIM composite images in Fig. 7.3. Here, the same laser beam is used for the induction of hypericin PDT and FLIM composite image recording. Resorufin is again mainly located in the surrounding medium, as demonstrated by FLTs of 3 ns around the glioma cell (Fig. 7.3, blue). This enables once more a good cell-medium contrast and allows to detect, at which stage the medium enters the cell. Immediately after PDT induction (Fig. 7.3a – b), the cell morphology is unchanged and the glioma cell keeps its elongated, narrow shape. Hypericin is accumulated throughout the entire cell with the largest concentration inside the ER, as illustrated by the bright green color for hypericin FLTs of 7 – 8 ns (Fig. 7.3a, position 3). In the cell nucleus (position 4), three nucleoli are weakly visible (position 5). In comparison to only hypericin and resorufin treatments (Fig. 7.2), cells with additionally supplemented PI exhibit overall increased FLTs, as indicated by ER, cytoplasm or nucleoli FLTs (Fig. 7.3a, position 2 – 5). This can be explained by the fact that PI already intercalated to a small extent into DNA / RNA inside the cell and thus raise the FLTs measured by fast FLIM. As a result, the displayed FLTs represent average values for hypericin and PI that shift towards lower FLTs in case hypericin is the dominant probe or towards higher FLTs in case the PI amount increases in the cell. Additionally, the cellular autofluorescence and small amounts of resorufin inside the cell also contribute to the observed FLTs that can cause FLT average variations between the cells. Relating fluorescence spectra in Fig. 7.3i, acquired at the positions marked in Fig. 7.3a, confirm the observations made by FLIM composite images. The largest hypericin concentration is found in the ER, indicated by its high fluorescence intensity (position 3), followed by the second largest hypericin enrichment in the cytoplasm (position 2). Additionally, hypericin is also located in the cell nucleus und nucleoli, but to a much smaller extent, as can be seen by its weak fluorescence at position 4 and 5. Again, resorufin is mainly detected outside the cell (position 1), however, a small shoulder at 585 nm in all fluorescence spectra indicates the presence of resorufin inside the glioma cell. Progressing PDT causes the cell morphology to change distinctly, which is expressed by cell deformation and excessive membrane bleb formation (Fig. 7.3c – e). This cell damage induces PI to primarily enter the nucleus and accumulate in two nucleoli, as shown by the increase of the FLT to 12 ns (Fig. 7.3d, position 5). Slightest PI concentrations are again detectable due to the high sensitivity of the microscope setups. Overall, three large blebs are formed along different cell membrane regions (position 6, greenish). This is also visible in the associated fluorescence spectra (Fig. 7.3j), as the bubble spectrum (position 6) closely resembles the spectral signature of the nucleus and cytoplasm. Since the ER (position 3) is not damaged yet, the highest concentration of hypericin can still be found here, whereas resorufin is mainly detected outside the cell (position 1). Besides hypericin, the spectrum of the nucleolus at position 5 additionally shows the spectral signature of PI. At final PDT steps (Fig. 7.3f – h), the glioma cell is completely rounded and the shift of FLTs to 9 – 10 ns in the cytoplasm suggests that the amount of PI bound to DNA has further increased in comparison to earlier stages (Fig. 7.3g, h, yellow-orange). Remaining ER parts can be observed by the green spots in the cytoplasm, which exhibit a FLT of 6 – 7 ns. The FLT of 12 ns observed in the nucleus (red color) suggest a strong accumulation of PI and indicates the cell death. Overall, the fluorescence intensity is increased in the entire cell, which is illustrated by the brighter and more intense false colors of the FLTs. The pronounced PI fluorescence in the nucleus is also highlighted by the related fluorescence spectra (Fig. 7.3k), which reveal high PI fluorescence intensities (position 4 and 5). PI, however, is present in the whole cell, as shown by the fluorescence spectra of the cytoplasm, former ER and the giant final bubble (positions 2 – 6). However, in the cytoplasm (position 2) and the ER (position 3), the hypericin concentration is still large enough to be detected. A comparable PDT progression of another single glioma cell with hypericin and PI is depicted in a second sequence of FLIM composite images in Fig. S7.4 (A6, Appendix). Corresponding control experiments of cells without hypericin incubation are again shown in Fig. S7.2 and Fig. S7.3. (A6, Appendix).

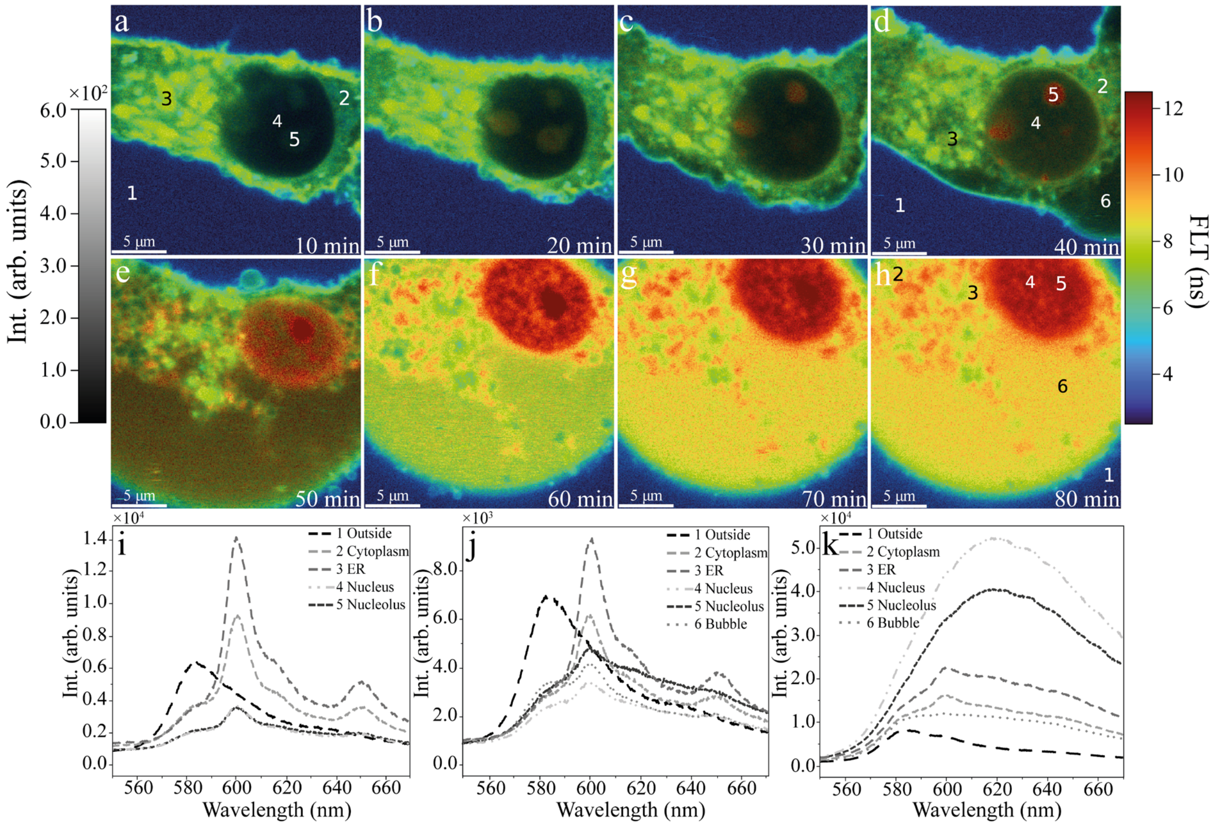

__Figure 7.3.__ FLIM and fluorescence spectra analysis of hypericin PDT on a single glioma cell after hypericin-, PI- and resorufin-treatment. Different phases of PDT-induced cell death are illustrated by FLIM composite images in (a-h) and the corresponding fluorescence spectra are shown in (i-k). In (a – b), the single glioma cell has an elongated shape, showing its intact constitution. Again, hypericin is mainly located inside the ER, but can be detected throughout the cell, as shown by the bright green false-color representing FLTs of 7 – 8 ns. The surrounding medium is enriched with resorufin with a FLT of 3 ns. PI fluorescence cannot be detected, which further confirms the intact cellular condition. The progressing damage in (c) and (d) leads to cell deformation and cell membrane bleb formation. Furthermore, intercalation of PI inside the nucleoli can be observed by an increase of the FLT to 12 ns (c, d red). In (e), the morphological shape of the cell body starts to become circular and PI is increasingly intercalated into DNA / RNA in the cytoplasm and nucleus, shown by an FLT of 12 ns. In (f – h) the round cell morphology and the pronounced PI intercalation in the nucleus indicates the final cell death. Additionally, an overall increased fluorescence intensity inside the cell can be observed. The fluorescence spectra in (i) confirm that hypericin is primarily localized in the ER (position 3), but it can also be found in the cytoplasm (position 2) and the nucleus (position 4). Resorufin is mainly observed outside the cell (position 1), but small amounts are still present in the cytoplasm (position 2) and the nucleus (position 4). Due to the progressing cell damage, PI intercalates in the nucleoli, as shown by the fluorescence spectrum in (j). A highly intense PI fluorescence dominates in the nucleus when the cell is dead (k, position 4 and 5). At this stage (k), the first hypericin maximum at 595 nm is only visible in the cytoplasm (position 2) and ER spectrum (position 3), whereas resorufin can mainly be detected extracellularly, but also as a shoulder in the cytoplasm (position 2), ER (position 3) and bubble spectrum (position 6).

Besides the localization of hypericin, the excitation of the photosensitizer is crucial for the PDT efficiency. Hence, different laser wavelengths might yield different results and a comparison of hypericin PDT steps for 405 nm and 561 nm laser induction-wavelengths is displayed by FLIM composite images in Fig. 7.4. Both laser wavelengths were chosen due to their varying hypericin excitations. While 405 nm induces an excitation from the electronic ground state S_0 to the second excited state S_2, 561 nm causes an excitation from the ground state S_0 to the first excited state S_1. Since the transition of hypericin to the triplet state proceeds from S_1, the 561 nm-induced excitation is assumed to be more effective and to result in a faster PDT progression. In comparison, initial internal conversion from S_2 to S_1 has to take place for the 405 nm excitation prior to a transfer from S_1 to the triplet state. Consequently, the 405 nm PDT initiation is expected to be less efficient and slower. Additionally, 405 nm and 561 nm laser wavelengths were selected based on the similar hypericin absorption strength for both and thus to highlight the difference between the S_1 and S_2 transitions even more. If a laser wavelength of a hypericin absorption maxima would have been chosen, the PDT is expected to progress much faster, which hampers the detection of single PDT steps. In Fig. 7.4, glioma cells are incubated with hypericin and supplemented with PI. Since no resorufin is used, the background of the images is black as no medium fluorescence is detectable. At the beginning of the 405 nm laser irradiation, which causes both FLIM composite image acquisition and PDT induction by a single beam, the glioma cell has an elongated shape with its nucleus in the center (Fig. 7.4a, black). The cell is entirely enriched with hypericin and in part also with PI, as indicated by the average FLT between 7.5 – 8.5 ns (Fig. 7.4a, blue-green). Nucleoli are only slightly visible by a weak FLT increase to 8.5 ns. FLT differences compared to previous hypericin and PI treated cells result from a varying ratio of autofluorescence, hypericin and PI fluorescence that slightly differ for each cell. As a first damaging step, the 405 nm irradiation causes the typical cell shrinkage, which results in a more rounded shape (Fig. 7.4b). After cell shrinkage, membrane blebs are formed along large parts of the membrane (Fig. 7.4c). Inside the blebs, PI is enriched, which can be observed by the characteristic FLT of 12 ns. Overall, PI accumulation also increases in the cytoplasm and nucleoli, indicated by a FLT shift from 7.5 ns to 9 ns in the cytoplasm and a more intense false-color for a FLT of 12 ns in the nucleoli (Fig. 7.4c). With ongoing PDT progression, the cell further contracts and becomes rounder, while PI continues to be enriched inside and also starts to accumulate in the cell nucleus (Fig. 7.4d). Smaller bleb formation is decreased, but instead one large bleb emerges at one site of the cell membrane. Additionally, highly intense blebs appear with a FLT of 9.5 ns. At the final stage of cell death, PI is intercalated to a large extent in the nucleus, as can be seen by the 12 ns FLT in this region (Fig. 7.4e, red). In comparison, the 561 nm laser-induced PDT has also no effect on the cellular morphology at the beginning and the cell maintains its regular shape (Fig. 7.4f). Hypericin is mainly accumulated in the ER in close proximity to the nucleus (black), but also in the cytoplasm and cell membrane, which can be deduced by FLTs between 8.5 – 9.5 ns. These FLTs represent again FLT averages for autofluorescence, hypericin and PI. As a result of continuous irradiation, the cell becomes increasingly rounder and pronounced membrane bleb formation of the whole cell membrane occurs (Fig. 7.4g-h). Here, blebs are also enriched with PI, indicated by the weakly intense false-color for a PI FLT of 12 ns (Fig. 7.4h, red). Blebs are further extending in size before the cell shape is almost completely rounded and only small bubbles with raised PI concentrations emerge (Fig. 7.4h-i). In addition, an increased uptake and intercalation of PI can also be noticed in the cytoplasm, as is shown by an increasing appearance of 12 ns FLTs (Fig. 7.4i-j). At the final damaging stage, the cell is again completely rounded with an increased PI intercalation (12 ns). The last FLIM image acquisition (Fig. 7.4j) for the 561 nm excitation could not be completed due to detector saturation and thus was stopped to protect the SPAD from severe damage.

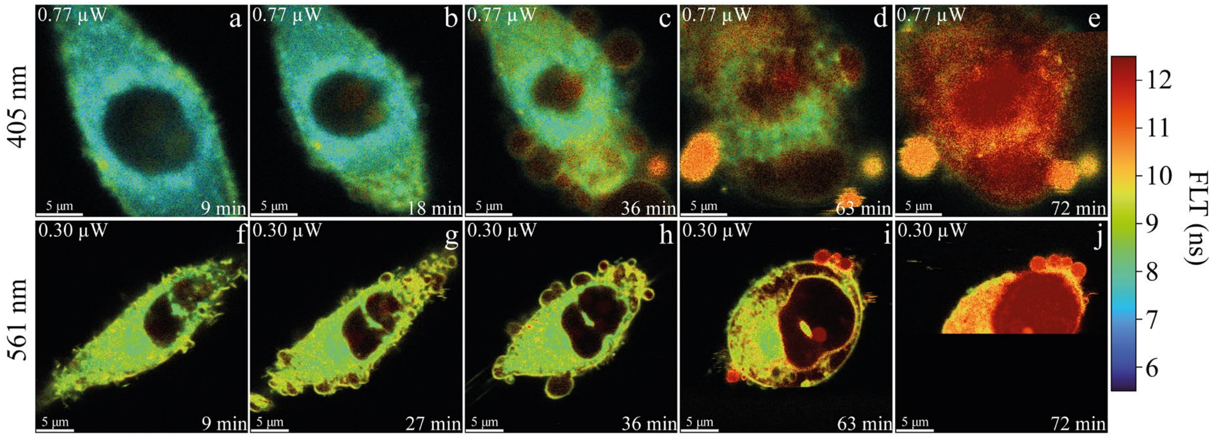

Figure 7.4. Comparison of PDT-induced cell death progression using 405 nm (a-e) and 561 nm (f-j) laser wavelengths. Glioma cells were only incubated with hypericin and PI for this comparison. Typical cell shrinkage, bleb formation and cell rounding are observed for both laser wavelengths. At the beginning, hypericin and PI are already enriched within the cells, as indicated by the FLT averages of 7 – 9.5 ns (a, f). With ongoing PDT, PI increasingly enters the cell via the stressed cell membrane and thus initially appears in the emerging blebs, as shown by the PI FLT of 12 ns (c, d, g, h, i). When the cell is dead, its morphology is completely round and a final large bleb is formed. Additionally, PI is intercalated into the DNA inside the nucleus (e, j). In case of the 561 nm excitation, the final FLIM image recording was not completed as a result of detector oversaturation and terminated to protect the SPAD.

7.5 Discussion

FLIM examination of hypericin PDT on glioma cells with a 405 nm laser revealed a sequence of cell damaging steps that include cell shrinkage, cell rounding, membrane bleb formation and medium penetration (Fig. 7.2, Fig. 7.3, Fig. 7.4a-e). Hypericin uptake by the cells was confirmed by its characteristic fluorescence spectrum and FLT. Its largest accumulation was found in the ER with a FLT of 6 – 7 ns, followed by an enrichment in the cytoplasm with a FLT of 4.5 – 7 ns and in the cell membrane with a FLT of 5 – 7 ns (Fig. 7.2a, h; Fig. 7.3a, i). In case hypericin and resorufin are the only used probes, variations of hypericin FLTs can be explained by a differing autofluorescence, locally different microenvironments in the organelles and variable small amounts of resorufin inside the cell (Fig. 7.2). If PI is additionally present in the cell, FLT averages are caused by a varying proportion of autofluorescence, hypericin, resorufin and PI. Due to the induction of PDT, glioma cells initially shrink (Fig. 7.2b – d), which can be deduced from a loss of cell volume in two stages. At first, water, intracellular ions and cytoplasmic content are released via the cell membrane to maintain a normal cell density. Second, degraded macromolecules are additionally expected to be discarded from the cell as a consequence of an early stage of apoptosis [413,414]. A further involvement of K^+-ion channels is discussed to contribute to the shrinkage process. Overall, this shrinkage already implies that hypericin PDT of glioma cells triggers apoptosis. Afterwards, large membrane blebs are formed, which are caused by a detachment of the membrane-cytoskeleton (actomyosin cortex) [415,416]. Membrane blebs are morphologically characterized by a bubble-like protrusion on the cell surface [417] that can expand and retract over time [418]. During bleb expansion, the pressure inside the cell temporarily increases and cytoplasm from the cell body flows into the bleb [418]. This type of membrane blebbing was reported to be a typical feature of apoptotic cell death. Other bleb types can appear for necrosis, which are described to be larger, more transparent and non-retractable in comparison to apoptosis and are caused by an ion influx that initiates water to enter the cell [415,419]. The observation of partly small, retracting blebs, which expanded to larger ones during hypericin PDT would suggest that apoptosis is initially induced and followed by necrosis after continued irradiation. Blebs were additionally shown to exhibit PI fluorescence, indicated by an FLT of 12 ns (Fig. 7.4c), which demonstrates that PI is intercalated into RNA or DNA fragments. This leads to the conclusion that blebs are either filled with PI containing cytoplasm or become externally filled by PI medium crossing the cell membrane. Based on Fig. 7.2d and Fig. 7.3d, FLTs in the blebs are between 4 – 7 ns, not equal to the FLTs of 3 – 4 ns expected for resorufin. Consequently, they seem to be filled with PI containing cytoplasm and not with external medium. The assumption of an initial apoptotic and continued necrotic cell death mechanism is also supported by the next stage of cell damage (Fig. 7.2g, Fig. 7.3h), i.e. cell fill-up with medium. This can be clearly observed in Fig. 7.2g, where the cell is filled with medium containing resorufin resulting in FLTs of 3 – 3.5 ns. In case of Fig. 7.3h, resorufin fluorescence is completely superimposed by PI fluorescence due to its high intensity and thus only PI FLT can be observed. Medium entering is expected to result from membrane disruption followed by bleb formation, although no clear holes can be resolved in the cell membrane. Widefield fluorescence images revealed that membrane rupture happens in an explosive manner and cytosolic content is released (Fig. S7.5, yellow arrow, Supplementary Information, A6, Appendix). The abrupt pressure release due to membrane rupture is defined to be a necrotic attribute, which further emphasizes the previously stated cell death theory [420]. After membrane disruption, large amounts of PI diffuse into the cell at once and are assumed to intercalate mainly in DNA fragments in cytoplasm and nucleus (Fig. 7.3h, k, Fig. 7.4e). This is also confirmed by a high PI fluorescence intensity, which is much more intense than in previous stages and can only result due to an PI intercalation into DNA (Fig. 7.3h, k, Fig. 7.4e, intense red color, Fig. S7.5). Additionally, no apoptotic bodies occur that also underline a tendency towards necrosis. However, one exception could be the glioma cell in Fig. 7.4a-e, which exhibits two partly secreted extracellular vesicles attached to one formed bleb with FLTs of 9.5 ns (Fig. 7.4d, e, bottom right corner). Both vesicles reveal a high PI intercalation due to their intense false-color and could be interpreted as apoptotic bodies. The same might be true for the glioma cell in Fig. 7.4f-j, as one vesicle is also completely detached from the cell (Fig. 7.4g, bottom left corner). Besides, the ER is entirely decomposed and ER fragments can only be recognized by average hypericin-PI FLT of 7 ns (Fig. 7.2g, Fig. 7.3h). Major ER damage is assumed since hypericin is mainly accumulated in the ER and thus leading to highest PDT-induced ROS production. This results in a significant level of ER stress during PDT until the ER is completely disrupted. ER as important reaction site in hypericin PDT is highly linked to mitochondria via mitochondria-associated membranes (MAMs) that are stated to play a role in various cell death principles in cancer, including apoptosis and necrosis [421]. The type of death mechanism to be activated is supposed to be strongly dependent on the stressors, availability of certain compounds in ER and mitochondria and on cellular, environmental conditions [422-424]. Especially, ER stress is reported to primarily induce apoptosis [425-427], but was in some cases also shown to cause necrosis [428-431]. Based on the analysis of FLIM composite images, apoptotic and necrotic features were observed for hypericin PDT on glioma cells that suggests apoptosis to be the initial mechanism followed by necrosis after sustained irradiation, which was illustrated in a stepwise manner.

The irradiation with different laser wavelengths (405 nm and 561 nm) to induce hypericin PDT demonstrated similar damaging steps of glioma cells. This was illustrated by a series of FLIM composite images for both (Fig. 7.4). However, the 561 nm hypericin PDT was triggered with a much lower laser power (0.3 µW) than PDT initiated by 405 nm (0.77 µW) to observe a comparable number of steps until cell death (Fig. 7.4f-j). One reason for the differently required laser powers can be deduced from the hypericin transitions to the excited state that differ for a 405 nm excitation ($S_0 \rightarrow S_2$) compared to a 561 nm excitation ($S_0 \rightarrow S_1$). Another reason derives from a much lower photon yield for 405 nm at comparable energy as for 561 nm, which directly correlates with the triplet quantum yield since each photon can only induce one triplet formation. In case of a more comparable laser power for both wavelengths (405 nm: 0.77 µW and 561 nm: 1 µW), a faster PDT progression takes place for the 561 nm excitation due to the directly induced transition of hypericin to S_1 and the transfer from here to the triplet state (Fig. S7.6, A6, Appendix).

In control experiments without hypericin (Fig. S7.2 and Fig. S7.3, A6, Appendix), no morphological changes due to laser irradiation and only small FLT variations were observed. FLTs are again average values and result either from cellular autofluorescence and PI (Fig. S7.2) or from cellular autofluorescence and resorufin (Fig. S7.3), as the only fluorescence probes detectable in the cells, respectively. PI is also initially intercalated into control cells as for hypericin-incubated ones, but its fluorescence in the controls is not superimposed by the much more intense hypericin fluorescence. Thus, FLT averages between 10 – 12 ns for 405 nm and 14 ns for 561 nm result (Fig. S7.2). In control cells with resorufin, also no morphology modifications and FLT alterations were noticed. Here, cellular autofluorescence and again small proportions of resorufin inside the cell cause a FLT average of 1.5 ns in the nucleus and 2 – 2.5 ns in the cytoplasm, whereas the surrounding medium with highly enriched resorufin exhibits a FLT between 3 – 3.5 ns (Fig. S7.3).

7.6 Conclusion

In this work, the mechanism of hypericin-induced PDT was investigated in single glioma cells. For this purpose, glioma cells were incubated with hypericin and supplemented with two additional fluorescence markers resorufin and PI. These three fluorescence markers were chosen since they have strongly differing FLTs, which allows to easily distinguish them in the glioma cell. Furthermore, all three markers serve a specific purpose, i.e. hypericin was deployed as photosensitizer for PDT, resorufin is used to label the surrounding medium and PI indicates the cell death. The combination of all three fluorescence compounds enabled to investigate individual steps of hypericin PDT on glioma cells and deduce specific damaging patterns that were assigned to various programmed cell death attributes. Two different laser wavelengths (405 nm and 561 nm) were applied for hypericin PDT initiation and recording of FLIM composite images to unveil the consecutive stages of cell damage and death. After 405 nm laser-induction, initial cell body shrinkage and bleb formation were allocated to be typical features of apoptosis, while the final bleb outcome, the usual absence of apoptotic bodies and the explosive membrane rupture were identified as necrotic cell death characteristics. In accordance with control cells, all observed cellular changes during hypericin PDT were proven to be treatment-specific and not to be triggered by laser irradiation alone. As a result, hypericin PDT on glioma cells was found to be primarily apoptosis followed by necrosis. A PDT initiation with 561 nm revealed a comparable progression of cell damaging at much lower laser power (0.3 µW) than for 405 nm (0.77 µW). However, a faster PDT progress was achieved with 561 nm at a more comparable laser power (1 µW) as for 405 nm (0.77 µW). This was explained by triggering a different hypericin transition with 561 nm ($S_0 \rightarrow S_1$) in comparison to 405 nm ($S_0 \rightarrow S_2$). Our study generated new insights and perspectives on hypericin PDT that should contribute to implement and subsequently improve its application in brain tumor treatments.

7.7 Declarations

Funding: This study was funded by the doctoral program of the University of Tübingen and Reutlingen University "Intelligente Prozess- und Materialentwicklung in der Biomateriomics (IPMB)", which is supported by the MWK Baden-Württemberg (PhD student fellowship to MCB and MS). Additionally, this work was supported by a MINT-funded project from Vector Stiftung Stuttgart.

8. Conclusion and Outlook

In the first part of this thesis, spectroscopy-based multivariate models were developed and investigated as diagnostic instruments for various aspects in tumor diagnosis. Powerful models were generated on basis of elastic light scattering spectroscopic imaging, Raman imaging and FTIR microspectroscopic data. The models exposed even slightest tissue variations and enabled to explain them by the biological background. They were shown to be the key in differentiating between tumors and normal tissues and could even distinguish between varying tumor entities. Tissue preparation-related influences could additionally be revealed. Furthermore, the models were suitable to predict and classify tumors and tissues of undetermined origin. This is of particular importance in an early and accurate tumor diagnosis. It is conceivable to implement certain models in a clinical routine.

A comparative study of Whiskbroom and Pushbroom DF ELSS imaging models was performed to ascertain whether one of both models can better distinguish between altered tissue (mainly SCC), gland / muscle and epithelium of mouse tongues. To generate the ELS data sets, a DF adaption was previously implemented to prevent the specularly reflected light from detection. Tongue cross-sections of mice were prepared on gold-coated objective slides to increase the detection outcome of diffusely scattered light. Whiskbroom and Pushbroom imaging data were separately analyzed with PCA, which revealed a segregation of normal tissues from SCC on PC1 and PC2 and a differentiation of gland / muscle from epithelium on PC4. This arrangement was achieved for both PCAs, but was slightly better for Pushbroom. Most dominant effects on PC1 and PC2 were related to changes in cell nuclei size or deducible from differences in structural tissue alignment. Tissue heterogeneity was additionally termed to affect the cluster order on PC2 of the Pushbroom PCA. Overall sinusoidal or ripple patterns pointed to a superposition of many scattering events that were assigned to Mie scattering and especially emphasized by PC4. Final PCA-DA models attained outstanding performance values between 98 – 99 % and could accurately predict a great majority of model-unknown tongue regions. A slightly better prediction outcome, however, was obtained by the Pushbroom PCA-DA. Prediction results of the models were confirmed by a comparison with the HE-characterization of the tongue cross-sections. Beyond the better Pushbroom PCA-DA model, Pushbroom DF ELSS imaging was suggested to be easier applicable in a clinical context with regard to acquisition time, costs and practicability. A thorough testing of resection margins in the future should verify whether the PCA-DA models are capable to correctly identify remaining tumor parts. If not, an extension of Pushbroom and Whiskbroom DF ELSS imaging data should be considered. The models could additionally be expanded by imaging data of different tumorigenic intermediate stages, including e.g. hyperplasia, dysplasia or severe dysplasia. This would greatly improve the early diagnosis of head and neck tumors in the oral cavity. For this purpose, a larger mouse sample set would, however, be needed to cover the intermediate stages.

A successful differentiation of two parotid tumor entities and normal salivary gland was enabled by a Raman imaging-based multivariate model. It was established on basis of representative human Warthin tumor, pleomorphic adenoma and normal salivary gland samples. Raman imaging data of all tissues were previously acquired and used to calculate Raman mean spectra prior to multivariate model formation. The comparison of mean spectra already demonstrated high band similarities between the tumors and normal salivary gland. Only minor spectral differences, including band appearance, relations and intensity, were observed. Most Raman bands contributed to a distinction between salivary gland and tumor entities and could mainly be ascribed to changes in RNA / DNA, lipids, proteins, collagen and triglycerides. These effects were explained by variations in RNA / DNA contents, a dysregulation of protein / lipid production, an increased fatty acid synthesis and an altered collagen composition, abundance and type between the tissues. Large band similarities in all mean spectra required a further analysis of the data by PCA. PC1 and PC2 already separated the Warthin tumor from pleomorphic adenoma and salivary gland, which was mostly deducible from tyrosine-, carotenoids-, cholesterol- and protein / lipid-associated attributes. A further segregation of salivary gland and pleomorphic adenoma, however, was only possible by PC5 and could be derived from protein-, lipid- cytosine-, collagen-, NADH-, and tryptophan-related influences. Potential reasons for these impacts were mainly derived from tumor-specific features, such as an enhanced metabolic activity or an increase in biomass. The final Raman imaging-based PCA-DA model achieved high performance values of 94 – 95 %. This was also reflected by its good prediction outcome, as all model-unknown parotid tumor and salivary gland spectra were correctly predicted except for one pleomorphic adenoma. Prediction results were assessed by a corresponding HE-diagnosis of the tissues. In addition to Warthin tumor and pleomorphic adenoma, far more benign parotid tumor entities exist that should be considered for a future extension of the PCA-DA model. As the PCA-DA prediction was only performed in a proof-of-principle manner, a larger model testing will be required to verify already obtained results. The acquired Raman images could directly be evaluated with other multivariate methods, such as multivariate image analysis (MIA), that might be more suitable for spectroscopic image analysis. This approach could generate an image contrast based on the underlying multivariate discrimination that directly illustrates the different tumor entities.

FTIR-based multivariate models were established to examine the impact of different preparation protocols on two parotid tumors and salivary gland tissue. For that purpose, four common preparations, including cryoconservation, formalin fixation, paraffin embedding and dewaxing, were applied on Warthin tumor, pleomorphic adenoma and normal salivary gland. FTIR spectra of the parotid tissues were measured and mean spectra were initially calculated for band comparison and assignment prior to model formation. Intense CH_2 / CH_3 bands appeared in the “in paraffin” mean spectrum due to intensity increasing effects by the underlying paraffin. Largest variations and lowest intensities of these bands were observed in the “dewaxed” spectrum as a result of dewaxing-related alterations that caused a lipid and protein removal from the tissues. Highly similar band patterns of “native” and “formalin” pointed out that formalin fixation hardly impact the tissue composition. Large band similarities between the mean spectra required the FTIR spectra to be analyzed by PCA to deduce further tissue-related changes that were caused by the preparation methods. For that purpose, FTIR spectra of parotid tumors and salivary gland were separately investigated by PCA. All models revealed identical separations for the "in paraffin" cluster on PC1, followed by a segregation of the "dewaxed" group on PC2 and only a partial differentiation of "native" / "formalin" on PC3. The "in paraffin" separation on PC1 was shown to be caused by a significant impact on the CH_2 / CH_3 band region induced by paraffin. Dewaxing-related extraction of lipophilic components from the tissues, however, were responsible for the "dewaxing" cluster segregation on PC2. Reasons for the poor distinction of "native" and "formalin" by PC3 were derived from a slow native tissue degradation and a potentially failing lipid stabilization during fixation. Final PCA-DA models enabled to quantitatively describe the extent of group differentiation by their performance parameters. Accuracy values between 76 % and 89 % were acceptable, but indicated that not a complete cluster segregation could be achieved. Improved cluster separations were accomplished by a three-class PCA-DA, which considered "native" / "formalin" as one tissue group. PCA-DAs additionally allowed an internal validation by assigning FTIR spectra to the groups as if they were not model-included. This also corroborated the PCA results. Formalin fixation was stated to hardly effect the tissue composition while simultaneously preserving the tissues. Thus, it is most suitable for tissue preparation and can easily be implemented in a clinical workflow. As the effect of tissue preparation and fixation was only shown on parotid tissues, other tissues should be comparably treated and analyzed to determine whether the same preparation effects appear. At different fixation conditions (concentration, duration), formalin might have an impact on the tissues, which should be investigated by FTIR-based multivariate models to define ideal preparation terms.

In the second part of this thesis, PDT with hypericin was examined as a new potential therapy for primary brain tumors. New perspectives of hypericin uptake, distribution and interaction were generated with *in vitro* glioma cell spheroids and the analysis of their cryosections by fluorescence microscopy. This was studied in consideration of different incubation times and hypericin concentrations. Short incubation times and low concentrations induced an increased uptake of hypericin in peripheral spheroid areas that progressively decreased towards the spheroid center. This hypericin gradient was associated with variations in cell cycle state or metabolic activity of different spheroid layers and discussed to result from an active uptake in outer layers and a passive one in inner layers. With longer incubation times and higher concentrations, hypericin was shown to be more homogeneously distributed across the spheroids. This was assumed to result from a deeper passive diffusion of hypericin into the spheroids. Hypericin accumulation and distribution were additionally expected to be influenced by cell-cell- or cell-matrix interactions and membrane protein activities. Potential effects of the spheroid microenvironment on hypericin FLTs were additionally investigated on the basis of spheroid cryosections and determined by FLIM. FLT gradients to the spheroid core were observed for short incubation times that were only partially explainable by a pH-decrease in the same direction. Changes in metabolic pathways under increasingly hypoxic conditions were discussed to additionally contribute the obtained FLT gradients. As a result of long incubation times, hypericin FLTs were overall more homogeneous with comparatively shorter FLTs at the spheroid edge and longer FLTs towards the spheroid center. One possible reason for short FLTs in outer layers was deduced from highly agglomerated hypericin and resulting FRET- or excimer-like interactions that caused a fluorescence quenching and FLT decrease. Another reason was derived from a primary hypericin accumulation in lysosomes at the spheroid periphery that was associated with an increase in refractive index and thus with a decreasing FLT. In future experiments, microenvironmental effects in spheroids should specifically be triggered by chemicals, that are known to intervene in e.g. the metabolism, in order to determine their impact on hypericin FLTs. This should be investigated on basis of an improved cryosection preparation protocol that will ensure a higher spheroid stability during sectioning.

Hypericin PDT as potential treatment for primary brain tumors was studied in single glioma cells by FLIM to reveal new insights of glioma-specific photodamage and determine the cell death mechanism. While hypericin simultaneously functioned as photosensitizer and fluorescence probe, resorufin and PI were deployed as additional fluorescence markers for the medium environment and used as cell death label, respectively. Individual damaging steps were illustrated by different series of FLIM composite images that consisted of fast FLIM images superimposed on fluorescence intensity images. PDT application initially induced a cell shrinkage and rounding, followed by bleb formations of the cell membrane. Cell shrinkage was explained by a loss of cell volume and defined as an apoptotic death attribute, whereas bleb formation and increase were allocated to apoptosis and necrosis. The additional detection of PI FLTs and absent resorufin FLTs in the blebs demonstrated that they were filled with PI containing cytoplasm instead of an external influx of surrounding medium. With on-going PDT progression, cells became finally filled-up with medium as a consequence of massive, explosive membrane rupture. This was discussed to cause an instant release of cytosolic content and an immediate diffusion of large PI amounts into the cell body, which is accompanied by PI intercalation into DNA fragments in cytoplasm and nucleus. Explosive membrane disruption was shown by widefield fluorescence images and associated with necrosis. Additionally, the absence of apoptotic bodies in most cases emphasized necrosis to be the predominant mechanism at the final stage of PDT. As a whole, the observed damaging steps suggested an initial cell death mechanism of apoptosis followed by necrosis. Variations of laser wavelength (405 nm and 561 nm) for PDT initiation resulted in a comparable series of progression steps for a lower laser power of 561 nm (0.3 μW) than for 405 nm (0.77 μW). This was explained due to differences in hypericin transition to the excited state (561 nm: S_1, 405 nm: S_2). Control experiments confirmed that the observed effects were PDT-related and not caused by laser irradiation alone. As hypericin PDT was investigated for one hypericin concentration in the cells, other concentrations should additionally be studied to determine their effects on PDT progression and outcome. To more thoroughly understand the impact of PDT on certain cell organelles (e.g. Golgi apparatus, mitochondria), further fluorescence markers could be implemented that specifically target different organelles. This, however, would presuppose that these markers have different FLTs than the ones used so far.

9. Bibliography

1. Böhringer H, Werner N (2010) X-ray spectroscopy of galaxy clusters: studying astrophysical processes in the largest celestial laboratories. The Astronomy and Astrophysics Review 18 (1):127-196. doi:10.1007/s00159-009-0023-3

2. Spinoglio L, Alonso-Herrero A, Armus L, Baes M, Bernard-Salas J, Bianchi S, Bocchio M, Bolatto A, Bradford C, Braine J, Carrera FJ, Ciesla L, Clements DL, Dannerbauer H, Doi Y, Efstathiou A, Egami E, Fernández-Ontiveros JA, Ferrara A, Fischer J, Franceschini A, Gallerani S, Giard M, González-Alfonso E, Gruppioni C, Guillard P, Hatziminaoglou E, Imanishi M, Ishihara D, Isobe N, Kaneda H, Kawada M, Kohno K, Kwon J, Madden S, Malkan MA, Marassi S, Matsuhara H, Matsuura M, Miniutti G, Nagamine K, Nagao T, Najarro F, Nakagawa T, Onaka T, Oyabu S, Pallottini A, Piro L, Pozzi F, Rodighiero G, Roelfsema P, Sakon I, Santini P, Schaerer D, Schneider R, Scott D, Serjeant S, Shibai H, Smith JDT, Sobacchi E, Sturm E, Suzuki T, Vallini L, van der Tak F, Vignali C, Yamada T, Wada T, Wang L (2017) Galaxy Evolution Studies with the SPace IR Telescope for Cosmology and Astrophysics (SPICA): The Power of IR Spectroscopy. PASA 34:e057. doi:10.1017/pasa.2017.48

3. Muro CK, Doty KC, Bueno J, Halámková L, Lednev IK (2015) Vibrational Spectroscopy: Recent Developments to Revolutionize Forensic Science. Analytical Chemistry 87 (1):306-327. doi:10.1021/ac504068a

4. Jehlička J, Edwards HGM (2008) Raman spectroscopy as a tool for the non-destructive identification of organic minerals in the geological record. Organic Geochemistry 39 (4):371-386. doi:https: //doi.org/10.1016/j.orggeochem.2008.01.005

5. Cozzolino D, Roberts J (2016) Applications and Developments on the Use of Vibrational Spectroscopy Imaging for the Analysis, Monitoring and Characterisation of Crops and Plants. Molecules 21 (6):755

6. Gendrin C, Roggo Y, Collet C (2008) Pharmaceutical applications of vibrational chemical imaging and chemometrics: A review. Journal of Pharmaceutical and Biomedical Analysis 48 (3):533-553. doi:https://doi.org/10.1016/j.jpba.2008.08.014

7. Chan KLA, Govada L, Bill RM, Chayen NE, Kazarian SG (2009) Attenuated Total Reflection-FT-IR Spectroscopic Imaging of Protein Crystallization. Analytical Chemistry 81 (10):3769-3775. doi:10.1021/ac900455y

8. Bastiaens PI, Jovin TM (1996) Microspectroscopic imaging tracks the intracellular processing of a signal transduction protein: fluorescent-labeled protein kinase C beta I. Proceedings of the National Academy of Sciences 93 (16):8407-8412. doi:10.1073/pnas.93.16.8407

9. Bazett-Jones DP, Li R, Fussner E, Nisman R, Dehghani H (2008) Elucidating chromatin and nuclear domain architecture with electron spectroscopic imaging. Chromosome Res 16 (3):397. doi:10.1007/s10577-008-1237-3

10. Syed A, Smith EA (2017) Raman Imaging in Cell Membranes, Lipid-Rich Organelles, and Lipid Bilayers. Annual Review of Analytical Chemistry 10 (1):271-291. doi:10.1146/annurev-anchem-061516-045317

11. Hu K, Nguyen TDK, Rabasco S, Oomen PE, Ewing AG (2021) Chemical Analysis of Single Cells and Organelles. Analytical Chemistry 93 (1):41-71. doi:10.1021/acs.analchem.0c04361

12. Xu H, Nagasaka S, Kameta N, Masuda M, Ito T, Higgins DA (2017) Spectroscopic imaging studies of nanoscale polarity and mass transport phenomena in self-assembled organic nanotubes. Physical Chemistry Chemical Physics 19 (30):20040-20048. doi:10.1039/C7CP03672H

13. Ewing AV, Kazarian SG (2018) Recent advances in the applications of vibrational spectroscopic imaging and mapping to pharmaceutical formulations. Spectrochimica Acta Part A: Molecular and Biomolecular Spectroscopy 197:10-29. doi:https://doi.org/10.1016/j.saa.2017.12.055

14. Tiernan H, Byrne B, Kazarian SG (2020) ATR-FTIR spectroscopy and spectroscopic imaging for the analysis of biopharmaceuticals. Spectrochimica Acta Part A: Molecular and Biomolecular Spectroscopy 241:118636. doi:https://doi.org/10.1016/j.saa.2020.118636

15. Sung H, Ferlay J, Siegel RL, Laversanne M, Soerjomataram I, Jemal A, Bray F (2021) Global Cancer Statistics 2020: GLOBOCAN Estimates of Incidence and Mortality Worldwide for 36 Cancers in 185 Countries. CA Cancer J Clin 71 (3):209-249. doi:https://doi.org/10.3322/caac.21660

16. Jackson EL, Alvarez-Buylla A (2008) Characterization of Adult Neural Stem Cells and Their Relation to Brain Tumors. Cells Tissues Organs 188 (1-2):212-224. doi:10.1159/000114541

17. Sontheimer H (2008) A role for glutamate in growth and invasion of primary brain tumors. Journal of Neurochemistry 105 (2):287-295. doi:https://doi.org/10.1111/j.1471-4159.2008.05301.x

18. Chin D, Boyle GM, Porceddu S, Theile DR, Parsons PG, Coman WB (2006) Head and neck cancer: past, present and future. Expert Rev Anticancer Ther 6 (7):1111-1118. doi:10.1586/14737140.6.7.1111

19. Vehlow A, Cordes N (2013) Invasion as target for therapy of glioblastoma multiforme. Biochim Biophys Acta 1836 (2):236-244. doi:https://doi.org/10.1016/j.bbcan.2013.07.001

20. Davis ME (2016) Glioblastoma: Overview of Disease and Treatment. Clin J Oncol Nurs 20 (5 Suppl):S2-8. doi:10.1188/16.Cjon.S1.2-8

21. Johnson DE, Burtness B, Leemans CR, Lui VWY, Bauman JE, Grandis JR (2020) Head and neck squamous cell carcinoma. Nature Reviews Disease Primers 6 (1):92. doi:10.1038/s41572-020-00224-3

22. Thielker J, Grosheva M, Ihrler S, Wittig A, Guntinas-Lichius O (2018) Contemporary Management of Benign and Malignant Parotid Tumors. Frontiers in Surgery 5. doi:10.3389/fsurg.2018.00039

23. Smith J, Kendall C, Sammon A, Christie-Brown J, Stone N (2003) Raman Spectral Mapping in the Assessment of Axillary Lymph Nodes in Breast Cancer. Technol Cancer Res Treat 2 (4):327-331. doi:10.1177/153303460300200407

24. Surmacki J, Musial J, Kordek R, Abramczyk H (2013) Raman imaging at biological interfaces: applications in breast cancer diagnosis. Mol Cancer 12 (1):48. doi:10.1186/1476-4598-12-48

25. Abramczyk H, Brozek-Pluska B (2013) Raman Imaging in Biochemical and Biomedical Applications. Diagnosis and Treatment of Breast Cancer. Chem Rev 113 (8):5766-5781. doi:10.1021/cr300147r

26. Manciu FS, Ciubuc JD, Parra K, Manciu M, Bennet KE, Valenzuela P, Sundin EM, Durrer WG, Reza L, Francia G (2017) Label-Free Raman Imaging to Monitor Breast Tumor Signatures. Technol Cancer Res Treat 16 (4):461-469. doi:10.1177/1533034616655953

27. Wang M, Long F, Tang F, Jing Y, Wang X, Yao L, Ma J, Fei Y, Chen L, Wang G, Mi L (2017) Autofluorescence Imaging and Spectroscopy of Human Lung Cancer. Applied Sciences 7 (1):32

28. Krafft C, Codrich D, Pelizzo G, Sergo V (2008) Raman and FTIR microscopic imaging of colon tissue: a comparative study. Journal of Biophotonics 1 (2):154-169. doi:https: //doi.org/10.1002/jbio.200710005

29. Keller MD, Majumder SK, Kelley MC, Meszoely IM, Boulos FI, Olivares GM, Mahadevan-Jansen A (2010) Autofluorescence and diffuse reflectance spectroscopy and spectral imaging for breast surgical margin analysis. Lasers in Surgery and Medicine 42 (1):15-23. doi:10.1002/lsm.20865

30. Grillone GA, Wang Z, Krisciunas GP, Tsai AC, Kannabiran VR, Pistey RW, Zhao Q, Rodriguez-Diaz E, A'Amar OM, Bigio IJ (2017) The color of cancer: Margin guidance for oral cancer resection using elastic scattering spectroscopy. The Laryngoscope 127 (S4):S1-S9. doi:https: //doi.org/10.1002/lary.26763

31. Jerjes W, Swinson B, Johnson KS, Thomas GJ, Hopper C (2005) Assessment of bony resection margins in oral cancer using elastic scattering spectroscopy: a study on archival material. Arch Oral Biol 50 (3):361-366. doi:https://doi.org/10.1016/j.archoralbio.2004.08.003

32. Brown JQ, Bydlon TM, Richards LM, Yu B, Kennedy SA, Geradts J, Wilke LG, Junker MK, Gallagher J, Barry WT, Ramanujam N (2010) Optical Assesssment of Tumor Resection Margins in the Breast. IEEE Journal of Selected Topics in Quantum Electronics 16 (3):530-544. doi:10.1109/JSTQE.2009.2033257

33. Ghanate A, Kothiwale S, Singh S, Krishna CM, Bertrand D (2011) Comparative evaluation of spectroscopic models using different multivariate statistical tools in a multicancer scenario. Journal of Biomedical Optics 16 (2):025003

34. Mariani MM, Lampen P, Popp J, Wood BR, Deckert V (2009) Impact of fixation on in vitro cell culture lines monitored with Raman spectroscopy. Analyst 134 (6):1154-1161. doi:10.1039/B822408K

35. Meade AD, Clarke C, Draux F, Sockalingum GD, Manfait M, Lyng FM, Byrne HJ (2010) Studies of chemical fixation effects in human cell lines using Raman microspectroscopy. Analytical and Bioanalytical Chemistry 396 (5):1781-1791. doi:10.1007/s00216-009-3411-7

36. Bik E, Dorosz A, Mateuszuk L, Baranska M, Majzner K (2020) Fixed versus live endothelial cells: The effect of glutaraldehyde fixation manifested by characteristic bands on the Raman spectra of cells. Spectrochimica Acta Part A: Molecular and Biomolecular Spectroscopy 240:118460. doi:https://doi.org/10.1016/j.saa.2020.118460

37. Huang Z, McWilliams A, Lam S, English J, McLean DI, Lui H, Zeng H (2003) Effect of formalin fixation on the near-infrared Raman spectroscopy of normal and cancerous human bronchial tissues. Int J Oncol 23 (3):649-655. doi:10.3892/ijo.23.3.649

38. Chan JW, Taylor DS, Thompson DL (2009) The effect of cell fixation on the discrimination of normal and leukemia cells with laser tweezers Raman spectroscopy. Biopolymers 91 (2):132-139. doi:https://doi.org/10.1002/bip.21094

39. Verdonck M, Wald N, Janssis J, Yan P, Meyer C, Legat A, Speiser DE, Desmedt C, Larsimont D, Sotiriou C, Goormaghtigh E (2013) Breast cancer and melanoma cell line identification by FTIR imaging after formalin-fixation and paraffin-embedding. Analyst 138 (14):4083-4091. doi:10.1039/C3AN00246B

40. Kopec M, Błaszczyk M, Radek M, Abramczyk H (2021) Raman imaging and statistical methods for analysis various type of human brain tumors and breast cancers. Spectrochimica Acta Part A: Molecular and Biomolecular Spectroscopy 262:120091. doi:https://doi.org/10.1016/j.saa.2021.120091

41. Khanmohammadi M, Bagheri Garmarudi A, Samani S, Ghasemi K, Ashuri A (2011) Application of Linear Discriminant Analysis and Attenuated Total Reflectance Fourier Transform Infrared Microspectroscopy for Diagnosis of Colon Cancer. Pathology & Oncology Research 17 (2):435-441. doi:10.1007/s12253-010-9326-y

42. Li X, Yang T, Li S, Wang D, Song Y, Zhang S (2016) Raman spectroscopy combined with principal component analysis and k nearest neighbour analysis for non-invasive detection of colon cancer. LaPhy 26 (3):035702. doi:10.1088/1054-660x/26/3/035702

43. Liu W, Sun Z, Chen J, Jing C (2016) Raman Spectroscopy in Colorectal Cancer Diagnostics: Comparison of PCA-LDA and PLS-DA Models. Journal of Spectroscopy 2016:1603609. doi:10.1155/2016/1603609

44. Zhang K, Hao C, Man B, Zhang C, Yang C, Liu M, Peng Q, Chen C (2018) Diagnosis of liver cancer based on tissue slice surface enhanced Raman spectroscopy and multivariate analysis. Vib Spectrosc 98:82-87. doi:https://doi.org/10.1016/j.vibspec.2018.07.010

45. Kurachi C, Fontana C, Rosa L, Bagnato V (2008) Fluorescence spectroscopy for the detection of tongue carcinoma - validation in an animal model. Journal of Biomedical Optics 13 (3):034018

46. Luo Y, Liu H, Wu C, Paraskevaidi M, Deng Y, Shi W, Yuan Y, Feng R, Martin FL, Pang W (2021) Diagnostic segregation of human breast tumours using Fourier-transform infrared spectroscopy coupled with multivariate analysis: Classifying cancer subtypes. Spectrochimica Acta Part A: Molecular and Biomolecular Spectroscopy 255:119694. doi:https://doi.org/10.1016/j.saa.2021.119694

47. Kiesslich T, Krammer B, Plaetzer K (2006) Cellular Mechanisms and Prospective Applications of Hypericin in Photodynamic Therapy. Curr Med Chem 13 (18):2189-2204. doi:http: //dx.doi.org/10.2174/092986706777935267

48. Agostinis P, Berg K, Cengel KA, Foster TH, Girotti AW, Gollnick SO, Hahn SM, Hamblin MR, Juzeniene A, Kessel D, Korbelik M, Moan J, Mroz P, Nowis D, Piette J, Wilson BC, Golab J (2011) Photodynamic therapy of cancer: An update. CA Cancer J Clin 61 (4):250-281. doi:https: //doi.org/10.3322/caac.20114

49. Meulemans J, Delaere P, Vander Poorten V (2019) Photodynamic therapy in head and neck cancer: indications, outcomes, and future prospects. Current Opinion in Otolaryngology & Head and Neck Surgery 27 (2):136-141. doi:10.1097/moo.0000000000000521

50. Wang L, Yang H, Li B (2019) Photodynamic therapy for prostate cancer: a systematic review and meta-analysis. Prostate International 7 (3):83-90. doi:https://doi.org/10.1016/j.prnil.2018.12.002

51. Shackley DC, Briggs C, Gilhooley A, Whitehurst C, O'Flynn KJ, Betts CD, Moore JV, Clarke NW (2002) Photodynamic therapy for superficial bladder cancer under local anaesthetic. BJU Int 89 (7):665-670. doi:https://doi.org/10.1046/j.1464-410X.2002.02743.x

52. Allison R, Moghissi K, Downie G, Dixon K (2011) Photodynamic therapy (PDT) for lung cancer. Photodiagnosis Photodyn Ther 8 (3):231-239. doi:https://doi.org/10.1016/j.pdpdt.2011.03.342

53. Choudhary S, Nouri K, Elsaie ML (2009) Photodynamic therapy in dermatology: a review. Lasers Med Sci 24 (6):971-980. doi:10.1007/s10103-009-0716-x

54. Griffin LL, Lear JT (2016) Photodynamic Therapy and Non-Melanoma Skin Cancer. Cancers (Basel) 8 (10):98

55. Kvam E, Moan J (1990) A COMPARISON OF THREE PHOTOSENSITIZERS WITH RESPECT TO EFFICIENCY OF CELL IN ACTIVATION, FLUORESCENCE QUANTUM YIELD AND DNA STRAND BREAKS. Photochemistry and Photobiology 52 (4):769-773. doi:https: //doi.org/10.1111/j.1751-1097.1990.tb08680.x

56. Berlanda J, Kiesslich T, Engelhardt V, Krammer B, Plaetzer K (2010) Comparative in vitro study on the characteristics of different photosensitizers employed in PDT. J Photochem Photobiol B: Biol 100 (3):173-180. doi:https://doi.org/10.1016/j.jphotobiol.2010.06.004

57. Ritz R, Scheidle C, Noell S, Roser F, Schenk M, Dietz K, Strauss WSL (2012) In vitro comparison of hypericin and 5-aminolevulinic acid-derived protoporphyrin IX for photodynamic inactivation of medulloblastoma cells. PLoS One 7 (12):e51974-e51974. doi:10.1371/journal.pone.0051974

58. Zhang J, Jiang C, Figueiró Longo JP, Azevedo RB, Zhang H, Muehlmann LA (2018) An updated overview on the development of new photosensitizers for anticancer photodynamic therapy. Acta Pharmaceutica Sinica B 8 (2):137-146. doi:https://doi.org/10.1016/j.apsb.2017.09.003

59. Zhu W, Gao Y-H, Liao P-Y, Chen D-Y, Sun N-N, Nguyen Thi PA, Yan Y-J, Wu X-F, Chen Z-L (2018) Comparison between porphin, chlorin and bacteriochlorin derivatives for photodynamic therapy: Synthesis, photophysical properties, and biological activity. Eur J Med Chem 160:146-156. doi:https://doi.org/10.1016/j.ejmech.2018.10.005

60. Liu CD, Kwan D, Saxton RE, McFadden DW (2000) Hypericin and Photodynamic Therapy Decreases Human Pancreatic Cancer in Vitro and in Vivo. J Surg Res 93 (1):137-143. doi:https://doi.org/10.1006/jsre.2000.5949

61. Kim H, Kim SW, Seok KH, Hwang CW, Ahn J-C, Jin J-O, Kang HW (2018) Hypericin-assisted photodynamic therapy against anaplastic thyroid cancer. Photodiagnosis Photodyn Ther 24:15-21. doi:https://doi.org/10.1016/j.pdpdt.2018.08.008

62. Head CS, Luu Q, Sercarz J, Saxton R (2006) Photodynamic therapy and tumor imaging of hypericin-treated squamous cell carcinoma. World J Surg Oncol 4 (1):87. doi:10.1186/1477-7819-4-87

63. Buytaert E, Callewaert G, Hendrickx N, Scorrano L, Hartmann D, Missiaen L, Vandenheede JR, Heirman I, Grooten J, Agostinis P (2006) Role of endoplasmic reticulum depletion and multidomain proapoptotic BAX and BAK proteins in shaping cell death after hypericin-mediated photodynamic therapy. The FASEB Journal 20 (6):756-758. doi:https://doi.org/10.1096/fj.05-4305fje

64. RITZ R, ROSER F, RADOMSKI N, STRAUSS WSL, TATAGIBA M, GHARABAGHI A (2008) Subcellular Colocalization of Hypericin with Respect to Endoplasmic Reticulum and Golgi Apparatus in Glioblastoma Cells. Anticancer Res 28 (4B):2033-2038

65. Eriksson ESE, Santos DJVAd, Guedes RC, Eriksson LA (2009) Properties and Permeability of Hypericin and Brominated Hypericin in Lipid Membranes. J Chem Theory Comput 5 (12):3139-3149. doi:10.1021/ct9002702

66. Couldwell WT, Gopalakrishna R, Hinton DR, He S, Weiss MH, Apuzzo MLJ (1994) Hypericin: A Potential Antiglioma Therapy. Neurosurgery 35 (4):705-710

67. Noell S, Mayer D, Strauss WSL, Tatagiba MS, Ritz R (2011) Selective enrichment of hypericin in malignant glioma: Pioneering in vivo results. Int J Oncol 38 (5):1343-1348. doi:10.3892/ijo.2011.968

68. Ritz R, Müller M, Dietz K, Duffner F, Bornemann A, Roser F, Tatagiba M (2008) Hypericin uptake: A prognostic marker for survival in high-grade glioma. J Clin Neurosci 15 (7):778-783. doi:https://doi.org/10.1016/j.jocn.2007.03.022

69. Matsutani M (2004) Chemoradiotherapy for brain tumors: current status and perspectives. Int J Clin Oncol 9 (6):471-474. doi:10.1007/s10147-004-0456-7

70. Autier L, Clavreul A, Cacicedo ML, Franconi F, Sindji L, Rousseau A, Perrot R, Montero-Menei CN, Castro GR, Menei P (2019) A new glioblastoma cell trap for implantation after surgical resection. Acta Biomater 84:268-279. doi:https://doi.org/10.1016/j.actbio.2018.11.027

71. Robertson CA, Evans DH, Abrahamse H (2009) Photodynamic therapy (PDT): A short review on cellular mechanisms and cancer research applications for PDT. J Photochem Photobiol B: Biol 96 (1):1-8. doi:https://doi.org/10.1016/j.jphotobiol.2009.04.001

72. Kessel D (2020) Exploring Modes of Photokilling by Hypericin. Photochemistry and Photobiology 96 (5):1101-1104. doi:https://doi.org/10.1111/php.13275

73. Dolmans DEJGJ, Fukumura D, Jain RK (2003) Photodynamic therapy for cancer. Nature Reviews Cancer 3 (5):380-387. doi:10.1038/nrc1071

74. Garg AD, Nowis D, Golab J, Agostinis P (2010) Photodynamic therapy: illuminating the road from cell death towards anti-tumour immunity. Apoptosis 15 (9):1050-1071. doi:10.1007/s10495-010-0479-7

75. Lakowicz JR (2007) Principles of Fluorescence Spectroscopy. 3 edn. Springer Science+Business Media, New York. doi:https://doi.org/10.1007/978-0-387-46312-4

76. Valeur B, Berberan-Santos MN (2012) Molecular fluorescence: principles and applications. 2 edn. John Wiley & Sons. doi:10.1002/9783527650002

77. Bohr N (1925) Atomic Theory and Mechanics1. Nature 116 (2927):845-852. doi:10.1038/116845a0

78. Atkins P, De Paula J, Keeler J (2017) Atkins' physical chemistry. 11 edn. Oxford University Press, London, England

79. Wedler G, Freund H-J (2012) Lehrbuch der physikalischen Chemie, vol 1. John Wiley & Sons,

80. Kasha M (1950) Characterization of electronic transitions in complex molecules. Discuss Faraday Soc 9 (0):14-19. doi:10.1039/DF9500900014

81. Williams RT, Bridges JW (1964) Fluorescence of solutions: A review. J Clin Pathol 17 (4):371-394. doi:10.1136/jcp.17.4.371

82. Parson WW (2007) Modern optical spectroscopy, vol 2. 2 edn. Springer. doi:https: //doi.org/10.1007/978-3-662-46777-0

83. Lefebvre-Brion H, Field RW (2004) The spectra and dynamics of diatomic molecules: revised and enlarged edition. Elsevier,

84. Marian CM (2012) Spin–orbit coupling and intersystem crossing in molecules. WIREs Computational Molecular Science 2 (2):187-203. doi:https://doi.org/10.1002/wcms.83

85. Larkin P (2011) Infrared and Raman Spectroscopy: Principles and Spectral Interpretation. 1st edn. Elsevier,

86. Long DA (2002) The Raman effect: a unified treatment of the theory of Raman scattering by molecules. Wiley Chichester. doi:10.1002/0470845767

87. Tuchin VV (2015) Tissue Optics and Photonics: Light-Tissue Interaction. Journal of Biomedical Photonics & Engineering 1 (2):37. doi:10.18287/jbpe-2015-1-2-98

88. Colthup NB, Daly LH, E. WS (2012) Introduction to infrared and Raman spectroscopy. 3 edn. Academic Press,

89. Kubitscheck U (2017) Fluorescence microscopy: from principles to biological applications. 2 edn. John Wiley & Sons,

90. Bassler MC, Rammler T, Wackenhut F, zur Oven-Krockhaus S, Secic I, Ritz R, Meixner AJ, Brecht M (2022) Accumulation and penetration behavior of hypericin in glioma tumor spheroids studied by fluorescence microscopy and confocal fluorescence lifetime imaging microscopy. Analytical and Bioanalytical Chemistry 414 (17):4849-4860. doi:10.1007/s00216-022-04107-2

91. BECKER W (2012) Fluorescence lifetime imaging – techniques and applications. Journal of Microscopy 247 (2):119-136. doi:https://doi.org/10.1111/j.1365-2818.2012.03618.x

92. Bastiaens PIH, Squire A (1999) Fluorescence lifetime imaging microscopy: spatial resolution of biochemical processes in the cell. Trends Cell Biol 9 (2):48-52. doi:https://doi.org/10.1016/S0962-8924(98)01410-X

93. Mie G (1908) Beiträge zur Optik trüber Medien, speziell kolloidaler Metallösungen. AnP 330 (3):377-445. doi:10.1002/andp.19083300302

94. Bohren CF, Huffman DR (1983) Absorption and scattering of light by small particles. John Wiley & Sons,

95. van de Hulst HC (1981) Light scattering by small particles. Dover Publications, New York

96. Backman V, Gurjar R, Badizadegan K, Itzkan I, Dasari RR, Perelman LT, Feld MS (1999) Polarized light scattering spectroscopy for quantitative measurement of epithelial cellular structures in situ. IEEE Journal of Selected Topics in Quantum Electronics 5 (4):1019-1026. doi:10.1109/2944.796325

97. HILL SC, BENNER RE (1988) MORPHOLOGY-DEPENDENT RESONANCES. In: Optical Effects Associated with Small Particles. Wspc pp 1-61. doi:10.1142/9789814415804_0001

98. Szymanski W, Pohl FG, Wagner PE (1982) Observation of resonances for elastic light scattering by spherical particles. Journal of Colloid and Interface Science 85 (1):289-301. doi:https: //doi.org/10.1016/0021-9797(82)90257-0

99. Liu Y, Li X, Kim YL, Backman V (2005) Elastic backscattering spectroscopic microscopy. Optics Letters 30 (18):2445-2447. doi:10.1364/OL.30.002445

100. Dey P (2010) Cancer nucleus: Morphology and beyond. Diagn Cytopathol 38 (5):382-390. doi:https://doi.org/10.1002/dc.21234

101. Rebner K, Schmitz M, Boldrini B, Kienle A, Oelkrug D, Kessler RW (2010) Dark-field scattering microscopy for spectral characterization of polystyrene aggregates. Optics Express 18 (3):3116-3127. doi:https://doi.org/10.1364/OE.18.003116

102. Liu X, Huang Y, Kang JU (2011) Dark-field illuminated reflectance fiber bundle endoscopic microscope. Journal of Biomedical Optics 16 (4):046003

103. Basantia N, Nollet LM, Kamruzzaman M (2018) Hyperspectral Imaging Analysis and Applications for Food Quality. 1st edn. CRC Press, Boca Raton. doi:https://doi.org/10.1201/9781315209203

104. Manolakis DG, Lockwood RB, Cooley TW (2016) Hyperspectral Imaging Remote Sensing: Physics, Sensors, and Algorithms. Cambridge University Press, Cambridge. doi:DOI: 10.1017/CBO9781316017876

105. Halicek M, Fabelo H, Ortega S, Callico GM, Fei B (2019) In-Vivo and Ex-Vivo Tissue Analysis through Hyperspectral Imaging Techniques: Revealing the Invisible Features of Cancer. Cancers (Basel) 11 (6):756

106. Toporski J, Dieing T, Hollricher O (2018) Confocal Raman Microscopy, vol 66. Springer Series in Optical Sciences, vol 158. Springer,

107. Elliott AD (2020) Confocal Microscopy: Principles and Modern Practices. Current Protocols in Cytometry 92 (1):e68. doi:https://doi.org/10.1002/cpcy.68

108. Rayleigh (1879) XXXI. Investigations in optics, with special reference to the spectroscope. The London, Edinburgh, and Dublin Philosophical Magazine and Journal of Science 8 (49):261-274. doi:10.1080/14786447908639684

109. Novotny L, Hecht B (2006) Principles of nano-optics. Cambridge university press, New York

110. Cole RW, Jinadasa T, Brown CM (2011) Measuring and interpreting point spread functions to determine confocal microscope resolution and ensure quality control. Nat Protoc 6 (12):1929-1941. doi:10.1038/nprot.2011.407

111. Wong M-L (1994) Polarizability and tensor ellipsoid in the Raman effect. Vib Spectrosc 7 (2):197-199. doi:https://doi.org/10.1016/0924-2031(94)85031-3

112. Dey T (2022) Microplastic pollutant detection by Surface Enhanced Raman Spectroscopy (SERS): a mini-review. Nanotechnology for Environmental Engineering. doi:10.1007/s41204-022-00223-7

113. Esbensen K, Swarbrick B, Westad F, Whitcomb PJ, Anderson MJ (2018) Multivariate data analysis: an introduction to multivariate analysis, process analytical technology and quality by design. 6 edn. Camo,

114. Kessler W (2007) Multivariate datenanalyse: für die pharma, bio-und Prozessanalytik. John Wiley & Sons,

115. Jain AK, Duin RPW, Jianchang M (2000) Statistical pattern recognition: a review. ITPAM 22 (1):4-37. doi:10.1109/34.824819

116. Varmuza K, Filzmoser P (2009) Introduction to multivariate statistical analysis in chemometrics. CRC press,

117. Adams MJ (2004) Chemometrics in Analytical Spectroscopy. 2 edn. RSC Books, Cambridge

118. Freshney RI (2016) Culture of animal cells: a manual of basic technique and specialized applications. 7 edn. John Wiley & Sons,

119. Kapałczyńska M, Kolenda T, Przybyła W, Zając̨zkowska M, Teresiak A, Filas V, Ibbs M, Bliźniak R, Łuczewski Ł, Lamperska K (2018) 2D and 3D cell cultures – a comparison of different types of cancer cell cultures. Arch Med Sci 14 (4):910-919. doi:10.5114/aoms.2016.63743

120. Costa EC, Moreira AF, de Melo-Diogo D, Gaspar VM, Carvalho MP, Correia IJ (2016) 3D tumor spheroids: an overview on the tools and techniques used for their analysis. Biotechnol Adv 34 (8):1427-1441. doi:https://doi.org/10.1016/j.biotechadv.2016.11.002

121. Díaz P, Sandoval-Bórquez A, Bravo-Sagua R, Quest AFG, Lavandero S (2021) Perspectives on Organelle Interaction, Protein Dysregulation, and Cancer Disease. Frontiers in Cell and Developmental Biology 9. doi:10.3389/fcell.2021.613336

122. Pollard TD, Earnshaw WC, Lippincott-Schwartz J, Johnson G (2017) Cell biology. 3 edn. Elsevier Health Sciences, Philadelphia

123. Grunicke HH (1991) The cell membrane as a target for cancer chemotherapy. Eur J Cancer Clin Oncol 27 (3):281-284. doi:https://doi.org/10.1016/0277-5379(91)90516-G

124. Peterson CL, Laniel M-A (2004) Histones and histone modifications. Curr Biol 14 (14):R546-R551. doi:10.1016/j.cub.2004.07.007

125. Jevtić P, Edens LJ, Vuković LD, Levy DL (2014) Sizing and shaping the nucleus: mechanisms and significance. Curr Opin Cell Biol 28:16-27. doi:https://doi.org/10.1016/j.ceb.2014.01.003

126. Zink D, Fischer AH, Nickerson JA (2004) Nuclear structure in cancer cells. Nature Reviews Cancer 4 (9):677-687. doi:10.1038/nrc1430

127. Thorsness PE, Hanekamp T Mitochondria: Origin. In: eLS. doi:https: //doi.org/10.1038/npg.els.0001381

128. Fontanesi F Mitochondria: Structure and Role in Respiration. In: eLS. pp 1-13. doi:https: //doi.org/10.1002/9780470015902.a0001380.pub2

129. Frey TG, Mannella CA (2000) The internal structure of mitochondria. Trends in Biochemical Sciences 25 (7):319-324. doi:https://doi.org/10.1016/S0968-0004(00)01609-1

130. Giorgi C, Missiroli S, Patergnani S, Duszynski J, Wieckowski MR, Pinton P (2015) Mitochondria-Associated Membranes: Composition, Molecular Mechanisms, and Physiopathological Implications. Antioxidants & Redox Signaling 22 (12):995-1019. doi:10.1089/ars.2014.6223

131. Wallace DC (2012) Mitochondria and cancer. Nature Reviews Cancer 12 (10):685-698. doi:10.1038/nrc3365

132. Vyas S, Zaganjor E, Haigis MC (2016) Mitochondria and Cancer. Cell 166 (3):555-566. doi:https://doi.org/10.1016/j.cell.2016.07.002

133. Voeltz GK, Rolls MM, Rapoport TA (2002) Structural organization of the endoplasmic reticulum. EMBO reports 3 (10):944-950. doi:https://doi.org/10.1093/embo-reports/kvf202

134. Schwarz DS, Blower MD (2016) The endoplasmic reticulum: structure, function and response to cellular signaling. Cellular and Molecular Life Sciences 73 (1):79-94. doi:10.1007/s00018-015-2052-6

135. Moenner M, Pluquet O, Bouchecareilh M, Chevet E (2007) Integrated Endoplasmic Reticulum Stress Responses in Cancer. Cancer Res 67 (22):10631-10634. doi:10.1158/0008-5472.Can-07-1705

136. Yadav RK, Chae S-W, Kim H-R, Chae HJ (2014) Endoplasmic Reticulum Stress and Cancer. J Cancer Prev 19 (2):75-88. doi:10.15430/JCP.2014.19.2.75

137. Rios RM, Bornens M (2003) The Golgi apparatus at the cell centre. Curr Opin Cell Biol 15 (1):60-66. doi:https://doi.org/10.1016/S0955-0674(02)00013-3

138. Glick BS, Nakano A (2009) Membrane Traffic Within the Golgi Apparatus. Annual Review of Cell and Developmental Biology 25 (1):113-132. doi:10.1146/annurev.cellbio.24.110707.175421

139. Bajaj R, Warner AN, Fradette JF, Gibbons DL (2022) Dance of The Golgi: Understanding Golgi Dynamics in Cancer Metastasis. Cells 11 (9):1484

140. Luzio JP, Pryor PR, Bright NA (2007) Lysosomes: fusion and function. Nature Reviews Molecular Cell Biology 8 (8):622-632. doi:10.1038/nrm2217

141. Wartosch L, Bright NA, Luzio JP (2015) Lysosomes. Curr Biol 25 (8):R315-R316. doi:10.1016/j.cub.2015.02.027

142. Davidson SM, Heiden MGV (2017) Critical Functions of the Lysosome in Cancer Biology. Annual Review of Pharmacology and Toxicology 57 (1):481-507. doi:10.1146/annurev-pharmtox-010715-103101

143. Katt ME, Placone AL, Wong AD, Xu ZS, Searson PC (2016) In Vitro Tumor Models: Advantages, Disadvantages, Variables, and Selecting the Right Platform. Frontiers in Bioengineering and Biotechnology 4 (12). doi:10.3389/fbioe.2016.00012

144. Dubessy C, Merlin J-L, Marchal C, Guillemin F (2000) Spheroids in radiobiology and photodynamic therapy. Critical Reviews in Oncology/Hematology 36 (2):179-192. doi:https: //doi.org/10.1016/S1040-8428(00)00085-8

145. Yao G (2014) Modelling mammalian cellular quiescence. Interface Focus 4 (3):20130074. doi:10.1098/rsfs.2013.0074

146. Nik Nabil WN, Xi Z, Song Z, Jin L, Zhang XD, Zhou H, De Souza P, Dong Q, Xu H (2021) Towards a Framework for Better Understanding of Quiescent Cancer Cells. Cells 10 (3):562

147. Costa EC, de Melo-Diogo D, Moreira AF, Carvalho MP, Correia IJ (2018) Spheroids Formation on Non-Adhesive Surfaces by Liquid Overlay Technique: Considerations and Practical Approaches. Biotechnol J 13 (1):1700417. doi:10.1002/biot.201700417

148. Chatzinikolaidou M (2016) Cell spheroids: the new frontiers in in vitro models for cancer drug validation. Drug Discovery Today 21 (9):1553-1560. doi:https://doi.org/10.1016/j.drudis.2016.06.024

149. Hirschhaeuser F, Menne H, Dittfeld C, West J, Mueller-Klieser W, Kunz-Schughart LA (2010) Multicellular tumor spheroids: An underestimated tool is catching up again. J Biotechnol 148 (1):3-15. doi:https://doi.org/10.1016/j.jbiotec.2010.01.012

150. Thoma CR, Zimmermann M, Agarkova I, Kelm JM, Krek W (2014) 3D cell culture systems modeling tumor growth determinants in cancer target discovery. Adv Drug Del Rev 69-70:29-41. doi:https://doi.org/10.1016/j.addr.2014.03.001

151. Weiswald L-B, Bellet D, Dangles-Marie V (2015) Spherical Cancer Models in Tumor Biology. Neoplasia 17 (1):1-15. doi:https://doi.org/10.1016/j.neo.2014.12.004

152. Bernhard C, Roeters SJ, Franz J, Weidner T, Bonn M, Gonella G (2017) Repelling and ordering: the influence of poly(ethylene glycol) on protein adsorption. Physical Chemistry Chemical Physics 19 (41):28182-28188. doi:10.1039/C7CP05445A

153. Tee HT, Zipp R, Koynov K, Tremel W, Wurm FR (2020) Poly(methyl ethylene phosphate) hydrogels: Degradable and cell-repellent alternatives to PEG-hydrogels. Eur Polym J 141:110075. doi:https://doi.org/10.1016/j.eurpolymj.2020.110075

154. Millard M, Yakavets I, Zorin V, Kulmukhamedova A, Marchal S, Bezdetnaya L (2017) Drug delivery to solid tumors: the predictive value of the multicellular tumor spheroid model for nanomedicine screening. International Journal of Nanomedicine 12:7993-8007. doi:10.2147/IJN.S146927

155. Sant S, Johnston PA (2017) The production of 3D tumor spheroids for cancer drug discovery. Drug Discovery Today: Technologies 23:27-36. doi:https://doi.org/10.1016/j.ddtec.2017.03.002

156. Berens ME, Giese A (1999) "...those left behind." Biology and Oncology of Invasive Glioma Cells. Neoplasia 1 (3):208-219. doi:https://doi.org/10.1038/sj.neo.7900034

157. Zong H, Parada LF, Baker SJ (2015) Cell of Origin for Malignant Gliomas and Its Implication in Therapeutic Development. Cold Spring Harb Perspect Biol 7 (5). doi:10.1101/cshperspect.a020610

158. Colquhoun A (2017) Cell biology-metabolic crosstalk in glioma. The International Journal of Biochemistry & Cell Biology 89:171-181. doi:https://doi.org/10.1016/j.biocel.2017.05.022

159. Maher EA, Furnari FB, Bachoo RM, Rowitch DH, Louis DN, Cavenee WK, DePinho RA (2001) Malignant glioma: genetics and biology of a grave matter. Genes Dev 15 (11):1311-1333. doi:10.1101/gad.891601

160. Falk H, Meyer J, Oberreiter M (1992) Deprotonation and protonation of hydroxyphenanthroperylenes. Monatshefte für Chemie / Chemical Monthly 123 (3):277-284. doi:10.1007/bf00810476

161. Falk H, Meyer J (1994) On the homo- and heteroassociation of hypericin. Monatshefte für Chemie / Chemical Monthly 125 (6):753-762. doi:10.1007/bf01277637

162. Falk H (1999) From the Photosensitizer Hypericin to the Photoreceptor Stentorin— The Chemistry of Phenanthroperylene Quinones. Angew Chem Int Ed 38 (21):3116-3136. doi:https: //doi.org/10.1002/(SICI)1521-3773(19991102)38:21<3116::AID-ANIE3116>3.0.CO;2-S

163. Angerhofer A, Falk H, Meyer J, Schoppel G (1993) Lowest excited triplet states of hypericin and isohypericin. J Photochem Photobiol B: Biol 20 (2):133-137. doi:https://doi.org/10.1016/1011-1344(93)80142-V

164. Lavie G, Mazur Y, Lavie D, Meruelo D (1995) The chemical and biological properties of hypericin—a compound with a broad spectrum of biological activities. Med Res Rev 15 (2):111-119. doi:10.1002/med.2610150203

165. Buytaert E, Dewaele M, Agostinis P (2007) Molecular effectors of multiple cell death pathways initiated by photodynamic therapy. Biochim Biophys Acta 1776 (1):86-107. doi:https: //doi.org/10.1016/j.bbcan.2007.07.001

166. Lu S-L, Herrington H, Wang X-J (2006) Mouse models for human head and neck squamous cell carcinomas. Head Neck 28 (10):945-954. doi:https://doi.org/10.1002/hed.20397

167. Kim S (2009) Animal models of cancer in the head and neck region. Clin Exp Otorhinolaryngol 2 (2):55-60. doi:10.3342/ceo.2009.2.2.55

168. Tinhofer I, Braunholz D, Klinghammer K (2020) Preclinical models of head and neck squamous cell carcinoma for a basic understanding of cancer biology and its translation into efficient therapies. Cancers of the Head & Neck 5 (1):9. doi:10.1186/s41199-020-00056-4

169. El-Naggar AK, Chan JKC, Grandis JR, Takata T, Slootweg PJ (2017) WHO Classification of Head and Neck Tumours, vol 9th. IARC WHO Classification of Tumours, 4th edn. International Agency for Research on Cancer, Lyon

170. Downes DJ, Chonofsky M, Tan K, Pfannenstiel BT, Reck-Peterson SL, Todd RB (2014) Characterization of the mutagenic spectrum of 4-nitroquinoline 1-oxide (4-NQO) in Aspergillus nidulans by whole genome sequencing. G3 (Bethesda, Md) 4 (12):2483-2492. doi:10.1534/g3.114.014712

171. Li Q, Dong H, Yang G, Song Y, Mou Y, Ni Y (2020) Mouse Tumor-Bearing Models as Preclinical Study Platforms for Oral Squamous Cell Carcinoma. Front Oncol 10. doi:10.3389/fonc.2020.00212

172. Lan A, Li W, Liu Y, Xiong Z, Zhang X, Zhou S, Palko O, Chen H, Kapita M, Prigge JR, Schmidt EE, Chen X, Sun Z, Chen XL (2016) Chemoprevention of oxidative stress-associated oral

carcinogenesis by sulforaphane depends on NRF2 and the isothiocyanate moiety. Oncotarget 7 (33):53502-53514. doi:10.18632/oncotarget.10609

173. Ettl T, Schwarz-Furlan S, Gosau M, Reichert TE (2012) Salivary gland carcinomas. Oral Maxillofac Surg 16 (3):267-283. doi:10.1007/s10006-012-0350-9

174. Guzzo M, Locati LD, Prott FJ, Gatta G, McGurk M, Licitra L (2010) Major and minor salivary gland tumors. Critical Reviews in Oncology/Hematology 74 (2):134-148. doi:https: //doi.org/10.1016/j.critrevonc.2009.10.004

175. Eltoum I, Fredenburgh J, Myers RB, Grizzle WE (2001) Introduction to the Theory and Practice of Fixation of Tissues. Journal of Histotechnology 24 (3):173-190. doi:10.1179/his.2001.24.3.173

176. Thavarajah R, Mudimbaimannar V, Elizabeth J, Rao U, Ranganathan K (2012) Chemical and physical basics of routine formaldehyde fixation. J Oral Maxillofac Pathol 16 (3):400-405. doi:10.4103/0973-029x.102496

177. Eltoum I, Fredenburgh J, Grizzle WE (2001) Advanced Concepts in Fixation: 1. Effects of Fixation on Immunohistochemistry, Reversibility of Fixation and Recovery of Proteins, Nucleic Acids, and other Molecules from Fixed and Processed Tissues. 2. Developmental Methods of Fixation. Journal of Histotechnology 24 (3):201-210. doi:10.1179/his.2001.24.3.201

178. Kiernan JA (2000) Formaldehyde, Formalin, Paraformaldehyde And Glutaraldehyde: What They Are And What They Do. Microscopy Today 8 (1):8-13. doi:10.1017/S1551929500057060

179. Lam-ubol A, Kitrueangphatchara K, Putthanuparp T, Arayakhun R, Kwanthong R, Choonhawarakorn K (2018) Nonformalin Fixative Agents: A Comparative Study of Fixative Efficacy and Histomorphology. Int J Surg Pathol 26 (8):701-706. doi:10.1177/1066896918779450

180. Kouchmeshky A, McCaffery P (2020) Chapter Six - Use of fixatives for immunohistochemistry and their application for detection of retinoic acid synthesizing enzymes in the central nervous system. In: Pohl E (ed) Methods in Enzymology, vol 637. Academic Press, pp 119-150. doi:https: //doi.org/10.1016/bs.mie.2020.03.010

181. Krafft C, Schmitt M, Schie IW, Cialla-May D, Matthäus C, Bocklitz T, Popp J (2017) Label-Free Molecular Imaging of Biological Cells and Tissues by Linear and Nonlinear Raman Spectroscopic Approaches. Angew Chem Int Ed 56 (16):4392-4430. doi:10.1002/anie.201607604

182. Mian SA, Yorucu C, Ullah MS, Rehman IU, Colley HE (2017) Raman spectroscopy can discriminate between normal, dysplastic and cancerous oral mucosa: a tissue-engineering approach. J Tissue Eng Regen Med 11 (11):3253-3262. doi:10.1002/term.2234

183. Kumar S, Srinivasan A, Nikolajeff F (2018) Role of infrared spectroscopy and imaging in cancer diagnosis. Curr Med Chem 25 (9):1055-1072

184. Bray F, Ferlay J, Soerjomataram I, Siegel RL, Torre LA, Jemal A (2018) Global cancer statistics 2018: GLOBOCAN estimates of incidence and mortality worldwide for 36 cancers in 185 countries. CA Cancer J Clin 68 (6):394-424. doi:10.3322/caac.21492

185. Alsahafi E, Begg K, Amelio I, Raulf N, Lucarelli P, Sauter T, Tavassoli M (2019) Clinical update on head and neck cancer: molecular biology and ongoing challenges. Cell Death Dis 10 (8):540. doi:10.1038/s41419-019-1769-9

186. Ferlay J, Colombet M, Soerjomataram I, Mathers C, Parkin DM, Piñeros M, Znaor A, Bray F (2018) Estimating the global cancer incidence and mortality in 2018: GLOBOCAN sources and methods. Int J Cancer 144 (8):1941-1953. doi:10.1002/ijc.31937

187. Sano D, Myers JN (2007) Metastasis of squamous cell carcinoma of the oral tongue. Cancer Metastasis Rev 26 (3):645-662. doi:10.1007/s10555-007-9082-y

188. Sequeira I, Rashid M, Tomás IM, Williams MJ, Graham TA, Adams DJ, Vigilante A, Watt FM (2020) Genomic landscape and clonal architecture of mouse oral squamous cell carcinomas dictate tumour ecology. Nature Communications 11 (1):5671. doi:10.1038/s41467-020-19401-9

189. Tan NCW, Herd MK, Brennan PA, Puxeddu R (2012) The role of narrow band imaging in early detection of head and neck cancer. British Journal of Oral and Maxillofacial Surgery 50 (2):132-136. doi:https://doi.org/10.1016/j.bjoms.2010.12.001

190. Devpura S, Thakur JS, Sethi S, Naik VM, Naik R (2012) Diagnosis of head and neck squamous cell carcinoma using Raman spectroscopy: tongue tissues. Journal of Raman Spectroscopy 43 (4):490-496. doi:10.1002/jrs.3070

191. Dhingra JK, Zhang X, McMillan K, Kabani S, Manoharan R, Itzkan I, Feld MS, Shapshay SM (1998) Diagnosis of Head and Neck Precancerous Lesions in an Animal Model Using Fluorescence Spectroscopy. The Laryngoscope 108 (4):471-475. doi:10.1097/00005537-199804000-00002

192. Roy HK, Liu Y, Wali RK, Kim YL, Kromine AK, Goldberg MJ, Backman V (2004) Four-dimensional elastic light-scattering fingerprints as preneoplastic markers in the rat model of colon carcinogenesis. Gastroenterology 126 (4):1071-1081. doi:https://doi.org/10.1053/j.gastro.2004.01.009

193. Xu M, Wu T, Qu J (2008) Unified Mie and fractal scattering by cells and experimental study on application in optical characterization of cellular and subcellular structures. Journal of Biomedical Optics 13 (2):024015

194. Kim YL, Yang L, Wali RK, Roy HK, Goldberg MJ, Kromin AK, Kun C, Backman V (2003) Simultaneous measurement of angular and spectral properties of light scattering for characterization of tissue microarchitecture and its alteration in early precancer. IEEE Journal of Selected Topics in Quantum Electronics 9 (2):243-256. doi:10.1109/JSTQE.2003.814183

195. Bigio I, Bown S, Briggs G, Kelley C, Lakhani S, Pickard D, Ripley P, Rose I, Saunders C (2000) Diagnosis of breast cancer using elastic-scattering spectroscopy: preliminary clinical results. Journal of Biomedical Optics 5 (2):221-228. doi:https://doi.org/10.1117/1.429990

196. Canpolat M, Gökhan AG, Çiftçioğlu MA, Erin N (2008) Differentiation of Melanoma from Non-Cancerous Tissue in an Animal Model Using Elastic Light Single-Scattering Spectroscopy. Technol Cancer Res Treat 7 (3):235-240. doi:10.1177/153303460800700309

197. Gong J, Yi J, Turzhitsky VM, Muro K, Li X (2008) Characterization of malignant brain tumor using elastic light scattering spectroscopy. Dis Markers 25 (6):303-312. doi:10.1155/2008/208120

198. Müller MG, Valdez TA, Georgakoudi I, Backman V, Fuentes C, Kabani S, Laver N, Wang Z, Boone CW, Dasari RR, Shapshay SM, Feld MS (2003) Spectroscopic detection and evaluation of morphologic and biochemical changes in early human oral carcinoma. Cancer 97 (7):1681-1692. doi:10.1002/cncr.11255

199. Stefanakis M, Lorenz A, Bartsch JW, Bassler MC, Wagner A, Brecht M, Pagenstecher A, Schittenhelm J, Boldrini B, Hakelberg S, Noell S, Nimsky C, Tatagiba M, Ritz R, Rebner K, Ostertag E (2021) Formalin Fixation as Tissue Preprocessing for Multimodal Optical Spectroscopy Using the Example of Human Brain Tumour Cross Sections. Journal of Spectroscopy 2021:5598309. doi:10.1155/2021/5598309

200. Boldrini B, Kessler W, Rebner K, Kessler RW (2012) Hyperspectral Imaging: A Review of Best Practice, Performance and Pitfalls for in-line and on-line Applications. J Near Infrared Spectrosc 20 (5):483-508

201. Halicek M, Little JV, Wang X, Patel M, Griffith CC, El-Deiry MW, Chen AY, Fei B (2019) Optical Biopsy of Head and Neck Cancer Using Hyperspectral Imaging and Convolutional Neural Networks. Proceedings of SPIE--the International Society for Optical Engineering 10469:104690X. doi:10.1117/12.2289023

202. Chung H, Lu G, Tian Z, Wang D, Chen ZG, Fei B (2016) Superpixel-based spectral classification for the detection of head and neck cancer with hyperspectral imaging, vol 9788. SPIE Medical Imaging. SPIE. doi:https://doi.org/10.1117/12.2216559

203. Baker MJ, Trevisan J, Bassan P, Bhargava R, Butler HJ, Dorling KM, Fielden PR, Fogarty SW, Fullwood NJ, Heys KA, Hughes C, Lasch P, Martin-Hirsch PL, Obinaju B, Sockalingum GD, Sulé-Suso J, Strong RJ, Walsh MJ, Wood BR, Gardner P, Martin FL (2014) Using Fourier transform IR spectroscopy to analyze biological materials. Nat Protoc 9 (8):1771-1791. doi:10.1038/nprot.2014.110

204. Ostertag E, Stefanakis M, Rebner K, Kessler RW (2017) Elastic and inelastic light scattering spectroscopy and its possible use for label-free brain tumor typing. Analytical and Bioanalytical Chemistry 409 (28):6613-6623. doi:10.1007/s00216-017-0614-1

205. Li Q, He X, Wang Y, Liu H, Xu D, Guo F (2013) Review of spectral imaging technology in biomedical engineering: achievements and challenges. Journal of Biomedical Optics 18 (10):100901

206. Wallenius K, Lekholm U (1973) Oral cancer in rats induced by the water-soluble carcinogen 4-nitrochinoline N-oxide. Odontol Revy 24 (1):39-48

207. Sequeira I, Neves JF, Carrero D, Peng Q, Palasz N, Liakath-Ali K, Lord GM, Morgan PR, Lombardi G, Watt FM (2018) Immunomodulatory role of Keratin 76 in oral and gastric cancer. Nature Communications 9 (1):3437. doi:10.1038/s41467-018-05872-4

208. Vered M, Yarom N, Dayan D (2005) 4NQO oral carcinogenesis: animal models, molecular markers and future expectations. Oral Oncol 41 (4):337-339. doi:https: //doi.org/10.1016/j.oraloncology.2004.07.005

209. Tang X-H, Knudsen B, Bemis D, Tickoo S, Gudas LJ (2004) Oral Cavity and Esophageal Carcinogenesis Modeled in Carcinogen-Treated Mice. Clinical Cancer Research 10 (1):301-313. doi:10.1158/1078-0432.Ccr-0999-3

210. Slootweg PJ, El-Naggar AK (2018) World Health Organization 4th edition of head and neck tumor classification: insight into the consequential modifications. Virchows Archiv 472 (3):311-313. doi:10.1007/s00428-018-2320-6

211. Fidler I, Hart I (1982) Biological diversity in metastatic neoplasms: origins and implications. Science 217 (4564):998-1003. doi:10.1126/science.7112116

212. Lu G, Little JV, Wang X, Zhang H, Patel MR, Griffith CC, El-Deiry MW, Chen AY, Fei B (2017) Detection of Head and Neck Cancer in Surgical Specimens Using Quantitative Hyperspectral Imaging. Clinical Cancer Research 23 (18):5426-5436. doi:10.1158/1078-0432.Ccr-17-0906

213. Perelman LT, Backman V, Wallace M, Zonios G, Manoharan R, Nusrat A, Shields S, Seiler M, Lima C, Hamano T, Itzkan I, Van Dam J, Crawford JM, Feld MS (1998) Observation of Periodic Fine Structure in Reflectance from Biological Tissue: A New Technique for Measuring Nuclear Size Distribution. Physical Review Letters 80 (3):627-630. doi:10.1103/PhysRevLett.80.627

214. Choi J, Choo J, Chung H, Gweon D-G, Park J, Kim HJ, Park S, Oh C-H (2005) Direct observation of spectral differences between normal and basal cell carcinoma (BCC) tissues using confocal Raman microscopy. Biopolymers 77 (5):264-272. doi:10.1002/bip.20236

215. Favreau PF, Deal JA, Harris B, Weber DS, Rich TC, Leavesley SJ (2020) Label-free spectroscopic tissue characterization using fluorescence excitation-scanning spectral imaging. Journal of Biophotonics 13 (2):e201900183. doi:10.1002/jbio.201900183

216. Jolliffe I (2002) Principal Component Analysis Springer Series in Statistics, 2nd edn. Springer-Verlag New York, New York. doi:10.1007/b98835

217. Wold S, Esbensen K, Geladi P (1987) Principal component analysis. Chemometrics Intellig Lab Syst 2 (1):37-52. doi:https://doi.org/10.1016/0169-7439(87)80084-9

218. Chen Y, Zhu S, Fu S, Li Z, Huang F, Yin H, Chen Z (2020) Classification of hyperspectral images for detection of hepatic carcinoma cells based on spectral–spatial features of nucleus. Journal of Innovative Optical Health Sciences 13 (01):2050002. doi:10.1142/s1793545820500029

219. Backman V, Wallace MB, Perelman LT, Arendt JT, Gurjar R, Müller MG, Zhang Q, Zonios G, Kline E, McGillican T, Shapshay S, Valdez T, Badizadegan K, Crawford JM, Fitzmaurice M, Kabani S, Levin HS, Seiler M, Dasari RR, Itzkan I, Van Dam J, Feld MS (2000) Detection of preinvasive cancer cells. Nature 406 (6791):35-36. doi:10.1038/35017638

220. Jain PK, Lee KS, El-Sayed IH, El-Sayed MA (2006) Calculated Absorption and Scattering Properties of Gold Nanoparticles of Different Size, Shape, and Composition: Applications in Biological Imaging and Biomedicine. The Journal of Physical Chemistry B 110 (14):7238-7248. doi:10.1021/jp057170o

221. Schmitt JM, Kumar G (1998) Optical scattering properties of soft tissue: a discrete particle model. Applied Optics 37 (13):2788-2797. doi:10.1364/AO.37.002788

222. Kumar G, Schmitt J (1996) Micro-optical properties of tissue, vol 2679. Photonics West '96. SPIE,

223. Akbari H, Uto K, Kosugi Y, Kojima K, Tanaka N (2011) Cancer detection using infrared hyperspectral imaging. Cancer Sci 102 (4):852-857. doi:10.1111/j.1349-7006.2011.01849.x

224. Baltussen EJ, Kok EN, Brouwer de Koning S, Sanders J, Aalbers AG, Kok NF, Beets G, Flohil C, Bruin S, Kuhlmann KF, Sterenborg HJC, Ruers TJ (2019) Hyperspectral imaging for tissue classification, a way toward smart laparoscopic colorectal surgery. Journal of Biomedical Optics 24 (1):016002

225. Marusyk A, Polyak K (2010) Tumor heterogeneity: Causes and consequences. Biochim Biophys Acta 1805 (1):105-117. doi:https://doi.org/10.1016/j.bbcan.2009.11.002

226. Jacob R, Welkoborsky HJ, Mann WJ, Höfken F, Dienes HP, Freije JE (1996) Heterogeneity of Squamous Cell Carcinomas of the Head and Neck-Analysis of Tumor Biologic Factors and Proliferation Rates. The Laryngoscope 106 (9):1170-1175. doi:10.1097/00005537-199609000-00023

227. Egeblad M, Nakasone ES, Werb Z (2010) Tumors as organs: complex tissues that interface with the entire organism. Dev Cell 18 (6):884-901. doi:10.1016/j.devcel.2010.05.012

228. Fei B, Lu G, Wang X, Zhang H, Little JV, Patel MR, Griffith CC, El-Diery MW, Chen AY (2017) Label-free reflectance hyperspectral imaging for tumor margin assessment: a pilot study on surgical specimens of cancer patients. Journal of biomedical optics 22 (8):1-7. doi:10.1117/1.JBO.22.8.086009

229. Auner GW, Koya SK, Huang C, Broadbent B, Trexler M, Auner Z, Elias A, Mehne KC, Brusatori MA (2018) Applications of Raman spectroscopy in cancer diagnosis. Cancer Metastasis Rev 37 (4):691-717. doi:10.1007/s10555-018-9770-9

230. Bellisola G, Sorio C (2012) Infrared spectroscopy and microscopy in cancer research and diagnosis. Am J Cancer Res 2 (1):1-21

231. Kong K, Kendall C, Stone N, Notingher I (2015) Raman spectroscopy for medical diagnostics - From in-vitro biofluid assays to in-vivo cancer detection. Adv Drug Del Rev 89:121-134. doi:http://dx.doi.org/10.1016/j.addr.2015.03.009

232. Kaznowska E, Depciuch J, Szmuc K, Cebulski J (2017) Use of FTIR spectroscopy and PCA-LDC analysis to identify cancerous lesions within the human colon. Journal of Pharmaceutical and Biomedical Analysis 134:259-268. doi:https://doi.org/10.1016/j.jpba.2016.11.047

233. Devi S, Panigrahi P, Pradhan A (2014) Detecting cervical cancer progression through extracted intrinsic fluorescence and principal component analysis. Journal of Biomedical Optics 19 (12):127003

234. Francisco ALN, Correr WR, Azevedo LH, Kern VG, Pinto CAL, Kowalski LP, Kurachi C (2014) Fluorescence spectroscopy for the detection of potentially malignant disorders and squamous cell carcinoma of the oral cavity. Photodiagnosis Photodyn Ther 11 (2):82-90. doi:https: //doi.org/10.1016/j.pdpdt.2014.03.009

235. Cheng J-X, Xie XS (2015) Vibrational spectroscopic imaging of living systems: An emerging platform for biology and medicine. Science 350 (6264):aaa8870. doi:10.1126/science.aaa8870

236. Gao L, Smith RT (2015) Optical hyperspectral imaging in microscopy and spectroscopy – a review of data acquisition. Journal of Biophotonics 8 (6):441-456. doi:https://doi.org/10.1002/jbio.201400051

237. Anderson NG, Butler AP (2014) Clinical applications of spectral molecular imaging: potential and challenges. Contrast Media Mol Imaging 9 (1):3-12. doi:10.1002/cmmi.1550

238. Abdi H, Williams LJ (2010) Principal component analysis. WIREs Computational Statistics 2 (4):433-459. doi:https://doi.org/10.1002/wics.101

239. Gajjar K, Heppenstall LD, Pang W, Ashton KM, Trevisan J, Patel II, Llabjani V, Stringfellow HF, Martin-Hirsch PL, Dawson T, Martin FL (2013) Diagnostic segregation of human brain tumours using

Fourier-transform infrared and/or Raman spectroscopy coupled with discriminant analysis. Analytical Methods 5 (1):89-102. doi:10.1039/C2AY25544H

240. Croce AC, Bottiroli G (2014) Autofluorescence spectroscopy and imaging: a tool for biomedical research and diagnosis. Eur J Histochem 58 (4). doi:10.4081/ejh.2014.2461

241. Cui S, Zhang S, Yue S (2018) Raman Spectroscopy and Imaging for Cancer Diagnosis. J Health c Eng 2018:8619342. doi:10.1155/2018/8619342

242. Li Y, Pan J, Chen G, Li C, Lin S, Shao Y, Feng S, Huang Z, Xie S, Zeng H, Chen R (2013) Micro-Raman spectroscopy study of cancerous and normal nasopharyngeal tissues. Journal of Biomedical Optics 18 (2):027003

243. Ghassemi K M, Barzegari S, Hajian P, Zham H, Mirzaei HR, Shirazi FH (2021) Diagnosis of normal and malignant human gastric tissue samples by FTIR spectra combined with mathematical models. Journal of Molecular Structure 1229:129493. doi:https: //doi.org/10.1016/j.molstruc.2020.129493

244. Argov S, Ramesh J, Salman A, Sinelnikov I, Goldstein J, Guterman H, Mordechai S (2002) Diagnostic potential of FTIR microspectroscopy and advanced computational methods in colon cancer patients. Journal of Biomedical Optics 7 (2)

245. Bergner N, Romeike BFM, Reichart R, Kalff R, Krafft C, Popp J (2013) Tumor margin identification and prediction of the primary tumor from brain metastases using FTIR imaging and support vector machines. Analyst 138 (14):3983-3990. doi:10.1039/C3AN00326D

246. Dong L, Sun X, Chao Z, Zhang S, Zheng J, Gurung R, Du J, Shi J, Xu Y, Zhang Y, Wu J (2014) Evaluation of FTIR spectroscopy as diagnostic tool for colorectal cancer using spectral analysis. Spectrochimica Acta Part A: Molecular and Biomolecular Spectroscopy 122:288-294. doi:https: //doi.org/10.1016/j.saa.2013.11.031

247. Scheer M, Fuss J, Derman MA, Kreppel M, Neugebauer J, Rothamel D, Drebber U, Zoeller JE (2016) Autofluorescence imaging in recurrent oral squamous cell carcinoma. Oral Maxillofac Surg 20 (1):27-33. doi:10.1007/s10006-015-0520-7

248. ISRAEL Y, RACHMIEL A, ZIV G, NAGLER R (2016) Benign and Malignant Salivary Gland Tumors – Clinical and Demographic Characteristics. Anticancer Res 36 (8):4151-4154

249. Franzen A, Buchali A, Lieder A (2017) The rising incidence of parotid metastases: our experience from four decades of parotid gland surgery. Acta otorhinolaryngologica Italica: 37 (4):264-269. doi:10.14639/0392-100X-1095

250. Zhan KY, Khaja SF, Flack AB, Day TA (2016) Benign Parotid Tumors. Otolaryngol Clin North Am 49 (2):327-342. doi:https://doi.org/10.1016/j.otc.2015.10.005

251. Rahman QB, Iocca O, Kufta K, Shanti RM (2020) Global Burden of Head and Neck Cancer. Oral Maxillofac Surg Clin North Am 32 (3):367-375. doi:https://doi.org/10.1016/j.coms.2020.04.002

252. Aupérin A (2020) Epidemiology of head and neck cancers: an update. Curr Opin Oncol 32 (3):178-186. doi:10.1097/cco.0000000000000629

253. Mantsopoulos K, Velegrakis S, Iro H (2015) Unexpected Detection of Parotid Gland Malignancy during Primary Extracapsular Dissection. Otolaryngology–Head and Neck Surgery 152 (6):1042-1047. doi:10.1177/0194599815578104

254. Paluszkiewicz C, Roman M, Piergies N, Pięta E, Woźniak M, Guidi MC, Miśkiewicz-Orczyk K, Marków M, Ścierski W, Misiołek M, Drozdzowska B, Kwiatek WM (2021) Tracking of the biochemical changes upon pleomorphic adenoma progression using vibrational microspectroscopy. Sci Rep 11 (1):18010. doi:10.1038/s41598-021-97377-2

255. Postema RJ, van Velthuysen M-LF, van den Brekel MWM, Balm AJM, Peterse JL (2004) Accuracy of fine-needle aspiration cytology of salivary gland lesions in the netherlands cancer institute. Head Neck 26 (5):418-424. doi:https://doi.org/10.1002/hed.10393

256. Dostalova L, Kalfert D, Jechova A, Koucky V, Novak S, Kuchar M, Zabrodsky M, Novakova Kodetova D, Ludvikova M, Kholova I, Plzak J (2020) The role of fine-needle aspiration biopsy (FNAB) in the diagnostic management of parotid gland masses with emphasis on potential pitfalls. Eur Arch Otorhinolaryngol 277 (6):1763-1769. doi:10.1007/s00405-020-05868-1

257. Psychogios G, Bohr C, Constantinidis J, Canis M, Vander Poorten V, Plzak J, Knopf A, Betz C, Guntinas-Lichius O, Zenk J (2021) Review of surgical techniques and guide for decision making in the treatment of benign parotid tumors. Eur Arch Otorhinolaryngol 278 (1):15-29. doi:10.1007/s00405-020-06250-x

258. Yan B, Li Y, Yang G, Wen Z-n, Li M-l, Li L-j (2011) Discrimination of parotid neoplasms from the normal parotid gland by use of Raman spectroscopy and support vector machine. Oral Oncol 47 (5):430-435. doi:https://doi.org/10.1016/j.oraloncology.2011.02.021

259. Brozek-Pluska B, Kopec M, Niedzwiecka I, Morawiec-Sztandera A (2015) Label-free determination of lipid composition and secondary protein structure of human salivary noncancerous and cancerous tissues by Raman microspectroscopy. Analyst 140 (7):2107-2113. doi:10.1039/C4AN01394H

260. Meyer TJ, Gerhard-Hartmann E, Lodes N, Scherzad A, Hagen R, Steinke M, Hackenberg S (2021) Pilot study on the value of Raman spectroscopy in the entity assignment of salivary gland tumors. PLoS One 16 (9):e0257470. doi:10.1371/journal.pone.0257470

261. Mukherjee A, Lorenz A, Brecht M (2022) Determination and Monitoring of Quality Parameters: A Detailed Study of Optical Elements of a Lens-Based Raman Spectrometer. Applied Spectroscopy 76 (2):199-206

262. Bassler MC, Stefanakis M, Sequeira I, Ostertag E, Wagner A, Bartsch JW, Roeßler M, Mandic R, Reddmann EF, Lorenz A, Rebner K, Brecht M (2021) Comparison of Whiskbroom and Pushbroom darkfield elastic light scattering spectroscopic imaging for head and neck cancer identification in a mouse model. Analytical and Bioanalytical Chemistry 413 (30):7363-7383. doi:10.1007/s00216-021-03726-5

263. Talari ACS, Movasaghi Z, Rehman S, Rehman Iu (2015) Raman Spectroscopy of Biological Tissues. ApSRv 50 (1):46-111. doi:10.1080/05704928.2014.923902

264. Chan JW, Taylor DS, Zwerdling T, Lane SM, Ihara K, Huser T (2006) Micro-Raman Spectroscopy Detects Individual Neoplastic and Normal Hematopoietic Cells. Biophysical Journal 90 (2):648-656. doi:https://doi.org/10.1529/biophysj.105.066761

265. Bonnier F, Byrne HJ (2012) Understanding the molecular information contained in principal component analysis of vibrational spectra of biological systems. Analyst 137 (2):322-332. doi:10.1039/C1AN15821J

266. Liu Z, Davis C, Cai W, He L, Chen X, Dai H (2008) Circulation and long-term fate of functionalized, biocompatible single-walled carbon nanotubes in mice probed by Raman spectroscopy. Proceedings of the National Academy of Sciences 105 (5):1410-1415. doi:10.1073/pnas.0707654105

267. Dukor RK (2001) Vibrational Spectroscopy in the Detection of Cancer. In: Handbook of Vibrational Spectroscopy. doi:https://doi.org/10.1002/0470027320.s8107

268. Schulz H, Baranska M (2007) Identification and quantification of valuable plant substances by IR and Raman spectroscopy. Vib Spectrosc 43 (1):13-25. doi:https: //doi.org/10.1016/j.vibspec.2006.06.001

269. Gniadecka M, Wulf HC, Nymark Mortensen N, Faurskov Nielsen O, Christensen DH (1997) Diagnosis of Basal Cell Carcinoma by Raman Spectroscopy. Journal of Raman Spectroscopy 28 (2-3):125-129. doi:https://doi.org/10.1002/(SICI)1097-4555(199702)28:2/3<125::AID-JRS65>3.0.CO;2-#

270. Stone N, Kendall C, Smith J, Crow P, Barr H (2004) Raman spectroscopy for identification of epithelial cancers. Faraday Discuss 126 (0):141-157. doi:10.1039/B304992B

271. Cheng W-T, Liu M-T, Liu H-N, Lin S-Y (2005) Micro-Raman spectroscopy used to identify and grade human skin pilomatrixoma. Microscopy Research and Technique 68 (2):75-79. doi:https://doi.org/10.1002/jemt.20229

272. Silveira Jr. L, Sathaiah S, Zângaro RA, Pacheco MTT, Chavantes MC, Pasqualucci CAG (2002) Correlation between near-infrared Raman spectroscopy and the histopathological analysis of atherosclerosis in human coronary arteries. Lasers in Surgery and Medicine 30 (4):290-297. doi:https://doi.org/10.1002/lsm.10053

273. Ó Faoláin E, Hunter MB, Byrne JM, Kelehan P, McNamara M, Byrne HJ, Lyng FM (2005) A study examining the effects of tissue processing on human tissue sections using vibrational spectroscopy. Vib Spectrosc 38 (1):121-127. doi:https://doi.org/10.1016/j.vibspec.2005.02.013

274. Lau DP, Huang Z, Lui H, Man CS, Berean K, Morrison MD, Zeng H (2003) Raman spectroscopy for optical diagnosis in normal and cancerous tissue of the nasopharynx—preliminary findings. Lasers in Surgery and Medicine 32 (3):210-214. doi:10.1002/lsm.10084

275. Sahu A, Dalal K, Naglot S, Aggarwal P, Murali Krishna C (2013) Serum Based Diagnosis of Asthma Using Raman Spectroscopy: An Early Phase Pilot Study. PLoS One 8 (11):e78921. doi:10.1371/journal.pone.0078921

276. Almond LM, Hutchings J, Lloyd G, Barr H, Shepherd N, Day J, Stevens O, Sanders S, Wadley M, Stone N, Kendall C (2014) Endoscopic Raman spectroscopy enables objective diagnosis of dysplasia in Barrett's esophagus. Gastrointest Endosc 79 (1):37-45. doi:https://doi.org/10.1016/j.gie.2013.05.028

277. Calvo MB, Figueroa A, Pulido EG, Campelo RG, Aparicio LA (2010) Potential Role of Sugar Transporters in Cancer and Their Relationship with Anticancer Therapy. Int J Endocrinol 2010:205357. doi:10.1155/2010/205357

278. Romero-Garcia S, Lopez-Gonzalez JS, B´ez-Viveros JL, Aguilar-Cazares D, Prado-Garcia H (2011) Tumor cell metabolism. Cancer Biol Ther 12 (11):939-948. doi:10.4161/cbt.12.11.18140

279. Ackerman D, Simon MC (2014) Hypoxia, lipids, and cancer: surviving the harsh tumor microenvironment. Trends Cell Biol 24 (8):472-478. doi:https://doi.org/10.1016/j.tcb.2014.06.001

280. Zaidi N, Lupien L, Kuemmerle NB, Kinlaw WB, Swinnen JV, Smans K (2013) Lipogenesis and lipolysis: The pathways exploited by the cancer cells to acquire fatty acids. Prog Lipid Res 52 (4):585-589. doi:https://doi.org/10.1016/j.plipres.2013.08.005

281. Donadio E, Giusti L, Seccia V, Ciregia F, da Valle Y, Dallan I, Ventroni T, Giannaccini G, Sellari-Franceschini S, Lucacchini A (2013) New Insight into Benign Tumours of Major Salivary Glands by Proteomic Approach. PLoS One 8 (8):e71874. doi:10.1371/journal.pone.0071874

282. Kuhajda FP (2000) Fatty-acid synthase and human cancer: new perspectives on its role in tumor biology. Nutrition 16 (3):202-208. doi:https://doi.org/10.1016/S0899-9007(99)00266-X

283. Egeblad M, Rasch MG, Weaver VM (2010) Dynamic interplay between the collagen scaffold and tumor evolution. Curr Opin Cell Biol 22 (5):697-706. doi:https://doi.org/10.1016/j.ceb.2010.08.015

284. Chen P, Cescon M, Bonaldo P (2013) Collagen VI in cancer and its biological mechanisms. Trends Mol Med 19 (7):410-417. doi:https://doi.org/10.1016/j.molmed.2013.04.001

285. Chaplin AJ, Darke P, Patel S (1983) Tyrosine-rich crystals in pleomorphic adenomas of parotid glands. J Oral Pathol Med 12 (5):342-346. doi:https://doi.org/10.1111/j.1600-0714.1983.tb00346.x

286. Koklesova L, Liskova A, Samec M, Zhai K, Abotaleb M, Ashrafizadeh M, Brockmueller A, Shakibaei M, Biringer K, Bugos O, Najafi M, Golubnitschaja O, Büsselberg D, Kubatka P (2020) Carotenoids in Cancer Metastasis - Status Quo and Outlook. Biomolecules 10 (12):1653

287. Chimento A, Casaburi I, Avena P, Trotta F, De Luca A, Rago V, Pezzi V, Sirianni R (2019) Cholesterol and Its Metabolites in Tumor Growth: Therapeutic Potential of Statins in Cancer Treatment. Front Endocrinol (Lausanne) 9. doi:10.3389/fendo.2018.00807

288. Llaverias G, Danilo C, Mercier I, Daumer K, Capozza F, Williams TM, Sotgia F, Lisanti MP, Frank PG (2011) Role of Cholesterol in the Development and Progression of Breast Cancer. The American Journal of Pathology 178 (1):402-412. doi:https://doi.org/10.1016/j.ajpath.2010.11.005

289. Warnecke PM, Bestor TH (2000) Cytosine methylation and human cancer. Curr Opin Oncol 12 (1):68-73

290. Lunt SY, Heiden MGV (2011) Aerobic Glycolysis: Meeting the Metabolic Requirements of Cell Proliferation. Annual Review of Cell and Developmental Biology 27 (1):441-464. doi:10.1146/annurev-cellbio-092910-154237

291. Badawy AA-B (2018) Targeting tryptophan availability to tumors: the answer to immune escape? Immunol Cell Biol 96 (10):1026-1034. doi:https://doi.org/10.1111/imcb.12168

292. Betz V, Schneckenburger H, Alleroeder H, Sybrecht G, Meyer J-U (1995) Evaluation of changes in the NADH level between carcinogenic and normal tissue samples by use of fluorescence spectroscopy, vol 2324. International Symposium on Biomedical Optics Europe '94. SPIE,

293. Kalinski T, Hofmann H, Zwönitzer R, Bernarding J, Roessner A (2006) Virtuelle Mikroskopie und digitale Pathologie. Der Pathologe 27 (3):222-227. doi:10.1007/s00292-005-0781-2

294. Haroske G, Zwönitzer R, Hufnagl P, Haroske G, Bürrig KF, Füzesi L, Hofstädter F, Mörz M, Schrader J, Kayser G, Perez-Bouza A, Hufnagl P, Kalinski T, Zwönitzer R, Kommission Digitale P (2018) Leitfaden „Digitale Pathologie in der Diagnostik". Der Pathologe 39 (3):216-221. doi:10.1007/s00292-018-0433-y

295. Al-Janabi S, Huisman A, Van Diest PJ (2012) Digital pathology: current status and future perspectives. Histopathology 61 (1):1-9. doi:https://doi.org/10.1111/j.1365-2559.2011.03814.x

296. Niazi MKK, Parwani AV, Gurcan MN (2019) Digital pathology and artificial intelligence. The Lancet Oncology 20 (5):e253-e261. doi:https://doi.org/10.1016/S1470-2045(19)30154-8

297. Wang L, Mizaikoff B (2008) Application of multivariate data-analysis techniques to biomedical diagnostics based on mid-infrared spectroscopy. Analytical and Bioanalytical Chemistry 391 (5):1641-1654. doi:10.1007/s00216-008-1989-9

298. Baker MJ, Gazi E, Brown MD, Shanks JH, Gardner P, Clarke NW (2008) FTIR-based spectroscopic analysis in the identification of clinically aggressive prostate cancer. Br J Cancer 99 (11):1859-1866. doi:10.1038/sj.bjc.6604753

299. Kazarian SG, Chan KLA (2006) Applications of ATR-FTIR spectroscopic imaging to biomedical samples. Biochim Biophys Acta 1758 (7):858-867. doi:https://doi.org/10.1016/j.bbamem.2006.02.011

300. Petibois C, Desbat B (2010) Clinical application of FTIR imaging: new reasons for hope. Trends Biotechnol 28 (10):495-500. doi:https://doi.org/10.1016/j.tibtech.2010.07.003

301. Magalhães S, Goodfellow BJ, Nunes A (2021) FTIR spectroscopy in biomedical research: how to get the most out of its potential. ApSRv 56 (8-10):869-907. doi:10.1080/05704928.2021.1946822

302. Kümmel A, Selzer P, Beibel M, Gubler H, Parker CN, Gabriel D (2011) Comparison of Multivariate Data Analysis Strategies for High-Content Screening. J Biomol Screen 16 (3):338-347. doi:10.1177/1087057110395390

303. Lavine B, Workman J (2010) Chemometrics. Analytical Chemistry 82 (12):4699-4711. doi:10.1021/ac101202z

304. Ferrari C, Foca G, Ulrici A (2013) Handling large datasets of hyperspectral images: Reducing data size without loss of useful information. Anal Chim Acta 802:29-39. doi:https: //doi.org/10.1016/j.aca.2013.10.009

305. Pilling M, Gardner P (2016) Fundamental developments in infrared spectroscopic imaging for biomedical applications. Chemical Society Reviews 45 (7):1935-1957. doi:10.1039/C5CS00846H

306. Sahu R, Mordechai S (2005) Fourier transform infrared spectroscopy in cancer detection. Future Oncology 1 (5):635-647. doi:10.2217/14796694.1.5.635

307. Fernandez DC, Bhargava R, Hewitt SM, Levin IW (2005) Infrared spectroscopic imaging for histopathologic recognition. Nat Biotechnol 23 (4):469-474. doi:10.1038/nbt1080

308. Haaland DM, Jones HDT, Thomas EV (1997) Multivariate Classification of the Infrared Spectra of Cell and Tissue Samples. Applied Spectroscopy 51 (3):340-345. doi:10.1366/0003702971940468

309. Israel Y, Rachmiel A, Ziv G, Nagler R (2016) Benign and Malignant Salivary Gland Tumors - Clinical and Demographic Characteristics. Anticancer research 36 (8):4151-4154

310. El-Naggar AK, Chan JKC, Grandis JR, Takata T, Slootweg PJ (2017) WHO Classification of Head and Neck Tumours. International Agency for Research on Cancer,

311. Conti C, Ferraris P, Garavaglia M, Giorgini E, Rubini C, Sabbatini S, Tosi G (2009) Microimaging FTIR of head and neck tumors. IV. Microscopy Research and Technique 72 (2):67-75. doi:https://doi.org/10.1002/jemt.20644

312. Srinivasan M, Sedmak D, Jewell S (2002) Effect of Fixatives and Tissue Processing on the Content and Integrity of Nucleic Acids. The American Journal of Pathology 161 (6):1961-1971. doi:https://doi.org/10.1016/S0002-9440(10)64472-0

313. Karlsson JOM, Toner M (1996) Long-term storage of tissues by cryopreservation: critical issues. Biomaterials 17 (3):243-256. doi:https://doi.org/10.1016/0142-9612(96)85562-1

314. Meryman HT (1956) Mechanics of Freezing in Living Cells and Tissues. Science 124 (3221):515-521. doi:10.1126/science.124.3221.515

315. Cocco C, Melis GV, Ferri G-L (2003) Embedding Media for Cryomicrotomy: An Applicative Reappraisal. Appl Immunohistochem Mol Morphol 11 (3):274-280

316. Buesa RJ, Peshkov MV (2009) Histology without xylene. Ann Diagn Pathol 13 (4):246-256. doi:https://doi.org/10.1016/j.anndiagpath.2008.12.005

317. Ali S, Bonnier F, Tfayli A, Lambkin H, Flynn K, McDonagh V, Healy C, Lee TC, Lyng F, Byrne H (2012) Raman spectroscopic analysis of human skin tissue sections ex-vivo: evaluation of the effects of tissue processing and dewaxing. Journal of Biomedical Optics 18 (6):061202

318. Meuse CW, Barker PE (2009) Quantitative Infrared Spectroscopy of Formalin-fixed, Paraffin-embedded Tissue Specimens: Paraffin Wax Removal With Organic Solvents. Appl Immunohistochem Mol Morphol 17 (6):547-552. doi:10.1097/PAI.0b013e3181a9300e

319. Hughes C, Gaunt L, Brown M, Clarke NW, Gardner P (2014) Assessment of paraffin removal from prostate FFPE sections using transmission mode FTIR-FPA imaging. Analytical Methods 6 (4):1028-1035. doi:10.1039/C3AY41308J

320. Zohdi V, Whelan DR, Wood BR, Pearson JT, Bambery KR, Black MJ (2015) Importance of Tissue Preparation Methods in FTIR Micro-Spectroscopical Analysis of Biological Tissues: ‘Traps for New Users’. PLoS One 10 (2):e0116491. doi:10.1371/journal.pone.0116491

321. Hackett MJ, McQuillan JA, El-Assaad F, Aitken JB, Levina A, Cohen DD, Siegele R, Carter EA, Grau GE, Hunt NH, Lay PA (2011) Chemical alterations to murine brain tissue induced by formalin fixation: implications for biospectroscopic imaging and mapping studies of disease pathogenesis. Analyst 136 (14):2941-2952. doi:10.1039/C0AN00269K

322. Stefanakis M, Lorenz A, Bartsch JW, Bassler MC, Wagner A, Brecht M, Pagenstecher A, Schittenhelm J, Boldrini B, Hakelberg SJJos (2021) Formalin fixation as tissue preprocessing for multimodal optical spectroscopy using the example of human brain tumour cross sections. 2021

323. Talari ACS, Martinez MAG, Movasaghi Z, Rehman S, Rehman IU (2017) Advances in Fourier transform infrared (FTIR) spectroscopy of biological tissues. ApSRv 52 (5):456-506. doi:10.1080/05704928.2016.1230863

324. Movasaghi Z, Rehman S, ur Rehman DI (2008) Fourier Transform Infrared (FTIR) Spectroscopy of Biological Tissues. ApSRv 43 (2):134-179. doi:10.1080/05704920701829043

325. Barth A (2007) Infrared spectroscopy of proteins. Biochim Biophys Acta 1767 (9):1073-1101. doi:https://doi.org/10.1016/j.bbabio.2007.06.004

326. Lorenz-Fonfria VA (2020) Infrared Difference Spectroscopy of Proteins: From Bands to Bonds. Chem Rev 120 (7):3466-3576. doi:10.1021/acs.chemrev.9b00449

327. DiDonato D, Brasaemle DL (2003) Fixation Methods for the Study of Lipid Droplets by Immunofluorescence Microscopy. J Histochem Cytochem 51 (6):773-780. doi: 10.1177/002215540305100608

328. Ferlay J, Colombet M, Soerjomataram I, Parkin DM, Piñeros M, Znaor A, Bray F (2021) Cancer statistics for the year 2020: An overview. Int J Cancer 149 (4):778-789. doi:https: //doi.org/10.1002/ijc.33588

329. Agostinis P, Vantieghem A, Merlevede W, de Witte PAM (2002) Hypericin in cancer treatment: more light on the way. The International Journal of Biochemistry & Cell Biology 34 (3):221-241. doi:http://dx.doi.org/10.1016/S1357-2725(01)00126-1

330. Liu Q, Wackenhut F, Hauler O, Scholz M, zur Oven-Krockhaus S, Ritz R, Adam P-M, Brecht M, Meixner AJ (2020) Hypericin: Single Molecule Spectroscopy of an Active Natural Drug. The Journal of Physical Chemistry A 124 (12):2497-2504. doi:10.1021/acs.jpca.9b11532

331. Liu Q, Wackenhut F, Wang L, Hauler O, Roldao JC, Adam P-M, Brecht M, Gierschner J, Meixner AJ (2021) Direct Observation of Structural Heterogeneity and Tautomerization of Single Hypericin Molecules. The Journal of Physical Chemistry Letters 12 (3):1025-1031. doi:10.1021/acs.jpclett.0c03459

332. Liu Q, Wang L, Roldao JC, Adam P-M, Brecht M, Gierschner J, Wackenhut F, Meixner AJ (2021) Theoretical and Experimental Evidence of Two-Step Tautomerization in Hypericin. Advanced Photonics Research 2 (6):2000170. doi:https://doi.org/10.1002/adpr.202000170

333. Wang L, Liu Q, Wackenhut F, Brecht M, Adam P-M, Gierschner J, Meixner AJ (2022) Monitoring tautomerization of single hypericin molecules in a tunable optical λ/2 microcavity. The Journal of Chemical Physics 156 (1):014203. doi:10.1063/5.0078117

334. Kleemann B, Loos B, Scriba TJ, Lang D, Davids LM (2014) St John's Wort (Hypericum perforatum L.) Photomedicine: Hypericin-Photodynamic Therapy Induces Metastatic Melanoma Cell Death. PLoS One 9 (7):e103762. doi:10.1371/journal.pone.0103762

335. Dong X, Zeng Y, Zhang Z, Fu J, You L, He Y, Hao Y, Gu Z, Yu Z, Qu C, Yin X, Ni J, Cruz LJ (2020) Hypericin-mediated photodynamic therapy for the treatment of cancer: a review. Journal of Pharmacy and Pharmacology 73 (4):425-436. doi:10.1093/jpp/rgaa018

336. Nakajima N, Kawashima N (2012) A basic study on Hypericin-PDT in vitro. Photodiagnosis Photodyn Ther 9 (3):196-203. doi:https://doi.org/10.1016/j.pdpdt.2012.01.008

337. Uzdensky AB, Ma L-W, Iani V, Hjortland GO, Steen HB, Moan J (2001) Intracellular Localisation of Hypericin in Human Glioblastoma and Carcinoma Cell Lines. Lasers Med Sci 16 (4):276-283. doi:10.1007/pl00011364

338. Huntosova V, Nadova Z, Dzurova L, Jakusova V, Sureau F, Miskovsky P (2012) Cell death response of U87 glioma cells on hypericin photoactivation is mediated by dynamics of hypericin subcellular distribution and its aggregation in cellular organelles. Photochemical & Photobiological Sciences 11 (9):1428-1436. doi:10.1039/C2PP05409D

339. Ritz R, Wein HT, Dietz K, Schenk M, Roser F, Tatagiba M, Strauss WSL (2007) Photodynamic therapy of malignant glioma with hypericin: comprehensive in vitro study in human glioblastoma cell lines. Int J Oncol 30 (3):659-667

340. Saw CLL, Olivo M, Soo KC, Heng PWS (2006) Delivery of hypericin for photodynamic applications. Cancer Lett 241 (1):23-30. doi:https://doi.org/10.1016/j.canlet.2005.10.020

341. Frantz C, Stewart KM, Weaver VM (2010) The extracellular matrix at a glance. J Cell Sci 123 (24):4195-4200. doi:10.1242/jcs.023820

342. Edmondson R, Broglie JJ, Adcock AF, Yang L (2014) Three-dimensional cell culture systems and their applications in drug discovery and cell-based biosensors. Assay Drug Dev Technol 12 (4):207-218. doi:10.1089/adt.2014.573

343. Olive PL, Durand RE (1994) Drug and radiation resistance in spheroids: cell contact and kinetics. Cancer Metastasis Rev 13 (2):121-138. doi:10.1007/bf00689632

344. Mellor HR, Ferguson DJP, Callaghan R (2005) A model of quiescent tumour microregions for evaluating multicellular resistance to chemotherapeutic drugs. Br J Cancer 93 (3):302-309. doi:10.1038/sj.bjc.6602710

345. Hoffmann OI, Ilmberger C, Magosch S, Joka M, Jauch K-W, Mayer B (2015) Impact of the spheroid model complexity on drug response. J Biotechnol 205:14-23. doi:https: //doi.org/10.1016/j.jbiotec.2015.02.029

346. Mehta G, Hsiao AY, Ingram M, Luker GD, Takayama S (2012) Opportunities and challenges for use of tumor spheroids as models to test drug delivery and efficacy. Journal of Controlled Release 164 (2):192-204. doi:https://doi.org/10.1016/j.jconrel.2012.04.045

347. Kamuhabwa AAR, Huygens A, De Witte PAM (2003) Photodynamic therapy of transitional cell carcinoma multicellular tumor spheroids with hypericin. Int J Oncol 23 (5):1445-1450. doi:10.3892/ijo.23.5.1445

348. Huygens A, Huyghe D, Bormans G, Verbruggen A, Kamuhabwa AR, Roskams T, De Witte PAM (2003) Accumulation and Photocytotoxicity of Hypericin and Analogs in Two- and Three-Dimensional Cultures of Transitional Cell Carcinoma Cells. Photochemistry and Photobiology 78 (6):607-614. doi:https://doi.org/10.1562/0031-8655(2003)0780607AAPOHA2.0.CO2

349. Huygens A, Kamuhabwa AR, Roskams T, Cleynenbreugel Bv, Poppel Hv, Witte PAMd (2005) Permeation of hypericin in spheroids composed of different grade transitional cell carcinoma cell lines and normal human urothelial cells. J Urol 174 (1):69-72. doi:doi:10.1097/01.ju.0000162037.49102.56

350. Roelants M, Van Cleynenbreugel B, Lerut E, Van Poppel H, de Witte PAM (2011) Human serum albumin as key mediator of the differential accumulation of hypericin in normal urothelial cell spheroids versusurothelial cell carcinoma spheroids. Photochemical & Photobiological Sciences 10 (1):151-159. doi:10.1039/C0PP00109K

351. Kessel D (2020) Hypericin Accumulation as a Determinant of PDT Efficacy. Photochemistry and Photobiology 96 (5):1144-1147. doi:https://doi.org/10.1111/php.13302

352. Crnolatac I, Huygens A, Agostinis P, Kamuhabwa AR, Maes J, Van Aerschot A, De Witte PAM (2007) In vitro accumulation and permeation of hypericin and lipophilic analogues in 2-D and 3-D cellular systems. Int J Oncol 30 (2):319-324. doi:10.3892/ijo.30.2.319

353. Casciari JJ, Sotirchos SV, Sutherland RM (1988) Glucose Diffusivity in Multicellular Tumor Spheroids. Cancer Res 48 (14):3905-3909

354. Riffle S, Hegde RS (2017) Modeling tumor cell adaptations to hypoxia in multicellular tumor spheroids. J Exp Clin Cancer Res 36 (1):102. doi:10.1186/s13046-017-0570-9

355. Keith B, Simon MC (2007) Hypoxia-Inducible Factors, Stem Cells, and Cancer. Cell 129 (3):465-472. doi:https://doi.org/10.1016/j.cell.2007.04.019

356. Lakner PH, Monaghan MG, Möller Y, Olayioye MA, Schenke-Layland K (2017) Applying phasor approach analysis of multiphoton FLIM measurements to probe the metabolic activity of three-dimensional in vitro cell culture models. Sci Rep 7 (1):42730. doi:10.1038/srep42730

357. Cong A, Pimenta RML, Lee HB, Mereddy V, Holy J, Heikal AA (2019) Two-photon fluorescence lifetime imaging of intrinsic NADH in three-dimensional tumor models. Cytometry Part A 95 (1):80-92. doi:https://doi.org/10.1002/cyto.a.23632

358. Okkelman IA, Dmitriev RI, Foley T, Papkovsky DB (2016) Use of Fluorescence Lifetime Imaging Microscopy (FLIM) as a Timer of Cell Cycle S Phase. PLoS One 11 (12):e0167385. doi:10.1371/journal.pone.0167385

359. Penjweini R, Deville S, D'Olieslaeger L, Berden M, Ameloot M, Ethirajan A (2015) Intracellular localization and dynamics of Hypericin loaded PLLA nanocarriers by image correlation spectroscopy. Journal of Controlled Release 218:82-93. doi:https://doi.org/10.1016/j.jconrel.2015.09.064

360. Taroni P, Valentini G, Comelli D, D'Andrea C, Cubeddu R, Hu D-N, Roberts JE (2005) Time-resolved Microspectrofluorimetry and Fluorescence Lifetime Imaging of Hypericin in Human Retinal Pigment Epithelial Cells. Photochemistry and Photobiology 81 (3):524-528. doi:https://doi.org/10.1111/j.1751-1097.2005.tb00220.x

361. Huntosova V, Alvarez L, Bryndzova L, Nadova Z, Jancura D, Buriankova L, Bonneau S, Brault D, Miskovsky P, Sureau F (2010) Interaction dynamics of hypericin with low-density lipoproteins and U87-MG cells. Int J Pharm 389 (1):32-40. doi:https://doi.org/10.1016/j.ijpharm.2010.01.010

362. Lakowicz JR, Szmacinski H, Nowaczyk K, Berndt KW, Johnson M (1992) Fluorescence lifetime imaging. Analytical Biochemistry 202 (2):316-330. doi:https://doi.org/10.1016/0003-2697(92)90112-K

363. Suhling K, French PMW, Phillips D (2005) Time-resolved fluorescence microscopy. Photochemical & Photobiological Sciences 4 (1):13-22. doi:10.1039/B412924P

364. Chang MC, Petrich JW, McDonald DB, Fleming GR (1983) Nonexponential fluorescence decay of tryptophan, tryptophylglycine, and glycyltryptophan. Journal of the American Chemical Society 105 (12):3819-3824. doi:10.1021/ja00350a013

365. Morsy MA, Al-Somali AM, Suwaiyan A (1999) Fluorescence of Thymine Tautomers at Room Temperature in Aqueous Solutions. The Journal of Physical Chemistry B 103 (50):11205-11210. doi:10.1021/jp990858e

366. Carlsson J, Acker H (1988) Relations between ph, oxygen partial pressure and growth in cultured cell spheroids. Int J Cancer 42 (5):715-720. doi:https://doi.org/10.1002/ijc.2910420515

367. Chowdhury PK, Ashby KD, Datta A, Petrich JW (2000) Effect of pH on the Fluorescence and Absorption Spectra of Hypericin in Reverse Micelles. Photochemistry and Photobiology 72 (5):612-618. doi:https://doi.org/10.1562/0031-8655(2000)0720612EOPOTF2.0.CO2

368. Liu J, Saw C, Olivo M, Sudhaharan T, Ahmed S, Heng P, Wohland T (2009) Study of interaction of hypericin and its pharmaceutical preparation by fluorescence techniques. Journal of Biomedical Optics 14 (1):014003

369. Liu PY, Chin LK, Ser W, Chen HF, Hsieh CM, Lee CH, Sung KB, Ayi TC, Yap PH, Liedberg B, Wang K, Bourouina T, Leprince-Wang Y (2016) Cell refractive index for cell biology and disease diagnosis: past, present and future. LChip 16 (4):634-644. doi:10.1039/C5LC01445J

370. Strickler SJ, Berg RA (1962) Relationship between Absorption Intensity and Fluorescence Lifetime of Molecules. The Journal of Chemical Physics 37 (4):814-822. doi:10.1063/1.1733166

371. Tregidgo C, Levitt J, Suhling K (2008) Effect of refractive index on the fluorescence lifetime of green fluorescent protein. Journal of Biomedical Optics 13 (3):031218

372. Khaitan D, Chandna S, Arya MB, Dwarakanath BS (2006) Establishment and characterization of multicellular spheroids from a human glioma cell line; Implications for tumor therapy. J Transl Med 4:12-12. doi:10.1186/1479-5876-4-12

373. Acker H, Holtermann G, Bölling B, Carlsson J (1992) Influence of glucose on metabolism and growth of rat glioma cells (C6) in multicellular spheroid culture. Int J Cancer 52 (2):279-285. doi:https://doi.org/10.1002/ijc.2910520221

374. Kunz-Schughart LA, Doetsch J, Mueller-Klieser W, Groebe K (2000) Proliferative activity and tumorigenic conversion: impact on cellular metabolism in 3-D culture. American Journal of Physiology-Cell Physiology 278 (4):C765-C780. doi:10.1152/ajpcell.2000.278.4.C765

375. Mukherjee P, Adhikary R, Halder M, Petrich JW, Miskovsky P (2008) Accumulation and Interaction of Hypericin in Low-density Lipoprotein— A Photophysical Study. Photochemistry and Photobiology 84 (3):706-712. doi:https://doi.org/10.1111/j.1751-1097.2007.00234.x

376. Byeon CC, McKerns MM, Sun W, Nordlund TM, Lawson CM, Gray GM (2004) Excited state lifetime and intersystem crossing rate of asymmetric pentaazadentate porphyrin-like metal complexes. Applied Physics Letters 84 (25):5174-5176. doi:10.1063/1.1763983

377. Chandana SR, Movva S, Arora M, Singh T (2008) Primary brain tumors in adults. Am Fam Physician 77 (10):1423-1430

378. Oliver TG, Wechsler-Reya RJ (2004) Getting at the Root and Stem of Brain Tumors. Neuron 42 (6):885-888. doi:https://doi.org/10.1016/j.neuron.2004.06.011

379. Castro MG, Cowen R, Williamson IK, David A, Jimenez-Dalmaroni MJ, Yuan X, Bigliari A, Williams JC, Hu J, Lowenstein PR (2003) Current and future strategies for the treatment of malignant brain tumors. Pharmacol Ther 98 (1):71-108. doi:https://doi.org/10.1016/S0163-7258(03)00014-7

380. Tan AC, Ashley DM, López GY, Malinzak M, Friedman HS, Khasraw M (2020) Management of glioblastoma: State of the art and future directions. CA Cancer J Clin 70 (4):299-312. doi:https://doi.org/10.3322/caac.21613

381. Behin A, Hoang-Xuan K, Carpentier AF, Delattre J-Y (2003) Primary brain tumours in adults. The Lancet 361 (9354):323-331. doi:https://doi.org/10.1016/S0140-6736(03)12328-8

382. Louis DN, Perry A, Reifenberger G, von Deimling A, Figarella-Branger D, Cavenee WK, Ohgaki H, Wiestler OD, Kleihues P, Ellison DW (2016) The 2016 World Health Organization Classification of Tumors of the Central Nervous System: a summary. Acta Neuropathol 131 (6):803-820. doi:10.1007/s00401-016-1545-1

383. Tran B, Rosenthal MA (2010) Survival comparison between glioblastoma multiforme and other incurable cancers. J Clin Neurosci 17 (4):417-421. doi:https://doi.org/10.1016/j.jocn.2009.09.004

384. Eljamel MS (2008) Fluorescence image-guided surgery of brain tumors: Explained step-by-step. Photodiagnosis Photodyn Ther 5 (4):260-263. doi:https://doi.org/10.1016/j.pdpdt.2008.11.003

385. Nagaya T, Nakamura YA, Choyke PL, Kobayashi H (2017) Fluorescence-Guided Surgery. Front Oncol 7. doi:10.3389/fonc.2017.00314

386. Wei L, Roberts DW, Sanai N, Liu JTC (2019) Visualization technologies for 5-ALA-based fluorescence-guided surgeries. Journal of Neuro-Oncology 141 (3):495-505. doi:10.1007/s11060-018-03077-9

387. Ahrens LC, Krabbenhøft MG, Hansen RW, Mikic N, Pedersen CB, Poulsen FR, Korshoej AR (2022) Effect of 5-Aminolevulinic Acid and Sodium Fluorescein on the Extent of Resection in High-Grade Gliomas and Brain Metastasis. Cancers (Basel) 14 (3):617

388. Tewari KM, Eggleston IM (2018) Chemical approaches for the enhancement of 5-aminolevulinic acid-based photodynamic therapy and photodiagnosis. Photochemical & Photobiological Sciences 17 (11):1553-1572. doi:10.1039/C8PP00362A

389. Graham CA, Cloughesy TF (2004) Brain tumor treatment: Chemotherapy and other new developments. Semin Oncol Nurs 20 (4):260-272. doi:https://doi.org/10.1016/j.soncn.2004.07.006

390. Herbert S, Walter S 5-ALA in the management of malignant glioma. Lasers in Surgery and Medicine 0 (0). doi:10.1002/lsm.22933

391. Castano AP, Demidova TN, Hamblin MR (2004) Mechanisms in photodynamic therapy: part one—photosensitizers, photochemistry and cellular localization. Photodiagnosis Photodyn Ther 1 (4):279-293. doi:https://doi.org/10.1016/S1572-1000(05)00007-4

392. Mahmoudi K, Garvey KL, Bouras A, Cramer G, Stepp H, Jesu Raj JG, Bozec D, Busch TM, Hadjipanayis CG (2019) 5-aminolevulinic acid photodynamic therapy for the treatment of high-grade gliomas. Journal of Neuro-Oncology 141 (3):595-607. doi:10.1007/s11060-019-03103-4

393. Cornelius JF, Slotty PJ, El Khatib M, Giannakis A, Senger B, Steiger HJ (2014) Enhancing the effect of 5-aminolevulinic acid based photodynamic therapy in human meningioma cells. Photodiagnosis Photodyn Ther 11 (1):1-6. doi:https://doi.org/10.1016/j.pdpdt.2014.01.001

394. Shah ET, Mesrati HAO, Aldallal UJ, Abdulwahab F, Henari FZ, Safrany ST (2021) Assessing the photodynamic therapeutic effects of 5-aminolevulinic acid on human colon cancer cells using light-emitting diodes. World Acad Sci J 3 (5):43. doi:10.3892/wasj.2021.114

395. Guney Eskiler G, Deveci Ozkan A, Sozen Kucukkara E, Kamanlı AF, Gunoğlu B, Yıldız MZ (2020) Optimization of 5-aminolevulinic acid-based photodynamic therapy protocol for breast cancer cells. Photodiagnosis Photodyn Ther 31:101854. doi:https://doi.org/10.1016/j.pdpdt.2020.101854

396. Atif M, Fakhar-e-Alam M, Firdous S, Zaidi SSZ, Suleman R, Ikram M (2010) Study of the efficacy of 5-ALA mediated photodynamic therapy on human rhabdomyosarcoma cell line (RD). Laser Physics Letters 7 (10):757-764. doi:10.1002/lapl.201010061

397. Ehrenberg B, Anderson JL, Foote CS (1998) Kinetics and Yield of Singlet Oxygen Photosensitized by Hypericin in Organic and Biological Media. Photochemistry and Photobiology 68 (2):135-140. doi:10.1111/j.1751-1097.1998.tb02479.x

398. Delaey EM, Obermuëller R, Zupkó I, De Vos D, Falk H, De Witte PAM (2001) In Vitro Study of the Photocytotoxicity of Some Hypericin Analogs on Different Cell Lines. Photochemistry and Photobiology 74 (2):164-171. doi:https://doi.org/10.1562/0031-8655(2001)0740164IVSOTP2.0.CO2

399. Kanduc D, Mittelman A, Serpico R, Sinigaglia E, Sinha AA, Natale C, Santacroce R, Di Corcia MG, Lucchese A, Dini L, Pani P, Santacroce S, Simone S, Bucci R, Farber E (2002) Cell death: Apoptosis versus necrosis (Review). Int J Oncol 21 (1):165-170. doi:10.3892/ijo.21.1.165

400. D'Arcy MS (2019) Cell death: a review of the major forms of apoptosis, necrosis and autophagy. Cell Biol Int 43 (6):582-592. doi:https://doi.org/10.1002/cbin.11137

401. Saraste A, Pulkki K (2000) Morphologic and biochemical hallmarks of apoptosis. Cardiovasc Res 45 (3):528-537. doi:10.1016/s0008-6363(99)00384-3

402. Coleman ML, Sahai EA, Yeo M, Bosch M, Dewar A, Olson MF (2001) Membrane blebbing during apoptosis results from caspase-mediated activation of ROCK I. Nat Cell Biol 3 (4):339-345. doi:10.1038/35070009

403. Van Cruchten S, Van den Broeck W (2002) Morphological and Biochemical Aspects of Apoptosis, Oncosis and Necrosis. Anat Histol Embryol 31 (4):214-223. doi:https://doi.org/10.1046/j.1439-0264.2002.00398.x

404. Rana PS, Mudrak NJ, Lopez R, Lynn M, Kershner L, Model MA (2017) Phase separation in necrotic cells. Biochemical and Biophysical Research Communications 492 (3):300-303. doi:https: //doi.org/10.1016/j.bbrc.2017.08.123

405. Yu P, Zhang X, Liu N, Tang L, Peng C, Chen X (2021) Pyroptosis: mechanisms and diseases. Signal Transduction and Targeted Therapy 6 (1):128. doi:10.1038/s41392-021-00507-5

406. Tonnus W, Meyer C, Paliege A, Belavgeni A, von Mässenhausen A, Bornstein SR, Hugo C, Becker JU, Linkermann A (2019) The pathological features of regulated necrosis. The Journal of Pathology 247 (5):697-707. doi:https://doi.org/10.1002/path.5248

407. Zhang Q, Li Z-h, Li Y-y, Shi S-j, Zhou S-w, Fu Y-y, Zhang Q, Yang X, Fu R-q, Lu L-c (2015) Hypericin-photodynamic therapy induces human umbilical vein endothelial cell apoptosis. Sci Rep 5:18398. doi:10.1038/srep18398

408. Barathan M, Mariappan V, Shankar EM, Abdullah BJ, Goh KL, Vadivelu J (2013) Hypericin-photodynamic therapy leads to interleukin-6 secretion by HepG2 cells and their apoptosis via recruitment of BH3 interacting-domain death agonist and caspases. Cell Death Dis 4 (6):e697-e697. doi:10.1038/cddis.2013.219

409. Berlanda J, Kiesslich T, Oberdanner CB, Obermair FJ, Krammer B, Plaetzer K (2006) Characterization of Apoptosis Induced by Photodynamic Treatment with Hypericin in A431 Human Epidermoid Carcinoma Cells. 25 (1-2):173-188. doi:10.1615/JEnvironPatholToxicolOncol.v25.i1-2.100

410. Mikeš J, Kleban J, Sačková V, Horváth V, Jamborová E, Vaculová A, Kozubík A, Hofmanová J, Fedoročko P (2007) Necrosis predominates in the cell death of human colon adenocarcinoma HT-29 cells treated under variable conditions of photodynamic therapy with hypericin. Photochemical & Photobiological Sciences 6 (7):758-766. doi:10.1039/B700350A

411. Pfaffel-Schubart G, Scalfi-Happ C, Rück A (2008) Early and late apoptotic events induced in human glioblastoma cells by Hypericin PDT. Medical Laser Application 23 (1):25-30. doi:https: //doi.org/10.1016/j.mla.2007.11.003

412. Pevna V, Wagnières G, Huntosova V (2021) Autophagy and Apoptosis Induced in U87 MG Glioblastoma Cells by Hypericin-Mediated Photodynamic Therapy Can Be Photobiomodulated with 808 nm Light. Biomedicines 9 (11):1703

413. Benson RS, Heer S, Dive C, Watson AJ (1996) Characterization of cell volume loss in CEM-C7A cells during dexamethasone-induced apoptosis. American Journal of Physiology-Cell Physiology 270 (4):C1190-C1203. doi:10.1152/ajpcell.1996.270.4.C1190

414. Doonan F, Cotter TG (2008) Morphological assessment of apoptosis. Methods 44 (3):200-204. doi:https://doi.org/10.1016/j.ymeth.2007.11.006

415. Zhang Y, Chen X, Gueydan C, Han J (2018) Plasma membrane changes during programmed cell deaths. Cell Res 28 (1):9-21. doi:10.1038/cr.2017.133

416. Fackler OT, Grosse R (2008) Cell motility through plasma membrane blebbing. J Cell Biol 181 (6):879-884. doi:10.1083/jcb.200802081

417. Gores GJ, Herman B, Lemasters JJ (1990) Plasma membrane bleb formation and rupture: A common feature of hepatocellular injury. Hepatology 11 (4):690-698. doi:https: //doi.org/10.1002/hep.1840110425

418. Bovellan M, Fritzsche M, Stevens C, Charras G (2010) Death-associated protein kinase (DAPK) and signal transduction: blebbing in programmed cell death. The FEBS Journal 277 (1):58-65. doi:https://doi.org/10.1111/j.1742-4658.2009.07412.x

419. Okada Y, Maeno E, Shimizu T, Dezaki K, Wang J, Morishima S (2001) Receptor-mediated control of regulatory volume decrease (RVD) and apoptotic volume decrease (AVD). The Journal of Physiology 532 (1):3-16. doi:https://doi.org/10.1111/j.1469-7793.2001.0003g.x

420. Rello S, Stockert JC, Moreno V, Gámez A, Pacheco M, Juarranz A, Cañete M, Villanueva A (2005) Morphological criteria to distinguish cell death induced by apoptotic and necrotic treatments. Apoptosis 10 (1):201-208. doi:10.1007/s10495-005-6075-6

421. Danese A, Patergnani S, Bonora M, Wieckowski MR, Previati M, Giorgi C, Pinton P (2017) Calcium regulates cell death in cancer: Roles of the mitochondria and mitochondria-associated membranes (MAMs). Biochim Biophys Acta 1858 (8):615-627. doi:https: //doi.org/10.1016/j.bbabio.2017.01.003

422. Kim J-S, He L, Lemasters JJ (2003) Mitochondrial permeability transition: a common pathway to necrosis and apoptosis. Biochemical and Biophysical Research Communications 304 (3):463-470. doi:https://doi.org/10.1016/S0006-291X(03)00618-1

423. Iurlaro R, Muñoz-Pinedo C (2016) Cell death induced by endoplasmic reticulum stress. The FEBS Journal 283 (14):2640-2652. doi:https://doi.org/10.1111/febs.13598

424. Orrenius S, Gogvadze V, Zhivotovsky B (2015) Calcium and mitochondria in the regulation of cell death. Biochemical and Biophysical Research Communications 460 (1):72-81. doi:https: //doi.org/10.1016/j.bbrc.2015.01.137

425. Tabas I, Ron D (2011) Integrating the mechanisms of apoptosis induced by endoplasmic reticulum stress. Nat Cell Biol 13 (3):184-190. doi:10.1038/ncb0311-184

426. Gorman AM, Healy SJM, Jäger R, Samali A (2012) Stress management at the ER: Regulators of ER stress-induced apoptosis. Pharmacol Ther 134 (3):306-316. doi:https: //doi.org/10.1016/j.pharmthera.2012.02.003

427. Logue SE, Cleary P, Saveljeva S, Samali A (2013) New directions in ER stress-induced cell death. Apoptosis 18 (5):537-546. doi:10.1007/s10495-013-0818-6

428. Ullman E, Fan Y, Stawowczyk M, Chen HM, Yue Z, Zong WX (2008) Autophagy promotes necrosis in apoptosis-deficient cells in response to ER stress. Cell Death Differ 15 (2):422-425. doi:10.1038/sj.cdd.4402234

429. Shore GC, Papa FR, Oakes SA (2011) Signaling cell death from the endoplasmic reticulum stress response. Curr Opin Cell Biol 23 (2):143-149. doi:https://doi.org/10.1016/j.ceb.2010.11.003

430. Redza-Dutordoir M, Averill-Bates DA (2016) Activation of apoptosis signalling pathways by reactive oxygen species. Biochim Biophys Acta 1863 (12):2977-2992. doi:https: //doi.org/10.1016/j.bbamcr.2016.09.012

431. Lin H, Peng Y, Li J, Wang Z, Chen S, Qing X, Pu F, Lei M, Shao Z (2021) Reactive Oxygen Species Regulate Endoplasmic Reticulum Stress and ER-Mitochondrial Ca2+Crosstalk to Promote Programmed Necrosis of Rat Nucleus Pulposus Cells under Compression. Oxid Med Cell Longev 2021:8810698. doi:10.1155/2021/8810698

Appendix

A1. Supplementary Information for Chapter 2.1.2: Mathematical Description of Mie Scattering

In the Mie formalism, electromagnetic fields, travelling in a homogeneous, isotropic medium (vacuum or single particle), need to fulfil the vector wave equations $\nabla^2 E + k^2 E = 0$ and $\nabla^2 B + k^2 B = 0$ with $k^2 = \omega^2 \varepsilon \mu$ at continuous permeability μ and continuous, complex permittivity ε that are based on Maxwell's equations. Both formulas include the light wave vector k, which is influenced by the surrounding medium and described by the angular frequency of the field ω, μ and ε. According to Maxwell, the fields additionally depend on each other by $\nabla \times E = i\omega\mu B$ and $\nabla \times B = -i\omega\varepsilon E$ and show no divergence due to $\nabla \cdot E = 0$ and $\nabla \cdot B = 0$. Two vector functions M and N are established with respect to these criteria, but can additionally be expressed by a product of a scalar function α and a (constant) vector. If the scalar function α is a solution to the scalar wave equation $\nabla^2 \alpha + k^2 \alpha = 0$, the conditions for the vector wave equations are fulfilled. This allows a reduction of the problem, as only a solution for α need to be found that serves the scalar wave equation. Since α is the key function to satisfy the vector wave equations, it is also considered as the generating function for the vector harmonics M. Waves by a homogeneous sphere justify α to be ideally constructed in spherical polar coordinates (r, θ, ϕ). Consequently, the linearly independent solution of the scalar wave equation by using α in spherical polar coordinates results in a three-term expression, also depicted in spherical polar coordinates [94,95]:

$$\text{Term (1): } \Theta_{even} = \cos(m\phi) \text{ and } \Theta_{odd} = \sin(m\phi) \text{ with } m \geq 0 \tag{A1.1}$$

$$\text{Term (2): } \int_{-1}^{1} P_l^m \cos(\theta) P_{l'}^m \cos(\theta) d\theta = \delta_{l,l'} \frac{2}{2l+1} \frac{(l+m)!}{(l-m)!} \text{ with } \theta = \pi \text{ and } \theta = 0,\ l = m, m+1 \ldots \tag{A1.2}$$

$$\text{Term (3): } j_l(\rho) = \sqrt{\frac{\pi}{2\rho}} J_{l+1/2}(\rho) \text{ and } y_l(\rho) = \sqrt{\frac{\pi}{2\rho}} Y_{l+1/2}(\rho) \text{ with } \rho = kr \tag{A1.3}$$

The first term (1) assumes the generating function α to be only dependent on the azimuthal angle ϕ, effecting all values m to be equal or higher than one. Term (2) refers to orthogonal Legendre functions of the first kind, including degree l and order m. Additionally, the Legendre functions are represented by the Kronecker delta $\delta_{l,l'}$, which is either unity at $l = l'$ or otherwise assigned to zero. In case the order $m = 0$, the Legendre functions are denoted as Legendre polynomials P_l. The third solutions (3) are the first and second kind spherical Bessel functions $j_l(\rho)$ and $y_l(\rho)$ with a dimensionless variable $\rho = kr$ and a constant factor $\sqrt{\pi/2}$. To summarize the solution of the scalar wave equation, two final equations of α are established [94,95]:

$$\alpha_{even,m,l} = \cos(m\phi) P_l^m\big(cos(\theta)\big) z_l(kr) \tag{A1.4}$$

$$\alpha_{odd,m,l} = \sin(m\phi) P_l^m\big(cos(\theta)\big) z_l(kr) \tag{A1.5}$$

with z_l representing either $j_l(\rho)$, $y_l(\rho)$ or any linear combination of both spherical Bessel functions. As a result, the vector wave equations for the vector functions M and N are now satisfied and can be delineated by these solutions, generating the vector spherical harmonics $M_{odd,m,l}$ and $N_{even,m,l}$. Any description of a scattering wave inside or outside a sphere is based on the infinite expansion of these vector spherical harmonics. To develop the expansion, all related coefficients need to be initially determined. For that reason, a x-polarized, scattered plane wave $E_i = E_0 e^{ikrcos\theta} \hat{e}_x$ shown in spherical polar coordinates with $\hat{e}_x = \sin(\theta) cos(\phi) \hat{e}_r + \cos(\theta)\cos(\phi)\,\hat{e}_\theta - sin(\phi)\hat{e}_\phi$ is expanded by applying the vector spherical harmonics [94,95]:

$$E_i = E_0 \sum_{l=1}^{\infty} i^l \frac{2l+1}{l(l+1)} \big(M_{odd,1,l} - iN_{even,1,l}\big) \tag{A1.6}$$

whereby $E_0 i^l\, 2l + 1/l(l+1)$ depicts the coefficient for $M_{odd,m,l}$ and $-iE_0 i^l\, 2l + 1/l(l+1)$ is the coefficient for $N_{even,m,l}$. Based on eq. A1.6, the electric and magnetic fields of incident and scattered x-polarized plane waves can be separately developed inside and outside the homogeneous, isotropic sphere. Due to the overall orthogonality of the vector spherical harmonics, the defined boundary conditions at the sphere's edge and the underlying incident plane wave expansion, different plane wave expansions are evolved for the electric fields scattered from and inside the sphere. While only $j_l(\rho)$ is applicable as Bessel function to describe the electric field within the sphere, the outgoing asymptotic Hankel function h_l, a specialized Bessel function, is appropriate to characterize the scattering electric field. As a consequence, two different field expansions derive [94,95]:

$$E_{inside} = \int_{l=1}^{\infty} E_l (c_l M_{odd,1,l} - i d_l N_{even,1,l}) \tag{A1.7}$$

$$E_{scattering} = \int_{l=1}^{\infty} E_l (i a_l N_{even,1,l} - b_l M_{odd,1,l}) \tag{A1.8}$$

with $E_l = i^l E_0\,(2l+1)/l(l+1)$. Corresponding magnetic field expansions result from the respective curls of the electric field expansions. Both fields of the sphere E_{inside} and $E_{scattering}$ are additionally angle-dependent, which is expressed by the implementation of θ-including functions π_l and τ_l for $M_{odd,m,l}$ and $N_{even,m,l}$. As functions of $\sin(\theta)$ and $\cos(\theta)$, π_l and τ_l depict alternating functions that are defined as [94,95]:

$$\pi_l = \frac{P_l^1}{\sin(\theta)} = \frac{2l-1}{l-1}\cos(\theta)\,\pi_{l-1} - \frac{l}{l-1}\pi_{l-2} \tag{A1.9}$$

$$\tau_l = \frac{dP_l^1}{d\theta} = lcos(\theta)\pi_l - (l+1)\pi_{l-1} \tag{A1.10}$$

Within a range between 0° and 360°, positive and negative values can be assigned for both, revealing a varying number and size of lobes with increasing l and differences in lobe orientation. As a result, the plane wave behavior of a sphere is strongly influenced by the angle θ, which specifies the dominant direction of wave propagation or scattering. This directly correlates with the sphere size, since a more pronounced forward-directed scattering appears with increasing size. Besides, further sphere-related attributes, such as the refractive index N and the surrounding medium, impact the scattered and inner plane wave. These are represented by the so-far unknown coefficients c_l and d_l in eq. A1.11 / A1.12 as well as a_l and b_l in eq. A1.13 / A1.14, which are the inside and scattering coefficients, respectively. All coefficients are obtained by solving the respective linear equations in the corresponding expansion, considering boundary conditions in-between the sphere and the medium. The final solutions of the sphere inside and scattering coefficients are [94,95,87]:

$$c_l = \frac{\mu_1 j_l(x)[xh_l(x)]' - \mu_1 h_l(x)[xj_l(x)]'}{\mu_1 j_l(mx)[xh_l(x)]' - \mu h_l(x)[mxj_l(mx)]'} \tag{A1.11}$$

$$d_l = \frac{\mu_1 m j_l(x)[xh_l(x)]' - \mu_1 m h_l(x)[xj_l(x)]'}{\mu m^2 j_l(mx)[xh_l(x)]' - \mu_1 h_l(x)[mxj_l(mx)]'} \tag{A1.12}$$

$$a_l = \frac{\mu m^2 j_l(mx)[xj_l(x)]' - \mu_1 j_n(x)[mxj_l(mx)]'}{\mu m^2 j_l(mx)[xh_l(x)]' - \mu_1 h_l(x)[mxj_l(mx)]'} \tag{A1.13}$$

$$b_l = \frac{\mu_1 j_l(mx)[xj_l(x)]' - \mu j_l(x)[mxj_l(mx)]'}{\mu_1 j_l(mx)[xh_l(x)]' - \mu h_l(x)[mxj_l(mx)]'} \tag{A1.14}$$

whereby the sphere size is specified by $x = 2\pi Nr/\lambda$ and the refractive index N is given by the relative refractive index $m = N_1/N$. For the size parameter, r is the sphere radius, whereas N_1 and N stand for the refractive index of the sphere and the surrounding medium, respectively. All expressions in brackets with prime imply the derivation of the respective argument within the brackets. A simplification of the scattering coefficient equations (A1.13 and A1.14) can be achieved by considering $N_1 = N$ and introducing the Riccati-Bessel functions, substituting $\Psi_l(\rho) = \rho j_l(\rho)$ and $\xi_l(\rho) = \rho h_l(\rho)$. For certain sphere sizes or frequencies, the coefficient dominators of a_l and b_l can become small, which causes the related scattering modes to dominate the scattering field. As these sphere-characteristic frequencies are mainly complex frequencies, composed of a real and imaginary part, no direct connection to the initiating electromagnetic frequency can often be drawn. Only if the imaginary part is neglectable, the sphere frequency correlates with the incident electromagnetic frequency that triggers the excitation of the scattering modes. In general, the overall scattering pattern of a spherical particle consists of a high number of superimposing normal modes, which are differently weighted depending on the corresponding scattering coefficients. These patterns are normally characterized by an interference structure, superimposed by an irregular ripple behavior [94,95].

A2. Supplementary Information for Manuscript I: Comparison of Whiskbroom and Pushbroom Darkfield Elastic Light Scattering Spectroscopic Imaging for Head and Neck Cancer Identification in a Mouse Model

Data preprocessing is essential to extract the hidden ELS information from the obtained image spectra for Whiskbroom and Pushbroom imaging. Several preprocessing steps were performed in order to allow a tissue differentiation based on ELS from the lingual tissue specimens: moving average smoothing with 47 segment points, baseline offset correction, gap derivation (1st derivative, gap size: 15 pts.) and range-normalization. Exemplary preprocessed ELS spectra for EP, GM and AT, acquired by both imaging methods, are shown in Fig. S3.1.

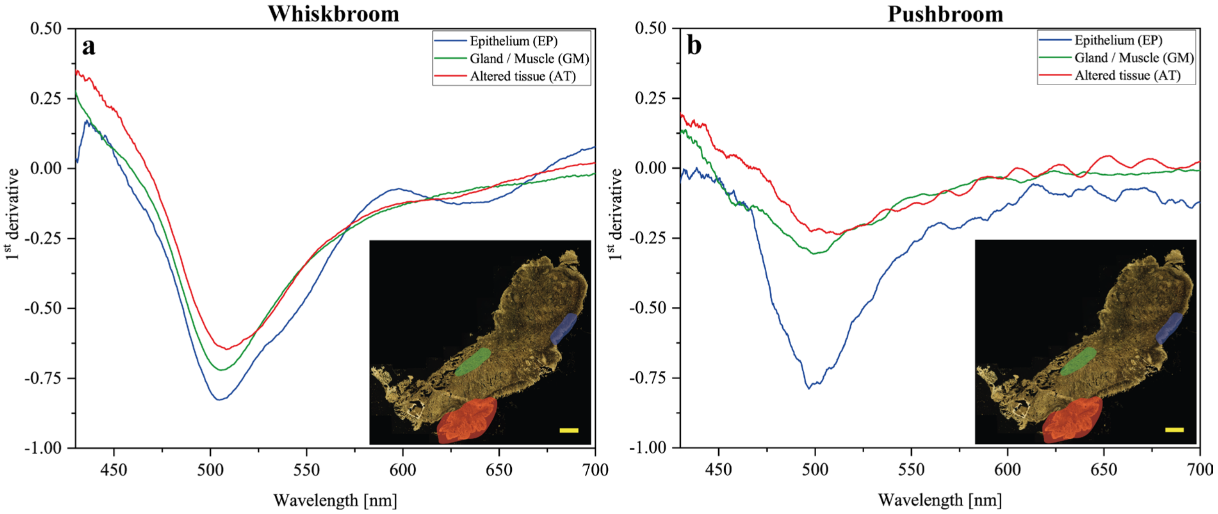

Figure S3.1. *Exemplary preprocessed ELS spectra of EP (blue), GM (green) and AT (red) tissue used for Whiskbroom (a) and Pushbroom (b) PCA-DA model formation. By applying the described preprocessing steps (moving average smoothing with 47 segment points, baseline offset correction, gap derivation (1st derivative, gap size: 15 pts.) and range-normalization), the periodic scattering structure can be extracted and become more clearly visible. Although spectra were acquired in a wavelength range of 412 - 975 nm for Whiskbroom and 398 - 715 nm for Pushbroom detection, only the wavelength region from 430 - 700 nm is shown for reasons of comparability. Each preprocessed spectrum corresponds to one tissue type, exemplarily indicated by the colored ellipses in the DF image of one tissue section. Yellow scale bar: 1000 µm.*

For the sake of completeness, the respective 2D scores plots of PC3 vs. PC2 and PC4 vs. PC3 for the Whiskbroom and Pushbroom PCA are displayed in Fig. S3.2 and S3.3. Corresponding loadings plots for both PCAs are additionally illustrated.

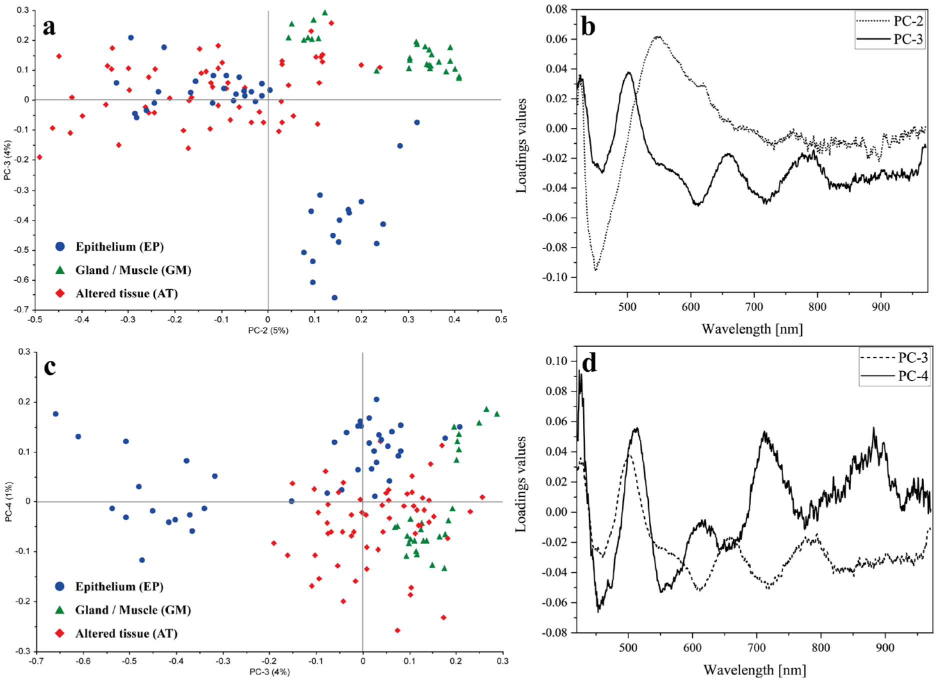

Figure S3.2. *2D scores plot of the Whiskbroom PCA for the differentiation of EP (blue), GM (green) and AT (red). In (a): The 2D scores plot of PC3 against PC2 reveals the distinct separation of the GM and AT groups and a splitting of the EP cluster in two, of which one is completely overlapping with the AT cluster. A further splitting of the GM into two subpopulations is also observable. PC2 explains 5 %, whereas PC3 represents 4 % of the overall variance. In (b): Corresponding loading plots for PC2 and PC3 of the calculated PCA. In (c): The 2D scores plot of PC4 against PC3 still reveals a splitting of the EP and GM cluster into two subgroups, respectively. However, no overlapping of the EP and AT conglomerations is visible, but instead one of the GM subgroups extend into the AT cluster. In this case, PC3 still represents 3 % and PC4 describes 1 % of the total variance. In (d): Corresponding loading plots for PC3 and PC4 of the calculated PCA.*

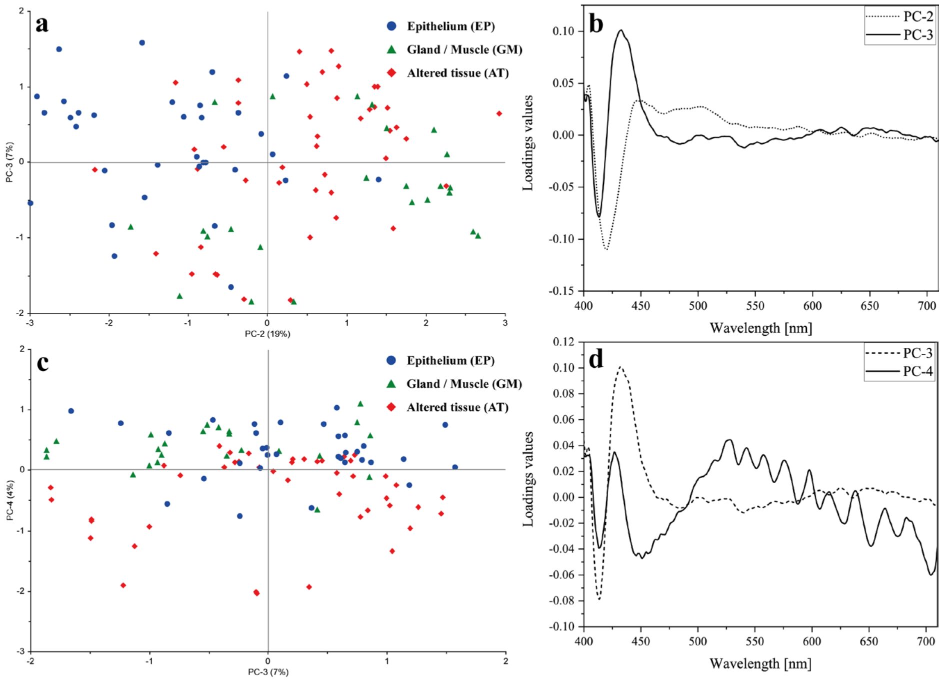

Figure S3.3. *2D scores plot of the Pushbroom PCA for the differentiation of EP (blue), GM (green) and AT (red). In (a): The 2D scores plot of PC3 against PC2 reveals no separation of the GM, AT and EP groups. All three tissue clusters are significantly overlapping and show no separation tendency at all. As demonstrated above, a splitting of the GM group is recognized. PC2 explains 19 %, whereas PC3 represents 7 % of the overall variance. In (b): Corresponding loading plots for PC2 and PC3 of the calculated PCA. In (c): The 2D scores plot of PC4 against PC3 only reveals a slight trend of tissue type segregation. The AT cluster mainly relates to negative score vales for PC4, whereas the EP and GM groups primarily obtain positive score values for PC4. PC3 still represents 7 % and PC4 describes 4 % of the total variance. In (d): Corresponding loading plots for PC3 and PC4 of the calculated PCA.*

The calculation of the overall accuracy, sensitivity, specificity and precision is based on the classification outcome of the Whiskbroom and Pushbroom PCA-DA models in terms of true positive and negative cases as well as false positive and negative ones. All results are summarized in the confusion matrix for each model, which are depicted in Tab. S3.1 and S3.2.

Table S3.1. *Confusion matrix of the Whiskbroom PCA-DA model. Each column of the displayed matrix represents the number of ELS spectra included in the Whiskbroom model, which are 58 AT, 28 GM and 41 EP spectra. Each matrix row, however, lists the model's prediction results of the respective tissue type group. For the Whiskbroom model, 41 EP out of 41 EP spectra and 28 GM out of 28 GM spectra were correctly assigned. Compared to that, 56 AT were matching the total amount of 58 AT spectra, whereas 2 AT were attributed to EP.*

Confusion matrix Whiskbroom PCA-DA		**Actual**		
		Altered tissue (AT)	Gland /Muscle (GM)	Epithelium (EP)
Predicted	Altered tissue (AT)	56	0	0
	Gland / Muscle (GM)	0	28	0
	Epithelium (EP)	2	0	41

Table S3.2. *Confusion matrix of the Pushbroom PCA-DA model. Each column of the displayed matrix represents the number of ELS spectra included in the Pushbroom model, which are 44 AT, 24 GM and 32 EP spectra. Each matrix row, however, lists the model's prediction results of the respective tissue type group. For the Pushbroom model, 44 AT out of 44 AT spectra were correctly assigned. Compared to that, 23 GM out of 24 GM and 32 EP out of 33 EP were correctly matching, whereas 1 GM and 1 EP were attributed to either EP or GM.*

Confusion matrix Pushbroom PCA-DA		**Actual**		
		Altered tissue (AT)	Gland /Muscle (GM)	Epithelium (EP)
Predicted	Altered tissue (AT)	44	0	0
	Gland / Muscle (GM)	0	23	1
	Epithelium (EP)	0	1	32

The total variances of the PCA-DA models are expressed as an accumulation of the individual PC-variances. For each PC, the calculated variance identifies how well the investigated samples are described by the PC and thus how much variation in the data can be explained by the corresponding model. Since the model formation is based on the calibration data set, a calibration variance of the model can be defined. A model testing, however, is accomplished by a model validation and thus a validation variance can additionally be calculated. In case both parameters do not exhibit a similar trend, the calibration or testing data might not be representative. In Fig. S3.4, a summary of the total variances is illustrated for each PCA-DA model.

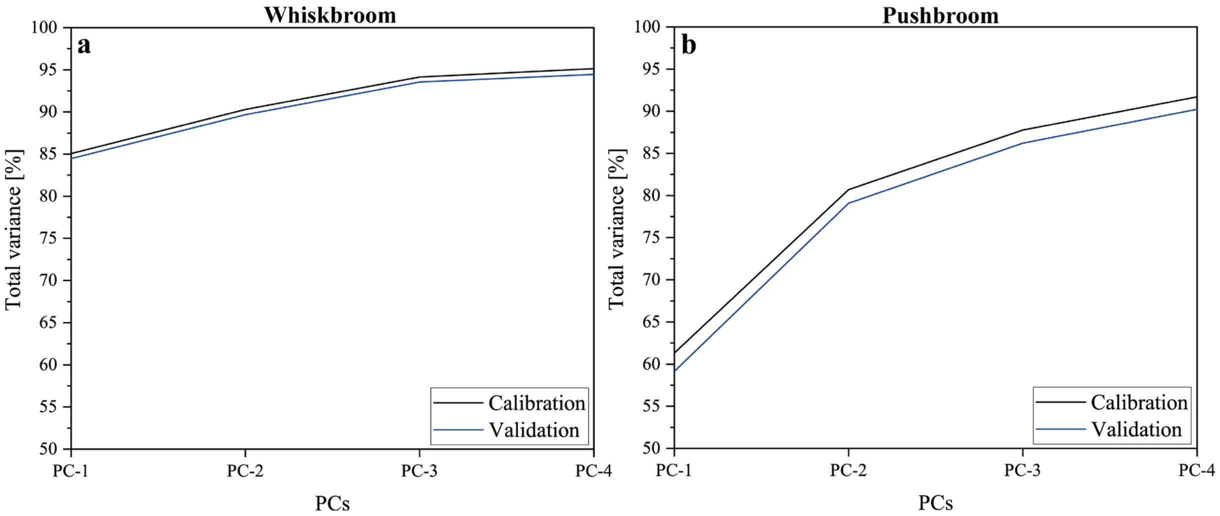

Figure S3.4. *Overview of the total variances for PC-1 to PC-4 of the Whiskbroom (a) and Pushbroom (b) PCA-DA model, respectively. In (a): PC-1 of the Whiskbroom model already explains 85 % of the data's total variance, which finally adds up to 95 % considering PC-1 to PC-4 (a). In (b): For the Pushbroom model, PC-1 illustrates 61 % of the total variance, whereas the accumulation of all four PCs describes 90 % (b). The calibration and validation variance reveal almost identical curve shapes for both models and thus calibration as well as testing data sets are well explained by the two models.*

A3. Supplementary Information for Manuscript II: Differentiation of Salivary Gland and Tumor Entities by Raman Imaging combined with Multivariate Data Analysis

Overall Raman mean spectra of normal salivary gland (green), Warthin tumor (blue) and pleomorphic adenoma (red) are illustrated within 900 – 1700 cm^{-1} in Fig. S4.1. The superposition of all three spectra shows the great resemblance and the high number of identical Raman bands. Only small differences between the tissue types can be recognized.

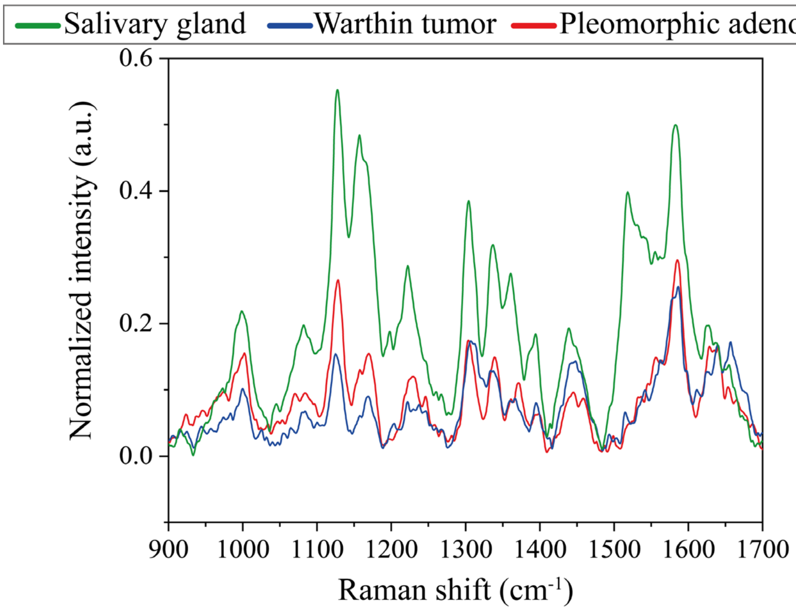

Figure S4.1. *Superimposed Raman mean spectra of normal salivary gland (green), Warthin tumor (blue) and pleomorphic adenoma (red) within 900 – 1700* cm^{-1}*. The spectral pattern of all three tissue types is very similar. Only minor changes in band relations or manifestations are noticeable.*

In Fig. S4.2, the complete PCA evaluation, represented with all used PCs (PC1 – PC5), is illustrated. The respective 2D score plots (a, c, e, g) and corresponding loadings (b, d, f, h) of PC1 – PC5 are displayed. The requirement of five PCs corroborates the complexity of the spectral data and the large information content obtained by Raman imaging.

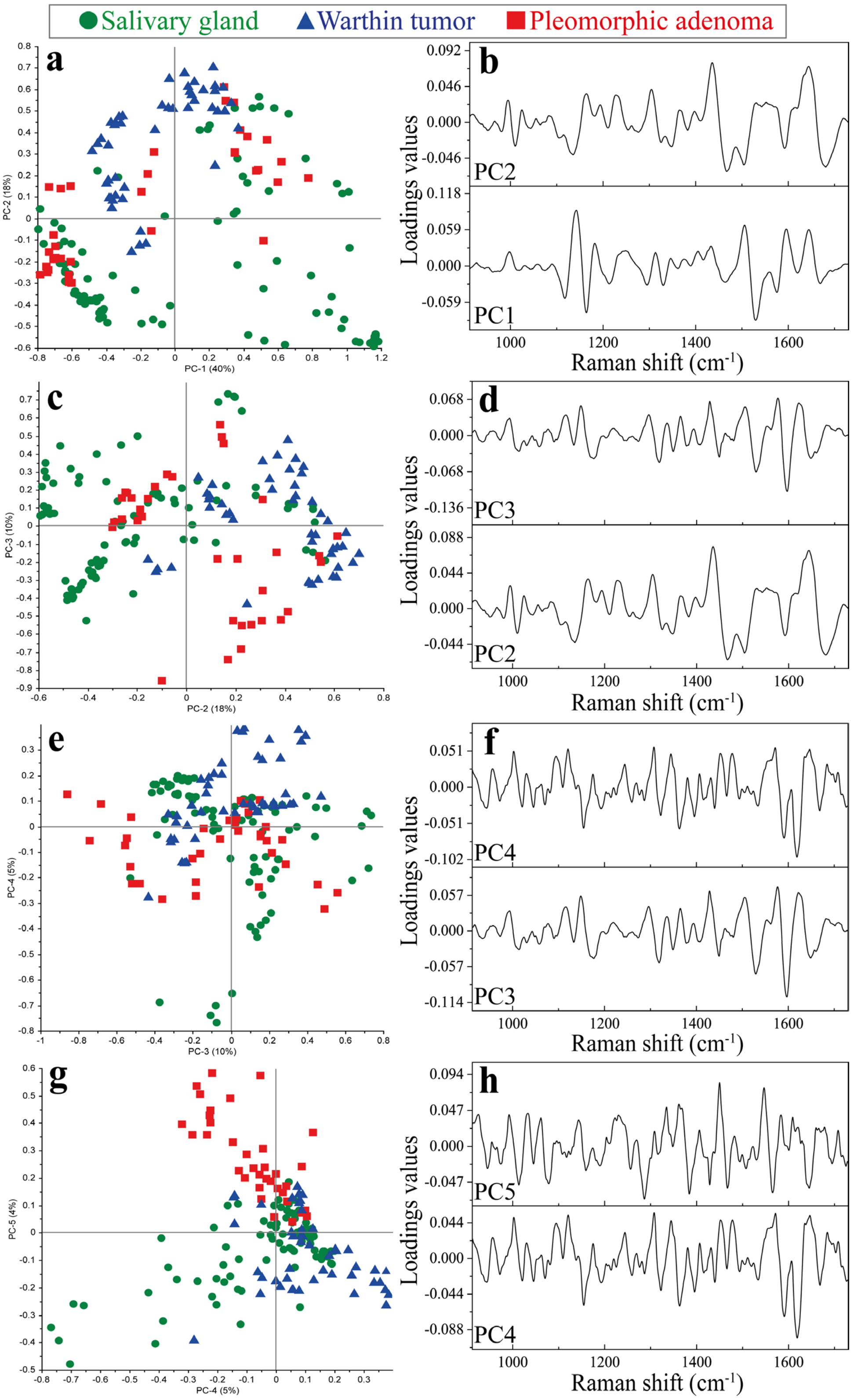

Figure S4.2. *2D score plots and corresponding loading plots of the Raman PCA model (a-h). Five PCs (PC1-PC5) are required to enable a complete differentiation of normal salivary gland (green circles), Warthin tumor (blue triangles) and pleomorphic adenoma (red squares). PC1 describes 40 % of the total model variance, whereas PC2, PC3, PC4 and PC5 account for 18 %, 10 %, 5 % and 4 %, respectively. Two consecutive PCs are always plotted against one another in the 2D score plots, which are PC2 vs. PC1 (a) with related loading plot (b), PC3 vs. PC2 (c) with related loading plot (d), PC4 vs. PC3 (e) with related loading plot (f) and PC5 vs. PC4 (g) with related loading plot (h).*

To demonstrate the clear differentiation between parotid tissue clusters by the PCA model, various perspectives on the 3D scores plot are shown in Fig. S4.3. The different angles of view reveal that the tissue groups are distinctly separated from one another with only minor overlaps at the center, independently of the plot orientation. Additionally, all plot perspectives display the necessity of the three PCs to achieve a good cluster segregation.

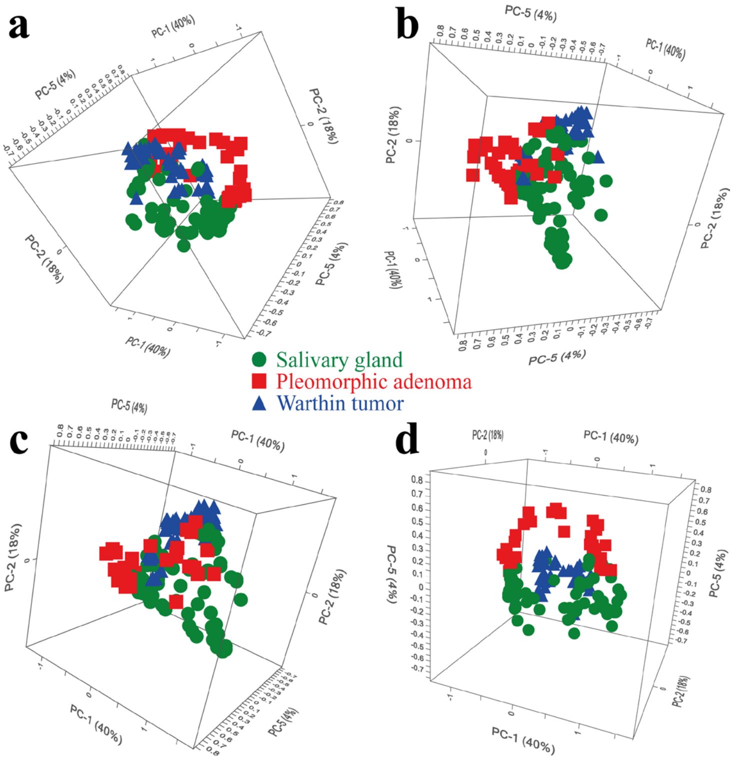

Figure S4.3. Different perspectives of the 3D PCA scores plot for distinguishing salivary gland, Warthin tumor and pleomorphic adenoma. A distinct separation of salivary gland (green dots), Warthin tumor (blue triangles) and pleomorphic adenoma (red boxes) is achieved by PC1 (40 %), PC2 (18 %) and PC5 (4 %) with minor overlaps between the groups. The varying angles of view on the 3D scores plot confirm the cluster segregation to be independent of the plot orientation.

The DA was computed by using the PCA score values and the Mahalanobis distance algorithm with five PCs. As a result, the confusion matrix of the PCA-DA is obtained and presented in Tab. S4.1. Raman mean spectra assignments, summarized in the confusion matrix, represent an internal model validation, of which each model spectrum is allocated to one tissue cluster as if it was not actually included in the model. Based on this outcome, performance parameters can be calculated.

Table S4.1. Confusion matrix of the final Raman PCA-DA model. An overall model accuracy of 94 % was achieved, which is also represented by the high number of correctly assigned model-included Raman mean spectra for all tissue types.

Confusion matrix of the parotid tissue PCA-DA		**Actual**		
		Salivary gland	Pleomorphic adenoma	Warthin tumor
Predicted	Salivary gland tissue	91	3	3
	Pleomorphic adenoma	3	31	1
	Warthin tumor	0	1	43

A4. Supplementary Information for Manuscript III: The Impact of Standard Tissue Preparation Protocols of Salivary Gland Tumors investigated by Fourier-Transform Infrared Microspectroscopy

A baseline-correction of FTIR mean spectra for “native”, “formalin”, “in paraffin” and “dewaxed” tissue was performed to achieve a good spectra comparability and thus enable an evaluation of band intensity changes and differences in signal relations. This spectra comparison was performed individually for each parotid tissue type (salivary gland, Warthin tumor, pleomorphic adenoma). An overview of the FTIR mean spectra for each sample preparation and tissue type is illustrated in Fig. S5.1.

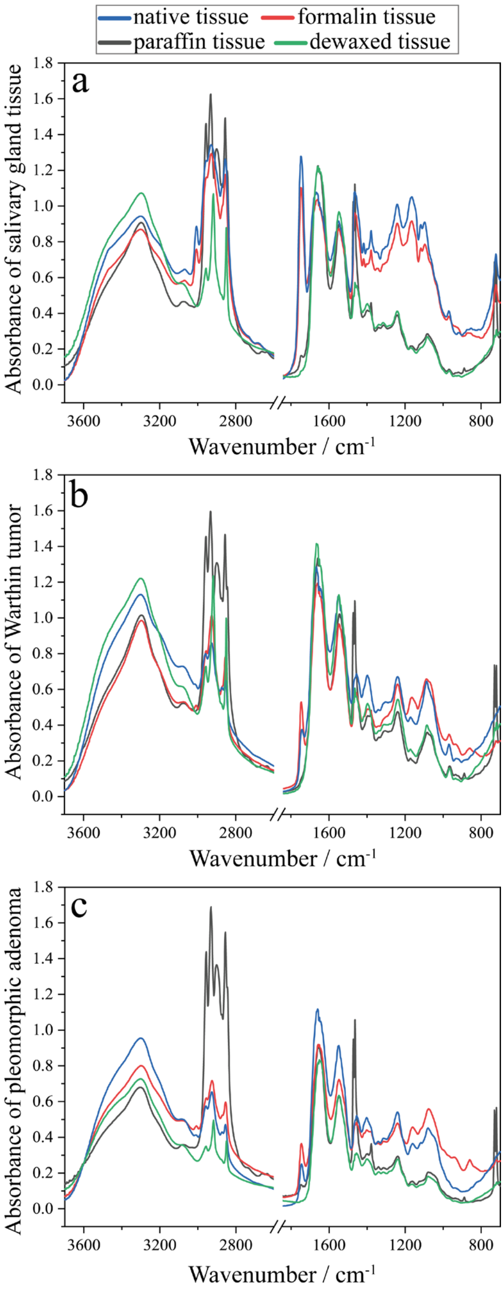

__Figure S5.1.__ IR band relation and intensity comparison between the different sample preparations, illustrated individually for each tissue type: (a) salivary gland tissue, (b) Warthin tumor, (c) pleomorphic adenoma. All FTIR mean spectra were baseline corrected. The “native”, “formalin”, “in paraffin” and “dewaxed” preparations are shown in blue, red, grey and green, respectively.

As a result of the DA calculation, confusion matrices are obtained, which summarize the correctly and falsely assigned FTIR spectra (predicted spectra) and correlate them to their known affiliation (actual spectra). The total number of FTIR spectra included in the PCA-DA model is illustrated in the matrix columns, whereas the assigned spectra of each method are listed in each matrix row. Using this terminology, false positive / negative predictions and true positive / negative predictions can be identified. Confusion matrices of PCA-DA models for each parotid tissue type are presented in Tab. S5.1 – S5.3, whereas matrices with combined “native” and “formalin” data sets are listed in Tab. S5.4 – S5.6.

Table S5.1. *Confusion matrix of salivary gland tissue PCA-DA with four classes.*

Confusion matrix salivary gland tissue PCA-DA		**Actual**			
		in paraffin	formalin	native	dewaxed
Predicted	in paraffin	270	0	0	0
	formalin	0	192	96	9
	native	0	77	174	0
	dewaxed	0	1	0	260

Table S5.2. *Confusion matrix of Warthin tumor PCA-DA with four classes.*

Confusion matrix Warthin tumor PCA-DA		**Actual**			
		in paraffin	formalin	native	dewaxed
Predicted	in paraffin	150	0	0	0
	formalin	0	131	47	0
	native	0	19	103	0
	dewaxed	0	0	0	150

Table S5.3. *Confusion matrix of pleomorphic adenoma PCA-DA with four classes.*

Confusion matrix pleomorphic adenoma PCA-DA		**Actual**			
		in paraffin	formalin	native	dewaxed
Predicted	in paraffin	120	4	2	0
	formalin	0	84	69	1
	native	0	31	48	5
	dewaxed	0	1	1	114

Table S5.4. *Confusion matrix of salivary gland tissue PCA-DA with three classes.*

Confusion matrix salivary gland tissue PCA-DA		**Actual**		
		in paraffin	formalin + native	dewaxed
Predicted	in paraffin	270	0	0
	formalin + native	0	540	15
	dewaxed	0	0	254

Table S5.5. *Confusion matrix of Warthin tumor PCA-DA with three classes.*

Confusion matrix Warthin tumor PCA-DA		Actual		
		in paraffin	formalin + native	dewaxed
Predicted	in paraffin	150	1	0
	formalin + native	0	299	0
	dewaxed	0	0	150

Table S5.6. *Confusion matrix of pleomorphic adenoma PCA-DA with three classes.*

Confusion matrix pleomorphic adenoma PCA-DA		Actual		
		in paraffin	formalin + native	dewaxed
Predicted	in paraffin	120	0	0
	formalin + native	0	231	6
	dewaxed	0	2	114

Corresponding classification results of model-included FTIR spectra by “native” and “formalin” combined PCA-DAs with their related model quality parameters are shown in Tab. S5.7. In comparison to “native” and “formalin” separately-treated models, higher numbers of correct spectra assignments were achieved and thus overall improved quality parameters result.

Table S5.7. *Model quality parameters for salivary gland tissue, Warthin tumor and pleomorphic adenoma three-class PCA-DA models. “Native” and “formalin” are combined as one class. The robustness of the models can be deduced from the total and percentage amount of correctly-assigned FTIR spectra for each preservation method. Based on this assignment, the model parameters accuracy, sensitivity, specificity and precision are calculated.*

Entity	Fixation method	Total spectra	Correctly predicted	Correctly predicted / %	Accuracy / %	Sensitivity / %	Specificity / %	Precision / %
salivary gland tissue	in paraffin	270	270	100	99	98	99	99
	formalin + native	540	540	100				
	dewaxed	269	254	94				
Warthin tumor	in paraffin	150	150	100	100	100	100	100
	formalin + native	300	299	100				
	dewaxed	150	150	100				
pleomorphic adenoma	in paraffin	120	120	100	97	97	98	97
	formalin + native	233	231	99				
	dewaxed	120	114	95				

A5. Supplementary Information for Manuscript IV: Accumulation and Penetration Behavior of Hypericin in Glioma Tumor Spheroids studied by Fluorescence Microscopy and Confocal Fluorescence Lifetime Imaging Microscopy

For an improved visualization of the hypericin accumulation in spheroids, fluorescence images of hypericin and Hoechst 33342 are displayed as separated channel images for outer and inner sections of the 5 min incubation period (Fig. S6.1a-d). Single channel images are used to proof the presence of hypericin throughout each section, since the hypericin emission is sometimes hardly visible in the fluorescence images in Fig. 6.2.

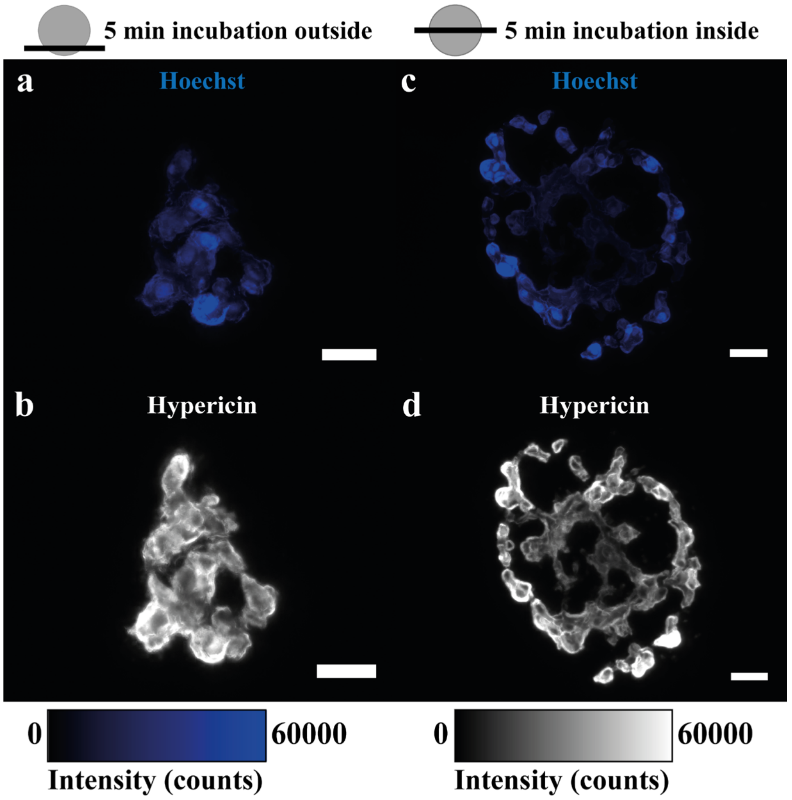

Figure S6.1. Verification and illustration of hypericin in outer and inner spheroid sections for a 5 min incubation period. Hoechst 33342 fluorescence by cell nuclei (blue) and hypericin fluorescence (white) are shown separately for outer and inner sections, respectively (a, c and b, d). Single channel fluorescence images of hypericin are used to demonstrate that hypericin is present throughout the sections, indicated by the white color (b, d). For a 5 min incubation, the outer section reveals a more homogeneous hypericin intensity distribution compared to the inner one (b, d), exhibiting a hypericin intensity gradient. Intensity drops in-between result from holes in the sections. As a consequence of section preparation, cutting elongation, compression and regions without cells can occur. Thus, sections might appear differently shaped or patchy. The scale bars of all fluorescence images are 25 µm.

Control spheroids without hypericin treatment were additionally analyzed by fluorescence intensity imaging and FLIM (Fig. S6.2). For fluorescence intensity imaging, control spheroids were stained with Hoechst 33342 to reveal cell nuclei inside the investigated sections (Fig. S6.2a). Besides the Hoechst fluorescence, no additional fluorescence was detectable. FLIM analysis showed homogeneously distributed FLTs mostly below 2.5 ns across control sections (Fig. S6.2b). Both techniques demonstrate large deviations from hypericin-incubated spheroids in terms of fluorescence intensity and FLT.

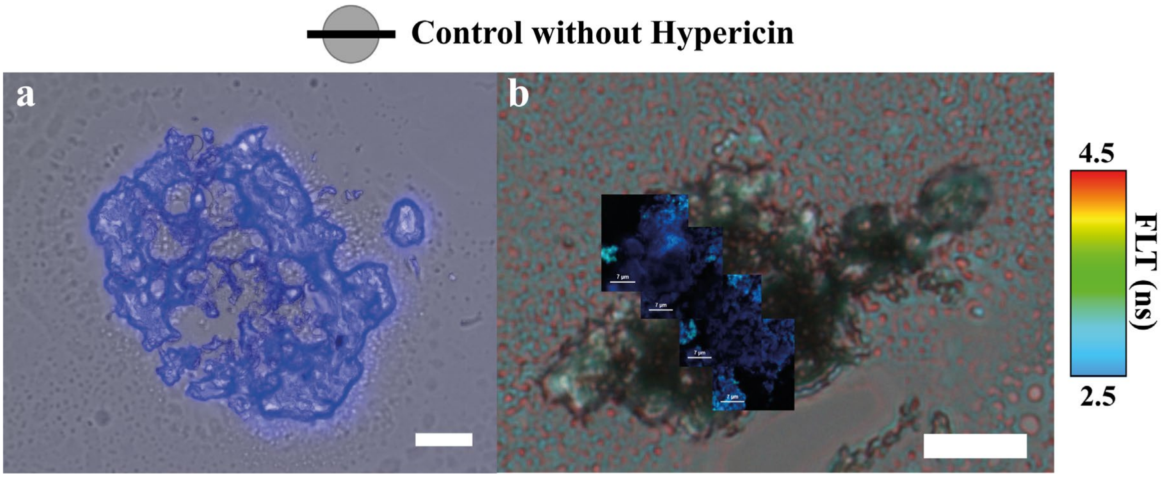

Figure S6.2. *Control spheroids without hypericin incubation analyzed by nucleus fluorescence intensity and FLIM. In (a): Hoechst 33342 nucleus stained fluorescence image (blue) overlaid on top of a brightfield image of the same spheroid section. The scale bar of the fluorescence image is 25 µm. In (b): Composite image of a control spheroid with a FLT below 2.5 ns. Composite images were generated by combining FLIM images (24 x 24 µm) and corresponding brightfield images. To enable a precise assignment and good visualization of the FLIM images, brightfield images are zoomed-in, thus the sections appear larger. The corresponding scale bar of the brightfield image equals 25 µm. Both techniques demonstrate a clear absence of hypericin inside the spheroid.*

Comparable to Fig. S6.1, separated fluorescence channel images of hypericin (Fig. S6.3b, d, f, h) and Hoechst 33342 (Fig. S6.3a, c, e, g) are depicted in Fig. S6.3 for the investigated incubation concentrations. Again, hypericin single channel images are utilized to examine whether hypericin was enriched at the inner section center.

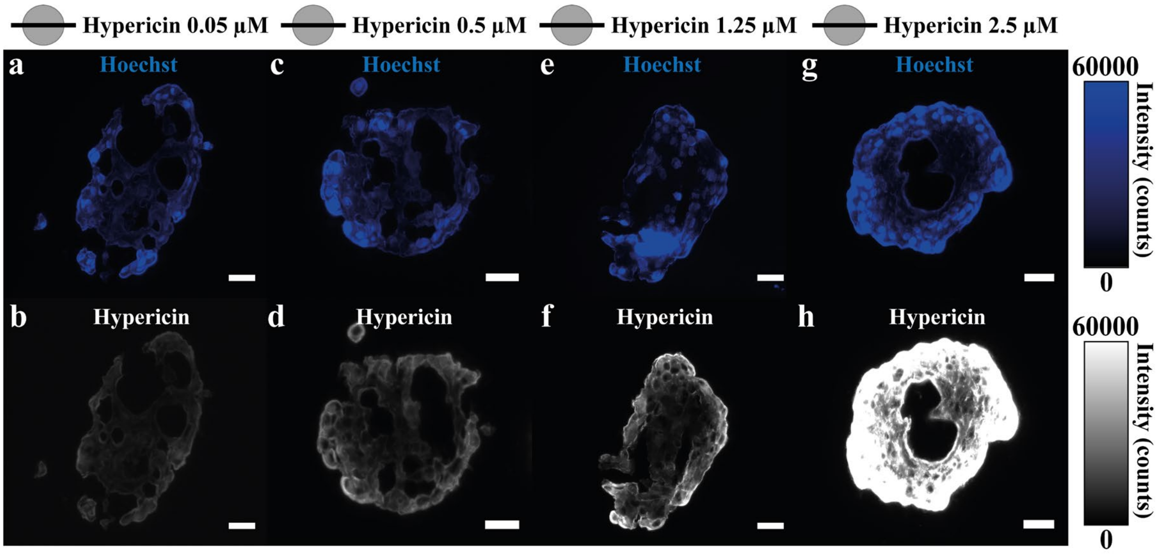

Figure S6.3. *Verification and illustration of hypericin in inner spheroid sections for different hypericin incubation concentrations. Hoechst 33342 fluorescence by cell nuclei (blue) and hypericin fluorescence (white) are exhibited separately for inner sections (a, c, e, g and b, d, f, h). Single channel fluorescence images of hypericin are used to demonstrate that hypericin also penetrated to the spheroid core, indicated by the white color (b, d, f, h). Inner spheroid sections of all incubation concentrations (0.05 µM, 0.5 µM, 1.25 µM, 2.5 µM) reveal hypericin intensity gradients. Here, 0.05 µM and 0.5 µM concentrations result in a small hypericin intensity increase at the annular area of the sections, but overall hypericin intensities are low (b, d). Within the peripheral regions of the 1.25 µM and 2.5 µM sections, hypericin is accumulated to a larger extent, indicated by the higher fluorescence intensity in these regions (f, h). Inside the 1.25 µM section, hypericin is present in considerably smaller amounts compared to the annular outer areas. For the 2.5 µM section, a continuously decreasing hypericin intensity towards the center is observable. This section reveals highest hypericin intensities compared to all investigated concentrations. As a consequence of section preparation, cutting elongation, compression and regions without cells can occur. Thus, sections might appear differently shaped or patchy. The scale bars of all fluorescence images are 25 µm.*

In order to prove the presence of hypericin in the entire inner spheroid sections, fluorescence spectra were acquired across the inner sections. A line scan across the section of a 5 min incubated spheroid is illustrated as 2D surface plot in Fig. S6.4. This plot displays the fluorescence maxima of hypericin at 600 nm and 650 nm in varying intensities and the y-axis represents the lateral position in the section. The spectral data demonstrates that hypericin is present all over the sections (Fig. S6.4a, b).

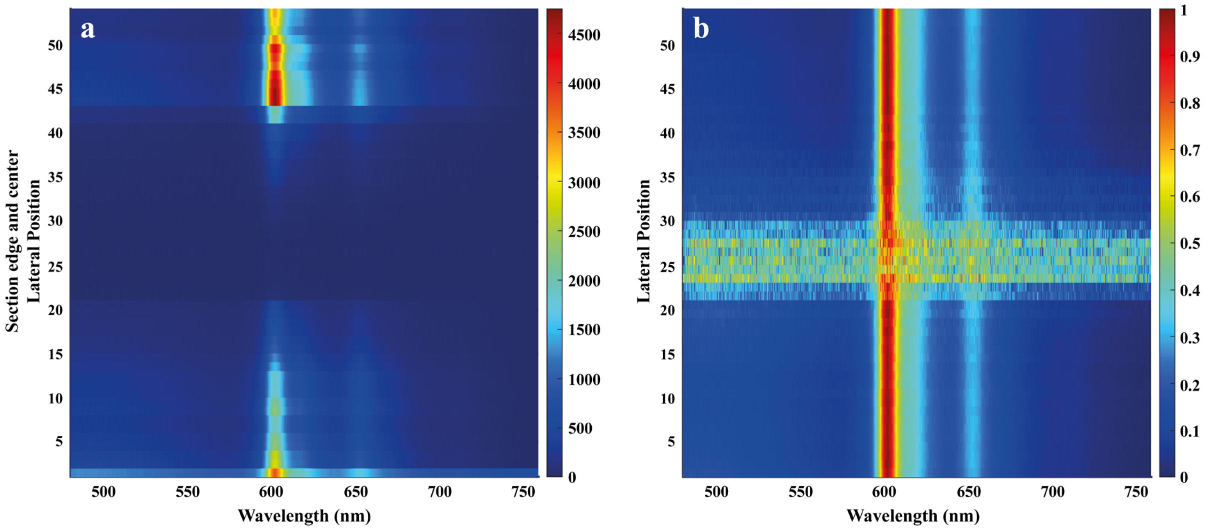

Figure S6.4. *2D surface plots of spectral line scans across inner spheroid sections after 5 min incubation with hypericin. In (a), the plot is shown with a color scale bar of intensity values in counts, whereas in (b), the same spectra are shown with normalized intensity values. In both plots, hypericin fluorescence maxima at 600 nm and 650 nm are visible at all lateral positions throughout the inner section. At the section edges, overall higher hypericin intensities are detectable compared to the section center, thus displaying the intensity gradients observed for short incubation times. In the section center (between lateral position 15 and 40), almost no hypericin intensity is visible in (a). However, the normalized intensity plot in (b) demonstrates that hypericin can be detected throughout the whole section, although its intensity and thus accumulation in the section center is small.*

Hypericin in different tumor spheroid regions was investigated by comparing outer and inner sections after varying spheroid incubation times, illustrated in Fig. S6.5. This was examined by fluorescence intensity imaging and FLIM. Initially, fluorescence intensity images of whole spheroids are shown prior to section preparation (Fig. S6.5, 1st column). A comparison of fluorescence images between outer and inner sections reveals the reduced accumulation of hypericin towards the spheroid core (Fig. S6.5, 2nd and 3rd column). On the other hand, FLIM reveals cellular environmental differences from the spheroid outside to the inside due to hypericin FLT changes (Fig. S6.5, 4th and 5th column). An overview of all outer and inner spheroid comparisons with different incubation durations is summarized in Fig. S6.5.

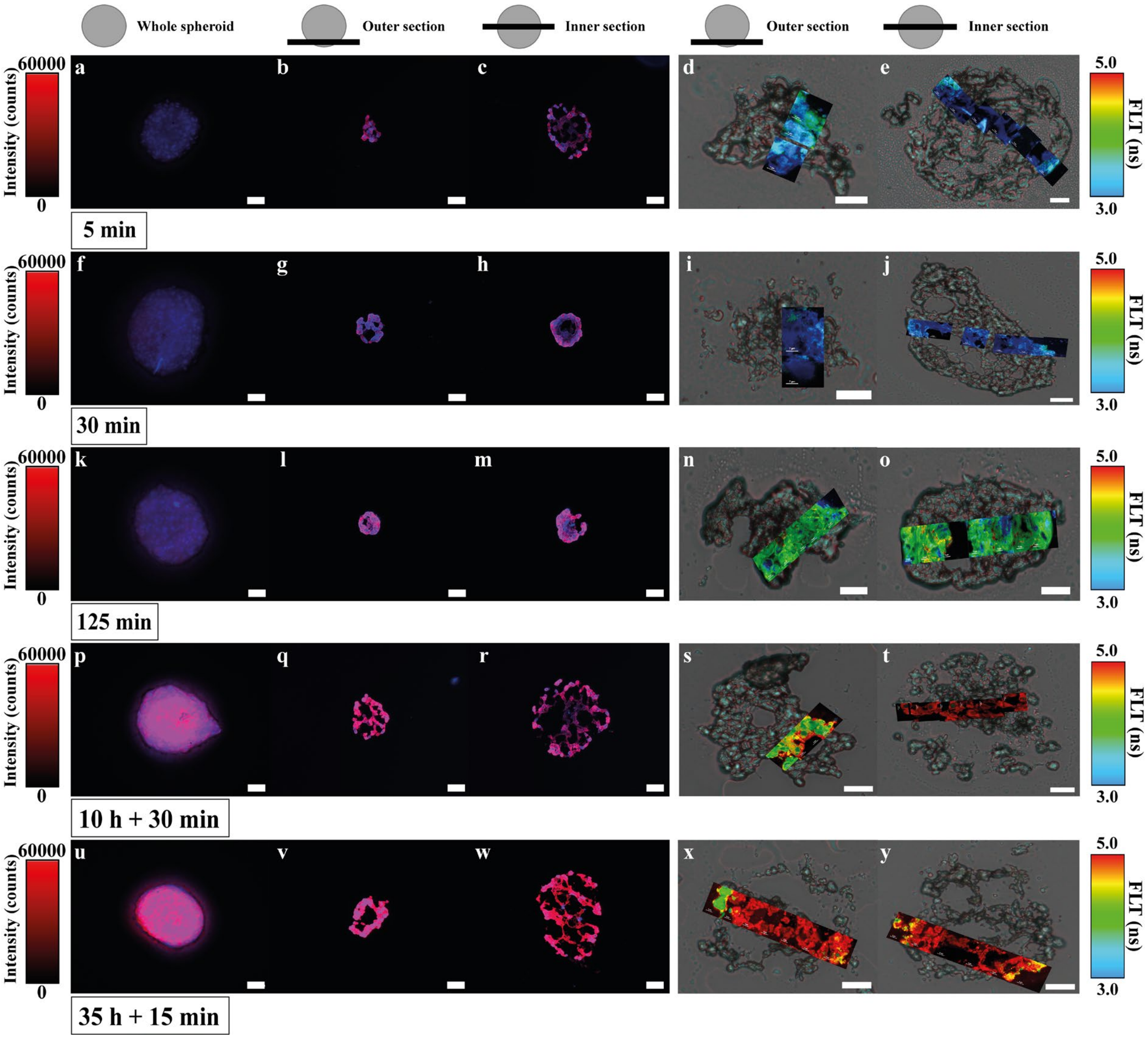

Figure S6.5. *Comparison of outer and inner spheroid sections after different incubation periods, analyzed by fluorescence intensity imaging and FLIM. Cell nuclei are stained with Hoechst 33342 and illustrated by the blue color, whereas hypericin fluorescence is shown in red color. Fluorescence imaging of whole spheroids already indicates an increasing hypericin enrichment by the more intense red color at longer incubation times (a, f, k, p, u). With increasing incubation duration, hypericin accumulates not only in the outer spheroid layers to an increasing extent, but also towards the spheroid center (b, g, l, q, v and c, h, m, r, w). For short incubation durations (5 min, 30 min, 125 min), hypericin gradients towards the spheroid core are noticeable (c, h, m), whereas longer incubation periods (10 h + 30 min, 35 h + 15 min) result in a more homogeneous hypericin distribution (r, w). The scale bars of all fluorescence images are 50 µm. For FLIM investigation, composite images were generated by combining FLIM images (24 x 24 µm) and corresponding brightfield images. To enable a precise assignment and good visualization of the FLIM images, brightfield images are zoomed-in, thus the sections appear larger. Corresponding scale bars of the brightfield images are equal to 25 µm (white). Composite images reveal FLT gradients from outer to inner spheroid sections for short incubation times (5 min, 30 min) (d, i and e, j). The 125 min incubation displays homogeneous FLT distributions for both sections (n, o) with FLTs of 4 ns. Longer incubation durations (10 h + 30 min, 35 h + 15 min), however, reveal an inversion of hypericin FLTs, since outer sections show, at least partially, shorter FLTs of 4 ns (s, x) compared to inner ones (5 ns; t, y). These short FLTs appear either at the section edge or throughout the whole section (s, x). As a consequence of section preparation, cutting elongation, compression and regions without cells can occur. Thus, sections might appear differently shaped or patchy.*

Due to the expectation of pH changes towards the spheroid core, fluorescence spectra and FLTs of hypericin are analyzed at different pH levels. Fig. S6.6 shows the corresponding hypericin fluorescence spectra depending on pH. The fluorescence intensity of hypericin is affected by the pH alterations in the incubation medium with hypericin and the largest fluorescence intensity is observed at pH 7.

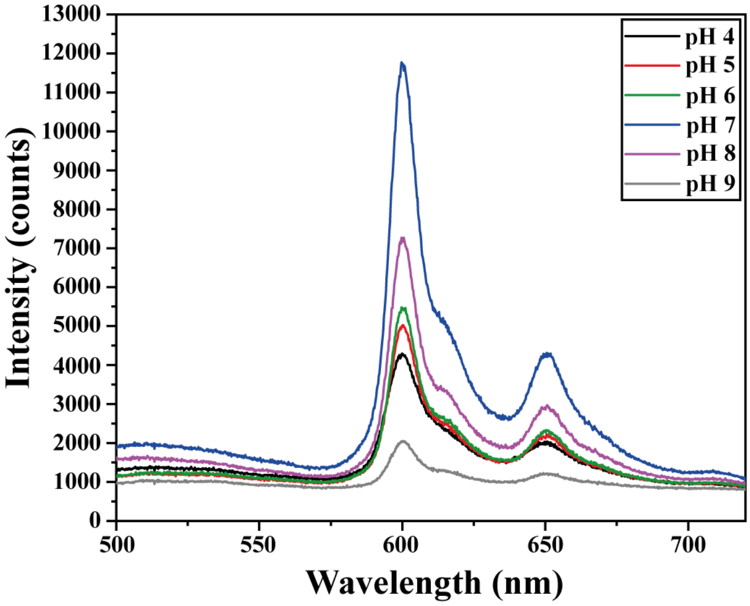

Figure S6.6. *Hypericin spectra of the used incubation media with pH values adjusted between 4 and 9. Highest hypericin fluorescence intensities are observed for a physiological pH of 7 and 8, whereas the lowest intensity occurs at pH 9.*

A6. Supplementary Information for Manuscript V: Investigation of Cell Death induced by Hypericin-based Photodynamic Therapy on Glioma Single Cells using Confocal Fluorescence Lifetime Imaging Microscopy

As part of the hypericin PDT investigation, single glioma cells were treated with hypericin and resorufin to unveil individual damaging steps of the cell. For this purpose, hypericin functions as the photosensitizer, whereas resorufin was initially metabolized by the cells and is used as fluorescence probe for the surrounding medium. All induced PDT steps of cell damaging and death are recorded by fast FLIM and shown by a detailed series of FLIM composite images. Aside from the series shown in Fig. 7.2 in the main manuscript, a second sequence of fast FLIM composite images for hypericin PDT after resorufin metabolism is given in Fig. S7.1. Due to the high similarity between both series, a high reproducibility of the experiments can be deduced.

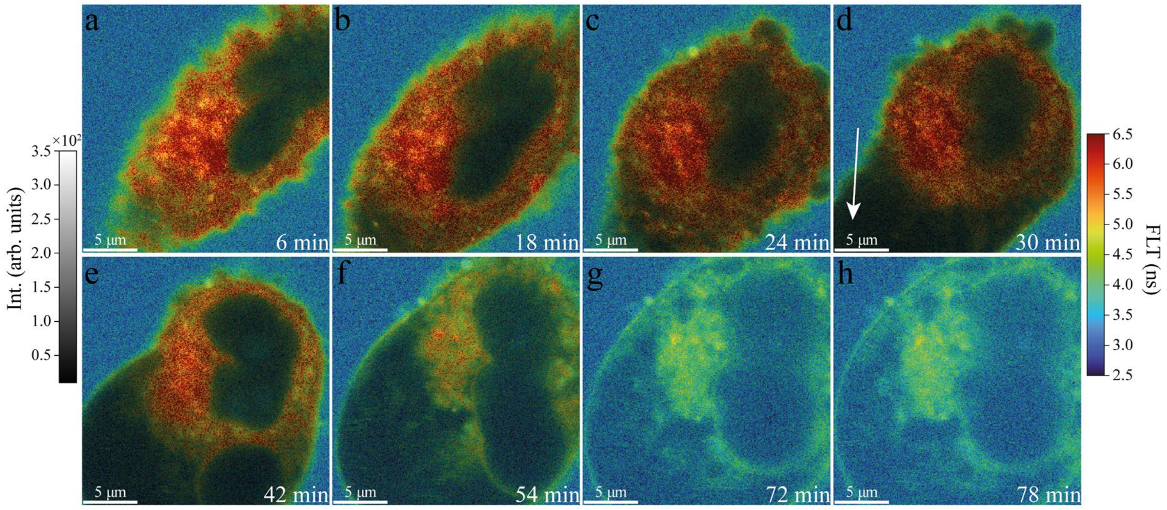

Figure S7.1. *A second FLIM composite image series of hypericin PDT on a single glioma cell after hypericin incubation and resorufin conversion. In (a), hypericin is entirely accumulated throughout the morphologically-intact cell, as implied by FLTs of 6 – 6.5 ns (red). A slightly brighter red false-color indicates the location of the ER in close proximity to the cell nucleus, where the largest hypericin accumulation can be found. The cell membrane is visualized by FLTs of 4.5 ns (green) that is also associated with hypericin. In the cellular environment, resorufin is mainly present, as is shown by a FLT of 3 – 3.5 ns (blue). In (b – d), the cell initially shrinks and assumes an increasingly rounded shape as a result of PDT initiation, which is followed by small bleb formations (c) and finally by generating one big bubble (d, white arrow). At progressed PDT levels, the cellular morphology becomes even more rounded (e) and resorufin in the surrounding medium continuously enters the cytoplasm, as can be recognized by an increasing FLT shift towards 3 – 4 ns in the cytoplasm (f – h). Additionally, FLTs of the perinuclear region decreases from 6 – 6.5 ns to 5 – 4 ns, which is accompanied by a complete cell body rounding (g, h).*

To rule out that this sequence is solely caused by the laser irradiation, control glioma cells are measured at comparable or higher laser powers (1 – 3 µW) than the ones used for hypericin PDT induction (1 µW). A comparison of control glioma cells, only supplemented with PI, is illustrated by FLIM composite images for 405 nm and 561 nm laser irradiations (Fig. S7.2). In a comparable irradiation timeframe as for hypericin PDT, no morphological cell changes are observed for both laser wavelengths (Fig. S7.2, 405 nm a-c; 561 nm d-f). The shown control cells maintain their shape and no FLT variations are observable throughout irradiation. Cell fluorescence results from the cell autofluorescence and the already incorporated PI, which is shown by PI FLTs between 9 – 12 ns for 405 nm and FLTs between

10 – 15 ns for 561 nm. Noticeably, PI is barely accumulated in the ER and thus FLTs are significantly decreased compared to other cell compartments (ER 405 nm: 5 – 6 ns, ER 561 nm: 8 – 9 ns).

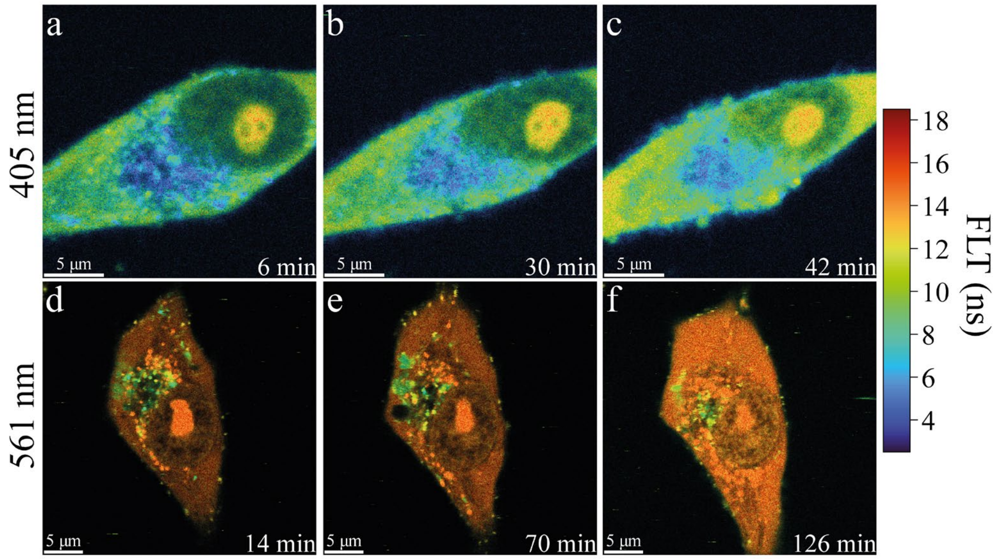

Figure S7.2. *Comparison of FLIM composite images for 405 nm (a-c) and 561 nm (d-f) laser-irradiated control glioma cells supplemented with PI. Compared to PDT used laser powers, the irradiation of control cells was performed at comparable or higher laser powers (1-3 µW) to demonstrate that the laser alone is not responsible for cell death induction. The cell morphology stays constant and no variations in FLTs within the cells are observable throughout the series, respectively. Clearly, both sequences demonstrate that PI enters the cell directly from the beginning, as shown by FLTs between 10 – 12 ns for 405 nm (a-c) and 14 ns for 561 nm (d-f) in various cell organelles. Especially, the accumulation of PI in the nucleolus is dominant.*

Control cells without hypericin were additionally investigated after resorufin conversion to enable a good FLT contrast by the medium. An overview of the corresponding FLIM composite images is given in Fig. S7.3. These experiments should again confirm that the applied laser irradiation cannot induce cell damage, indicated by morphology changes or FLT variations of the cell. Furthermore, these experiments show that autofluorescence of the cells is rather low and has a short FLT below 3 ns.

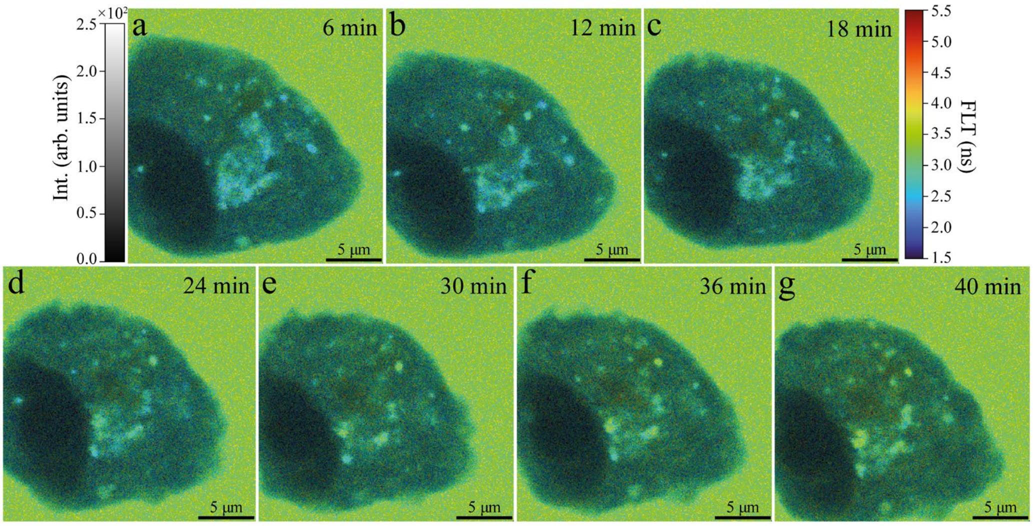

Figure S7.3. *Glioma control cell with resorufin in the surrounding medium. No morphological alterations occur throughout the constant irradiation with a 405 nm laser (a-g). The cell is mainly characterized by its autofluorescence, but also in part by small levels of resorufin inside the cell that cause a combined FLT average of 1.5 ns in the nucleus and 2 – 2.5 ns in the cytoplasm (a-g). Resorufin is highly enriched in the medium with FLT values of 3 – 3.5 ns.*

Comparable to Fig. S7.1, another FLIM composite image sequence of hypericin PDT on a PI supplemented and resorufin converted glioma cell is illustrated in Fig. S7.4. Here, similar PDT stages appear, as were already identified for other glioma cells at similar conditions (Fig. 7.3, main manuscript). Again, the high similarity between different cells with identical fluorescence probe terms underlines the extraordinary experimental reproducibility.

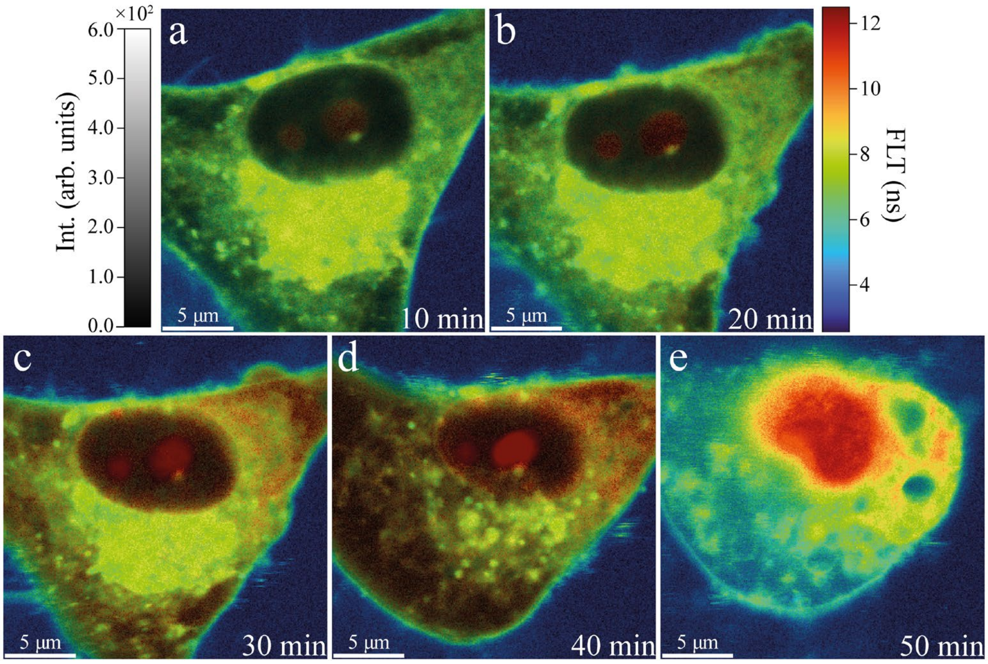

__Figure S7.4.__ A second FLIM composite image series of hypericin PDT on a single glioma cell after hypericin incubation, PI supplementation and resorufin conversion. Initially, the triangle-shaped cell maintains an intact morphology and shows again the highest hypericin accumulation in the ER, indicated by the bright greenish false-color for FLTs of 8 – 9 ns (a). The cytoplasm reveals a homogeneous FLT distribution of 6 – 7 ns, which corresponds to an average FLT of autofluorescence, hypericin, PI and resorufin (a, green). PI is already implied in the nucleoli (a, red, 12 ns), whereas the surrounding medium is mainly enriched with resorufin (a, blue, 3 ns). Due to PDT initiation, PI uptake continuously increases, at first within the nucleoli (intense red, b) and further on also in the cytoplasm (red, c, d). This additionally entails morphological changes, such as cell body shrinkage, rounding and membrane blebbing until one final bleb is formed (c, d). At the last PDT stage, PI is highly enriched inside the whole nucleus and also to a large extent in the cytoplasm (e). This is implied by the intense red and yellow false-colors of 12 ns and 9 ns FLTs, respectively (e). In particular, PI uptake by the cell is associated with entering of the surrounding medium at a certain damaging level (e). As a result, FLT averages of 4 – 6 ns and 8 – 10 ns can be observed inside the cell (e).

The acquisition of fluorescence widefield images enabled to reveal even smaller steps in hypericin PDT progression of single glioma cells (Fig. S7.5). This was especially important to detect the explosive membrane rupture, which would otherwise not be possible due to the defined recording parameters for FLIM. However, only steady-state fluorescence was measurable in this mode and consequently no differentiation between the fluorescence probes hypericin, resorufin and PI can be achieved.

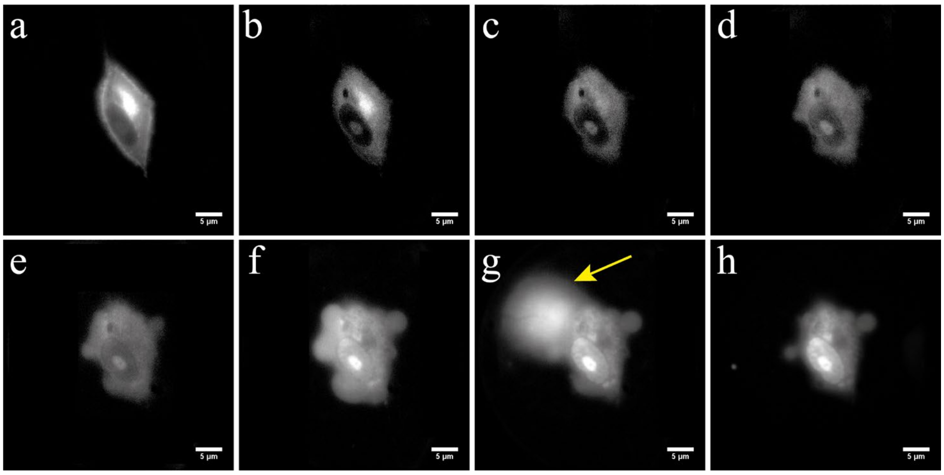

Figure S7.5. *Series of widefield fluorescence images of hypericin PDT on a glioma single cell. Different stages of cell damage are illustrated, including cell body rounding (c-d), membrane bleb formation (d-f) and explosive membrane rupture (g, yellow arrow) until the cell is finally dead (h). This membrane rupture (g) is accompanied by an extensive release of cytoplasm content into the extracellular environment. Fluorescence intensity is continuously increasing, which can be deduced from progressive PI entering and its RNA / DNA intercalation in the cellular body. The scale bars are 5 µm.*

Since the used laser wavelengths, 405 nm and 561 nm, trigger either an hypericin excitation from S_0 to S_2 (405 nm) or from S_0 to S_1 (561 nm), differences in the PDT process are expected. Both wavelengths were applied at almost comparable laser powers (405 nm: 0.77 µW, 561 nm: 1 µW) to unveil morphology and FLT changes, which are summarized by a series of FLIM composite images, respectively (Fig. S7.6). The comparison of the two series revealed that the 561 nm induced PDT proceeds faster than initiated by 405 nm, which results from the hypericin transfer from S_0 to S_1 and from S_1 directly to the triplet state.

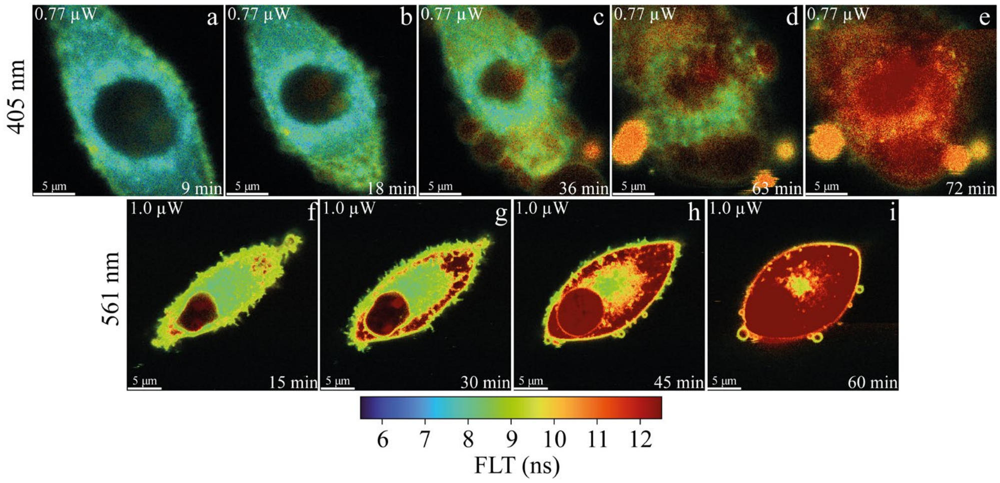

Figure S7.6. *Comparison of PDT-induced cell death progression using 405 nm (a-e) and 561 nm (f-i) laser wavelengths at comparable laser power (405 nm: 0.77 µW, 561 nm: 1 µW). Individual damage steps are displayed for the 405 nm excitation with a laser power of 0.77 µW, involving cell shrinkage, bleb formation and cell rounding (a-e). FLT averages in the cytoplasm, ER and cell membrane lie between 7 – 9.5 ns, especially at the onset of PDT (a, b). As a result of proceeding PDT, PI is increasingly accumulated in the blebs and also penetrates further into the cell body, shown by PI FLTs of 12 ns (c, d, red). Finally, the cell death is indicated by the intense PI fluorescence in the nucleus, which is implied by the intense red color of the 12 ns PI FLT (e). 405 nm induced PDT lasts up to 72 min for the used excitation powers until PI is highly enriched in the nucleus and cell death is reached. In contrast, 561 nm excitation already causes severe cell stress at the beginning of the experiment, which can be deduced from the high PI intercalation in nucleoli and nucleus (f). PI faster penetrates the cell and also increasingly intercalates into DNA / RNA, revealed by the progressive PI FLT of 12 ns in the cytoplasm and nucleus (g-i). Additionally, no actual membrane blebbing appears and the cell shape only notably changes at the last PDT stage (i). 561 nm-initiated PDT takes 45 min to reach complete cell death.*

List of Abbreviations and Symbols

b_{Bayes}	discriminant vector
$B_{u,l}$	Einstein coefficient of stimulated absorption
d_j	discriminant scores
E	eigenvalue
E	residual matrix
$\vec{E}$	(external) electric field
ΔE	energy difference
e_i	charge dimensions
$f_j(x)$	density function
h	Planck's constant
$\hbar$	reduced Planck's constant
k_f	force constant
k_{nr}	nonradiative decay rate
l	class, group
m_{eff}	effective mass
N, n	refractive index
N_l	molecule's population in low states
n	objects
p	descriptive variables
p_A	loading vector
p_j	prior probability
$P(l\|x)$	posterior probability
Q	quantum yield
Q_{Ext}, Q_{Sca}	extinction, scattering cross section
q_0	equilibrium state
q	normal modes
q	normal coordinate
r_i	positioning
S_0	singlet ground state
S_1	first electronic state
S_2	second electronic state
T_1	triplet state
t	time
t_A	score vector

$V(x)$	potential energy
$W_{u \leftarrow l}$	rate of stimulated absorption
X	data matrix
$x, (x)$	object, particle size
$\tilde{\alpha}$	polarizability
Γ	radiative rate
ε	permittivity
λ	wavelength
$\lambda_{excitation}$	excitation wavelength
$\vec{\mu}, \mu$	(induced) dipole moment
μ	mean
μ	permeability
ν	frequency
ν	vibrational quantum number
$\tilde{\nu}$	wavenumbers
$\Delta\bar{\nu}$	wavenumbers (Raman shift)
$\rho(\nu)$	energy spectral density
Σ	covariance matrix
τ	fluorescence lifetime
$\langle\tau\rangle_f$	average lifetime
$\langle\tau\rangle_a$	amplitude-averaged lifetime
Ψ	wavefunction
ω	oscillation frequency
2D	two-dimensional
3D	three-dimensional
4HAQO	4-hydroxyaminoquinoline-1-oxide
4NQO	4-nitroquinoline-1-oxide
5-ALA	5-aminolevulinic acid
ADC	analog-to-digital converter
AT	altered tissue
ATP	adenosine triphosphate
BBB	blood-brain-barrier
CCD	charge-coupled device
CFD	function discriminator
DA	Bayesian discriminant analysis
DF	darkfield

DF ELSS	darkfield elastic light scattering spectroscopy
DMSO	dimethyl sulfoxide
DNA	deoxyribonucleic acid
ECM	extracellular matrix
ELS	elastic light scattering
ELSS	elastic light scattering spectroscopy
EP	epithelium
ER	endoplasmic reticulum
FBS	fetal bovine serum
FCS	fetal calve serum
FFPE	formalin-fixed-paraffin-embedded
FLIM	fluorescence lifetime imaging microscopy
FLT	fluorescence lifetimes
FRET	Förster resonance energy transfer
FTIR	Fourier-transform infrared
FWHM	full width at half maximum
GA	gain amplifier
GM	glandular and muscle tissue
HE	haematoxylin and eosin
HN	head and neck
HNSCC	head and neck squamous cell carcinomas
HSI	hyperspectral imaging
IC	internal conversion
IR	infrared
IRF	instrument response function
ISC	intersystem crossing
MAMs	mitochondria-associated membranes
MCT	mercury cadmium telluride
MEM	Eagle's minimum essential medium
MIA	multivariate image analysis
mtPTP	mitochondrial permeability transition pores
MVA	multivariate data analysis
NA	numerical aperture
NAD, NAD^+, NADH	nicotinamide adenine dinucleotide
$NADP^+$, NADPH	nicotinamide adenine dinucleotide phosphate
NBI	narrowband imaging
NIR	near-infrared

O.C.T.™, OCT	optimal cutting temperature compound
OSCCs	oral squamous cell carcinomas
PALM	photo-activated localization microscopy
PBS	phosphate buffered saline
PC	principal component
PCA	principal component analysis
PDD	photodynamic diagnostics
PDT	photodynamic therapy
PEG	poly(ethylene glycol)
PI	propidium iodide
PMMA	poly(methyl methacrylate)
poly-HEMA	poly(2-hydroxyethyl methacrylate)
PPIX	protoporphyrin IX
PS	polystyrene
PSF	point-spread-function
PVA	poly(vinyl alcohol)
RNA	ribonucleic acid
ROS	reactive oxygen species
SCC	squamous cell carcinomas
SGT	salivary gland tumors
SNV	standard normal variate
SOFI	super-resolution optical fluctuation imaging
SPAD	single photon avalanche diode
STORM	stochastic optical reconstruction microscopy
TAC	time-to-amplitude converter
TCSPC	time-correlated single photon counting
TGN	trans-Golgi network
WD	window discriminator
WHO	World Health Organization

List of Figures

Figure 2.1. Simplified Jablonski diagram of electronic and vibrational processes for absorption, fluorescence, Raman, Infrared (IR) absorption and phosphorescence. 6

Figure 2.2. Instrumental setups for steady-state and time-resolved fluorescence imaging. 11

Figure 2.3. Mie scattering of single PMMA and PS particles with different sizes. 15

Figure 2.4. Tissue scattering effects on basis of Mie theory and DF illumination principle. 17

Figure 2.5. Principle of HSI. 18

Figure 2.6. Confocal detection principle and basics of Raman scattering. 22

Figure 2.7. IR absorption as a result of dipole moment variations, initiated by molecular vibrations. 24

Figure 2.8. Schematic structure and principle of PCA. 26

Figure 2.9. Schematic illustration of different DA separators. 31

Figure 2.10. Concept of 2D cell culture. 33

Figure 2.11. Cell spheroid structure, formation and treatment. 37

Figure 2.12. Mechanism of PDT with hypericin. 39

Figure 2.13. Chemical-induced head and neck squamous cell carcinoma (HNSCC) mouse model. ... 40

Figure 2.14. Salivary gland tumor resection, preparation and spectroscopic analysis. 41

Figure 2.15. Fixation mechanisms for cells and tissues. 42

Figure 3.1. Principle of tumor induction in C57Bl/6N genetic mice. 48

Figure 3.2. Schematic illustration of the HSI PCA-DA model development and validation workflow applied for an OSCC mouse model. 49

Figure 3.3. Comparison of Whiskbroom and Pushbroom principles (a,b) accomplished by the two instrumental setups (c,d). 51

Figure 3.4. Histological description of representative tissue regions for epithelium (EP), gland / muscle (GM) and altered tissue (AT). 54

Figure 3.5. PCA model based on Whiskbroom data for the differentiation of EP (blue), GM (green) and AT (red). 56

Figure 3.6. PCA model based on Pushbroom data for the differentiation of EP (blue), GM (green) and AT (red). 59

Figure 3.7. Classification principle of the PCA-DA models. 61

Figure 4.1. Schematic acquisition workflow for Raman imaging of parotid tissue cross-sections and data extraction. 74

Figure 4.2. Overall Raman mean spectra of normal salivary gland (green), Warthin tumor (blue) and pleomorphic adenoma (red). 77

Figure 4.3. PCA model for the differentiation of salivary gland, Warthin tumor and pleomorphic adenoma. 79

Figure 4.4. Schematic description of the external PCA-DA validation. 80

Figure 5.1. Workflow of tissue preparation for FTIR microspectroscopic measurements. 89

Figure 5.2. Identification of different tissue measurement regions for FTIR microspectroscopy........ 90
Figure 5.3. HE-stained examples of pleomorphic adenoma (a) and Warthin tumor (b). 91
Figure 5.4. FTIR average spectra of each preservation method (“native” (blue), “formalin” (red), “in paraffin” (grey), “dewaxed” (green)) for the three investigated tissue types, salivary gland tissue (a), Warthin tumor (b) and pleomorphic adenoma (c). 93
Figure 5.5. PCA models for salivary gland tissue (a), Warthin’s tumor (b) and pleomorphic adenoma (c) in terms of different preservation procedures (“native” (light blue), “formalin” (green), “in paraffin” (red), “dewaxed” (blue)).. 96
Figure 6.1. a) Schematic illustration of tumor spheroid formation in a 96-well plate by the forced-floating method. b) Phase contrast image of a U-87 MG tumor spheroid. 104
Figure 6.2. Investigation of hypericin penetration into spheroids by comparing outer and inner spheroid sections. 108
Figure 6.3. Influence of different incubation concentrations on hypericin uptake and penetration. .. 109
Figure 6.4. Impact of different incubation times on hypericin at the spheroid center. 111
Figure 6.5. Hypericin fluorescence spectra of inner spheroid sections treated for different incubation times (a) and FLTs as well as hypericin maxima intensities depending on pH (b). 112
Figure 7.1. Investigation principle of hypericin PDT on single glioma cells. 121
Figure 7.2. FLIM and fluorescence spectra analysis of hypericin PDT on a single glioma cell following hypericin- and resorufin-treatment. 126
Figure 7.3. FLIM and fluorescence spectra analysis of hypericin PDT on a single glioma cell after hypericin-, PI- and resorufin-treatment. 128
Figure 7.4. Comparison of PDT-induced cell death progression using 405 nm (a-e) and 561 nm (f-j) laser wavelengths. 130
Figure S3.1. Exemplary preprocessed ELS spectra of EP (blue), GM (green) and AT (red) tissue used for Whiskbroom (a) and Pushbroom (b) PCA-DA model formation. XIII
Figure S3.2. 2D scores plot of the Whiskbroom PCA for the differentiation of EP (blue), GM (green) and AT (red). XIV
Figure S3.3. 2D scores plot of the Pushbroom PCA for the differentiation of EP (blue), GM (green) and AT (red). XIV
Figure S3.4. Overview of the total variances for PC-1 to PC-4 of the Whiskbroom (a) and Pushbroom (b) PCA-DA model. XVI
Figure S4.1. Superimposed Raman mean spectra of normal salivary gland (green), Warthin tumor (blue) and pleomorphic adenoma (red) within 900 – 1700 cm^{-1}. XVII
Figure S4.2. 2D score plots and corresponding loading plots of the Raman PCA model (a-h). XVIII
Figure S4.3. Different perspectives of the 3D PCA scores plot for distinguishing salivary gland, Warthin tumor and pleomorphic adenoma. XIX

Figure S5.1. IR band relation and intensity comparison between the different sample preparations, illustrated individually for each tissue type: (a) salivary gland tissue, (b) Warthin tumor, (c) pleomorphic adenoma. XX

Figure S6.1. Verification and illustration of hypericin in outer and inner spheroid sections for a 5 min incubation period. XXIII

Figure S6.2. Control spheroids without hypericin incubation analyzed by nucleus fluorescence intensity and FLIM. XXIV

Figure S6.3. Verification and illustration of hypericin in inner spheroid sections for different hypericin incubation concentrations. XXIV

Figure S6.4. 2D surface plots of spectral line scans across inner spheroid sections after 5 min incubation with hypericin. XXV

Figure S6.5. Comparison of outer and inner spheroid sections after different incubation periods. XXVI

Figure S6.6. Hypericin spectra of the used incubation media with pH values adjusted between 4 and 9. XXVII

Figure S7.1. A second FLIM composite image series of hypericin PDT on a single glioma cell after hypericin incubation and resorufin conversion. XXVIII

Figure S7.2. Comparison of FLIM composite images for 405 nm (a-c) and 561 nm (d-f) laser-irradiated control glioma cells supplemented with PI. XXIX

Figure S7.3. Glioma control cell with resorufin in the surrounding medium. XXIX

Figure S7.4. A second FLIM composite image series of hypericin PDT on a single glioma cell after hypericin incubation, PI supplementation and resorufin conversion. XXX

Figure S7.5. Series of widefield fluorescence images of hypericin PDT on a glioma single cell.. XXXI

Figure S7.6. Comparison of PDT-induced cell death progression using 405 nm (a-e) and 561 nm (f-i) laser wavelengths at comparable laser power. XXXI

List of Tables

Table 3.1. Advantages and disadvantages of Whiskbroom and Pushbroom imaging listed by several criteria. 46

Table 3.2. Model-related quality parameters of the Whiskbroom PCA-DA. 57

Table 3.3. Model-related quality parameters of the Pushbroom PCA-DA. 60

Table 3.4. Summary of the PCA-DA model classification results and HE-diagnosed conclusions. 61

Table 4.1. Raman band assignments for salivary gland, Warthin tumor, pleomorphic adenoma. 77

Table 4.2. Model performance parameters for the tissue entity distinction. 80

Table 4.3. Prediction outcome of model-unknown Raman mean spectra. 81

Table 5.1. Spectral band assignment for salivary gland tissue, Warthin tumor, pleomorphic adenoma, formalin pure and paraffin pure FTIR average spectra. 94

Table 5.2. Model quality parameters for salivary gland tissue, Warthin tumor and pleomorphic adenoma PCA-DA models. 97

Table S3.1. Confusion matrix of the Whiskbroom PCA-DA model. XV

Table S3.2. Confusion matrix of the Pushbroom PCA-DA model. XV

Table S4.1. Confusion matrix of the final Raman PCA-DA model. XIX

Table S5.1. Confusion matrix of salivary gland tissue PCA-DA with four classes. XXI

Table S5.2. Confusion matrix of Warthin tumor PCA-DA with four classes. XXI

Table S5.3. Confusion matrix of pleomorphic adenoma PCA-DA with four classes. XXI

Table S5.4. Confusion matrix of salivary gland tissue PCA-DA with three classes. XXI

Table S5.5. Confusion matrix of Warthin tumor PCA-DA with three classes. XXII

Table S5.6. Confusion matrix of pleomorphic adenoma PCA-DA with three classes. XXII

Table S5.7. Model quality parameters for salivary gland tissue, Warthin tumor and pleomorphic adenoma three-class PCA-DA models. XXII

List of Publications

Published Manuscripts

1. *Mona Stefanakis* and **Miriam C. Bassler***, Tobias R. Walczuch, Elena Gerhard-Hartmann, Almoatazbellah Youssef, Agmal Scherzad, Manuel Stöth, Edwin Ostertag, Rudolf Hagen, Maria Steinke, Stephan Hackenberg, Marc Brecht, Till Jasper Meyer*; The Impact of Tissue Preparation on Salivary Gland Tumors Investigated by Fourier-Transform Infrared Microspectroscopy, J. Clin. Med. **2023**, 12, 569, https://doi.org/10.3390/ jcm12020569

2. ***Miriam C. Bassler**, Tim Rammler, Frank Wackenhut, Sven zur Oven-Krockhaus, Ivona Secic, Rainer Ritz, Alfred J. Meixner, Marc Brecht*; Accumulation and penetration behavior of hypericin in glioma tumor spheroids studied by fluorescence microscopy and confocal fluorescence lifetime imaging microscopy, Anal. Bioanal. Chem. 414, 4849–4860 (**2022**), https://doi.org/10.1007/s00216-022-04107-2

3. *Mona Stefanakis, **Miriam C. Bassler**, Thorsten Böltzig, Edwin Ostertag, Dominik Allnoch, Ralf Zuber, Marc Brecht, Karsten Rebner*; Improved Process Control by Using the Effective Scattering Coefficients to Determine the Fat Content in Homogenized Cow-Based Milk with Multivariate Data Modeling, ACS Food Sci. Technol. (**2022**), 2, 548–557 https://doi.org/10.1021/acsfoodscitech.1c00435

4. ***Miriam C. Bassler**, Mona Stefanakis, Inês Sequeira, Edwin Ostertag, Alexandra Wagner, Jörg W. Bartsch, Marion Roeßler, Robert Mandic, Eike F. Reddmann, Anita Lorenz, Karsten Rebner, Marc Brecht*; Comparison of Whiskbroom and Pushbroom darkfield elastic light scattering spectroscopic imaging for head and neck cancer identification in a mouse model, Anal. Bioanal. Chem. 413, 7363–7383 (**2021**), https://doi.org/10.1007/s00216-021-03726-5

5. *Mona Stefanakis, Anita Lorenz, Jörg W. Bartsch, **Miriam C. Bassler**, Alexandra Wagner, Marc Brecht, Axel Pagenstecher, Jens Schittenhelm, Barbara Boldrini, Sabrina Hakelberg, Susan Noell, Christopher Nimsky, Marcos Tatagiba, Rainer Ritz, Karsten Rebner, and Edwin Ostertag*; Formalin Fixation as Tissue Preprocessing for Multimodal Optical Spectroscopy Using the Example of Human Brain Tumour Cross Sections, Journal of Spectroscopy, **2021**, Article ID 5598309, https://doi.org/10.1155/2021/5598309

6. *Quan Liu, Frank Wackenhut, Otto Hauler, **Miriam Scholz**, Sven zur Oven-Krockhaus, Rainer Ritz, Pierre-Michel Adam, Marc Brecht, Alfred J. Meixner*; Hypericin: Single Molecule Spectroscopy of an Active Natural Drug, J. Phys. Chem. A **2020**, 124, 12, 2497–2504, https://doi.org/10.1021/acs.jpca.9b11532

7. *Edwin Ostertag, **Miriam Scholz**, Julia Klein, Karsten Rebner, and Dieter Oelkrug*; Pigmentation of White, Brown, and Green Chicken Eggshells Analyzed by Reflectance, Transmittance, and Fluorescence Spectroscopy, ChemistryOpen **2019**, 8, 1084–1093, https://doi.org/10.1002/open.201900154

Prepared Manuscripts

8. ***Miriam C. Bassler****, Mona Stefanakis, Elena Gerhard-Hartmann, Ashutosh Mukherjee, Almoatazbellah Youssef, Rudolf Hagen, Agmal Scherzad, Manuel Stöth, Edwin Ostertag, Maria Steinke, Marc Brecht, Stephan Hackenberg, Till Jasper Meyer*; Differentiation of salivary gland and tumor entities by Raman imaging combined with multivariate data analysis

9. ***Miriam C. Bassler*****, Jonas Hiller*, Frank Wackenhut, Sven zur Oven-Krockhaus, Rainer Ritz, Kai Braun, Alfred J. Meixner, Marc Brecht*; Investigation of cell death induced by hypericin-based photodynamic therapy on glioma single cells using confocal fluorescence lifetime imaging microscopy

Declaration of Contribution

Nr.	Accepted publication yes/no	List of authors	Position of candidate in list of authors	Scientific ideas by the candidate (%)	Data generation by the candidate (%)	Analysis and interpretation by the candidate (%)	Paper writing done by the candidate (%)
1.	Yes	Mona Stefanakis* and Miriam C. Bassler*, Tobias R. Walczuch, Elena Gerhard-Hartmann, Almoatazbellah Youssef, Agmal Scherzad, Manuel Stöth, Edwin Ostertag, Rudolf Hagen, Maria Steinke, Stephan Hackenberg, Marc Brecht, Till Jasper Meyer	1 (*shared)	50	10	60	60
2.	Yes	Miriam C. Bassler, Tim Rammler, Frank Wackenhut, Sven zur Oven-Krockhaus, Ivona Secic, Rainer Ritz, Alfred J. Meixner, Marc Brecht	1	90	70	70	90
3.	Yes	Mona Stefanakis, Miriam C. Bassler, Thorsten Böltzig, Edwin Ostertag, Dominik Allnoch, Ralf Zuber, Marc Brecht, Karsten Rebner	2	0	10	10	50
4.	Yes	Miriam C. Bassler, Mona Stefanakis, Inês Sequeira, Edwin Ostertag, Alexandra Wagner, Jörg W. Bartsch, Marion Roeßler, Robert Mandic, Eike F. Reddmann, Anita Lorenz, Karsten Rebner, Marc Brecht	1	70	60	60	90
5.	Yes	Mona Stefanakis, Anita Lorenz, Jörg W. Bartsch, Miriam C. Bassler, Alexandra Wagner, Marc Brecht, Axel Pagenstecher, Jens Schittenhelm, Barbara Boldrini, Sabrina Hakelberg, Susan Noell,	4	5	0	5	5

Nr.	Accepted publication yes/no	List of authors	Position of candidate in list of authors	Scientific ideas by the candidate (%)	Data generation by the candidate (%)	Analysis and interpretation by the candidate (%)	Paper writing done by the candidate (%)
		Christopher Nimsky, Marcos Tatagiba, Rainer Ritz, Karsten Rebner, and Edwin Ostertag					
6.	Yes	Quan Liu, Frank Wackenhut, Otto Hauler, Miriam Scholz, Sven zur Oven-Krockhaus, Rainer Ritz, Pierre-Michel Adam, Marc Brecht, Alfred J. Meixner	4	0	5	5	0
7.	Yes	Edwin Ostertag, Miriam Scholz, Julia Klein, Karsten Rebner, and Dieter Oelkrug	2	10	20	10	20
8.	No	Miriam C. Bassler, Mona Stefanakis, Elena Gerhard-Hartmann, Ashutosh Mukherjee, Almoatazbellah Youssef, Rudolf Hagen, Agmal Scherzad, Manuel Stöth, Edwin Ostertag, Maria Steinke, Marc Brecht, Stephan Hackenberg, Till Jasper Meyer	1	50	90	90	90
9.	No	Miriam C. Bassler*, Jonas Hiller*, Frank Wackenhut, Sven zur Oven-Krockhaus, Rainer Ritz, Kai Braun, Alfred J. Meixner, Marc Brecht	1 (*shared)	90	50	60	80

Acknowledgments

I would like to express my honest appreciation to all persons, who had accompanied me along the way to finish this doctoral thesis: First of all, my sincerest gratitude goes to my supervisor **Prof. Dr. Marc Brecht**, who guided me with his experience and knowledge throughout the last years and who was always open to new ideas or projects. I am grateful for all your input and support as well as our scientific exchange. Thank you for teaching me the scientific mindset and encouraging me to work independently and focused. Furthermore, I would like to sincerely thank **Prof. Dr. Alfred J. Meixner**, **Prof. Dr. Karsten Rebner**, **Prof. Dr. Ralf Kemkemer** and **Prof. Dr. Petra Kluger** for the opportunity to perform parts of my experiments in their laboratories and for fruitful discussions. I really appreciated your great concession and your trust to let me work in your groups. Additionally, I would like to express many thanks to **Prof. Dr. Thomas Chassé** and **Prof. Dr. Erik Schäffer** for agreeing to be my second correspondent of the thesis and one of my disputation examiners.

Special thanks go to **Dr. Edwin Ostertag** and **Dr. Frank Wackenhut** for their scientific guidance and their extraordinary help with all manuscript preparations from start to finish. Thank you for sharing your experiences on a professional and personal level with me. Many and warmest thanks I would like to extend to my friends and closest colleagues **Mona Stefanakis**, **Kerstin Frey**, **Karen Ende**, **Dr. Svenja Nellinger**, **Alexandra Wagner**, **Julia Steinbach**, **Ashutosh Mukherjee**, **Kiriaki Athanasopulu** and **Benjamin Naggay** for their mental and professional assistance throughput all phases of this work. You were always most understanding, helpful and supportive in every step along the way! I also thank my colleagues **Dr. Anita Lorenz**, **Tobias Drieschner**, **Tim Bäuerle**, **Barbara Boldrini**, **Alexander Stuhl** and **Mohammad Al Ktash** for introducing me to the instrumental setups and your technical advice.

Additionally, I want to thank the whole Meixner group, especially **Tim Rammler**, **Jonas Hiller**, **Dr. Sven zur Oven-Krockhaus**, **Dr. Quan Liu** and **Dr. Kai Braun** for their great help with FLIM experiments, sharing their knowledge and expertise with me and our good and productive cooperation. I want to further thank the whole Kluger group, especially **Franziska Albrecht**, **Sophia Nowakowski**, **Jannis Wollschlaeger**, **Lisa Michalek** and **Freia Schmidt** for cordially accepting me to work in their group and helping me out with either experimental supplies or scientific advice. Moreover, many thanks go to **Prof. Dr. Jörg Bartsch**, **Dr. Inês Sequeira**, **Dr. Marion Roeßler**, **Prof. Dr. Robert Mandic**, **Dr. Till Meyer** and **Dr. Dr. Elena Gerhard-Hartmann** for providing and preparing the tissue samples, their histological characterization and the valuable input on the manuscripts.

Financial support was provided by the MINT-funding of **Vector Stiftung Stuttgart** and the Cooperative Doctoral Fellowship Reutlingen-Tübingen “Intelligent process and material development in Biomateriomics”, sponsored by the **Ministry of Science, Research and Arts Baden-Württemberg**. I want to thank all doctoral candidates and supervising professors of the fellowship program for the regular scientific exchange and the constructive discussions in our seminars.

My second most important gratitude goes to my parents **Bernd** and **Charlotte**, my sister **Sandra**, my parents-in-law **Peter** and **Ursula** and my brother-in-law **Stefan** for their love, encouragement and constant advice in every respect. Only with your support I kept going, even in the hardest times! Last but not least, the most important gratitude I want to express to my husband **Florian**, to whom I am dedicating this thesis! I cannot thank you enough for your incredible patience, sympathy and understanding over the last years! Thank you for all the backup and strength you gave me! You are my unfailing pillar without whom I could not stand!

Affirmation in Lieu of an Oath

I hereby affirm that the doctoral thesis, entitled “Spectroscopic and Multivariate Approaches for Tumor Diagnostics and -Therapy” is my own work, written independently and without assistance other than the resources cited. Literal or textual quotes are labeled as such. I have indicated the bodies of work, including tables and illustrations, which originate from earlier work of other authors. In each case, I have quoted the origin thereof. I declare that the guidelines for ensuring good scientific practice at the University of Tübingen have been maintained. This doctoral thesis has not been submitted, in neither identical nor similar form, to any other examination authority or university, and has not yet been published. I affirm in lieu of oath that these statements are true and that nothing has been withheld. I am aware that a false statement on oath shall be punished with imprisonment for up to three years or a fine.

Lichtenstein, 11/07/2022

Miriam Corina Bassler

Eidesstaatliche Erklärung

Ich erkläre hiermit, dass ich die zur Promotion eingereichte Arbeit mit dem Titel „Spectroscopic and Multivariate Approaches for Tumor Diagnostics and -Therapy“ selbstständig verfasst, nur die angegebenen Quellen und Hilfsmittel benutzt und wörtlich oder inhaltlich übernommene Zitate also solche gekennzeichnet habe. Ich erkläre, dass die Richtlinien zur Sicherung guter wissenschaftlicher Praxis der Universität Tübingen beachtet wurden. Ich versichere an Eides statt, dass diese Angaben wahr sind und dass ich nichts verschwiegen habe. Mir ist bekannt, dass die falsche Angabe einer Versicherung an Eides statt mit Freiheitsstrafe bis zu drei Jahren oder mit Geldstrafe bestraft wird.

Lichtenstein, 07.11.2022

Miriam Corina Bassler